UNIVERSITÀ
DEGLI STUDI
DI PADOVA

Administrative unit: University of Padova

Department: **Land, Environment, Agriculture and Forestry (LEAF)**

PhD Program: **Land, Environment, Resources and Health (LERH)**

Batch: XXXIV

MONITORING AND ASSESSMENT OF THE IMPACT OF HUMAN ACTIVITIES ON ECO-ENVIRONMENT BASED ON REMOTE SENSING

Joint observation from daytime and nighttime satellites

PhD Program Coordinator: Prof. Marco Borga

Supervisor: Prof. Francesco Marinello
Co-Supervisor: Prof. Zhifeng Wu

External evaluators: Prof. Serena Ceola (Università di Bologna)
Prof. Jun Li (Sun Yat-sen University)

PhD candidate: Zihao Zheng

UNIVERSITÀ DEGLI STUDI DI PADOVA

Sede Amministrativa: Università degli Studi di Padova

Dipartimento Territorio e Sistemi Agro-Forestali (TESAF)

CORSO DI DOTTORATO DI RICERCA: **Land, Environment, Resources, Health (LERH)**

Ciclo: XXXIV

MONITORAGGIO E VALUTAZIONE DELL'IMPATTO DELLE ATTIVITÀ UMANE SULL'ECO-AMBIENTE BASATO SUL TELERILEVAMENTO

Osservazione congiunta di satelliti diurni e notturni

Coordinatore: Prof. Marco Borga

Supervisore: Prof. Francesco Marinello
Co-Supervisore: Prof. Zhifeng Wu

Valutatori esterni: Prof. Serena Ceola (Università di Bologna)
Prof. Jun Li (Sun Yat-sen University)

PhD candidate: Zihao Zheng

Acknowledgements

Time passes quickly like a white pony's shadow across a crevice. It seems like yesterday when I first came to Padua and to the Agripolis campus. Looking back on the three years I spent pursuing my Ph.D. degree at the University of Padova, I have many emotions and people that I would like to acknowledge.

The first person I would like to thank is my supervisor, Prof. Francesco Marinello. I am grateful to him for offering me a Ph.D. position and bringing me into his group, which is caring, enthusiastic and rigorous group. Throughout the three-year study period, his divergent thinking can always give me the greatest inspiration and hints when I encounter difficulties in my research. Also, his support and assistance in attending international academic conferences gave me a wonderful opportunity to exchange and learn from my peers. With his great humanity, he supported my three years of doctoral studies (both in Italy and in China) and gained a lot.

Prof. Zhifeng Wu is my co-supervisor during my studies in China. He provided me with excellent laboratories and facilities for my research and study in China and gave me enthusiastic and productive advice on my activities. His vast background knowledge of geography and ecology provided me with another perspective to think about the phenomena on the earth's surface, which is crucial to advance my research.

I would like to express my gratitude to my colleagues and friends that I worked with in the Italian office, Tatev, Marco, Ahmed, Alessia and Alexander. I would like to thank them for their help and enthusiasm when I joined the office, they actively shared their knowledge, smiles and tasty food with me. Thanks to them, my life in Italy has been sunnier and I have greater expectations to return to Italy. Wish them a brilliant life in their next days too!

Also, I would like to acknowledge my Chinese colleagues and friends. The candidates, Qifei and Lingzi, who belonged to the same Ph.D. program as me, and we shared the same apartment during our period in Italy. Many thanks to them for sharing with me in their lives and work and making my Italian life full of memories. There were also candidates from other departments, such as Zhicheng from the Department of Geosciences and Yanzhang and Xinyuan from the Department of Psychology, and we planned many trips to Europe to enrich my holiday life.

I want to express my gratitude to my thesis reviewers. Their revisions significantly contributed to improving the quality of this work.

Last, I would like to express my gratitude to my family for their support and concern for me. Especially Mrs. Zheng, who took care of family maintenance and chores while I was pursuing my Ph.D. in Italy, allowed me to carry out my research without distractions. Her support and tolerance, her love and care for me are the biggest reliance and motivation for my challenging work. She is the light in my life when I am in the dark.

Table of Contents

Acknowledgements 1
Summary 6
Sommario 7
1. Introduction 8
1.1 Background 8
1.2 Research questions and objectives 14
1.3 Explanation of the thesis format 15
2. The desaturation method of DMSP/OLS nighttime light data based on vector data: taking the rapidly urbanized China as an example [1] 17
2.1 Abstract 17
2.2 Introduction 17
2.3 Previous approach to reduce NTL saturation 19
2.4 Implementation of VDANTLI 22
2.5 Results and Analysis 24
2.5.1 Assessment of VDANTLI desaturation capacity 24
2.5.2 Temporal and Resolution Characteristics of VDANTLI 31
2.6 Discussion 34
2.6.1 Influence of auxiliary parameters on desaturated model 34
2.6.2 Challenges in VDANTLI applications 36
2.7 Conclusions 36
References 38
3. The interannual calibration and global nighttime light fluctuation assessment based on pixel-level linear regression analysis [2] 41
3.1 Abstract 41
3.2 Introduction 41
3.3 Data 44
3.4 Methods 45
3.4.1 Interannual Calibration of DMSP/OLS NTL Time Series Datasets 45
3.4.2 Evaluation of Calibration Results 48
3.4.3 Global Light Intensity Change Analysis 49
3.5 Results 50
3.5.1 Interannual Correction Results of NTL Datasets 50
3.5.2 Evaluation of Interannual Calibration Performance 51
3.5.3 Global Night Lighting Intensity Changes 56
3.6 Discussion 61
3.6.1 PBPIF-based Calibration Model and Comparison of Results 61
3.6.2 Fluctuation Characteristics of NTL 63
3.7 Conclusions 65
References 67
4. A Simple Method for Near-Real-Time Monthly Nighttime Light Image Production [3] 70
4.1 Abstract 70
4.2 Introduction 70
4.3 Data and study area 71

4.4 Method 72
4.4.1 Filtering of Cloud-Polluted Pixels 72
4.4.2 Reduces Moonlight Radiation 73
4.5 Data validation 75
4.6 Discussion 79
4.7 Conclusion 80
References 82
5. Pixel-level cross-sensor calibration quality identification method for extended nighttime light products [4] 83
5.1 Abstract 83
5.2 Introduction 83
5.3 Data sources 85
5.4 Methods 86
5.4.1 General procedures 86
5.4.2 Pixel-level light radiation trend analysis 87
5.4.3 Pixel-level logical diagnostics 88
5.5 Results 91
5.5.1 Global light radiation $PCI_{Standard}$ layer 91
5.5.2 PCI Results of LiNTL and ChenNTL 94
5.5.3 Quality assessment of LiNTL and ChenNTL 95
5.6 Discussion 96
5.6.1 Differences between $ENQI_{LiNTL}$ and $ENQI_{ChenNTL}$ 96
5.6.2 Advantages and potential compared to TSOL 98
5.7 Conclusion 99
References 101
Supplementary files 104
6. Africa's protected areas are brightening at night: a long-term light pollution monitor based on nighttime light imagery [5] 109
6.1 Abstract 109
6.2 Introduction 109
6.3 Materials and methods 111
6.3.1 Study area 111
6.3.2 Data sources 112
6.3.3 Methods 113
6.4 Results 115
6.4.1 Light pollution dynamics of PAs 115
6.4.2 Categorized light pollution of PAs 117
6.4.3 Links between human activity and light pollution in PAs 119
6.5 Discussion 122
6.5.1 Light pollution characteristics of PAs 122
6.5.2 Potential and challenges of aligned NTL data for light pollution studies in PAs 124
6.5.3 Further research 126
6.6 Conclusion 126
References 128
7. Exploration of eco-environment and urbanization changes in coastal zones: A case study in China over

the past 20 years [6] 131
7.1 Abstract 131
7.2 Introduction 131
7.3 Study area and data sources 133
7.3.1 Study area 133
7.3.2 Data and Pre-processing 134
7.4 Methods 135
7.4.1 Construction of RSEI 135
7.4.2 Construction of the nighttime light index 136
7.4.3 Coupling coordination model 137
7.5 Results 137
7.5.1 Eco-environment in the coastal zone 137
7.5.2 Nighttime light in coastal areas 140
7.5.3 Interaction between eco-environment and urbanization 142
7.6 Discussion 146
7.6.1 Improvement of coastal ecological environment 146
7.6.2 Urbanization process of coastal cities 147
7.6.3 Interaction between urbanization and eco-environment 148
7.6.4 Potentials and limitations 149
7.7 Conclusion 149
References 151
8. Spatial and temporal characteristics of NO_2 pollution in China based on satellite observation platform [7] 156
8.1 Abstract 156
8.2 Introduction 156
8.3 Study area 158
8.4 Materials and methods 159
8.4.1 Data collection 159
8.4.2 Spatial–temporal variation models 161
8.4.3 Impact factors analysis 162
8.5 Results 164
8.5.1 Coherence of NO_2 surface concentration and tropospheric columns 164
8.5.2 Spatial–temporal characteristics of tropospheric NO_2 columns 165
8.5.3 Impact factors of tropospheric NO_2 columns 172
8.6 Discussion 174
8.6.1 Division line of tropospheric NO_2 columns 174
8.6.2 Spatial−temporal characteristics comparison at different administrative units level 175
8.6.3 The impact factors analysis at different administrator units level 177
8.7 Conclusions 178
References 181
9. Global-scale detection of human activities and ecological status dynamics 185
9.1 Abstract 185
9.2 Introduction 185
9.3 Methods 187
9.3.1 Overview 187

9.3.2 Defining the Human Activity Zone Grid 187
9.3.3 Modified RSEI and its dynamics 188
9.3.4 Long-term nighttime light dynamic identification 190
9.4 Results 190
9.4.1 Global dynamics of nighttime light intensity 190
9.4.2 Global environmental conditions dynamics 192
9.4.3 Coordination coupling between human activities and eco-environment 195
9.5 Discussion 197
9.5.1 Performance validation of MRSEI and PCI layers 197
9.5.2 Spatial heterogeneity of human activities on the environment 200
9.6 Conclusions 204
References 206
10. Discussion 208
11. Conclusions 212
References 213
Annexes 218
Annex 1: Detection of city integration processes in rapidly urbanizing areas based on remote sensing imagery [8] 219
Background 219
Study areas 219
Satellite images 220
Results 221
References 223
Annex 2: The balance of eco-environment and urbanization development in the Yangtze River Delta Urban Agglomeration based on GEE [9] 225
Background 225
Study areas 225
Methods 226
Results 227
References 230

Summary

Since the Industrial Revolution, rapid global population growth and intense urbanization processes have led to overexploitation of natural resources and reshaped the land surface. According to the IPCC Climate Change 2021 report, human activities have caused global warming, the climate system has experienced widespread and rapid changes, and the probability of compound extreme weather events increased significantly. Therefore, timely monitoring of human activities and the natural environment is of great importance to the sustainable development of human society. Since there are several limitations to the commonly used ground-based monitoring solutions, remote sensing platforms, which can quickly obtain regional and even global information on surface processes, have become an essential tool for Earth observations. Thus, this thesis aims to explore the integration of daytime and nighttime remote sensing to track the dynamics of human activity footprints and eco-environment, and to quantitatively assess the interactions between them, which is valuable for promoting SDGs. To achieve this objective, a series of efforts both in data processing and application exploration were implemented. First, the calibration models for saturation phenomena and interannual turbulence present in NTL data were developed. Second, based on the most advanced Black Marble Suite data, a method for near real-time composited monthly NTL images was proposed, which provided an important support for short-term period event effect detection. In addition, the quality flag layers for the widely used ENTL data today have been produced and open sourced. Finally, human activities and eco-environmental dynamics at local, regional and global scales were assessed and discussed through NTL data and RSEI models. Although these efforts deserve to be advanced and refined, the works in this thesis has led to some new intellectual discoveries. Some of the models and data products developed in the thesis have been applied by other scholars to regional studies in different contexts, which is encouraging. In conclusion, the work in this thesis expands the perspective of Earth observation and makes a positive contribution to help us understand human-environment interactions more precisely.

Sommario

A partire dalla rivoluzione industriale, la rapida crescita della popolazione globale e gli intensi processi di urbanizzazione hanno portato a un eccessivo sfruttamento delle risorse naturali e hanno rimodellato la superficie terrestre. Secondo il rapporto IPCC Climate Change 2021, le attività umane hanno causato un riscaldamento globale: il sistema climatico ha sperimentato cambiamenti diffusi e rapidi, e la probabilità di eventi meteorologici estremi composti è aumentata notevolmente. Pertanto, il monitoraggio tempestivo delle attività umane e dell'ambiente naturale è di grande importanza per lo sviluppo sostenibile della società. Poiché ci sono diverse limitazioni alle soluzioni di monitoraggio a terra comunemente usate, le piattaforme di telerilevamento, che possono ottenere rapidamente informazioni regionali e persino globali sui processi di superficie, sono diventate uno strumento essenziale per le osservazioni della terra. Così, questa tesi mira ad esplorare l'integrazione del telerilevamento diurno e notturno per tracciare le dinamiche delle impronte delle attività umane e dell'eco-ambiente, e per valutare quantitativamente le interazioni tra loro: tutti questo è di grande importanza per la promozione degli Obiettivi di Sviluppo Sostenibile. Per raggiungere questo obiettivo, è stata implementata una serie di attività di ricerca sia nell'elaborazione dei dati che nell'esplorazione delle applicazioni. In primo luogo, sono stati sviluppati i modelli di calibrazione per i fenomeni di saturazione e turbolenza interannuale presenti nei dati NTL. In secondo luogo, è stato proposto un metodo basato sui dati più avanzati di Black Marble Suite, per le immagini mensili NTL composte in tempo quasi reale, il quale ha fornito un importante supporto per il rilevamento degli effetti degli eventi a breve termine. Inoltre, sono stati prodotti e resi open source i livelli di riferimento di qualità per i dati ENTL, attualmente molto utilizzati . Infine, le attività umane e le dinamiche ecoambientali a scala locale, regionale e globale sono state valutate e discusse attraverso i dati NTL e i modelli RSEI. Anche se questi lavori meritano di essere avanzati e raffinati, i risultati riportati in questa tesi hanno portato ad alcune nuove scoperte intellettuali. Alcuni dei modelli e dei prodotti di dati sviluppati nella tesi sono stati applicati da altri studiosi a studi regionali in diversi contesti, il che è incoraggiante. In conclusione, il lavoro in questa tesi espande la prospettiva dell'osservazione della Terra e dà un contributo positivo per aiutarci a capire le interazioni uomo-ambiente in modo più preciso.

1. Introduction

1.1 Background

Humankind is experiencing a new epoch, characterized by an unprecedented pressure exerted on the planet: many scientists recognize a new geological era, namely Anthropocenee (Nijhuis and Jauslin, 2015; Basu and Das, 2021). The most significant feature of the Anthropocene is the expansion of human activities, the dramatic increase of intensity, and ultimately triggering the rapid urbanization process globally (Chwałczyk, 2020). According to the World Bank, the global population in 2020 was 7.753 billion and the urban population was 4.352 billion. As urbanization continues, the share of urban population will reach 68% by 2050 (Figure 1.1, Ritchie and Roser, 2018). The rapid growth of urbanization has had a profound impact on countries and regions, especially on developing countries . For example , over the past four decades of reform and opening up, China's urbanization has made impressive achievements worldwide , with the urbanization rate rising from 17.9% in 1978 to 60.6% in 2019, with an average annual growth rate of 1.04% (Shao et al., 2020).

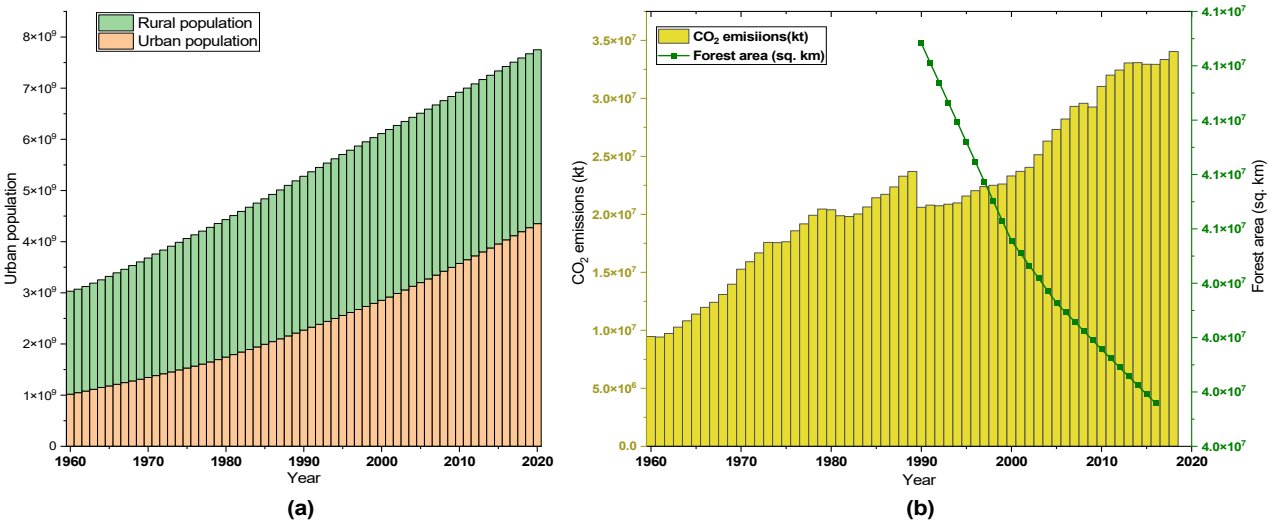

Figure 1.1. The dynamics of (a) global urban population, rural population, (b) total CO_2 emissions and forest area over the past decades (derived from World Bank database).

Although urbanization has been effective in boosting regional economic development and improving social and public welfare, etc., extensive research work has highlighted the side effects of u aggressive urbanization (Li et al., 2012; Uttara et al., 2012; Srinivasan et al., 2013; Nathaniel and Adeleye, 2021). Within the context of rapid urbanization on a global scale, increasing human activities are continuously reshaping the surface environment and are serving as a major driver of global environmental and ecological change. For example, the continued rise in urban population density stimulates the uncontrolled expansion of built-up land, and the natural landscapes are rapidly transformed into artificial landscape (Zhu et al., 2020; Zhou et al., 2021). The transformation of natural cover and impervious surfaces further exacerbates the urban heat island effect and brings about greater energy consumption, pollutant emissions (Ma and Peng, 2021; Xu et al., 2021b). Besides, fossil fuel consumption and deforestation are accelerating global warming and leading to further

extinction of living species at an unprecedented rate (Petrakopoulou et al., 2020; Gatti et al., 2021). On August 9, 2021, the Intergovernmental Panel on Climate Change (IPCC) released its Sixth Assessment Report, which clearly states that global warming will reach at least 1.5 °C under all emissions scenarios, and even under the most ambitious low-emissions scenario, global warming will reach 1.5 °C by the 2130s (Figure 1.2, IPCC, 2021).

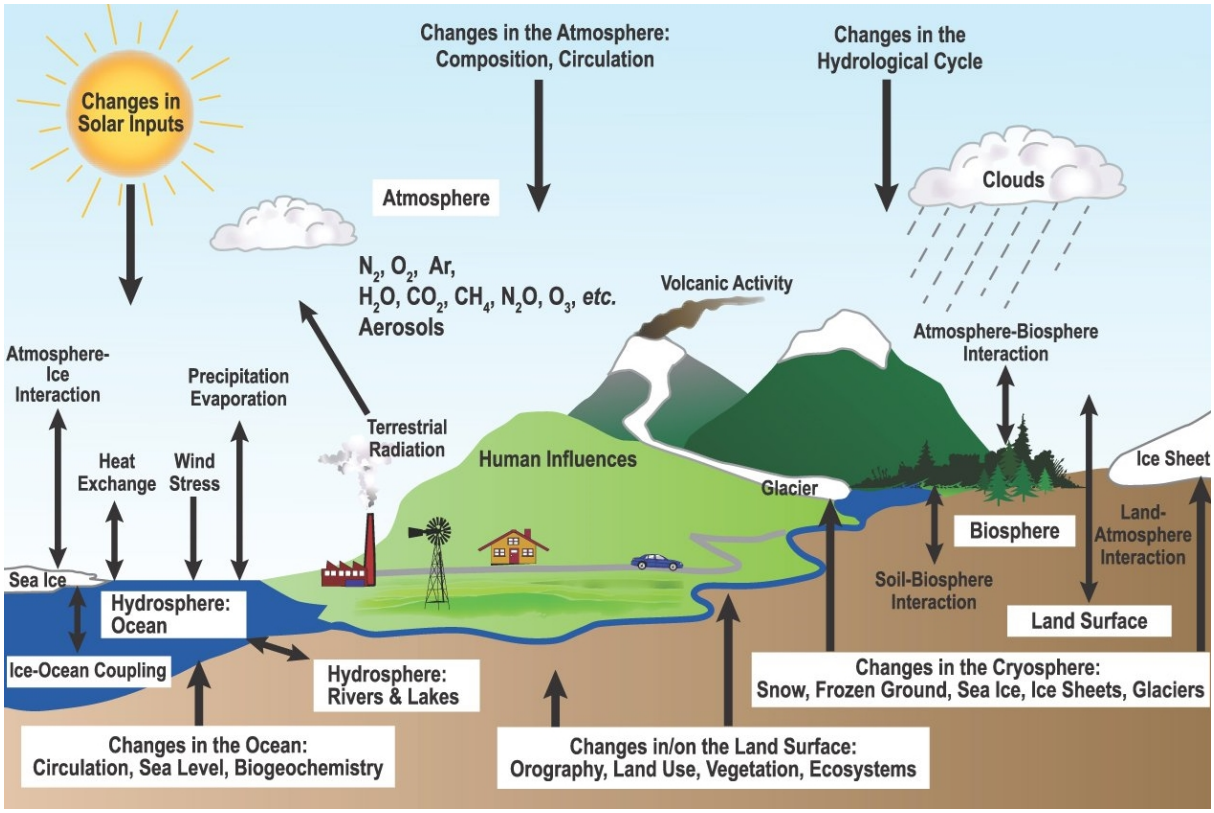

Figure 1.2. Schematic view of the components of the climate system, their processes and interactions. (Sources: IPCC report- historical overview of climate change-science FAQ 1.2)

As a positive response to global development and climate-environmental change, the proposed UN Sustainable Development Goals (SDGs) set goals and directions for development and efforts in various regions and countries, especially the Target 15 (Protect, restore and promote sustainable use of terrestrial ecosystems, sustainably manage forests, combat desertification, halt and reverse land degradation, and halt biodiversity loss, Figure 1.3) (Kavvada et al., 2020). Considering the scale and dynamism of global environmental change and human activities, remote sensing technology, which has developed at a rapid pace in recent years, provides crucial data support for the realization of SDGs, offering new perspectives to improve our understanding of urbanization and environmental change. Satellite images of the Earth's surface, observed from space by remote sensing satellites, make it possible to monitor, analyze, assess and predict what changes are occurring on the Earth's surface, making it possible to quantify and track the dynamics of human activities and their environmental impacts (Li et al., 2020). With the advancement of sensor technology, remote sensing-based applications have changed from single, static analysis to multi-temporal, multi-source fusion dynamic monitoring, which matches the requirements of ecological environment monitoring. Therefore, the past decades have witnessed an abundance of research and application work based on remote sensing platforms,

which have provided important support for ecological environmental protection, mainly including natural disaster monitoring (Zhao et al., 2018), water environment monitoring (Sagan et al., 2020), urban sprawl (Chettry and Surawar, 2021), urban green space investigation (Shin et al., 2020), and urban heat island effect (Kim and Brown, 2021).

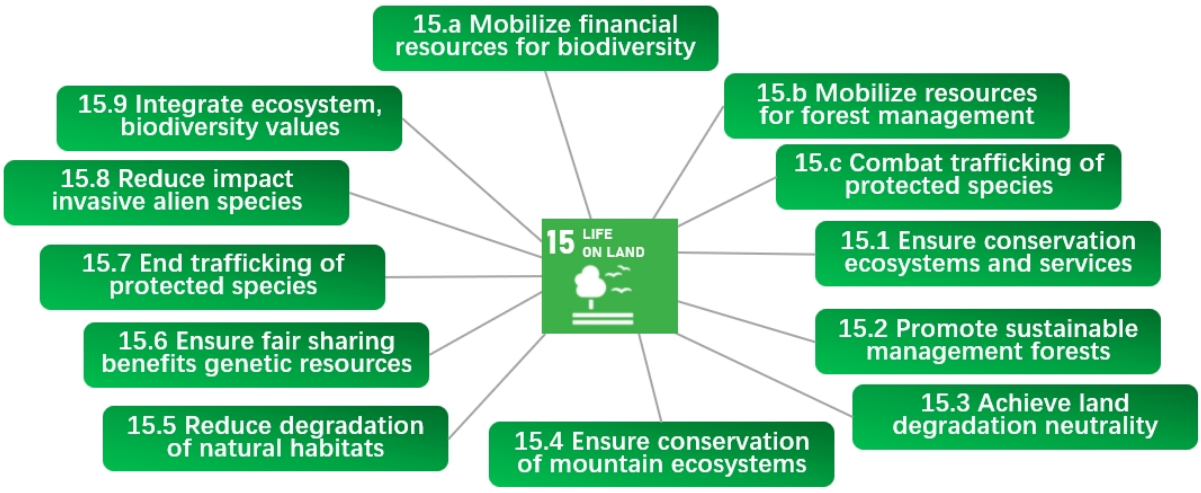

Figure 1.3. Target 15 of the UN Sustainable Development Goals (SDGs).

As remote sensing technology becomes more mature, the progress of remote sensing-based Land Surface Ecological Status (LSES) monitoring is remarkable. Compared with traditional ground-based in situ monitoring, which is a time-consuming, expensive and labor-intensive method, the monitoring scheme based on daytime optical remote sensing can quickly obtain spectral information of regional and even global targets and retrieve various ecological indicators, thus becoming an indispensable method for LSES monitoring. Currently, the spectral indices based on remote sensing spectral inversion for monitoring LSES can be broadly classified as single-element type and element-integrated type. The single element indices of spectral inversion can be categorized as 1) **vegetation indices**, including Ratio Vegetation Index (Major et al., 1990), Normalized Difference Vegetation Index (Goward et al., 1991), Enhanced Vegetation Index (Nagler et al., 2005), Green Vegetation Index (Chen et al., 1993), Perpendicular Vegetation Index (Richardson and Wiegand, 1977), Soil-Adjusted Vegetation Index (Huete, 1988), etc.; 2) **soil moisture indices**, including MODIS short-wave infrared spectral-based soil moisture retrieval models (Zhao et al., 2010), normalized spectral slope absorption indices (Zheng et al., 2015) and the red near-infrared spectral-based soil moisture retrieval model (Li et al., 2018); 3) **evapotranspiration**, including the SEBAL model (Bastiaanssen et al., 1998), the METRIC model (Allen et al., 2007) and the exponential evapotranspiration model (Yao et al., 2011); 4) **land surface thermal environment**, including single channel algorithm (Jiménez-Muñoz et al., 2008), split window algorithm (Wan and Dozier, 1996) and neural network based algorithm (Mao et al., 2018). The single-element type indices can only explain one aspect of ecological characteristics, while in fact, the interaction among indicators in the whole surface ecological environment integrally affects the whole ecosystem and cannot be separated separately. Therefore, based on single-element indices, some indices and models that integrate multiple elements to express the state of surface ecological environment in an integrated manner have been proposed. Comparing to single-element models, multiple element indices together are used to identify more features that

can complementarily capture LSES changes to monitor their status. The most widely used and representative element-integrated index is the Remote Sensing Based Ecological Index (RSEI) proposed by Xu (2013), which integrates four ecological indicators of greenness, humidity, heat and dryness to reflect the regional ecological environment, and overcomes the shortcomings of a single indicator by aggregating multidimensional indicators through principal component transformation (Xu et al., 2018). Although RSEI is currently widely used for regional and small-scale dynamic monitoring of surface ecological environment, it still faces some limitations, such as instability of temperature, fluctuation of time-series values, and uncertainty of applicability for large scale studies, which need to be improved and tested in the following research.

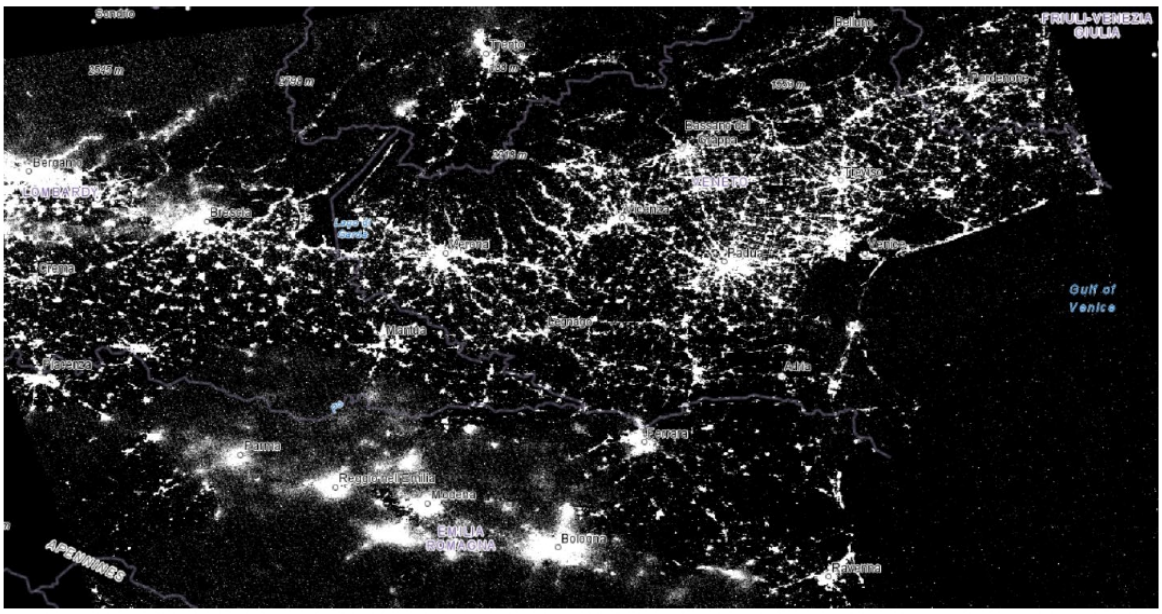

Figure 1.4 The nighttime light in Veneto, Italy (November 18, 2018, imaged by Luojia-1 01).

Differently from daytime optical remote sensing, nighttime light (NTL) remote sensing can detect faint light radiated from the ground surface at night, which is not accessible by daytime optical remote sensing. Since most of the surface NTL radiation comes from artificial lighting devices used in human activities, nighttime light images have been proven to reflect more intuitively the differences in human activities at night. With the advantages of large coverage, fast timeliness and easy access, NTL images are suitable for multi-scale, long time series of urbanization and human footprint tracking, and they provide a new perspective for perceiving the ever-changing world (Figure 1.4). Up to now, there are several satellite projects carrying sensors with NTL imaging capability, such as Defense Meteorological Satellite Program/Operational Linescan System (DMSP/OLS, Small et al., 2005), Suomi National Polar Partnership/Visible Infrared Imaging Radiometer Suite (NPP/VIIIRS, Hillger et al., 2013), Earth Remote Observation Satellite-B (EROS-B, Levin et al., 2014), Luojia-1 01 (Ou et al., 2019) and Jilin-1 (Guk and Levin, 2020). The spatial resolution of these light images has been changed from 1000 m to 0.92 m, and the spectral layer has been developed from single-band grayscale images to multi-band color images, providing more possibilities for night light remote sensing applications. Previous studies have shown that NTL remote sensing images can be used not only to analyze multi-scale urban spatial structure and evolution pattern, including urban elements and internal spatial structure (Chen et al., 2017), urban areas (Sutton, 2003), urban system hierarchical structure and urban clusters (Yu et

al., 2014; Tselios and Stathakis, 2020), but also to estimate multi-scale socio-economic development indicators, including population (Tan et al., 2018), GDP (Ma et al., 2012), electricity consumption (Jasiński, 2019), carbon emission (Yang et al., 2020), total freight (Shi et al., 2015), urban housing vacancy rate (Du et al., 2018), etc. In addition, there are also studies on the application of NTL images to urban public safety, including natural disasters (Ceola et al., 2014; Elshorbagy et al., 2017; Zhao et al., 2018), epidemics (Lan et al., 2021), festivals (Zhang et al., 2020), wars (Li et al., 2013), environment (Wang et al., 2016; Paranunzio et al., 2019), etc. Despite the richness of NTL data-based applications, the current use of NTL data still faces several challenges. For example, saturation phenomena (Zhang et al., 2013), halo effects (Abrahams et al., 2018), and interannual disruptions (Pandey et al., 2017) are widespread in DMSP/OLS data products, while NPP/VIIRS data are more susceptible to cloud (Cao et al., 2013), moonlight (Zheng et al., 2021), and atmospheric disturbances (Ceola et al., 2019; Wang et al., 2020) and induce seasonal effects (Levin, 2017) due to its shorter imaging and update intervals.

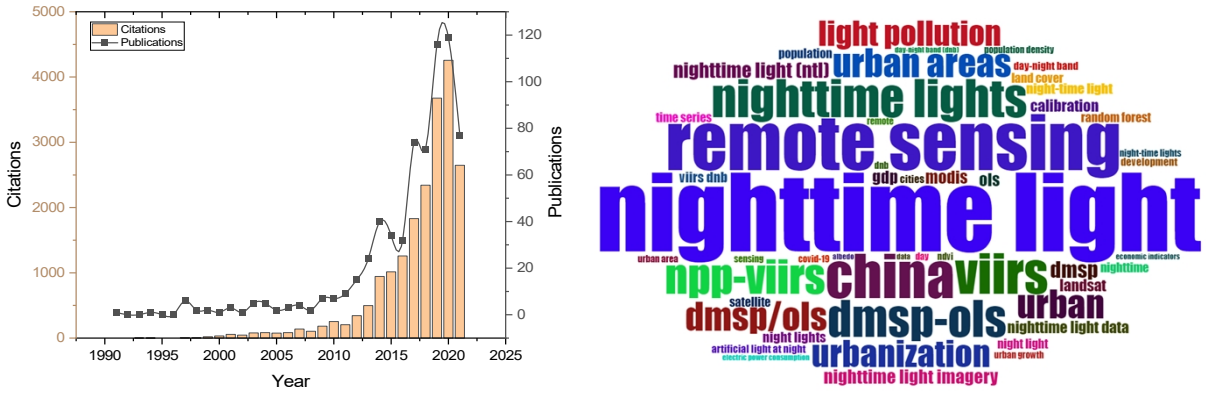

(a) (b)

Figure 1.5 Statistics of night lighting (NTL) publications: (a) published items and citations from 1991 to 2021, and (b) main topics of related publications.

Furthermore, with a desire to track anthropogenic footprints and urbanization over a longer span, the integration of DMSP/OLS and NPP/VIIRS data for global light radiation dynamics analysis has become the most attractive area of interest nowadays (Figure 1.5). However, the differences in sensor parameters and data performance between DMSP/OLS and NPP/VIIRS NTL images make it impossible to perform dynamic analysis directly using heterogenous NTL products. Therewith, calibration schemes, models at different scales were proposed, including power function transformation (Li et al., 2017), geographically weighted regression (Zheng et al., 2019), Sigmoid function (Zhao et al., 2019), Biphasic Dose Response model (Ma et al., 2020), neural network for cross-sensor calibration (Chen et al., 2021) of NTL products. While correction schemes and light alignment products are being developed and released, methods for assessing correction performance and NTL data continuity are still relatively lagging behind. Overall, NTL products provide us with a unique data base for tracking the footprint of human activities on a global scale, but they also face several challenges that deserve improvement and promotion.

With the continuous promotion of SDGs, the efficient realization of multi-scale dynamic monitoring of human activities and ecological environment conditions and quantitative analysis of the impact of human

activities on ecological environment demand full play of the performance advantages of daytime optical remote sensing and nighttime light remote sensing. Therefore, this thesis aims to explore the potential of integrated day-night remote sensing schemes for quantitative assessment of human activities and ecological conditions as well as the technical challenges that urgently need to be addressed. The results of the thesis not only contribute to explore the potential of multi-source remote sensing data applications, but also provide decision support for the coordinated development of urbanization and ecological environment.

1.2 Research questions and objectives

Given the continuous enrichment and development of multi-source remote sensing data, exploring the integration of daytime and nighttime multi-source remote sensing solutions to track the dynamics of anthropogenic footprints and ecological environments, and quantitatively assessing the interactions between them is valuable to advance the realization of SDGs.

Since, the current scheme for integrating day-night remote sensing faces uncertainties in data, methods and applications and still deserves to be optimized, the central questions of the research in this thesis are:

1) Which remote sensing data and models are applicable to human activities and eco-environment condition tracking?
2) What are the limitations of the above data and models for long-term, multi-scale applications and how to correct (calibrate) them?
3) What are the dynamics of human activities and ecology during the past decades and how have human activities affected the eco-environment?

The general purpose of this thesis is to conduct multi-view, multi-scale human footprint tracking and environmental condition dynamics analysis with the help of integrated daytime optical remote sensing and nighttime light remote sensing to help us more comprehensively understand the planet in a changing climate context.

The following specific objectives were identified in order to achieve the purpose of the thesis:

1) Develop a series of NTL calibration models to fix the flaws of NTL data in applications.
2) Develop extended NTL data quality monitoring method to evaluate the robustness and accuracy of long time series NTL dynamics.
3) Assess the applicability of NTL data for light pollution monitoring in special geographic units.
4) Validate the performance of new satellite data in tracking human footprints.
5) Evaluate the feasibility of RSEI indices for medium- and large-scale applications.
6) Indicate some preliminary suggestions to promote the coordination of human activities with the environment.

The promotion and implementation of the above-mentioned specific objectives would allow for more accurate and robust surface monitoring results based on day and night remote sensing imagery, and might help us to better understand the changing planet and be more prepared to achieve the SDGs.

1.3 Explanation of the thesis format

The thesis is organized by eight key chapters, each of them is a relatively self-contained paper completed during the Ph.D. project. An illustration of the structure of the thesis is drawn in Figure 1.6, which shows how these chapters (papers) are organized according to the research scale and subjects.

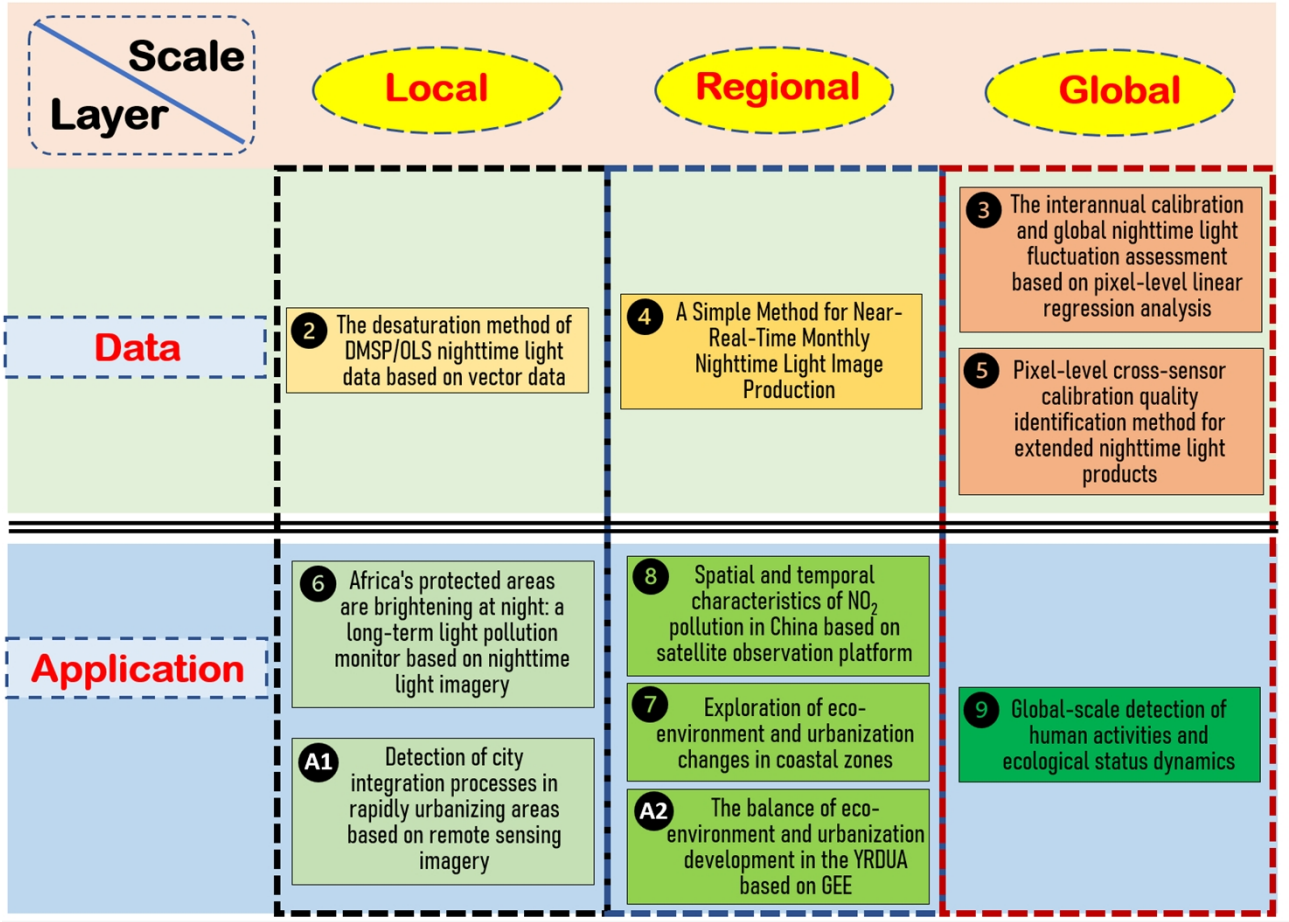

Figure 1.6. Structure chart of the thesis. Papers are presented as chapters of the thesis, and the numbers represent the chapter order.

Chapter 2 is a paper published in International Journal of Geographical Information Science, which proposes a vector data-based correction scheme for the saturation phenomenon that has plagued the urbanized central areas in the DMSP/OLS product, and validates it in three major urban cluster regions in China.

Chapter 3 is a paper published in Remote Sensing, which proposes a calibration model that automatically identifies pseudo-invariant feature pixels to address the inconsistency problem of the time-series DMSP/OLS products, and outputs calibrated global NTL images for the period 1992-2013.

Chapter 4 is a paper published in IEEE Geoscience and Remote Sensing Letters, which proposes a new scheme to produce monthly cloud-free and low-lunar interference NTL images in near real-time, and apply it to urban-scale human activity intensity tracking.

Chapter 5 is a paper submitted to IEEE Transactions on Geoscience and Remote Sensing, which proposes a pixel-scale quality identification strategy for the most representative ENTL products currently available, which is capable to quantitatively evaluate the data quality of ENTL.

Chapter 6 is a paper published in Global Environmental Change, which utilizes long-term ENTL data to track light pollution trajectories in a special geographic unit of African protected areas and assesses anthropogenic stress on protected areas, and the results of the research contribute positively to maintaining the nighttime habitat of protected areas and conserving biodiversity.

Chapter 7 is a paper published in Ecological Indicators, based on NTL and MODIS data products, which assesses the urbanization intensity and ecological quality of coastal areas in China and analyzes the coordination of development between them. The results of the study explore the applicability of the RSEI index to medium resolution imagery.

Chapter 8 is a paper published in Remote Sensing, with China as the study area, it explores the potential of the new atmospheric environmental monitoring satellite Sentinel-5P in inversion of tropospheric NO_2 pollutant concentrations and attempts to explain the sources and drivers of NO_2 pollution with the help of factor analysis.

Chapter 9 is an unpublished paper that explores global environmental change in the context of rapid urbanization. With the enormous computing power of the Google Earth Engine platform, it segments the global anthropogenic zones into a grid and dynamically analyzes the global anthropogenic and environmental conditions over the past 20 years.

In addition, there are two additional experiments included in the thesis that were carried out during the Ph.D. program. They were published in Land and Chinese journal respectively, and the core information was extracted and reported in the thesis. **Annex 1** is an additional case study that focused on a specific target in the urbanization process: the integrated city. In this case, four most representative integrated cities located at different stages of development in China were examined, and the variability in the development of these integrated cities was analyzed by monitoring land use transformation, light radiation dynamics and shift of center of gravity within different buffer zones of the city boundaries.

Annex 2 presents an experiment at the urban agglomeration scale. Although the RSEI and CNLI indicators, which have been applied at several scales, are still used in the analysis, we newly propose a planar development balance model to assess the development coordination within urban agglomerations. The proposed coupled coordination distance model divides the city's development stages through four quadrants, which is quite intuitive and concise.

2. The desaturation method of DMSP/OLS nighttime light data based on vector data: taking the rapidly urbanized China as an example [1]

2.1 Abstract

The saturation of night light data caused by sensor defects conceals the differences and details of light luminance in the urban area, which greatly limits the application of Nighttime Light (NTL) in the study of urbanization. Although some methods have been proposed to mitigate the saturation of NTL data, the research of desaturation is worth further advancing due to its shortcomings in highlighting light differences and spatial resolution. Therefore, we propose a new spectral index, the Vector Data Adjusted NTL Index (VDANTLI) after analyzing the influence of different auxiliary parameters on saturation elimination. Then, we select the three most developed urban agglomerations in China and make a series of qualitative and quantitative analysis. The results of various assessments confirm that VDANTLI can effectively alleviate NTL saturation and enhance urban lighting differences. Moreover, by dynamically adjusting the length of the grid and single-phase vector data modified time-series NTL data, we further achieve the resolution-series and time-series VDANTLI. Therefore, compared with previous desaturation models, the VDANTLI can be used as an effective indicator and even an indispensable basic data for urbanization research and socio-economic spatial analysis because of its unique advantages in spatial resolution and the capability in time-series native NTL desaturation.
Keywords: VDANTLI; urbanization; DMSP/OLS; saturation; China

2.2 Introduction

Since China's reform and opening up, a large number of rural people have migrated to cities with the adjustment of the policy of population mobility, which has greatly promoted the urbanization process in China, especially in the eastern coastal areas. China's sixth census data show that in the years 2005–2010, the eastern coastal region's population increased by about 33 million people (Wu and Zhu, 2016). The accelerated development of urbanization has greatly promoted the academic research on the process of urbanization. At present, the research of urbanization is focused on urban form, urban expansion and structure variety between cities (Weng, 2007; Ewing and Rong, 2008; Marshall, 2008; Deng et al., 2009; Cai et al., 2017). Among them, the research methods of the urbanization process based on Nighttime Light (NTL) have been constantly improved, and a great amount of fruitful results have been achieved (Chen et al., 2003; He et al., 2006; Zhang and Seto, 2011; Yu et al., 2014; Gao et al., 2015; Chen et al., 2017; Hu et al., 2017).

The Defense Meteorological Satellite Program/Operational Linescan System (DMSP/OLS) equipped with the Photo Multiplier Tube (PMT) can detect weak visible light-near infrared radiation at night. With this

[1] This Chapter relies on the paper "Zheng, Z., Chen, Y., Wu, Z., Ye, X., Guo, G., & Qian, Q. (2019). The desaturation method of DMSP/OLS nighttime light data based on vector data: Taking the rapidly urbanized China as an example. International Journal of Geographical Information Science, 33(3), 431-453.".
https://doi.org/10.1080/13658816.2018.1538516.

excellent nighttime light capture capability, the NTL (without radiation calibration) data from the DMSP/OLS are gradually used as a natural geospatial data for urbanization processes such as estimating the urbanization levels (Parés-Ramos et al., 2013; Zhang et al., 2013; Xu et al., 2014; Ma et al., 2015), population and GDP estimates (Zhuo et al., 2005; Amaral et al., 2006; Sutton et al., 2007) and energy consumption estimation (Chand et al., 2009; Letu et al., 2010).

However, in the process of using NTL data to analyze the urbanization and inner-urban structure, the upper limit of the DN value is only 63 due to the defects of the OLS sensor itself. This will cause saturation phenomena when using NTL data to describe the actual lighting intensity of the urban, especially in the urban central area. The saturation phenomenon makes the NTL data have an upper limit in depicting the actual lighting luminance, which weakens the depiction of the lighting detail difference in the urban centers. Furthermore, the loss of the details of the lighting intensity will inevitably reduce the accuracy of its application in the process of urbanization.

Therefore, finding a method or model that can effectively eliminate or mitigate the saturation problem has become one of the hotspots in the research of NTL data. In recent years, scholars around the world have proposed two perspectives of radiometric calibration and non-radiometric calibration for the desaturation of DMSP/OLS NTL data in urban central areas (Elvidge et al., 1999). Although radiometric calibration methods have a higher accuracy, only NOAA's National Centers for Environmental Information (NCEI, formerly the National Geophysical Data Center) has developed a limited amount of radiometric calibration data for a limited period of time due to the absence of on-board calibration systems and the higher complexity of the scaling algorithm. In the non-radiometric calibration studies, methods of eliminating saturation phenomenon are divided into two factions, **a)** Cross-correction based on Radiance Calibrated Nighttime Lights (RCNTL) in the invariant target area (Letu et al., 2011; Cao et al., 2015); **b)** Association-correction based on auxiliary data or parameters (Zhang et al., 2013; Zhuo et al., 2015; Liu et al., 2017).

Through the comparative analysis of the previous method based on the correction of saturation using auxiliary data or parameters, we found that the NTL data reflecting the luminance of night lights in cities is more closely related to the level of social and economic development than to vegetation or other natural factors (Zheng et al., 2018). Meanwhile, with the complexity of the structure and morphology of the city, policymakers and scientists urgently need a simple and effective high spatial resolution index that can help them to characterize urban structural features rapidly and accurately from a finer spatial scale. Thus, the purpose of this paper is to introduce a new auxiliary data as a correction parameter to correct the NTL data with the saturation phenomenon and propose a new spectral index, the Vector Data Adjusted NTL Index (VDANTLI), which combines vector data (road network data and Points of Interest (POI) data) with NTL and reduces the saturation phenomenon of NTL in urban cores. Moreover, we select the three most developed urban agglomerations in China (Figure 2.1) as case areas to evaluate the effect of correction saturation and explore the temporal and spatial characteristic of VDANTLI.

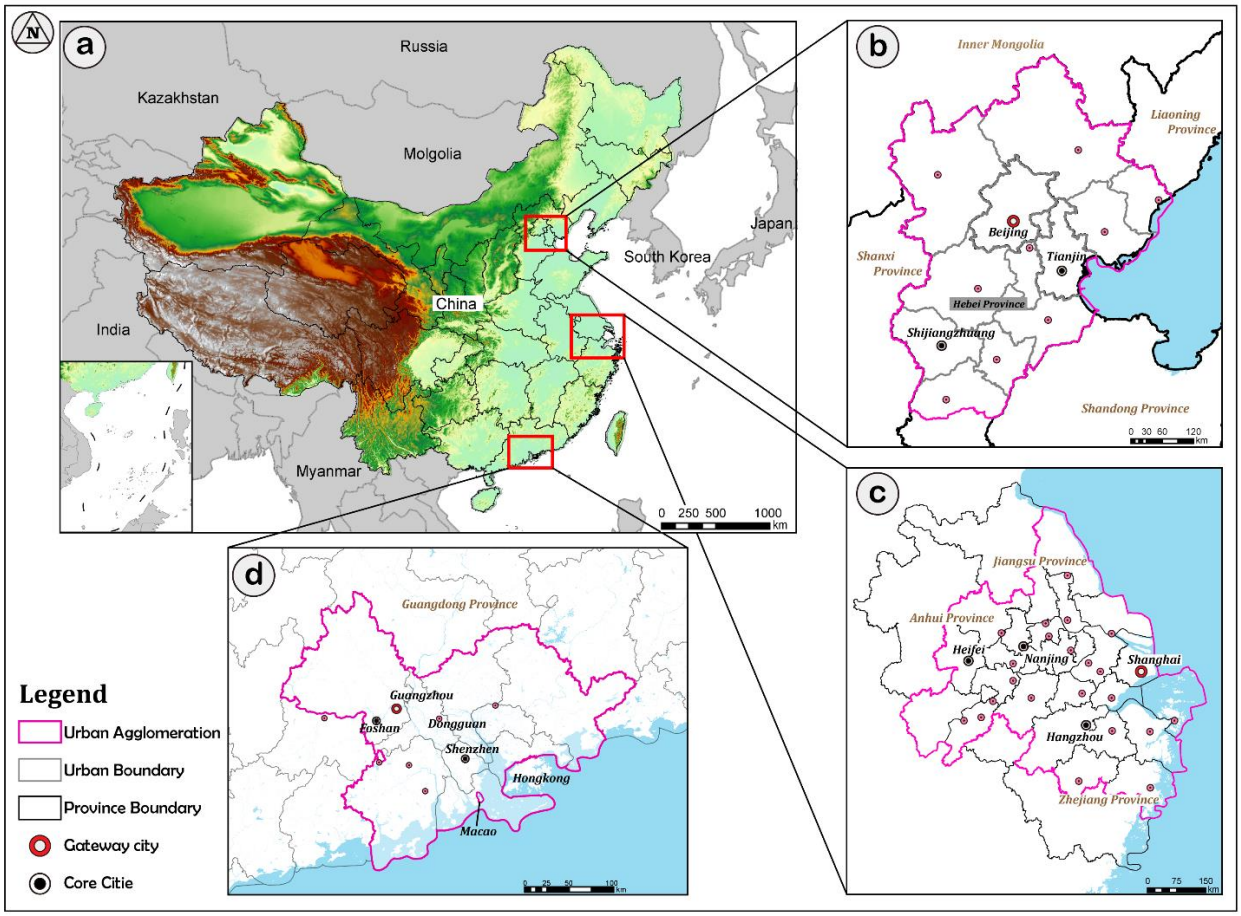

Figure 2.1. The spatial distribution of case areas for accuracy evaluation. They are the three most developed and representative urban agglomerations in China. Note: (a) Overview maps of case areas; (b) Location map of Beijing–Tianjin–Hebei Urban Agglomerations (BTHUA); (c) Location map of Yangtze River Delta Urban Agglomerations (YRDUA); (d) Location map of Pearl River Delta Urban Agglomerations (PRDUA).

2.3 Previous approach to reduce NTL saturation

Since the launch of the DMSP/OLS instrument and monitoring light intensity distribution on the earth's surface, scholars have been using NTL data to analyze the distribution of surface lights. Although the NTL is not directly generated by the observation of human settlements or urban land cover, the data are strongly correlated with many characteristics of urban settlements and levels of economic activity. However, the NTL data is not flawless when it comes to analyzing urban structures and economic intensity, especially in the urban central areas. Chief among the issues is the well-documented saturation of data values in core urban areas due to the limited radiometric range of the DMSP/OLS. If we can effectively relieve or eliminate the saturation phenomenon, the significance and scope of NTL data in the studies of urbanization and urban structure will be greatly expanded.

Since the advent of NTL's saturation, scholars around the world have begun to try to eliminate this phenomenon from different angles to better promote the application of NTL data. Over the past decade, there have been many meaningful results and models to eliminate saturation. As we mentioned earlier, the methods

of correction are mainly divided into two categories. However, non-radiometric calibration methods have made much more progress than radiometric calibration methods due to the complex calibration algorithms and mass data support requirements of radiometric calibration. The non-radiometric calibration methods are based on the key rationale that urban features or structure characteristics are highly correlated (positive or negative correlation) with auxiliary parameters or indicators.

It has been shown that land surface vegetation coverage and its distribution characteristics are closely and inversely correlated with impervious surfaces, a typical urban structural feature (Small, 2001; Pozzi and Small, 2005). Impervious surfaces affect not only the regional ecosystem and environment, but also the urbanization and the urban structures. The inverse relationship between vegetation coverage and urban impervious surfaces has prompted a series of attempts to use vegetation characteristics as supplementary data for correcting the saturation phenomena.

As one of the most widely used spectral indices in the remote sensing of vegetation, the Normalized Difference Vegetation Index (NDVI) facilitated numerous researches in vegetation and climate change (Ichii et al., 2002; Pettorelli et al., 2005) and land cover change at global scales (Lunetta et al., 2006; Morawitz et al., 2006). Owing to the simplicity and efficiency of characterize the vegetation health and distribution, NDVI bears the brunt of being chosen as an auxiliary parameter to eliminate NTL saturation phenomena. The Human Settlement Index (HSI) which combines DMSP/OLS and NDVI variables (Eq. 2.1) provides a new insight for mapping settlements at the regional or global scale and mitigates the saturation effects (Lu et al., 2008). As the first spectral index proposed by combining NTL and NDVI, HSI provides a new perspective in fusing multi-source remote sensing data for urban lighting studies.

$$HSI = \frac{(1 - NDVI) + NTL}{(1 - NTL) + NDVI + NDVI \times NTL} \tag{2.1}$$

Although HSI provided a better estimation performance than the single DMSP/OLS or NDVI variable, it still has some drawbacks. Among them, the over-correction in the transition zone where is adjacent to the urban core area and the contradiction between vegetation coverage and maximum brightness of night are the most prominent.

The Vegetation Adjusted Normalized Urban Index (VANUI) is also based on the realistic basis that the lower the vegetation coverage, the higher the luminance of night light, and vice versa. With the rapid urbanization process, the urban center areas such as the Central Business District (CBD) and large shopping districts have been artificially modified and constructed quite thoroughly, and often present a distribution of minimum vegetation coverage and extremely high building density. The VANUI was developed as a robust spectral index which uses an angularly corrected MODIS NDVI as a vegetation signal to mitigate the saturation of NTL and effectively enhance the variability of NTL in urban center areas (Zhang et al., 2013).

The VANUI is defined as:

$$VANUI = (1 - NDVI) \times NTL \tag{2.2}$$

According to the parenthetical expression, the lower the vegetation coverage, the higher the weight. Therefore, VANUI value in the urban cores areas is close to 1, while in the non-urban areas is close to 0. Compared to NTL and HSI, VANUI stretched NTL luminance differences between urban center areas and non-urban areas and significantly improved luminance detail in urban center areas.

Although VANUI can highlight spatial differences of lighting intensity in the urban areas with a long history, relatively slow development and stable development mode (such as San Francisco, New York, Cape Town, Tokyo, etc.), the spatial differences of lighting intensity in cities with fast urbanization (such as Beijing, Guangzhou, Shenzhen, etc.) are not obvious enough. The differences of the vegetation cover are not significant in the rapid urbanization of the city's potential saturation regions (Ma et al., 2014), and further leads to the fact that 1-NDVI cannot be adjusted in time which is difficult to alleviate the saturation phenomenon and highlights the spatial difference of night lighting intensity.

In order to remedy the deficiency of the VANUI in the rapid urbanization of cities, a new improved spectral index, the Enhanced Vegetation Index (EVI) Adjusted Nighttime Light Index (EANTLI) is proposed (Zhuo et al., 2015). The EANTLI use the Enhanced Vegetation Index as an auxiliary parameter for correcting saturation due to its advantages of anti-interference ability compared with NDVI (Huete et al., 2002). The rationale behind the EANTLI is similar to the VANUI that key urban features are inversely correlated with the vegetation coverage level.

The EANTLI is defined as:

$$EANTLI = \frac{1 + (nNTL - EVI)}{1 - (nNTL - EVI)} \times NTL \tag{2.3}$$

The evaluation of the EANTLI shows that it can quickly and better improve the gray saturation problem of DMSP/OLS NTL dates, distinguish the objects in saturated areas and estimate human activities, such as the consumption of urban electric energy (). However, it still has some limitations in some special areas, such as the mixed areas of water and land and the CBD. In the mixed land of water and land, because of the existence of scattered vegetation on land, the EVI is close to 0, which leads to an abnormally high EANTLI index value. On the contrary, due to the presence of some landscape vegetation, the EVI is not completely close to 0 in the CBD region, thus weakening the maximum value of the EANTLI index. The deviation of the two regions mentioned above are caused by the instability dependence of the EVI and the lighting intensity, which greatly limits the application of the EANTLI.

The results of the three spectral indices mentioned above implemented in the three major urban agglomerations in China (Figure 2.2) show that these spectral indexes constructed based on the vegetation index (NDVI and EVI) were improved significantly compared with the original NTL. From the corrected results, the correction effect of the EANTLI is the best, followed by the VANUI, while the HSI is the worst in comparison.

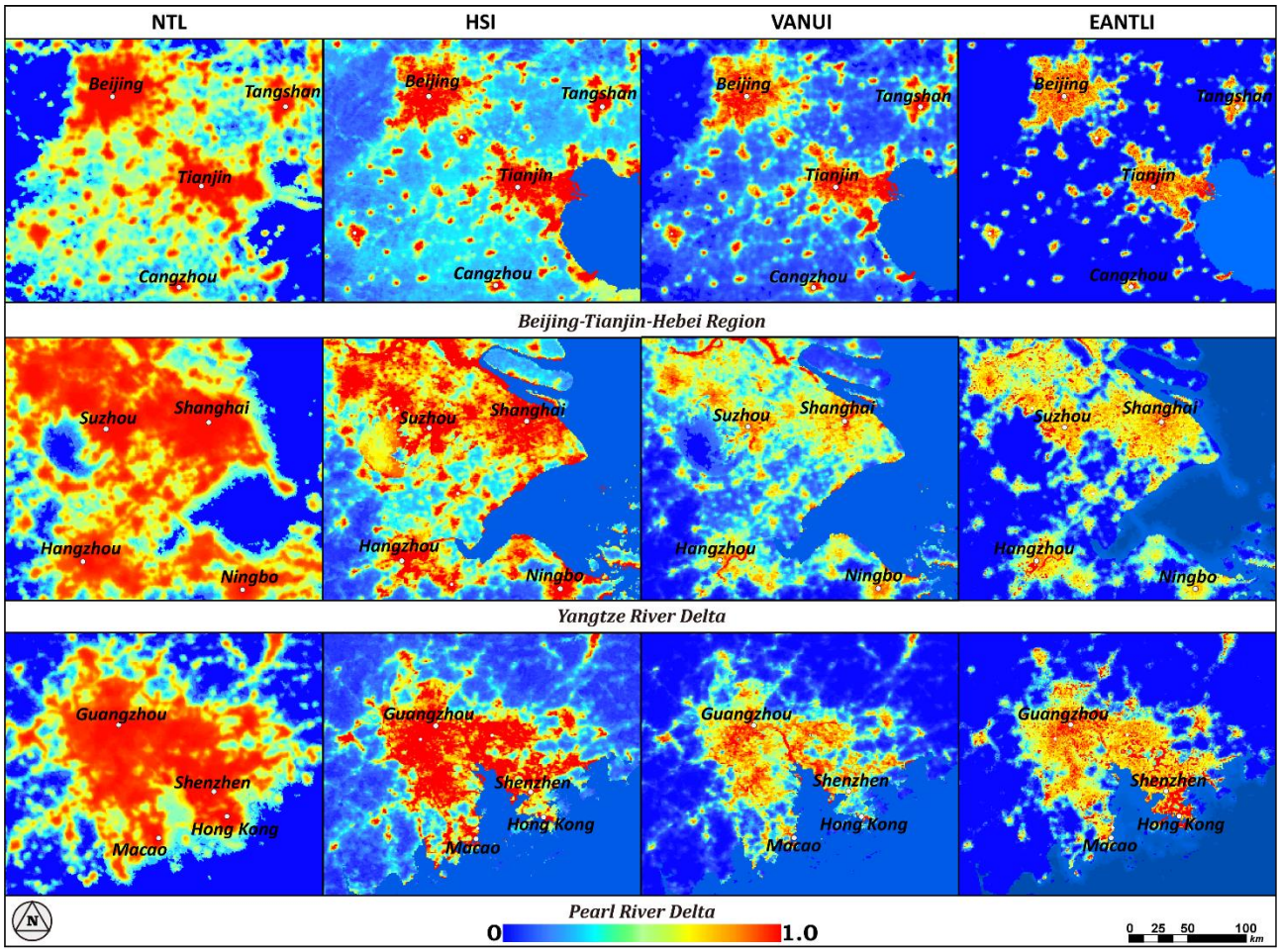

Figure 2.2. Normalized 2013 NTL with the saturation phenomenon and three spectral indexes for corrected saturation problem (HSI, VANUI, EANTLI) in the three largest urban agglomerations (BTHUA, YRDUA and PRDUA) in China.

2.4 Implementation of VDANTLI

In recent years, the rapid growth of spatial big data has created new opportunities and perspectives to discover the spatial characteristics of urban structures and human social activities. As an important part of spatial data, road network data and POI data have revealed the high correlation between urban structures (Zhao et al., 2011; Feng et al., 2014; Chi et al., 2016; Xu and Gao, 2016). Considering the positive correlation between the urban structure characteristics and vector data sets which consists of multi-level road network data and POI data, we propose to use the vector data sets as auxiliary parameter to correct the saturation of native NTL. The POI data and multi-level road network data used in this paper are obtained through the Amap (China's leading provider of digital map content, navigation and location-based services) Application Programing Interface (API) (http://lbs.amap.com/api/javascript-api/guide/map-data/introduction). Although the JavaScript API of Amap has been released in 2013, the road network and POI data used in this paper were collected in 2015 due to the difficulty of massive historical time-series vector data collection. Since the NTL data used for correction in this paper was in 2014, we used the Open Street Map (OSM) open-source road network data in 2014 to correct the Amap road network data in 2015 in order to minimize the disturbance caused by the data

acquisition time difference. However, for POI data, due to the lack of previous data, we were forced to use the 2015 POI data to participate in the NTL saturation correction. Considering the contribution of different POI type facilities to the nighttime light on the surface, we selected three types of POI data (Catering Services, Financial Services and Entertainment Services) as effective POI data to participate in the subsequent elimination of the saturation process. The facilities represented by these three types of POI data concentrate most of the people and energy in the city, which is highly synergistic with the intensity of nighttime light in reflecting the urban vitality structure. Meanwhile, according to the characteristics of each grade road network, we select urban expressways, urban inner roads and pedestrian roads as effective road network data. In addition, considering the difference in radius of service for different grades of roads, the roads are given different weights in the order of "urban expressway (weight:0.5) > urban inner road (weight:0.3)> pedestrian road (weight:0.2)" based on AHP.

We utilized the three level road network data and three types of POI data derived from vector data to generate the Grid Vector Data Density (GVDD). The gridding method can effectively realize the spatialization of variables, and can assemble discrete vector data on a single grid (Chen et al., 2016a; Guo et al., 2016). In this paper, the fishnet grids which cover the entire study area are created by spatial analysis tools, and the length of each grid is set to 500m. This means that the newly generated VDANTLI will have a higher spatial resolution than the original NTL in the process of subsequent correction of saturation (Figure 2.3). The GVDD is calculated based on the normalized the number of POI and the weight length of the road network which is covered by each grid (Eq. 2.4).

$$GVDD = Count_{norm}(POI_{Catering\ Services+Financial\ Services+Entertainment\ Services}) + Sum_{norm}(WL_{Road\ network_{level1,2,3}}) \quad (2.4)$$

$$VDANTLI = GVDD_{norm} \times NTL_{norm} \quad (2.5)$$

The native NTL values are scaled to the range of [0,63], which is not consistent with the range of the GVDD. To ensure that two variables can be executed at the same order of magnitude, we have normalized the GVDD and native NTL to the range of [0,1] respectively. Considering the long tail distribution of the native NTL and GVDD grid values, this paper selects the research area for subsequent evaluation of VDANTLI performance (BTHUA, YRDUA and PRDUA) as the normalization extent. The calculation method of the VDANTLI determines its two most important characteristics: the stronger ability to differentiate the NTL values and the ability to dynamically adjust spatial resolution. Hence, it is foreseeable that energy consumption, population density, urban heat island and other correlations analysis with VDANTLI participation will yield more accurate results.

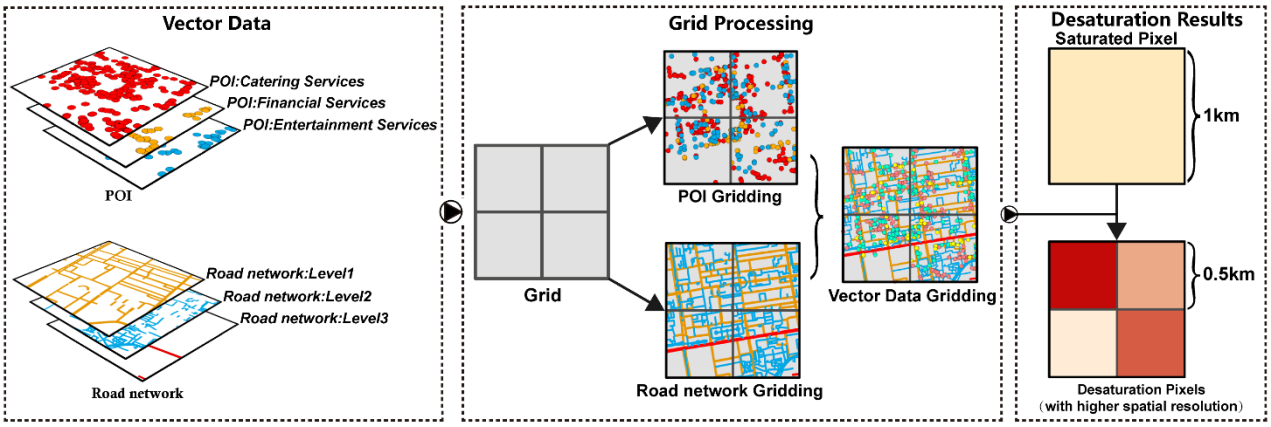

Figure 2.3. Methodology for correcting the saturation problem of NTL through the vector data. The corrected results have more light intensity differences and higher spatial resolution than the native NTL.

2.5 Results and Analysis

2.5.1 Assessment of VDANTLI desaturation capacity

We compare and evaluate the VDANTLI's ability to relieve the saturation of native NTL from qualitative and quantitative analysis. Firstly, we visually compare the VANUI, EANTLI and VDANTLI with the native NTL in region with the most saturated phenomenon. The PRDUA is an advanced manufacturing base and a modern service base with global influence. According to UN Habitat released by the world urban status report, with Guangzhou, Hongkong and Shenzhen as the core of the Pearl River Delta, this metropolitan area has become the world's largest super metropolitan area. We selected the largest saturation zone in the PRDUA for comparison and evaluation (Figure 2.4). In order to compare, we normalized the NTL and the three spectral indices. The comparison shows that the three spectral indexes can significantly eliminate the saturation of the NTL and increases inner-urban variability of NTL values. Furthermore, the EANTLI has a better effect than the VANUI in showing the difference in detail of night light luminance and the VDANTLI has obvious advantages over the EANTLI in both lighting detail and spatial resolution. More abundant lighting luminance difference and better spatial resolution can more accurately reflect the contours and structural features of the urban area. For a more specific comparison of the differences between the three spectral indices, we selected 6 typical regions for comparison. The Zumiao Commercial Zone (A), Shiqiao Commercial Zone (B) and Beijing Road Business Circle (E) are three of the most prosperous business districts in this saturated zone. Although both the EANTLI and the VDANTLI perform better than the VANUI in enhancing the luminance of the commercial area and suppressing the lighting intensity in the non-commercial areas, the spatial resolution of the VDANTLI is better than the EANTLI which can show the details and differences within the district. The VDANTLI also achieved the most abundant details of luminance detail in Guangzhou Higher Education Mega Center (C), which has 10 universities in approximately 20 square kilometers of land, with more than 200 thousand students and faculty. The Zhujiang New Town (D) is the CBD of this saturation region, which means the highest luminance of lights should be recorded. Different from the actual situation, the

VANUI and EANTLI did not effectively stretch the brightness of the CBD area, while the VDANTLI stretched more prominently. The Cuotou Grassed Island (F) is located in a semi urbanized area which consists of a large amount of water bodies, some vegetation and a small amount of buildings. The VANUI and EANTLI of this area is stretched to a high value, while the VDANTLI is reduced to a low value. In fact, due to the lack of commercial and residential land, the night lighting luminance in Cuotou Grassed Island (F) should be significantly lower than the urban core area. The reason for the inconformity of corrected saturation results in the same region is the different auxiliary correction parameters. Both the VANUI and EANTLI select vegetation index (NDVI for VANUI; EVI for EANTLI) as an auxiliary parameter, while VDANTLI selects vector data. The low vegetation cover caused by a large number of water bodies in Cuotou Grassed Island (F) is easy to confuse with the low vegetation cover caused by a wide area of impervious surface in the central city, which results in the wrong stretching of the VANUI and EANTLI.

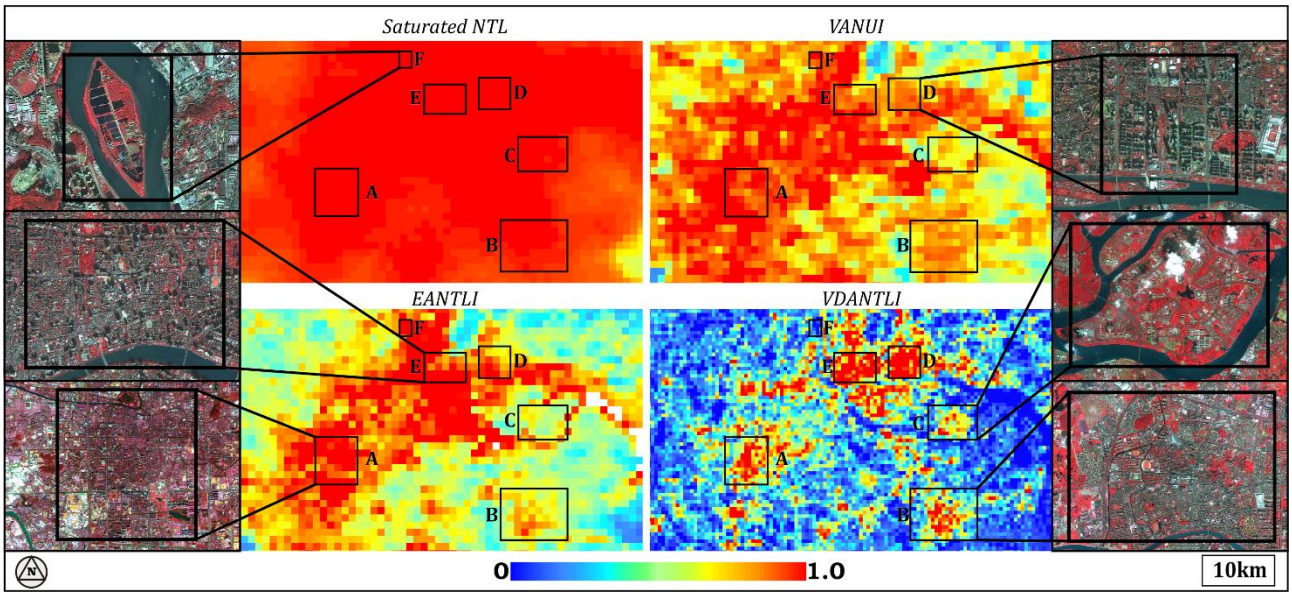

Figure 2.4. The 2013 normalized saturated NTL, VANUI, EANTLI and VDANTLI for select sample regions around the PRDUA. The VANUI, EANTLI and VDANTLI are normalized and are both scaled 0–1.0; the selected sample regions are Zumiao Commercial Zone (a), Shiqiao Commercial Zone (b), Guangzhou Higher Education Mega Center (c), Zhujiang New Town (d), Beijing Road Business Circle (e) and Cuotou Grassed Island (f). These areas are amplified and displayed through the Landsat-8 false color image.

Moreover, we selected the main urban area of Guangzhou as the interest area and used the land use data extracted from the high-resolution remote sensing satellite images (GF-1, 8m × 8m) to verify the accuracy of the night lighting data correction by various desaturation models. Considering the high correlation between night lighting and urban construction, we classify land use types into three categories (building area, water area, vegetation area) based on high resolution remote sensing images. The Kappa coefficient of the image classification result is 0.887, which can meet the precision requirement of the study. To reduce the effect of the light spillover effect, we conducted a sensitivity analysis to determine the appropriate threshold interval for lighting area. Specifically, we first select areas (i.e., suburban woodlands, lakes) where there is no light source in theory, and then calculate the mean of the normalized DN values in these areas. Finally, we set above

mean as the lower limit of the DN value range of the lighting area. For saturated NTL, VANUI, EANTLI and VDANTLI, the normalized DN values between 0.05 and 1 are considered as lighting area. The accuracy of the desaturation model can be effectively evaluated by comparing the area occupation ratio of the lighting area and the building area. The results showed that compared with VANUI and EANTLI, not only the area occupation ratio of lighting area (55.52%) extracted by VDANTLI was the closest to the building area's ratio (44.04%), but also the spatial pattern consistency was higher (Figure 2.5).

Second, we further compared the transect of the 2013 saturated NTL, VANUI, EANTLI, VDANTLI and RCNTL (the global nighttime lighting products without sensor saturation produced by combining sparse data acquired at low gain settings with operational data acquired at high gain settings) in the BTHUA, China (Figure 2.6). The transect passes through several major cities in the region, including Baoding, Beijing, Tangshan, Tianjin and Cangzhou. The comparison shows that the fluctuation curve of the VDANTLI is more similar to the RCNTL than others. It is worth noting that the VDANTLI maintains a wealth of lighting detail in the transition zone of the major cities (e.g. Pixel ID between 350 and 450, Figure 2.6). In order to further quantify the similarity between the spectral indices which are proposed to relieve the saturation phenomena and RCNTL, we performed linear regression analysis on BTHUA, YRDUA and PRDUA respectively. The results of regression analysis in the three regions showed that the correlation between VDANTLI and RCNTL was the highest, followed by EANTLI. For example, the BTHUA's scatter matrix result (Figure 2.7) shows a highest R^2 of 0.809 for a similar linear model between the VDANTLI and RCNTL. Moreover, the R^2 of 0.737 for a similar linear model between the EANTLI and RCNTL is higher than the R^2 of 0.418 for the VANUI and RCNTL, which further confirms the research findings of Zhuo et al. (2015) in the accuracy comparison of the EANTLI and VANUI. Interestingly, the R^2 of the linear regression model between the HSI, VANUI and EANTLI are both at a higher level (0.956 for HSI and VANUI, 0.739 for VANUI and EANTLI, 0.727 for HSI and EANTLI), which means there is a high correlation between them.

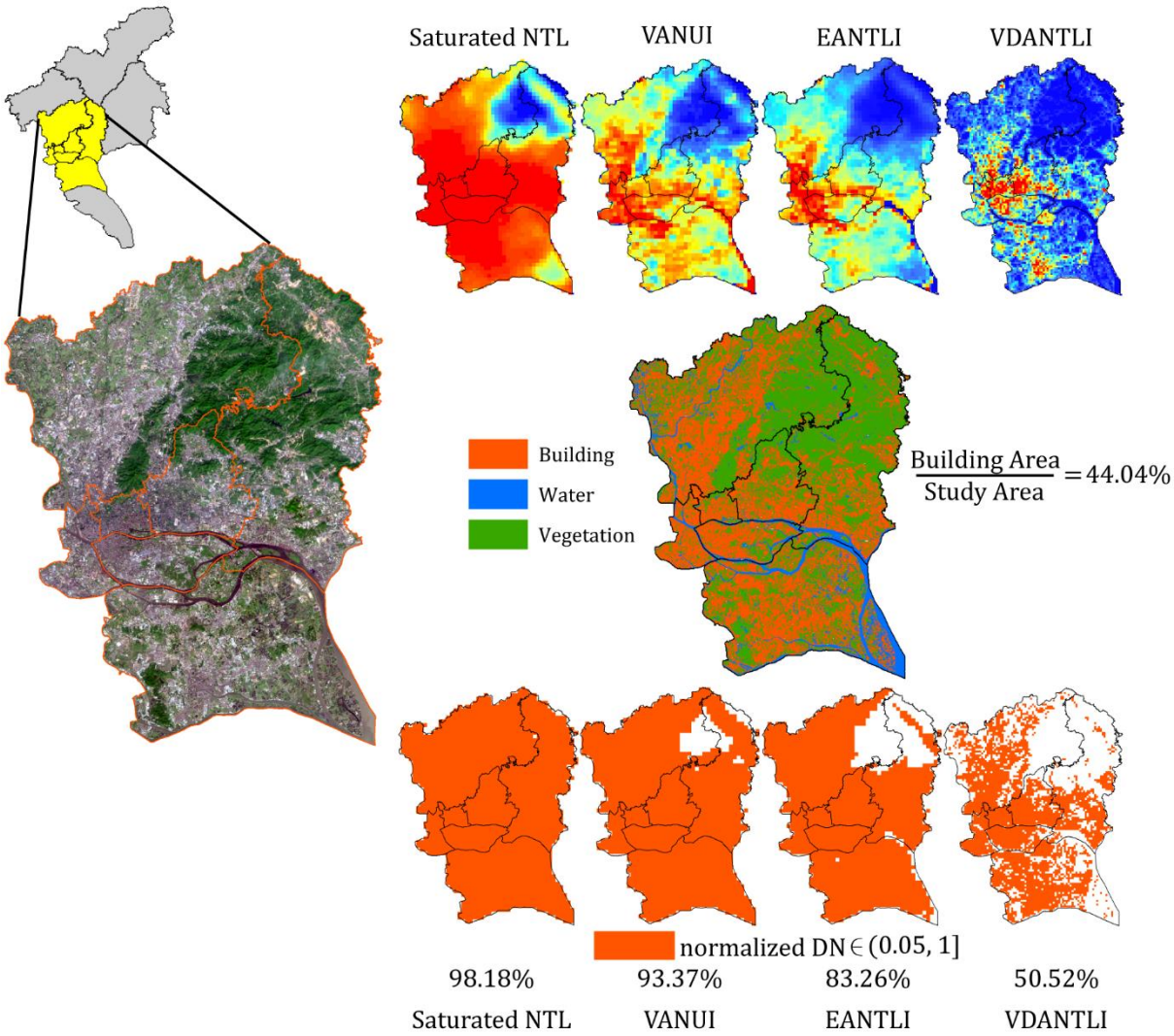

Figure 2.5. Comparison of the area occupation ratio of lighting area and the classification results of land use based on high resolution image extraction in the main city of Guangzhou. Saturated NTL, VANUI, EANTLI and VDANTLI are normalized to 0–1; normalized DN values between 0.05 and 1 are considered as light area.

Since the successful launch of National Polar-orbiting Operation Environmental Satellite System Preparatory Project (NPP) satellite in 2011, a new generation of nighttime light data sensed by Visible Infrared Imaging Radiometer Suite (VIIRS) has been applied to the study of surface monitoring. NPP/VIIRS inherits and optimizes the DMSP/OLS's detectability under the condition of faint light, which has a higher spatial resolution and radiation resolution than DMSP/OLS. Considering that NPP/VIIRS Day/Night band (DNB) data overcomes the DN value saturation defect of DMSP/OLS NTL data, we use the 2013 DNB data of NPP/VIIRS to further evaluate the performance of NTL, VANUI, EANTLI and VDANTLI. Since the National Oceanic and Atmospheric Administration-National Geophysical Data Center (NOAA-NGDC) provides only monthly DNB data in 2013, this paper uses the mean algorithm to calculate the 2013 annual DN synthetic data to reduce the impact of unstable light sources. In addition, some necessary data preprocessing (including projection, resampling, normalization, DMSP/OLS based abnormity elimination (Li et al., 2016) is also used to minimize the noise of the NPP/VIIRS DNB data. Specifically, we constructed the hexagonal grid covering the urban agglomerations (BTHUA, YRDUA and PRDUA) and counted the DN mean of spectral indexes and

NPP/VIIRS DNB data in the grid unit. The linear regression analysis was used to evaluate the fitting degree between the spectral indexes and DNB data. Among the R^2 of spectral indexes and DNB data, the fitting degree (R^2=0.846) between VDANTLI and DNB is the highest. The fitting degree of "NTL-DNB", "VANUI-DNB" and "EANTLI-DNB" is close, but it is obviously inferior to "VDANTLI-DNB" (Figure 2.8).

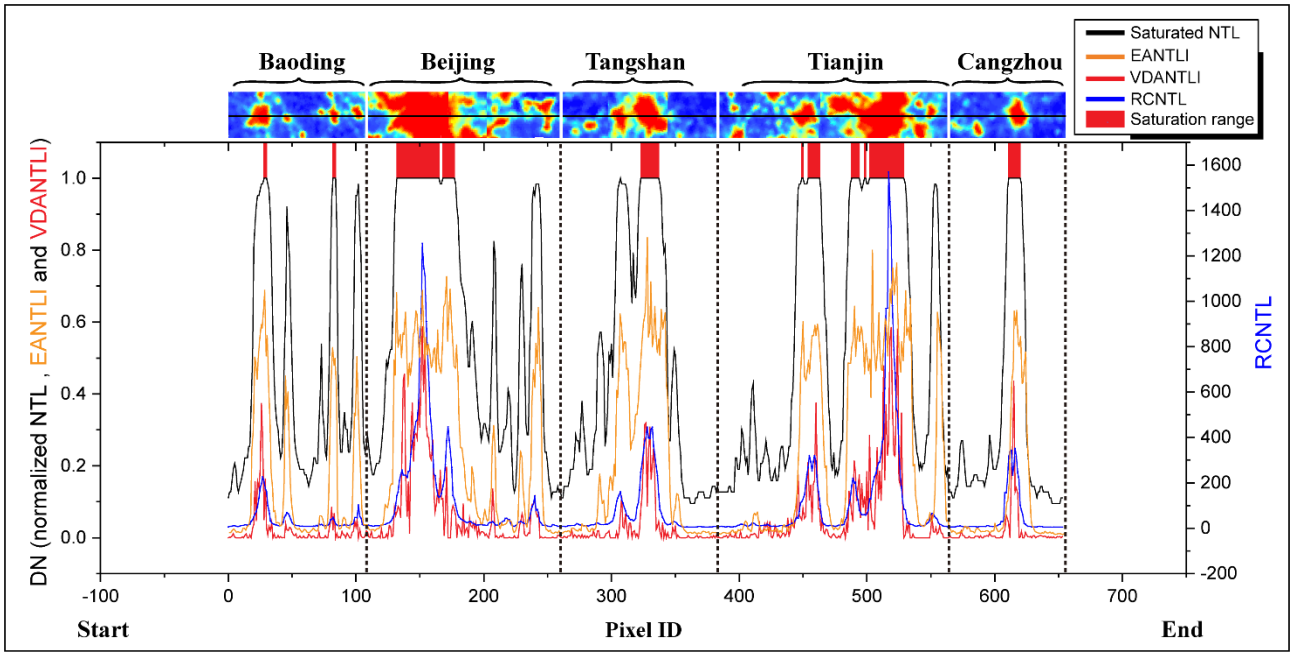

Figure 2.6. Transect of native NTL, HIS, VANUI, EANTLI and VDANTLI in BTHUA, China. The VDANTLI is redrawn at the lower part due to the higher spatial resolution.

Considering the high correlation between nighttime light data and socio-economic indicators, we selected 26 prefecture level cities in the YRDUA and analyzed the correlation between various spectral indices (including native NTL, HSI, VANUI, EANTLI and VDANTLI) and socio-economic indicators. As an important intersection zone for the B&R (Belt and Road Initiative) and the Yangtze River economic zone, the YRDUA is the most developed and urbanized area in China. According to the previous research results (Wu et al., 2013; Zhou et al., 2015; Cao et al., 2016; Shi et al., 2016a; Shi et al., 2016b), we selected GDP and Electricity Consumption (EC) as socio-economic indicators to participate in the correlation analysis. The 2013 GDP and EC data are obtained from the statistical yearbook of each prefecture-level city, the spectral indices of each city are collected by zonal statistics tools. The characteristics of normalized GDP, EC, NTL, HSI, VANUI, EANTLI and VDANTLI in 26 prefecture-level cities have strong similarities (Figure 2.9). Compared to the native NTL, the results of linear regression (Table 2.1) show that the correlation between the spectral indexes (VANUI, EANTLI and VDANTLI) and socio-economic indicators increased significantly. Specifically, the VDANTLI and EC have the highest R^2 of 0.978 whereas the R^2 for the EANTLI and EC is 0.895. In the correlation analysis of GDP and spectral indexes, the group "VDANTLI and GDP" also achieved the highest R^2 of 0.960.

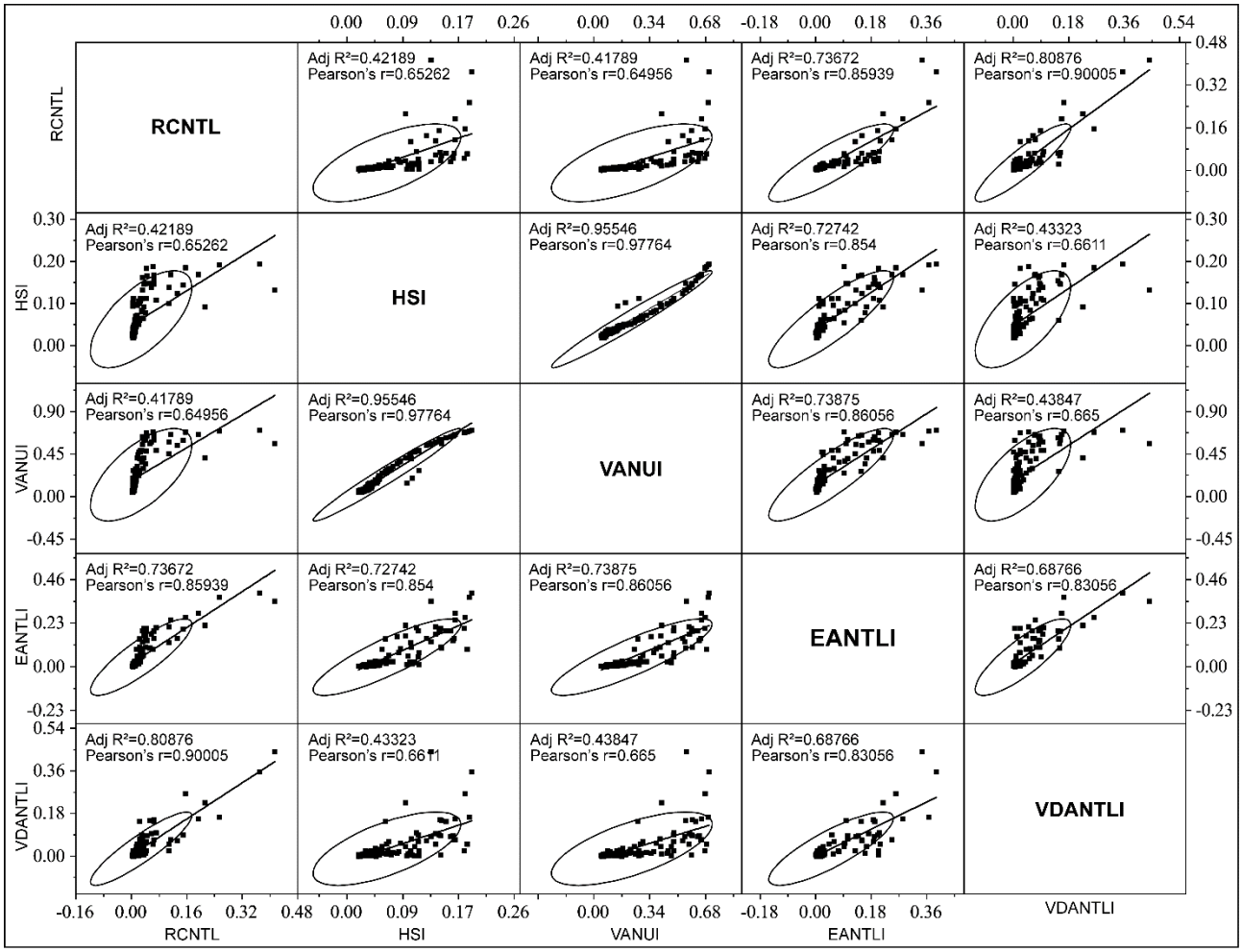

Figure 2.7. The scatter matrix between the HSI, VANUI, EANTLI, VDANTLI and RCNTL in study areas.

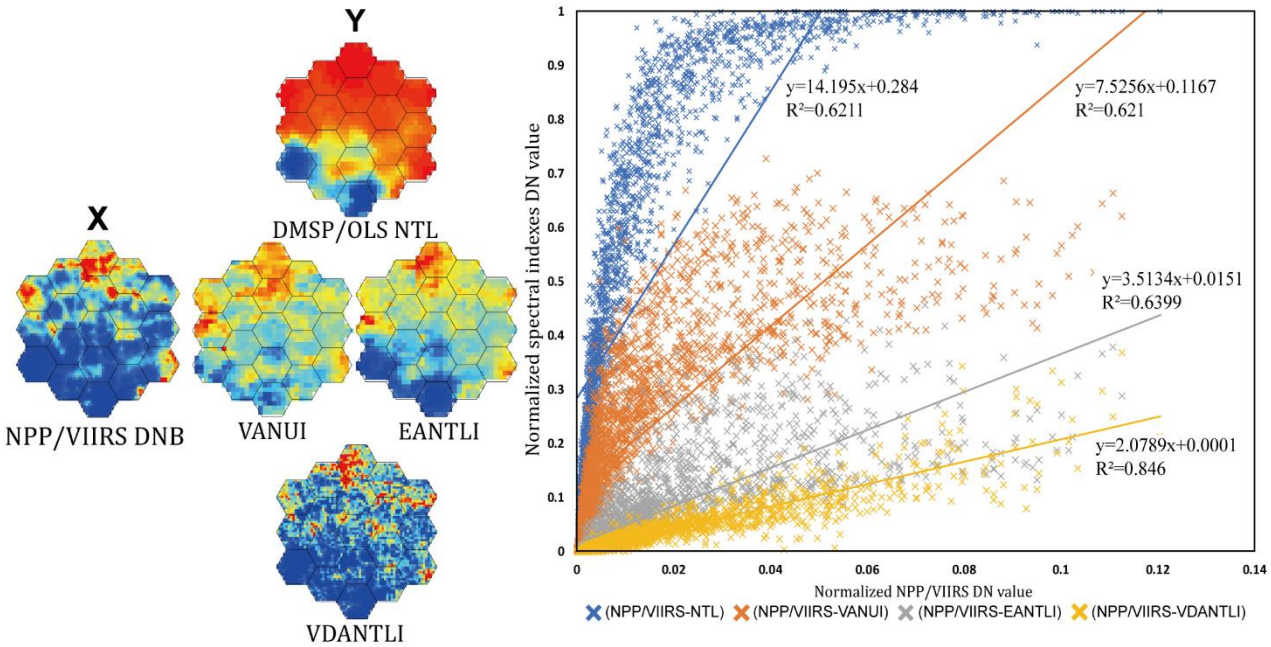

Figure 2.8. The linear regression analysis of spectral indexes and NPP/VIIRS DNB data.

We analyzed the three most developed urban agglomerations in China by four methods: visual contrast, transects comparison, land use characteristics verification and regression analysis (includes RCNTL regression

analysis, NPP/VIIRS DNB data regression analysis and socio-economic data regression analysis). All these assessments state clearly that the VANUI, EANTLI and VDANTLI can both effectively alleviate the saturation phenomenon of the NTL and highlight the details of lighting in the urban core areas, and have a higher correlation with the social-economic indicators of the city. In addition, the most notable is that the VDANTLI based on vector data has the best effect and performance in eliminating saturation, increasing inner-urban variability and correlation analysis with social-economic indicators.

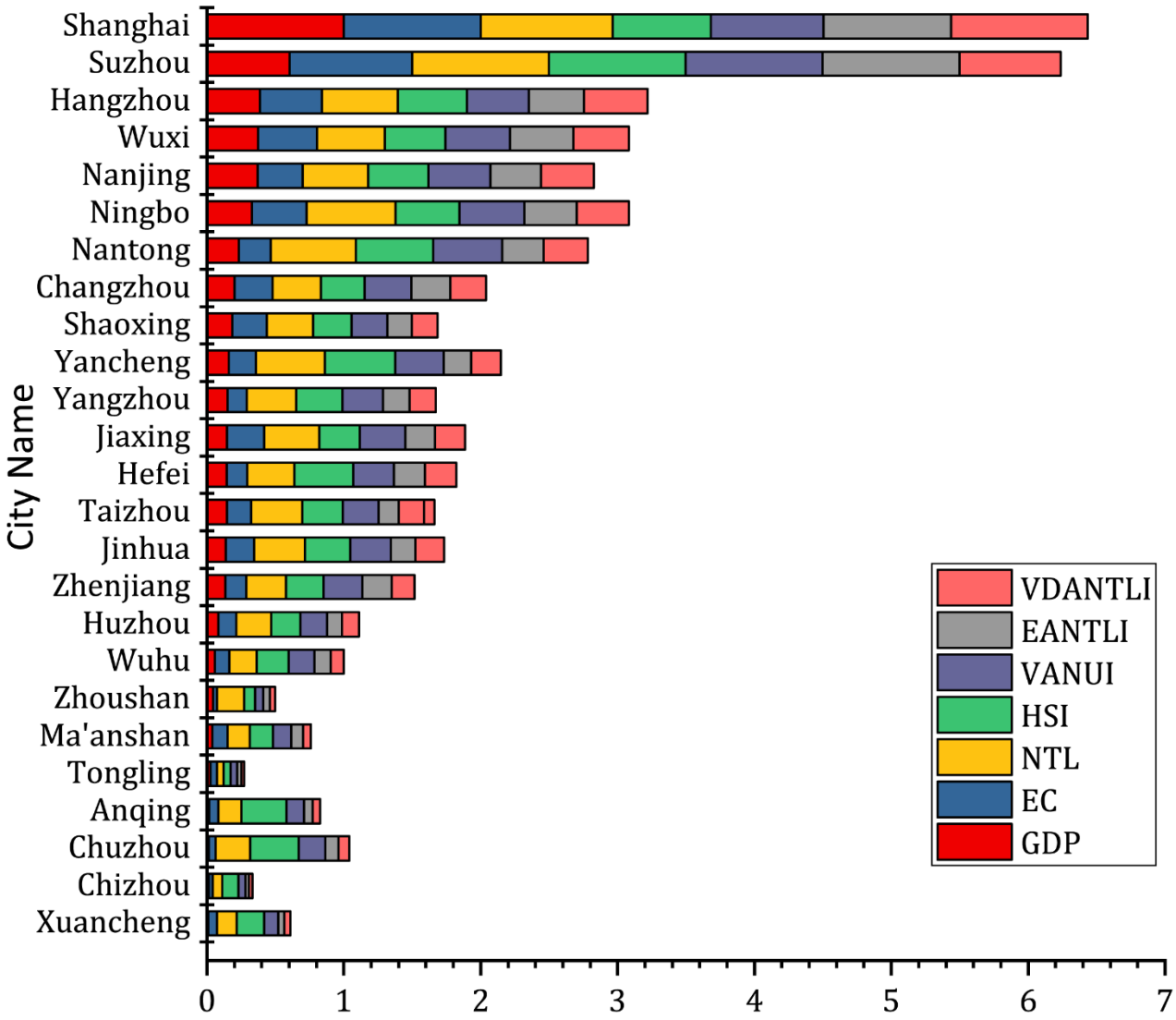

Figure 2.9. The Characteristics of Normalized GDP, EC, NTL, HIS, VANUI, EANTLI and VDANTLI in 26 prefecture-level cities, YRDUA.

Table 2.1 The Results of linear regression analysis between GDP, EC and the spectral indexes.

Spectral Indexes	Economic Indicators	Fitting function	R^2
Native NTL	GDP	$y = 2.885x - 2654.1$	0.813
	Electricity Consumption	$y = 0.2112x - 162.63$	0.851
HSI	GDP	$y = 25.338x - 2397.7$	0.632
	Electricity Consumption	$y = 1.9345x - 164.81$	0.720
VANUI	GDP	$y = 7.12x - 1846.3$	0.810
	Electricity Consumption	$y = 0.5329x - 113.53$	0.886

EANTLI	GDP	$y = 25.592x - 360.76$	0.895
	Electricity Consumption	$y = 1.899x + 0.6466$	0.952
VDANTLI	GDP	$y = 37.917x - 726.29$	0.978
	Electricity Consumption	$y = 2.688x - 9.9245$	0.960

2.5.2 Temporal and Resolution Characteristics of VDANTLI

Although the NTL data corrected by the vegetation index improved in accuracy, it still failed to break through the inherent spatial resolution due to the limited resolution of the NDVI or EVI. Due to the advantages of vector data in spatial resolution, the length of the grid can be dynamically set in the process of correcting saturation, and the spatial resolution of the VDANTLI is adjusted according to the needs of spatial analysis. In this paper, we have established the three different spatial resolution fishnets in Shanghai (the most economically developed city in China) and calculate the GVDD respectively (Figure 2.10). It is obvious that the VDANTLI within the spatial resolution of 250m depicts the unprecedented detail of nighttime light intensity, even the nuances of the city center can also be identified. The high spatial resolution NTL correction results preserve more characteristics of urban structure and economic activity, and can be combined with other geospatial data to produce more meaningful research results.

Dynamic research methods are very effective and important both in traditional geographical studies and in socioeconomic analyses (Liu et al., 2008; Chen et al., 2009; Chen et al., 2016b). Through a series of comparative analyses of time-series, one can clearly grasp the geographical process or socio-economic development trajectory, trends, and better understand the underlying mechanism behind them. Since the OLS sensors under the DMSP have been launched into orbit, a set of time-series of NTL data has been produced which provides a unique perspective for ground researchers to understand the urbanization process. As the research object in this paper, the DMSP/OLS NTL time-series dataset provides nighttime lighting data products of Average Visible, Stable Lights and Cloud Free Coverages from 1992 to 2013. Naturally, a worthy question arises: can a desaturation model based on vector data be able to correct the NTL of the time-series and how accurate is it?

In order to figure out the accuracy of the desaturation model for the time-series native NTL, we collected the NTL data for 7 years from 2000 to 2012 (2000, 2002, …, 2012) to assess the results of desaturation. Before desaturation, it is necessary to preprocess the acquired time-series NTL images in order to eliminate the obvious abnormal DN value fluctuation of NTL images acquired by different sensors in the same year and the same sensor in different years in the same year. In this paper, we used the invariant target region correction method proposed by Elvidge et al. (2009) to correct the time-series NTL images so as to promote the continuity and comparability of the NTL data. However, due to the lack of road network and POI data for the time-series before 2013, we tried to use the single period vector dataset as an auxiliary parameter to correct the time-series native NTL images. The theoretical basis for correcting time-series NTL images using vector data in 2013 is that: a) according to the calculation formula of VDANTLI (Eq. 2.5), the GVDD can not affect the DN value

in the non-lighting area, but only surge the difference in the lighting area; b) most cities in the process of rapid urbanization, the economic and social development of the city is continuously improved, and the road network is constantly being built and improved. This means that although we use the 2013 GVDD to correct NTL images before 2013, the results will still retain the vast majority of NTL information, and GVDD only serves to differentiate the DN values in the lighting area. Therefore, we selected the largest and most dynamic urban agglomeration in China, the YRDUA, and conducted linear regression analysis to quantitatively evaluate the correction results of the calibration model for the NTL time-series in typical urban agglomerations. The normalized NTL, EANTLI, VDANTLI, GDP, and EC of the 26 cities with different levels of development in the urban agglomeration are listed in Table 2.2. The fitting results of linear regression on the time-series (Figure 2.11) shows that the correlation between social-economic indicators and the VDANTLI was significantly higher and more stable than that of the EANTLI and native NTL. In particular, the shorter of the time interval between the NTL and the vector data, the higher the correlation coefficient between the VDANTLI and GDP. Compared with GDP, VDANTLI has a higher correlation with EC, which also reflects the ability of nighttime lights to assess surface energy consumption. The results verify the feasibility of a single period vector data correction time-series NTL data from the correlation analysis. The revised NTL data can not only accurately reflect the change of the urban economic development level in the time series, but also depict the spatial structure characteristics of cities.

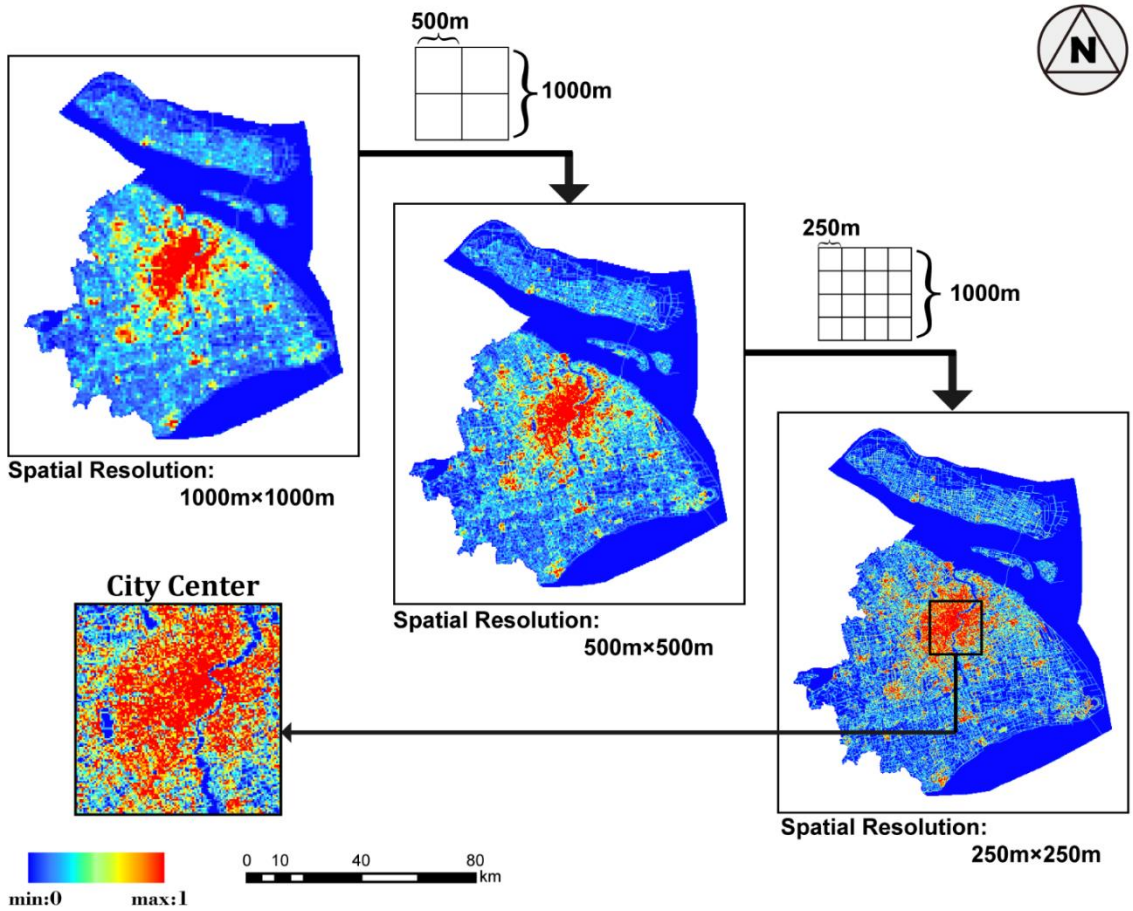

Figure 2.10. Multilevel spatial resolution of VDANTLI in Shanghai, China. The spatial resolutions are 1000, 500 and 250 m.

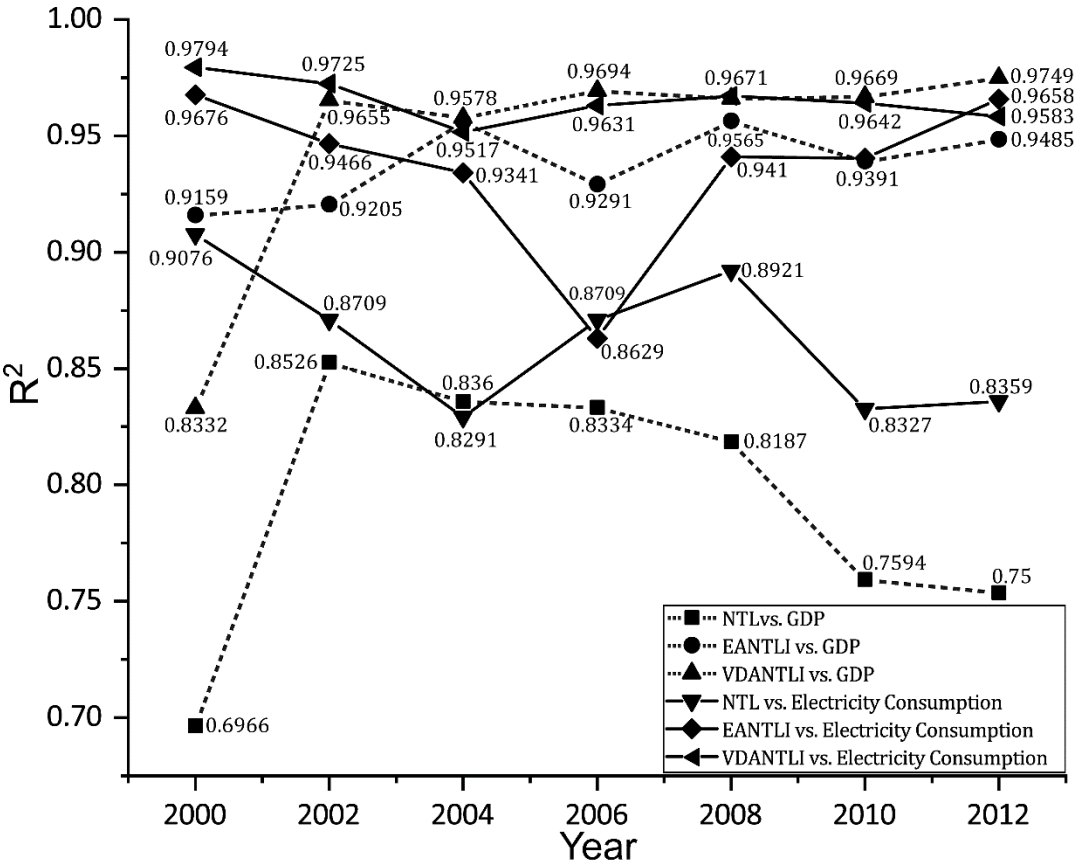

Figure 2.11. The fitting results of linear regression on the time-series. Note: Linear regression includes NTL vs. GDP, EANTLI vs. GDP, VDANTLI vs. GDP, NTL vs. EC, EANTLI vs. EC and VDANTLI vs. EC.

Table 2.2 The NTL, EANTLI, VDANTLI, GDP and EC of 26 prefecture-level cities in YRDUA from 2000 to 2012.Note: EC data for Jiangsu Province in 2000 and 2002 were incomplete; All variables are normalized to [0-1].

Time	Variable	Hangzhou	Hefei	Nanjing	Shanghai	…	Suzhou	Wuxi	Wuhu	Yangzhou
2000	NTL	0.47	0.26	0.39	1.00		0.59	0.33	0.14	0.27
	EANTLI	0.19	0.06	0.14	1.00		0.17	0.10	0.02	0.04
	VDANTLI	0.37	0.16	0.29	1.00		0.42	0.25	0.06	0.12
	GDP	0.30	0.10	0.17	1.00		0.07	0.09	0.06	0.03
	EC	0.28	0.06	nodata	1.00		nodata	nodata	0.02	nodata
2002	NTL	0.51	0.26	0.42	1.00		0.74	0.40	0.13	0.28
	EANTLI	0.13	0.07	0.18	1.00		0.20	0.15	0.02	0.05
	VDANTLI	0.40	0.18	0.33	1.00		0.52	0.31	0.06	0.13
	GDP	0.33	0.08	0.24	1.00		0.38	0.29	0.05	0.10
	EC	0.31	0.06	nodata	1.00		nodata	nodata	0.02	nodata
2004	NTL	0.53	0.28	0.43	1.00		0.88	0.45	0.14	0.28
	EANTLI	0.13	0.06	0.16	1.00	…	0.33	0.22	0.02	0.07
	VDANTLI	0.41	0.18	0.34	1.00		0.62	0.34	0.06	0.14
	GDP	0.31	0.07	0.24	1.00		0.43	0.29	0.04	0.10
	EC	0.33	0.06	0.18	1.00		0.47	0.30	0.02	0.07
2006	NTL	0.52	0.24	0.42	1.00		0.92	0.46	0.12	0.29
	EANTLI	0.12	0.06	0.11	1.00		0.31	0.18	0.01	0.05
	VDANTLI	0.40	0.17	0.32	1.00		0.63	0.35	0.06	0.14
	GDP	0.33	0.10	0.26	1.00		0.46	0.31	0.05	0.10
	EC	0.37	0.06	0.19	1.00		0.59	0.35	0.03	0.07
2008	NTL	0.57	0.32	0.46	0.99		1.00	0.52	0.17	0.32
	EANTLI	0.25	0.12	0.19	1.00		0.61	0.33	0.02	0.06
	VDANTLI	0.44	0.20	0.35	1.00		0.69	0.39	0.08	0.16

	GDP	0.34	0.12	0.27	1.00	0.50	0.32	0.05	0.12
	EC	0.38	0.06	0.27	1.00	0.75	0.41	0.04	0.10
2010	NTL	0.58	0.34	0.48	0.91	1.00	0.51	0.21	0.36
	EANTLI	0.20	0.10	0.19	1.00	0.73	0.30	0.03	0.09
	VDANTLI	0.46	0.22	0.37	1.00	0.72	0.40	0.09	0.18
	GDP	0.35	0.17	0.30	1.00	0.54	0.34	0.08	0.13
	EC	0.40	0.07	0.29	1.00	0.79	0.42	0.04	0.12
2012	NTL	0.59	0.31	0.46	0.88	1.00	0.49	0.20	0.35
	EANTLI	0.36	0.11	0.23	1.00	0.80	0.33	0.06	0.11
	VDANTLI	0.48	0.21	0.37	1.00	0.73	0.40	0.09	0.18
	GDP	0.39	0.21	0.36	1.00	0.60	0.38	0.09	0.15
	EC	0.44	0.08	0.31	1.00	0.88	0.43	0.05	0.13

2.6 Discussion

Through the desaturation assessment of three urban agglomerations with the largest and most pr ominent NTL saturation phenomenon in China, we further confirm the superiority of VDANTLI in eliminating saturation of urban central areas. In addition, different from the previous correction meth ods based on vegetation index, the proposed correction method shows better correction ability in spa tial and temporal resolution. The obtained VDANTLI data set can be applied to the research of urb anization process of typical urban agglomeration effectively (the VDANTL sample data can be down loaded via the link "https://figshare.com/articles/VDANTLI_Sample_Data/7200812").

2.6.1 Influence of auxiliary parameters on desaturated model

In general, for the same native NTL data, the differences in auxiliary parameters lead to differences in correction effects. The vegetation indexes are an effective and concise index to describe vegetation cover. Among them, the NDVI and EVI are the most widely used vegetation index. In the past few decades, the research of the NDVI and EVI has greatly promoted the development of remote sensing science, especially vegetation remote sensing science (Huete et al., 2002; Chen et al., 2006). Due to the outstanding ability of rapid monitoring of surface vegetation coverage and health status, the global land cover dynamics are constantly advancing and have achieved a series of fruitful research results. For correcting the saturation of native NTL, both the VANUI and EANTLI are established under the same assumption that the intensity of nighttime light intensity is inversely proportional to the density of vegetation distribution. Usually, the closer to the urban centers, the lower the vegetation coverage; the closer to the suburbs or the countryside, the higher the vegetation cover. This inverse relation has been introduced into the modified saturated model, and two spectral indices have been developed: VANUI and EANTLI.

However, the inverse relationship between this vegetation index (NDVI or EVI) and NTL is not absolutely stable. Different from some legacy cities which have developed over a long period, China's urban development is in a high-speed expansion process. With the continuous expansion of urban impervious surface, the vegetation types and coverage area decreased sharply, which inhibited the spatial heterogeneity of vegetation index. As mentioned earlier, due to the defects of DMSP/OLS sensors, the saturation phenomenon

of native NTL is mainly concentrated in the urban central areas. Therefore, in the urban central areas, using low spatial heterogeneity auxiliary parameters to correct the NTL data with low spatial heterogeneity, the results will be adversely affected and cannot highlight the city's brightness detail information. In addition, in some special areas or cities, the reverse relationship between the vegetation index and the brightness of the light is completely lost. As the hub of urban economic development, CBD brings together the economic, technological and cultural resources of the city, and is also the most concentrated area of night lights in the city (Liu et al., 2017). With the deepening of the concept of eco-green CBD, the current CBD is developing in the direction of the integration of modern business and natural ecology. The perfect afforestation system improved the vegetation coverage of CBD, which resulted in the higher vegetation index in the corrected saturation and suppressed the corrected nighttime light intensity. A different situation is when we use the vegetation index to correct the saturation problems in peri-urbanization regions. In the peri-urbanization regions around the city, due to the level of economic development and urban expansion, there will be some bare land and tributaries of rivers. These plots reduce vegetation cover in the area and incorrectly stretch the corrected intensity of the nighttime light. It is worth noting that the development and expansion process of some cities is different from that of traditional urban development in terms of vegetation coverage and urban development. The most typical characteristic of these cities is that they are located in the desert, such as Las Vegas, Nevada and Phoenix, Arizona (Zhang et al., 2013). These areas will adapt to the needs of livability in the process of urbanization, and constantly promote green vegetation coverage, including planting trees, building vegetation parks and golf lawns. Different from the cities mentioned above, the closer to the urban centers, the higher the vegetation coverage. As mentioned earlier, the VANUI and EANTLI are designed by assuming an inverse relationship between nighttime light intensity and vegetation abundance, and in these regions the modified saturation model based on the vegetation index may not be applicable.

Unlike the VANUI and EANTLI, the VDANTLI we proposed in this paper is based on a positive correlation between vector data sets and lighting intensity. It is well known that NTL is an important indicator of the earth's brightness at night which is directly determined by the light produced by human activity on the ground surface. The intensity of nighttime light produced by human activities is closely related to the level of economic development in the region and the types of human activities. In other words, NTL is a social economic indicator rather than a natural indicator, which explains why the use of the vegetation index to correct NTL may cause the deviation, or why the correlation between vegetation cover and light intensity is unstable. In recent years, with the development and practice of "big geospatial data" and "smart city", it is possible to obtain massive geospatial data. Among them, the multi-level road network data and POI data are two of the most widely used spatial data in the large geospatial data. With the development of the city, the road network and various service facilities are becoming more and more intensive. In short, the multi-level road network data can describe the spatial structure of the city, and POI data can reveal the configuration of the urban service resources. Further, the urban structure and the allocation of resources also determine the strength of the city's economy and human activities, and this is also the factual basis for the hypothesis of our proposed correction model.

2.6.2 Challenges in VDANTLI applications

Although the feasibility and reliability of VDANTLI are verified in many aspects, it has to be acknowledged that the desaturation model that we proposed still has some shortcomings. Firstly, there are inconsistencies in the acquisition time between multi-level road network data, POI data and native NTL data during the construction of GVDD. As geospatial large data began to open to the public in recent years, especially the authoritative Internet map suppliers, we cannot collect vector data within the native NTL data acquisition period. Therefore, this paper uses the road network data and POI data of 2015 in the process of calculating the GVDD, which will inevitably have an adverse effect on the results of desaturation. In order to minimize such interference, we made use of the OSM road network data of some cities in 2014 to correct the road network data from Amap. In the process of modifying the road network data, we find that the change of the road network in the adjacent years is small, basically, it is upgraded on the basis of the original road, and the number of newly developed roads is relatively small. Because we choose the unit road network length as an index in the calculation of GVDD, the impact of road upgrading on GVDD is limited. In addition, the results of desaturation correction for time-series NTL data also reflect the feasibility of this desaturation model. Besides, with the explosive growth of spatial data, the access threshold of the road network data and POI data is greatly reduced. The continuous and complete records of geospatial data provide a solid foundation for subsequent vector and image data fusion. Secondly, the integrity of the vector data set and the difficulty of getting the data will directly affect the range of the application of the model. In this paper, we use the multi-level road network data and the POI data in the mainland of China to do the saturation correction for native NTL and obtain some positive results. As we currently lack of a global multi-level road network data and POI data, this method cannot be extended to all parts of the world, but with the geographical spatial data of explosive growth, access to the global network and POI data will no longer be a problem. We are eager to work together with other regional scholars to eliminate the saturation of NTL on a global scale based on vector data sets.

Moreover, with the successful launch of the NPP satellite, its VIIRS began to collect data. The VIIRS inherits and develops the function of DMSP/OLS, the improved sensor has higher spatial resolution (500m), a wide range of radiation detection solves the saturation problem of nighttime light data, and a better on-board radiometric correction capability improves the quality of the data. The monthly composites and annual composites of Version 1 VIIRS DNB data are available for download from 2012 to the present. An unprecedented time span (1992-now) of urban development and dynamic analysis of structural change can be achieved by combining the time-series data of the corrected DMSP/OLS NTL data (1992-2013) and the NPP/VIIRS DNB data (2012-now).

2.7 Conclusions

In contrast to several previous methods for eliminating the saturation of native NTL data based on vegetation characteristics, we select multi-level road network data and POI data which are more closely related

to social and economic development as the correction parameters to correct the saturation of the NTL data, and propose a new spectral index: VDANTLI. In order to evaluate the accuracy of the modified saturation method proposed in this paper, we select the three most developed cities (the most concentrated area of saturation) in China, and carry out a series of quantitative and qualitative comparative analysis. Firstly, the comparative analysis of typical sample areas shows that the VDANTLI outperforms other indexes in highlighting the brightness of CBD lights and suppressing the brightness of bare land and mixed plots of water and land. Moreover, the comparative analysis of the building area (extracted from high resolution remote sensing images) and the lighting area also shows that VDANTLI has the highest accuracy and consistency in characterizing the real night lights. Secondly, the transect curves and spectral indexes regression analysis manifest that the VDANTLI is closer to the RCNTL in characterizing the luminance characteristics of lights in inner-urban areas. Considering the advantages of the new generation of night light data, we use the same period NPP/VIIRS DNB data and spectral indexes to carry out similarity evaluation, and the results also further confirm the good performance of VDANTLI. Thirdly, by comparing the other indices mentioned above, we find that the correlations between the VDANTLI and socio-economic indicators are higher and more stable, which means that the VDANTLI can be used as an effective data for socio-economic spatial analysis. Moreover, the VDANTLI, as a product of fusion of vector data and raster data, is not only an attempt to solve the problem of saturation of the NTL, but also a case of the combination of vector data and raster data. Considering the advantages of the VDANTLI in spatial resolution and the capability in time-series native NTL desaturation, the VDANTLI may become an indispensable basic data for long time-series of urban development studies, urban structure analysis, etc.

Acknowledgments：This study was jointly supported by Natural Science Foundation of Guangdong Province, China (Grant No.2016A030313551) and National Natural Science Foundation of China (Grant No. 41671430).

Conflicts of Interest: The authors declare no conflict of interest.

References

Amaral, S., Monteiro, A.M., Câmara, G. & Quintanilha, J. (2006) DMSP/OLS night-time light imagery for urban population estimates in the Brazilian Amazon. International journal of remote sensing 27, 855-870.

Cai, J., Huang, B. & Song, Y. (2017) Using multi-source geospatial big data to identify the structure of polycentric cities. Remote Sensing of Environment 202, 210-221.

Cao, Z., Wu, Z., Kuang, Y.-q. & Huang, N. (2015) Correction of DMSP/OLS night-time light images and its application in China. Journal of Geo-Information Science 17, 1092-1102.

Cao, Z., Wu, Z., Kuang, Y., Huang, N. & Wang, M. (2016) Coupling an intercalibration of radiance-calibrated nighttime light images and land use/cover data for modeling and analyzing the distribution of GDP in Guangdong, China. Sustainability 8, 108.

Chand, T.K., Badarinath, K., Elvidge, C. & Tuttle, B. (2009) Spatial characterization of electrical power consumption patterns over India using temporal DMSP-OLS night-time satellite data. International journal of remote sensing 30, 647-661.

Chen, J., Zhuo, L., Shi, P. & Toshiaki, I. (2003) The study on urbanization process in China based on DMSP/OLS Data: development of a light index for urbanization level estimation. Journal of Remote Sensing 7, 168-175.

Chen, P., Fedosejevs, G., Tiscareno-Lopez, M. & Arnold, J.G. (2006) Assessment of MODIS-EVI, MODIS-NDVI and VEGETATION-NDVI composite data using agricultural measurements: An example at corn fields in western Mexico. Environmental monitoring and assessment 119, 69-82.

Chen, Y., Chang, K., Han, F., Karacsonyi, D. & Qian, Q. (2016a) Investigating urbanization and its spatial determinants in the central districts of Guangzhou, China. Habitat International 51, 59-69.

Chen, Y., Wu, Z., Qian, Q., Zheng, Z. & Han, F., (2016b) Dynamic monitoring and spatiotemporal evolution of the coastline in Pearl River estuary in recent fifty years, 2016 4th International Workshop on Earth Observation and Remote Sensing Applications (EORSA). IEEE, pp. 87-91.

Chen, Y., Zhou, Q. & Chen, J. (2009) Spatiotemporal characteristics of land use and cover change in GuangZhou City in the past 30 years. Scientia Geographica Sinica 29, 368-374.

Chen, Z., Yu, B., Song, W., Liu, H., Wu, Q., Shi, K. & Wu, J. (2017) A new approach for detecting urban centers and their spatial structure with nighttime light remote sensing. IEEE Transactions on Geoscience and Remote Sensing 55, 6305-6319.

Chi, J., Jiao, L., Dong, T., Gu, Y. & Ma, Y. (2016) Quantitative identification and visualization of urban functional area based on POI data. Journal of Geomatics 41, 68-73.

Deng, J., Wang, K., Hong, Y. & Qi, J. (2009) Spatio-temporal dynamics and evolution of land use change and landscape pattern in response to rapid urbanization. Landscape and urban planning 92, 187-198.

Elvidge, C.D., Baugh, K.E., Dietz, J.B., Bland, T., Sutton, P.C. & Kroehl, H.W. (1999) Radiance calibration of DMSP-OLS low-light imaging data of human settlements. Remote Sensing of Environment 68, 77-88.

Elvidge, C.D., Ziskin, D., Baugh, K.E., Tuttle, B.T., Ghosh, T., Pack, D.W., . . . Zhizhin, M. (2009) A fifteen year record of global natural gas flaring derived from satellite data. Energies 2, 595-622.

Ewing, R. & Rong, F. (2008) The impact of urban form on US residential energy use. Housing policy debate 19, 1-30.

Feng, Z., Chen, Y., Qian, Q. & Wang, S. (2014) Relationship between the structure of urban traffic network and urban spatial expansion: A case study of Dongguan City. Journal of Geo-Information Science 16, 79-86.

Gao, B., Huang, Q., He, C. & Ma, Q. (2015) Dynamics of urbanization levels in China from 1992 to 2012: Perspective from DMSP/OLS nighttime light data. Remote Sensing 7, 1721-1735.

Guo, G., Zhou, X., Wu, Z., Xiao, R. & Chen, Y. (2016) Characterizing the impact of urban morphology heterogeneity on land surface temperature in Guangzhou, China. Environmental Modelling & Software 84, 427-439.

He, C., Shi, P., Li, J., Chen, J., Pan, Y., Li, J., . . . Ichinose, T. (2006) Restoring urbanization process in China in the 1990s by using non-radiance-calibrated DMSP/OLS nighttime light imagery and statistical data. Chinese Science Bulletin 51, 1614-1620.

Hu, Y.n., Peng, J., Liu, Y., Du, Y., Li, H. & Wu, J. (2017) Mapping development pattern in Beijing-Tianjin-Hebei urban agglomeration using DMSP/OLS nighttime light data. Remote Sensing 9, 760.

Huete, A., Didan, K., Miura, T., Rodriguez, E.P., Gao, X. & Ferreira, L.G. (2002) Overview of the radiometric and biophysical performance of the MODIS vegetation indices. Remote Sensing of Environment 83, 195-213.

Ichii, K., Kawabata, A. & Yamaguchi, Y. (2002) Global correlation analysis for NDVI and climatic variables and NDVI trends: 1982-1990. International journal of remote sensing 23, 3873-3878.

Letu, H., Hara, M., Tana, G. & Nishio, F. (2011) A saturated light correction method for DMSP/OLS nighttime satellite imagery. IEEE Transactions on Geoscience and Remote Sensing 50, 389-396.

Letu, H., Hara, M., Yagi, H., Naoki, K., Tana, G., Nishio, F. & Shuhei, O. (2010) Estimating energy consumption from night-time DMPS/OLS imagery after correcting for saturation effects. International journal of remote sensing 31, 4443-4458.

Li, Z., Hu, D., Li, J. & Cen, J. (2016) Simulation and spatialization of GDP in poverty areas based on night light imagery. Remote Sensing for Land and Resources 28, 168-174.

Liu, Y., Wang, L. & Long, H. (2008) Spatio-temporal analysis of land-use conversion in the eastern coastal China during 1996–2005. Journal of Geographical Sciences 18, 274-282.

Liu, Y., Yang, Y., Jing, W., Yao, L., Yue, X. & Zhao, X. (2017) A new urban index for expressing inner-city patterns based on MODIS LST and EVI regulated DMSP/OLS NTL. Remote Sensing 9, 777.

Lu, D., Tian, H., Zhou, G. & Ge, H. (2008) Regional mapping of human settlements in southeastern China with multisensor remotely sensed data. Remote Sensing of Environment 112, 3668-3679.

Lunetta, R.S., Knight, J.F., Ediriwickrema, J., Lyon, J.G. & Worthy, L.D. (2006) Land-cover change detection using multi-temporal MODIS NDVI data. Remote Sensing of Environment 105, 142-154.

Ma, L., Wu, J., Li, W., Peng, J. & Liu, H. (2014) Evaluating saturation correction methods for DMSP/OLS nighttime light data: A case study from China's cities. Remote Sensing 6, 9853-9872.

Ma, T., Zhou, Y., Zhou, C., Haynie, S., Pei, T. & Xu, T. (2015) Night-time light derived estimation of spatio-temporal characteristics of urbanization dynamics using DMSP/OLS satellite data. Remote Sensing of Environment 158, 453-464.

Marshall, J.D. (2008) Energy-efficient urban form. Environmental Science & Technology.

Morawitz, D.F., Blewett, T.M., Cohen, A. & Alberti, M. (2006) Using NDVI to assess vegetative land cover change in central Puget Sound. Environmental monitoring and assessment 114, 85-106.

Parés-Ramos, I.K., Álvarez-Berríos, N.L. & Aide, T.M. (2013) Mapping urbanization dynamics in major cities of Colombia, Ecuador, Perú, and Bolivia using night-time satellite imagery. Land 2, 37-59.

Pettorelli, N., Vik, J.O., Mysterud, A., Gaillard, J.-M., Tucker, C.J. & Stenseth, N.C. (2005) Using the satellite-derived NDVI to assess ecological responses to environmental change. Trends in ecology & evolution 20, 503-510.

Pozzi, F. & Small, C. (2005) Analysis of urban land cover and population density in the United States. Photogrammetric Engineering & Remote Sensing 71, 719-726.

Shi, K., Chen, Y., Yu, B., Xu, T., Chen, Z., Liu, R., . . . Wu, J. (2016a) Modeling spatiotemporal CO_2 (carbon dioxide) emission dynamics in China from DMSP-OLS nighttime stable light data using panel data analysis. Applied Energy 168, 523-533.

Shi, K., Chen, Y., Yu, B., Xu, T., Yang, C., Li, L., . . . Wu, J. (2016b) Detecting spatiotemporal dynamics of global electric power consumption using DMSP-OLS nighttime stable light data. Applied Energy 184, 450-463.

Small, C. (2001) Estimation of urban vegetation abundance by spectral mixture analysis. International journal of remote sensing 22, 1305-1334.

Sutton, P.C., Elvidge, C.D. & Ghosh, T. (2007) Estimation of gross domestic product at sub-national scales using nighttime satellite imagery. International Journal of Ecological Economics & Statistics 8, 5-21.

Weng, Y. (2007) Spatiotemporal changes of landscape pattern in response to urbanization. Landscape and urban planning 81, 341-353.

Wu, J., Wang, Z., Li, W. & Peng, J. (2013) Exploring factors affecting the relationship between light consumption and GDP based on DMSP/OLS nighttime satellite imagery. Remote Sensing of Environment 134, 111-119.

Wu, R. & Zhu, B. (2016) The unbalanced distribution of population in China and the stability of Heihe-Tengchong line. Chinese Journal of Population Science 36, 14-24.

Xu, T., Ma, T., Zhou, C. & Zhou, Y. (2014) Characterizing spatio-temporal dynamics of urbanization in China using time series of DMSP/OLS night light data. Remote Sensing 6, 7708-7731.

Xu, Z. & Gao, X. (2016) A novel method for identifying the boundary of urban built-up areas with POI data. Acta Geographica Sinca 71, 928-939.

Yu, B., Shu, S., Liu, H., Song, W., Wu, J., Wang, L. & Chen, Z. (2014) Object-based spatial cluster analysis of urban landscape pattern using nighttime light satellite images: A case study of China. International Journal of Geographical Information Science 28, 2328-2355.

Zhang, Q., Schaaf, C. & Seto, K.C. (2013) The vegetation adjusted NTL urban index: A new approach to reduce saturation and increase variation in nighttime luminosity. Remote Sensing of Environment 129, 32-41.

Zhang, Q. & Seto, K.C. (2011) Mapping urbanization dynamics at regional and global scales using multi-temporal DMSP/OLS nighttime light data. Remote Sensing of Environment 115, 2320-2329.

Zhao, W., Li, Q. & Li, B. (2011) Extracting hierarchical landmarks from urban POI data. Journal of Remote Sensing 15, 973-988.

Zheng, Z., Chen, Y., Wu, Z. & Zhang, Q. (2018) Method to reduce saturation of DMSP/OLS nighttime light data based on UNL. Journal of Remote Sensing 22, 161-173.

Zhou, Y., Ma, T., Zhou, C. & Xu, T. (2015) Nighttime light derived assessment of regional inequality of socioeconomic development in China. Remote Sensing 7, 1242-1262.

Zhuo, L., Chen, J., Shi, P., Gu, Z., Fan, Y. & Ichinose, T. (2005) Modeling population density of China in 1998 based on DMSP/OLS nighttime light image. Acta Geographica Sinica 60, 266-276.

Zhuo, L., Zhang, X., Zheng, J., Tao, H. & Guo, Y. (2015) An EVI-based method to reduce saturation of DMSP/OLS nighttime light data. Acta Geographica Sinca 70, 1339-1350.

3. The interannual calibration and global nighttime light fluctuation assessment based on pixel-level linear regression analysis [2]

3.1 Abstract

The Operational Linescan System (OLS) carried by the National Defense Meteorological Satellite Program (DMSP) can capture the weak visible radiation emitted from earth at night and produce a series of annual cloudless nighttime light (NTL) images, effectively supporting multi-scale, long-term human activities and urbanization process research. However, the interannual instability and sensor bias of NTL time series products greatly limit further studies of lighting data in time series with OLS. Several calibration models for OLS have been proposed to implement interannual corrections to improve the continuity and consistency of time series NTL products. However, due to the subjective factors intervention and insufficient automation in the calibration process, the interannual correction study of NTL time series images is still worth being developed further. Therefore, to avoid the involvement of subjective factors and to optimize the Pseudo-Invariant Features (PIF) identification, an interannual calibration model Pixel-based PIF (PBPIF) is proposed, which identifies PIF by pixel fluctuation characteristics. Results show that a PBPIF-based model can reduce subjective interference and improve the degree of automation during the NTL interannual calibration process. The calibration performance evaluation based on Total Sum of Lights (TSOL) and Sum of the Normalized Difference Index (SNDI) shows that compared to the traditional PIF-based (tPIF-based) and Ridgeline Sampling Regression based (RSR-based) models, the PBPIF-based one achieves better performance in reducing NTL interannual turbulence and minimizing the deviation between sensors. In addition, based on the corrected NTL time series products, pixel-level linear regression analysis is implemented to maximize the potential of the NTL resolution to produce global Light Intensity Change Coefficient (LICC). The results of global LICC can be widely applied to the detailed study of the characteristics of economic development and urbanization.

Keywords: DMSP/OLS; nighttime light; interannual correction; pseudo-invariant features

3.2 Introduction

Nighttime light (NTL) images effectively depict the distribution of artificial light on the earth's surface, and have become an important indicator of the intensity of urban social and economic activities, and has been widely used in urbanization research (Croft, 1978; Sutton et al., 1997; He et al., 2006; Lu et al., 2008; Ghosh et al., 2010; Cao et al., 2016; Xie et al., 2019). In particular, the unique advantage of NTL collections in space-time span makes it more straightforward to carry out a global economic assessment and regional development

[2] This Chapter relies on the paper "Zheng, Z., Yang, Z., Chen, Y., Wu, Z., & Marinello, F. (2019). The Interannual Calibration and Global Nighttime Light Fluctuation Assessment Based on Pixel-Level Linear Regression Analysis. Remote Sensing, 11(18), 2185." https://doi.org/https://doi.org/10.3390/rs11182185.

research, compared to traditional statistical index accounting, which usually takes administrative unit as a statistical unit, lacking effective and accurate spatial location information. Currently, NTL products that are widely used worldwide include Defense Meteorological Program/Operational Line-Scan System (DMSP/OLS) NTL datasets and National Polar-Orbiting Partnership/ Visible Infrared Imaging Radiometer Suite (NPP/VIIRS) Day/Night Band (DNB) datasets (Kyba et al., 2017; Wu and Wang, 2019; Zheng et al., 2019a). Elvidge et al. (2013) and Miller et al. (2012) have demonstrated the superior performance of the new generation of NPP/VIIRS DNB data in terms of light range, radiation calibration and resolution, especially compared to DMSP/OLS NTL data; nevertheless, the value of long-term historical DMSP/OLS NTL archives should not be underestimated, as it is an irreplaceable reference for recording global human activities, revealing the global economy and exploring urban development patterns in past decades (Zhang et al., 2016).

In recent years, DMSP/OLS NTL datasets have been widely applied in urbanization and economic development research around the world, including urban impervious expansion (Ma et al., 2014; Shao and Liu, 2014; Pok et al., 2017), urban development models (Liao et al., 2012; Yu et al., 2014; Ma et al., 2015) or population and Gross Domestic Product (GDP) estimation (Sutton, 2003; Li et al., 2013c; Wu et al., 2013b; Xie and Weng, 2016; Bennett and Smith, 2017). However, two main defects and limitations can be recognized in DMSP/OLS NTL time series datasets: the interannual instability of the same sensors and the deviations between different sensors in the same year. On the one hand, the regional or global nighttime light intensity over a long-time span usually shows a relatively stable trend. In fact, due to the interannual anomalous perturbation of the sensor, the observed annual Total Sum of Lights (TSOL) fluctuations from a certain sensor in the time series occasionally exhibit irregularity and randomness. On the other hand, the regional or global TSOL for a given year is constant, so the results observed by different sensors should theoretically be consistent. However, in NTL time series datasets, the TSOL recorded by different sensors in the same year is biased, due to the slightly different working conditions and performance between OLS sensors mounted on different satellites. Considering the enormous potential of NTL in describing socio-economic or human activities (Huang et al., 2014), consistent and comparable NTL time series images can help to further understand how human activities drive and respond to environmental changes (Pandey et al., 2017). Therefore, the systematic error correction (inter-annual correction) for comparative analysis of historical NTL time series datasets must be implemented.

For daytime optical remote sensing data, the methods of radiometric calibration mainly include absolute calibration and relative calibration. Absolute correction converts Digital Number (DN) value to radiation value taking advantage of transmission models or in-situ surface reflection measurement empirical models; relative correction achieves image matching by implementation of "constant" features of Pseudo-Invariant Features (PIF) between images (Jensen, 1986). Although these two types of calibration methods have achieved abundant results in daytime optical remote sensing data (Schott et al., 1988), a great challenge still remains for night light data due to the lack of onboard calibration systems and the difficulty of identifying PIF. At present, for the interannual correction method of NTL time series datasets, absolute correction based on surface reflectance

measurement is rare (Tuttle et al., 2014), and the relative correction using PIF has gradually become widespread (Hall et al., 1991; Liu et al., 2012; Li et al., 2013b; Pandey et al., 2013; Wu et al., 2013a; Elvidge et al., 2014; Hsu et al., 2015). Similar to the PIF-based relative correction model for daytime optical remote sensing data, the traditional PIFs-based (tPIF-based) NTL interannual correction uses prior knowledge (usually referring to the speed of economic development) to select specific "PIF" targets and set reference images, and uses PIF offset rules (correction functions) between uncalibrated and reference images to correct global images. Obviously, the core assumption of tPIF-based correction is that the attribute characteristics (DN values) of PIF objects should be kept constant between different images. Since the intensity of illumination emitted by PIF objects, especially local and small-scale PIF objects, is not completely constant (e.g., High-pressure Sodium (HPS) lamps losing 20% brightness during their lifetime (Bennie et al., 2014)), systematic and unknown deviations could arise during the correction process. Therefore, the pre-selection of constant PIF objects (pixels) is critical for the PIF-based interannual correction. Although the subsequent tPIF-based calibration methods differ in detail (calibration model, invariant target area), most of them follow the calibration paradigm proposed by Elvidge et al. (Elvidge et al., 2014). Recently, scholars have been expanding the methods of PIF pre-selection and are gradually changing from regional PIF to special light sources, including specific industrial parks (Bennie et al., 2014), streetlights (de Miguel et al., 2014) and artificial target light sources (Ryan et al., 2019). The above NTL interannual correction based on specific and small-scale light source object ensures the constant characteristic of PIF to a certain extent, but it is mostly suitable for local and small-scale light calibration. To avoid PIF recognition and to expand the applicable scenarios of the interannual correction model, based on the ridge regression model (Song et al., 2001), Zhang et al. (2016) proposed the Ridgeline Sampling Regression (RSR) model for the interannual correction by capturing the ridgeline function of the pixel density map between uncorrected and reference images. Theoretically, if there is no deviation between image pairs and no real change in NTL intensity, the ridge line of pixel density map will be in a perfect 1:1 diagonal line. However, the difference between images usually results in the non-linear distribution of ridges in density maps. Therefore, the correction function can be obtained by manually selecting point pairs on ridgelines with different DN values (Zhang et al., 2016).

Although the tPIF-based interannual correction model has been continuously promoted and successfully applied to the interannual correction of regional and global NTL time series, the subjective uncertainties caused by artificial PIF recognition should still be avoided as far as possible during image processing. Another prominent limitation is that the existing PIF selection schemes mostly use local and small-scale DN value deviation rules to correct global NTL data while ignoring regional differences in light image deviation, which were observed by Pandey et al. (2017). The RSR-based method of NTL interannual correction by capturing ridge function from pixel density map avoids the interference caused by PIF recognition, but a mass of useless pixels are included in scatter plotting and calculation, which makes image correction more complex and less automated (Zhang et al., 2016). Considering the shortcomings of tPIF-based and RSR-based correction models in the process of correction, this paper proposes a pixel-based PIF (PBPIF) interannual correction model to identify PIF based on fluctuation characteristics of the pixels themselves. Differently from the existing PIF

recognition and selection schemes, the PBPIF model generates multi-band NTL images by multi-band synthesis method, and carries out linear regression on the multi-band pixel values at each pixel position, one by one (Figure 3.1). According to the pixel-by-pixel regression coefficients, the automatic PIF recognition is realized in stable lighting areas worldwide, and the image calibration function is constructed based on the ridge features of PIF pixels. In addition, in order to evaluate the performance differences between the proposed PBPIF, tPIF-based and RSR-based calibration models, the global and national turbulence and sensor bias of NTL corrected by different models are compared. Finally, this paper further expands the global application of pixel regression based on the DMSP/OLS NTL time series images corrected by the PBPIF-based model. Finally, the paper further expands the application of PBPIF-based calibration results, performing linear regression on global stable light pixels and maps global Lighting Intensity Change Coefficient (LICC) from 1992 to 2013 to reveal global light fluctuation characteristics. The results of the research not only accurately reflect the long-term global land surface dynamic changes, but also provide important data to support global economic and urban development research.

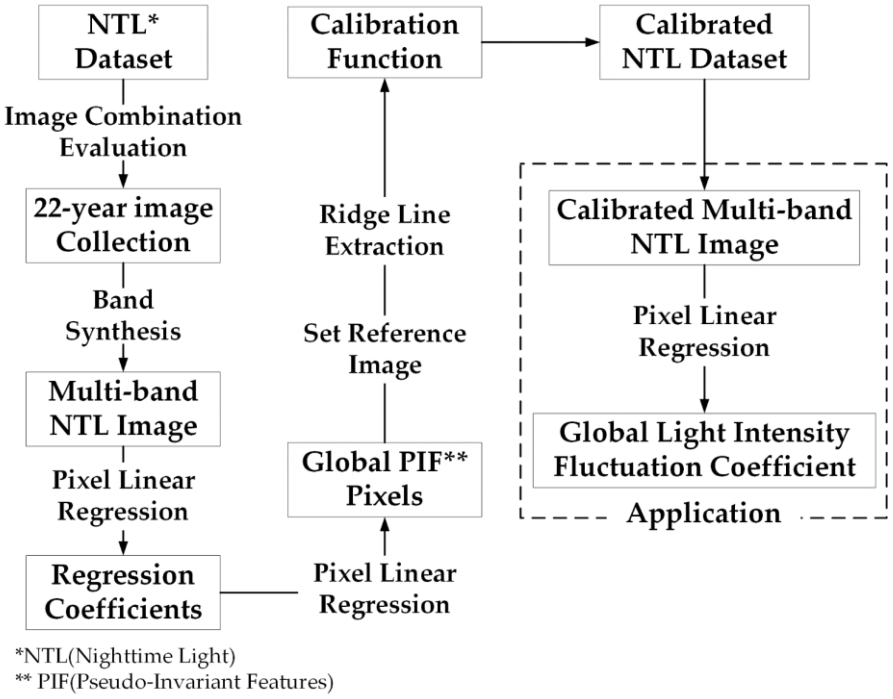

Figure 3.1. The technical flow chart of PBPIF-based interannual calibration.

3.3 Data

The DMSP/OLS NTL time series datasets are provided by the National Geophysical Data Center (NGDC), which is a stable lighting product in cities, the countryside and other places after eliminating the impact of accidental noise such as fire. The spatial resolution of the image is 30 arc seconds (the spatial resolution of the equator is about 1 km), and the DN value of the image represents the average light intensity, ranging from 1 to 63. The NTL datasets provide the longest span of light data to date, and the 22-year uninterrupted nighttime lighting image from 1992-2013 was rigorously screened and clouded. In fact, due to the long-time span, the

images were collected from six different satellites: F10, F12, F14, F15, F16 and F18.

Although the NTL datasets eliminate transient light noises such as fires or auroras, there are still non-negligible deviations and noises in the NTL datasets due to the large time span, cloud interference, sensor performance degradation and gap between sensors. Figure 3.2 shows the Total Sum of Lights (TSOL) interannual trend for each scene from different sensors over a 22-year period. There are large differences and disturbances in the NTL time series datasets, especially in the observations of different sensors. For example, there are obvious differences and jumps in the interannual fluctuations of the images collected by F15 and F16 sensors during their respective time periods. At the same time, in some years, such as 1998-2008, there were two different light images from two different sensors in the same year. Theoretically, the distribution characteristics of surface lighting and TSOL measured by the two sensors at the same time should be very close. Conversely, due to the possible interferences and deviations mentioned above, the TSOL of these images from different sensors in the same year is quite different, and the deviations show diversity in different years.

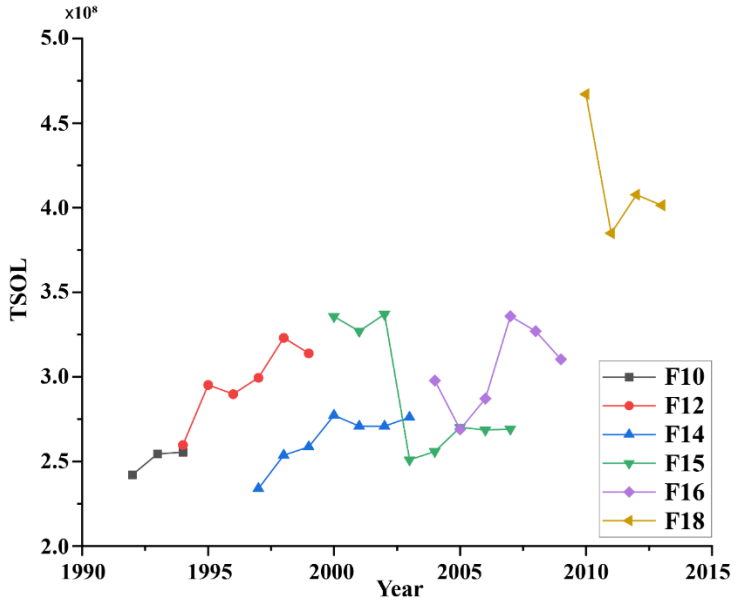

Figure 3.2. The TSOL of DMSP/OLS NTL time series datasets from F10, F12, F14, F15, F16, and F18 satellites.

3.4 Methods

3.4.1 Interannual Calibration of DMSP/OLS NTL Time Series Datasets

(1) Automatic Recognition of PIF

The most critical parameter affecting the calibration performance of the PIF-based calibration model is the PIF. Previous PIF-based calibration models often set specific PIF regions with reference to economic statistics, social development levels, etc., as for instance in Sicily (Elvidge et al., 2009; Elvidge et al., 2014), Heilongjiang Province (Liu et al., 2012), Puerto Rico (Wu et al., 2013a), Los Angeles (Hsu et al., 2015), Lucknow region (Pandey et al., 2013), South-west England (Bennie et al., 2014), etc. Although the PIF region

in the above model maintains a relatively stable level in the context of global economic development, there is still a risk of low change, as the positive correlation between the regional economic level and the TSOL is not fully matched. In addition, due to the excessive involvement of subjective factors the bias of PIF sample selection and the low degree of automation in PIF identification, an efficient multi-PIF sample and objective PIF selection method is worthy of being proposed. The widely used V4 version of DMSP/OLS NTL image has a global total of 7.25×10^8 pixels (43201×16801), in which most of the stable light pixels experienced a light intensity change (increase or decrease) over 22 years. Therefore, in order to minimize the risk of PIF low change, the proposed PIF automatic recognition method at the pixel level needs to be able to efficiently select the PIF pixels with the smallest light intensity change among the globally stable light area during the past 22 years.

In this paper, linear regression is performed on each pixel location of the 22-year NTL dataset, and the regression coefficient is used to identify the light intensity change rate of the pixel location to achieve quantitative evaluation. Due to the partial overlap of light images in 22 years (some years have light images from different sensors), it is necessary to compare the time series combinations from different sensors and select the group with the smallest disturbance to perform the change detection based on linear regression. In theory, with the development of economy, from 1992 to 2013, the global total lighting brightness should show a more obvious upward trend that matches the level of urbanization (Zhang and Seto, 2011; Cauwels et al., 2014). Therefore, the TSOL linear regression of light images under different combinations was implemented from 1992 to 2013 to measure the continuity of time series light images. By comparing the coefficients and R^2 of linear regression under different combinations, this paper finally selected the combinations of F101992, F101993, F121994, F121995, F121996, F121997, F121998, F121999, F152000, F152001, F152002, F142003, F162004, F162005, F162005, F162006, F162007, F162008, F162009, F182011, F182012 and F182013 to synthesize multi-band (22 bands) global lighting images. In addition, to eliminate the interference of non-light area on PIF pixel recognition and ensure that the acquired invariant target area has stable light and small fluctuation in the 22 years' time, zero-value pixels in the light images are not considered in the synthesis process. Theoretically, the change coefficient of the global stable light pixels should have a normal distribution, that is, the high-growth and high-attenuation pixels are in the normal distribution of the two tails (Figure 3.3). Considering the characteristics of PIF used to construct correction function (light intensity should keep low change rate) and according to the sensitivity analysis results, this paper chooses about 10% of the pixels (corresponding to a coefficient ± 0.05) as PIF pixels. By widely selecting 22-year weakly changing light pixels as PIF objects on a global scale, PIF samples can be greatly enriched, reducing the risk of low PIF changes and avoiding sample bias.

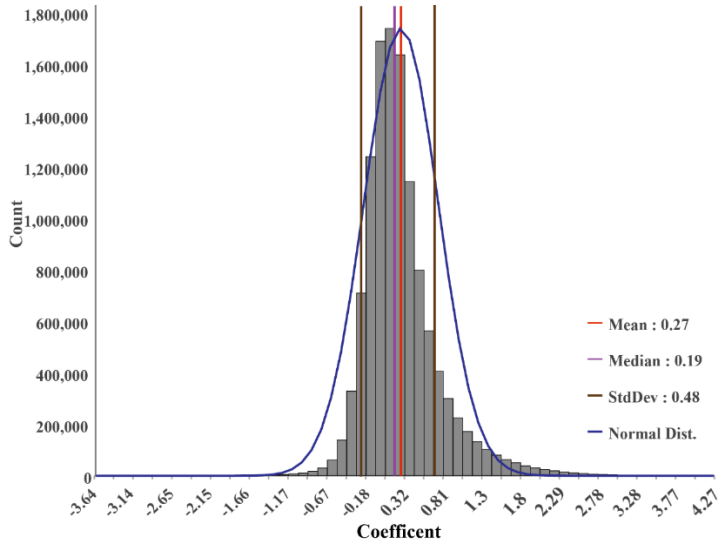

Figure 3.3. Regression coefficient histogram of global stable lighting pixels.

(2) Reference Image Selection

Until now, the existing interannual calibration methods for DMSP/OLS NTL datasets have been based on relative radiation correction. In the calibration process, the selected reference image is used as a standard, and uncorrected images are empirically calibrated to match reference images and improve the comparability of time series images. Therefore, the selection of reference images is particularly critical in the relative radiation calibration process. In long-term sequence NTL images, differences between images (including differences caused by actual surface changes and differences caused by noise, sensors, etc.) increase with time span. Naturally, the greater the time span between the selected reference image and the image to be corrected, the greater the difference between the images. In order to reduce the influence of time interval on image pairs, we refer to the selection of Zhang et al. (2016) and take the F152000 of NTL time series as the reference image. On the one hand, the observation time of F152000 is in the middle of 1992-2013 so it can minimize the time span between the reference image and uncorrected images to reduce the "burden" of calibration. On the other hand, there are two NTL images of F14 and F15 in 2000. Among them, the TSOL of NTL image from F14 sensor is low, and the F152000 is used as reference image because of its better continuity with F12 and F15 sensors.

(3) Calibration Function Setting

The PIF pixels of NTL images from F101992 to F182013 are extracted based on the results of PIF automatic recognition. The RSR is used to determine the interannual calibration function of the NTL time series image to improve the consistency of data collections. The RSR extracts the ridgeline by placing the reference image and the uncorrected image on the two axes of the scatter plot, respectively. The distorted ridgeline in the image scatter plot captures the deformation relationship between the reference image and the uncorrected image, which can be used to develop the correction equation.

In fact, in the previous RSR-based correction method, it is computationally intensive to incorporate all

the pixels of the global NTL image into the scatter plot of the image pair. Moreover, besides a small number of PIF pixels, the image scatters plot also contains massive actual DN change pixels on the surface, which are not necessary to be included in the calculation. Since the massive useless pixels are included in the scatter plot, the complexity of automatically extracting the ridgeline is steep and difficult to achieve. Therefore, Zhang et al. (2016) used the manually extracted data pairs to reduce the amount of ridgeline extraction calculations in the ridgeline extraction, which increased the subjective factors in the whole calibration process. Differently, the PBPIF proposed in this paper only retains about 10% of stable light pixels, which greatly reduces the calculation amount in the ridgeline extraction process, making the automatic ridgeline extraction possible. In addition, for the scatter plot of the extracted PIF pixels, the reference image pixel values correspond to a series of approximate uncalibrated image pixel values, which can be averaged to further reduce the computational complexity of ridge fitting. Finally, based on the deformation characteristics of ridgelines, cubic polynomials are used to define correction models:

$$y = ax^3 + bx^2 + cx + d \tag{3.1}$$

where y is the pixel value of the reference NTL image, x is the pixel value at the relevant location in the image to be corrected, and a, b, c and d are coefficients, respectively, which are estimated by the least square method.

3.4.2 Evaluation of Calibration Results

In order to evaluate the effectiveness of the interannual correction of DMSP/OLS NTL images, a common method is to compare the continuity of TSOL of time-series NTL images (Li et al., 2013a). TSOL is the sum of nighttime radiance and brightness in the region and is an important indicator to measure the overall trend of regional economic development. It is worth noting that TSOL is not a real physical quantity: by way of example, values are biased, as the high latitudes have more TSOL per square kilometer than low latitude countries. Considering that the latitude bias of TSOL is relatively stable and systematic, it still has a potential in the assessment of the performance of interannual corrections. Besides, the image collection of sensors in some years overlaps, so the difference between nighttime light images from different sensors in the same year is another important method to measure the correction effect. The Normalized Difference Index (NDI) is usually used to evaluate the difference of DN values between two periods of images in adjacent years. The larger the absolute value, the greater the interannual variation of the brightness of the light, and the greater the possibility of abnormal data fluctuation. The Sum of the Normalized Difference Index (SNDI) is the accumulation of NDI on the time axis, which can reflect the abnormal fluctuation level of the entire sequence image. TSOL, NDI and SNDI are defined as:

$$TSOL = \sum_{i}^{n} DN_i \tag{3.2}$$

$$NDI_t = \begin{cases} \frac{|TSOL_{mt} - TSOL_{nt}|}{TSOL_{mt} + TSOL_{nt}} & TSOL_{mt} + TSOL_{nt} \neq 0 \\ 0 & TSOL_{mt} + TSOL_{nt} = 0 \end{cases} \quad (3.3)$$

$$SNDI = \sum_{i=1}^{12} NDI_t \quad (3.4)$$

where DN_i is the light image pixel value of the i position; NDI_t is the NDI of year t, $TSOL_{mt}$ and $TSOL_{nt}$ are TSOL of two light images from m and n sensors in t year, respectively; $SNDI$ is the sum of 12 years of NDI, and t are 1994, 1997, 1998, 1999, 2000, 2001, 2002, 2003, 2004, 2005, 2006 and 2007, respectively.

3.4.3 Global Light Intensity Change Analysis

Due to the unique potential of night lighting in reflecting human vitality and revealing economic development on the surface, the study of the global economy and urbanization based on night lighting has been widely concerned and carried out. Among them, research on the interannual variation of light intensity has been continuously promoted, and abundant achievements have been reported (Ma et al., 2012; Ju et al., 2017; Zhang et al., 2018; Zhou et al., 2018; Chen et al., 2019). Limited to the continuity defect of DMSP/OLS NTL datasets, the light intensity trend analysis usually carries out TSOL comparison at national or regional scales. With the rapid economic development and in-depth analysis, TSOL change analysis at the global level has been unable to fully display the huge information hidden in the lighting data, and cannot meet the needs of sophisticated urbanization research. Therefore, based on the 22-years NTL collection calibrated by PBPIF-based model, the pixel value linear regression is used to measure the change characteristics of light intensity at the pixel scale (Figure 3.4). Specifically, we synthesized 22 corrected images from 1992 to 2013 and performed OLS regression on each pixel position to generate the LICC of each pixel position. The LICC is derived from the light intensity regression coefficient for 22 years at each pixel location, which can reflect the change rate of surface light intensity in the past 1992-2013. By mapping the global LICC, we can more accurately analyze the global light distribution and its spatial heterogeneity over the past 22 years.

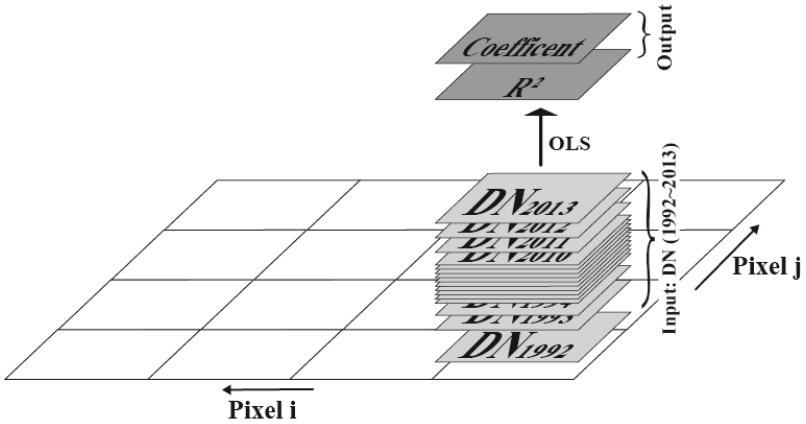

Figure 3.4. Linear regression of NTL fluctuation at pixel scale.

3.5 Results

3.5.1 Interannual Correction Results of NTL Datasets

Figure 3.5 shows the ridgeline extraction results of F101992-F182013 images, with F152000 taken as the reference image. The feature of ridgeline reflects the effect of correction function on uncorrected images, which can be roughly divided into three stages. In the stage of low DN value of uncorrected images (approximately lower than 20), the slope of ridgeline decreases continuously, reflecting that the gain amplitude of the correction function for the light intensity decreases as the DN value increases. In the middle of the uncorrected pixel DN value (in the range 20-45), the slope of the ridgeline is stable, reflecting that the gain amplitude of the correction function is consistent at this stage. For the stage of higher DN value of uncorrected pixels (DN values higher than 45), the slope of the ridgeline tends to show an upward trend, reflecting that with the rising of DN value pixels, the gain amplitude of correction function for corrected pixels increases continuously. In addition, the fitting degree of the ridgeline to scatter points also reflects the difference of correction function in different DN value stages: at the lower or higher DN value stage, the scatter points are more concentrated and closely matched with the ridgeline; for the middle range of DN value, the scatter points are characterized by a partial discrete distribution, and the degree of fitting with ridgeline decreases.

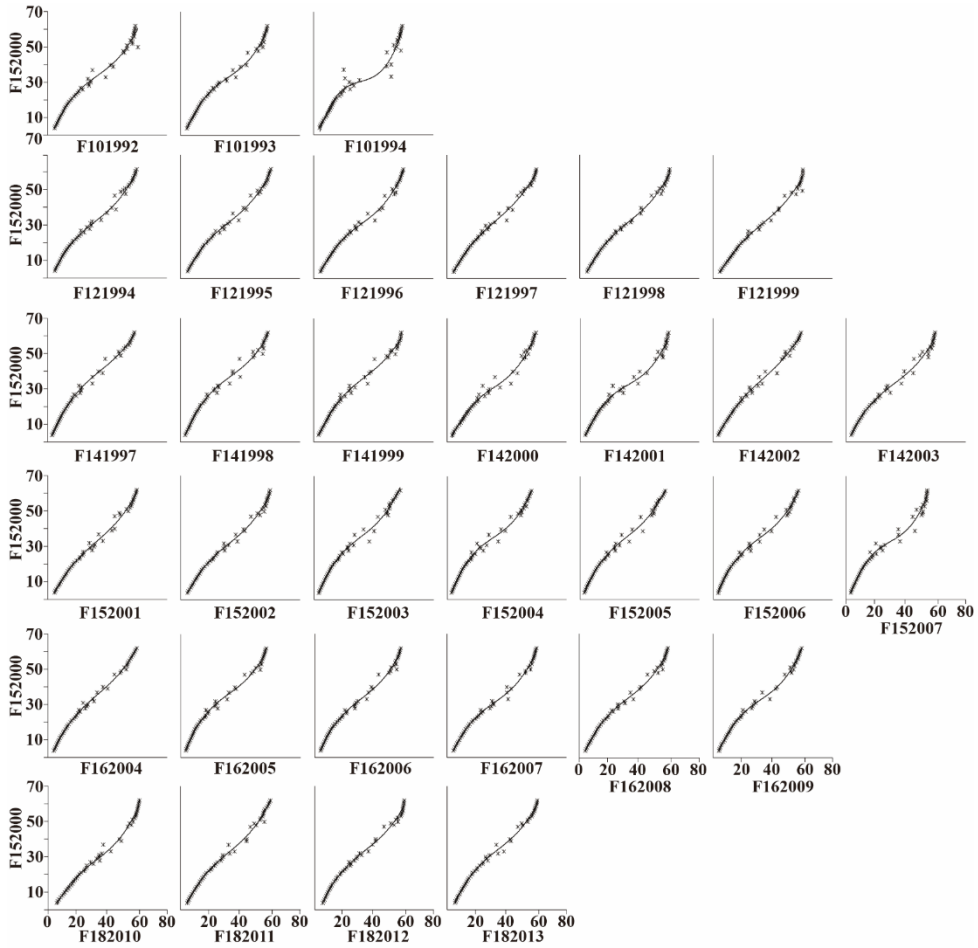

Figure 3.5. The image pair scatter plot and ridgeline from F101992 to F182013.

Since the relationship between the reference image and the uncorrected image reflected by the ridgeline is nonlinear with bending, the cubic polynomial can well capture the variation characteristics of the ridgeline. The correction function parameters and correlation coefficients of the uncorrected images of F101992 to F182013 are shown in Table 3.1. The R^2 of each correction function is higher than 0.96, which reflects the superiority of cubic polynomial in capturing ridgeline. It is noteworthy that among all correction functions, R^2 of F101994 one is the lowest (0.967), and the fitting effect is lower than that of other uncorrected images. Compared with the scatter plot of "F101994-F152000", the main reason for the low fitting effect is the lack and dispersion of scatter points in the middle part of DN value of uncorrected images.

Table 3.1. The NTL time series datasets correction function parameters.

Sensor	Year	y=ax3+bx2+cx+d				Adj.R^2
		a	b	c	d	
F10	1992	0.0005	-0.0512	2.3196	-5.6617	0.985
	1993	0.0006	-0.0593	2.4654	-5.7124	0.994
	1994	0.001	-0.0982	3.3487	-8.7948	0.967
F12	1994	0.0005	-0.0484	2.169	-5.0818	0.995
	1995	0.0004	-0.0396	2.0380	-5.1433	0.996
	1996	0.0005	-0.0486	2.2144	-5.3353	0.995
	1997	0.0004	-0.0382	1.9484	-4.2920	0.995
	1998	0.0004	-0.0398	2.0398	-5.8782	0.997
	1999	0.0003	-0.0299	1.8015	-4.7800	0.991
F14	1997	0.0004	-0.0447	2.2826	-3.1678	0.996
	1998	0.0005	-0.0519	2.3574	-3.8349	0.991
	1999	0.0004	-0.0429	2.2022	-3.4844	0.992
	2000	0.0006	-0.0565	2.3019	-3.789	0.989
	2001	0.0007	-0.0662	2.5309	-4.3559	0.991
	2002	0.0003	-0.0324	1.9512	-2.2158	0.995
	2003	0.0004	-0.0395	2.0087	-2.3651	0.991
F15	2000	0	0	1.0000	0	1.000
	2001	0.0004	-0.0374	1.9148	-4.1631	0.994
	2002	0.0004	-0.0396	2.0486	-5.3467	0.995
	2003	0.0006	-0.0582	2.3813	-2.0850	0.992
	2004	0.0007	-0.0671	2.5810	-2.7208	0.994
	2005	0.0005	-0.0498	2.2629	-2.2188	0.993
	2006	0.0006	-0.0570	2.3323	-1.6420	0.995
	2007	0.0008	-0.0784	2.9209	-4.1009	0.987
F16	2004	0.0004	-0.0396	2.0524	-3.3894	0.997
	2005	0.0006	-0.0583	2.4086	-2.7747	0.995
	2006	0.0005	-0.0491	2.2482	-2.8847	0.994
	2007	0.0005	-0.0483	2.2178	-4.8194	0.995
	2008	0.0005	-0.0479	2.2036	-4.3790	0.995
	2009	0.0006	-0.0580	2.4550	-4.5812	0.996
F18	2010	0.0005	-0.0455	2.0468	-8.3139	0.994
	2011	0.0004	-0.0395	2.0682	-5.7123	0.995
	2012	0.0004	-0.0411	2.1747	-7.1854	0.995
	2013	0.0005	-0.0480	2.2920	-6.9268	0.996

3.5.2 Evaluation of Interannual Calibration Performance

(1) PIF Recognition Results

As mentioned earlier, the core of the PBPIF-based calibration model is the automatic identification of PIF pixels worldwide. The multi-sample PIF pixels filtered by the light intensity change coefficient is the most prominent advantage of the proposed correction model. An essential condition for PIF pixels is to maintain a relatively stable intensity of light radiation over a long period of NTL collection. Figure 3.6 is a comparison of the mean DN values of PIF pixels in raw and calibrated NTL datasets. It can be found that the mean of PIF

pixels of NTL images before correction is less than that after correction, but the coefficient of variation (CV) is much higher than that after correction. In statistics, CV is a standardized measure of probability distribution dispersion, and is widely used in geoscience and social statistics research (Zheng et al., 2019c). The results show that after PBPIF-based model correction, the DN value of PIF in the whole time series is more concentrated, and the DN value is also increased slightly. The stability and constancy of PIF are important factors influencing the quality of PIF. The smaller CV value of the PIF in the NTL dataset indicates that the global PIF auto-recognition proposed in this paper have great advantages and potentials to avoid the risk of low PIF changes.

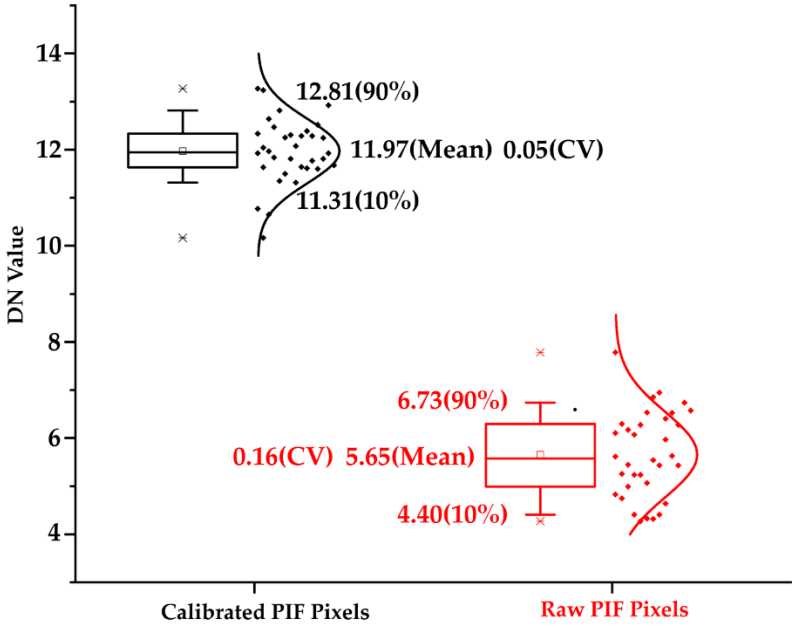

Figure 3.6. The DN value of PIF before and after correction based on PBPIF model.

(2) Global and regional TSOL continuity

As mentioned earlier, the most intuitive and prominent problem of DMSP/OLS NTL time series images is the turbulence and discontinuity of TSOL on the time axis. Therefore, the contrast TSOL continuity on the time axis can intuitively reflect the difference in the correction performance of different correction methods. To compare in a more comprehensive way the continuity and consistency of TSOL on the time axis, the global and different countries are used as spatial units for statistical TSOL. Selected countries include China, United States, Russia, France, Australia, Brazil, India, Egypt, Saudi Arabia and South Africa, which are representative countries on all continents. Meanwhile, the selected countries also have diversity in economic development speed and economic volume, such as China being the largest developing country, and during the period of study (1992-2013), the economic volume and economic development speed have undergone tremendous changes; the United States has maintained the world's largest economy during the NTL data coverage period, and is one of the richest, most developed and highest living standards countries in the world; South Africa is one of the largest and most developed economies in Africa, with the highest level of development and the most modern infrastructure in Africa. The trend line of TSOL in the world and 10 countries with different development backgrounds are shown in Figure 3.7.

Results show how, compared to raw NTL time series images, the TSOL continuity of the corrected images has been greatly improved. On the one hand, the smoothness of time series TSOL from the same sensor has been improved a lot; on the other hand, the deviation of TSOL from different sensors in the same year has also been reduced. Although different calibration models can effectively improve the continuity of the raw NTL datasets, the performance of RSR-based and PBPIF-based calibration is better than that of tPIF-based model, especially the tPIF-based correction results cannot effectively alleviate the interannual instability of sensors. The TSOL continuity of RSR-based and PBPIF-based calibration results is similar, but PBPIF-based calibration performs better on the F18 sensor.

It is noteworthy that the TSOL of countries with different backgrounds also shows diversity after interannual correction. We found that the TSOL continuity of developing countries in China, Brazil, India, Egypt, Saudi Arabia and South Africa was stronger than that of developed countries. In fact, during 1992-2013, the above-mentioned developing countries have made remarkable progress in domestic economic development and urbanization development. Therefore, although the economic volume of the above-mentioned developing countries lags behind that of developed countries, they achieved substantial growth in 22 years due to their small initial total economic volume (1992), which led to a significant increase in TSOL. Developed countries, such as the United States, have already been the largest economies in the world before the start of the study period. The huge economic volume cushions the fluctuation of economic development, resulting in a more stable TSOL change than developing countries. In addition, among the above countries, the fluctuation of TSOL in Russia is disordered and the TSOL in F142002 is extremely low. Previous studies have pointed out that in the high latitudes of the Northern Hemisphere (above 50°N), large-scale cloudiness, long sunshine time and aurora will interfere with the data quality and reduce the number of effective light pixels, resulting in poor performance of model correction (Pandey et al., 2017). Specifically, as a stable lighting product, V4 version NTL images exclude short-term light sources such as sunlit, moonlit, cloud interference and aurora. Due to the higher probability of the above interference factors in high latitudes, the number of effective light pixels in data products is unstable. Especially for F142002, the light pixels above 50°N were not recorded, which led to the sharp decrease of TSOL in Russia in 2002.

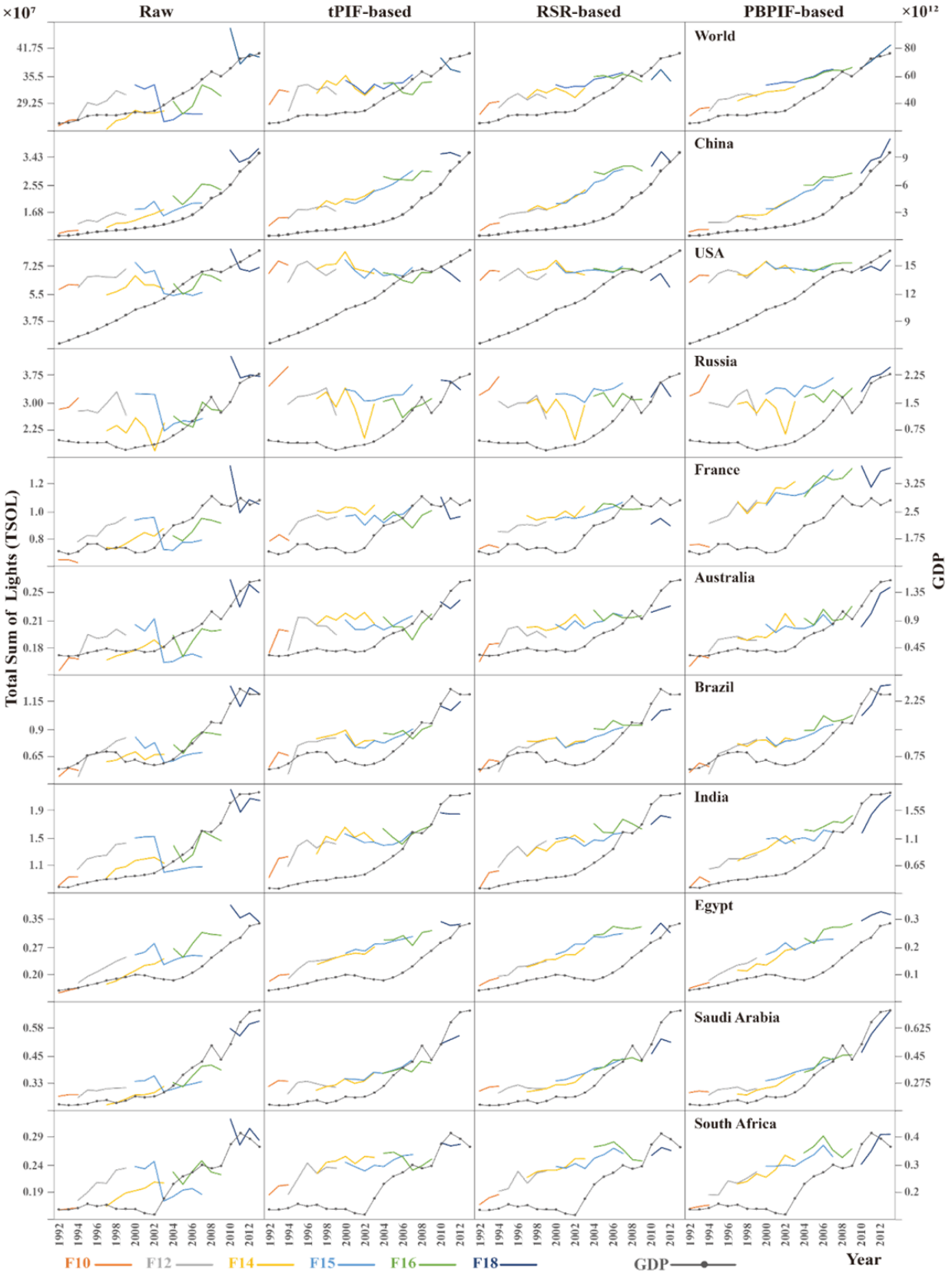

Figure 3.7. TSOL of time series NTL datasets in global and different countries.

(3) Comparison of SNDI

Besides intuitively comparing the continuity of TSOL in time series, SNDI is also widely used to evaluate

the different sensor biases in the same year in NTL images. Generally, the same region TSOL in a particular year is a relatively stable value, so even if observed by different sensors, the results should be kept in a very close range. Therefore, SNDI can quantitatively evaluate the correction performance of the model by accumulating TSOL differences among sensors in all years.

To this end, the SDNI of the raw NTL and corrected NTL images by different calibration models in more than 230 countries were counted, respectively. The results showed that at the global scale, the SNDI mean value of the interannual corrected NTL images was significantly lower than that of the raw NTL images (Figure 3.8). Among them, the SNDI mean value corrected by PBPIF-based model is 45% lower than that of raw image, 32% lower after RSR-based model correction, and 43% lower after tPIF-based model correction. The global SDNI comparison results show that PBPIF-based and the tPIF-based correction models have similar performances in reducing the deviation between sensors and are better than the RSR-based model.

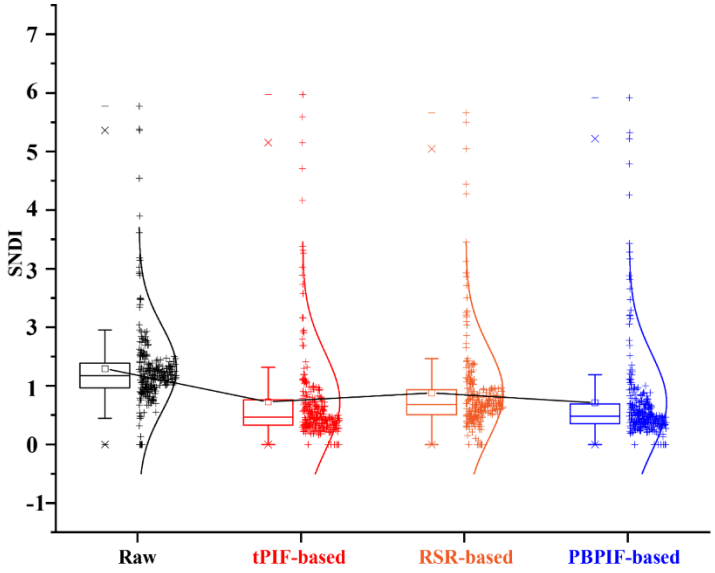

Figure 3.8. Comparison of global SDNI between raw NTL and corrected NTL.

In addition, the three calibration models can effectively reduce SNDI in most countries or regions of the world (Figure 3.9). After calibration by the three calibration models, about 92.5% of the countries or regions have different degrees of decline in SNDI. Specifically, for the raw NTL images, the low SNDI (SDNI < 0.5) country or region only accounts for 2%, and the relatively low SNDI (SDNI < 1.2) country or region accounts for 51%； for the images corrected by tPIF-based model, the low SNDI country or region only accounts for 50%, and the relatively low SNDI country or region accounts for 88%; for the images corrected by RSR-based model, the low SNDI country or region only accounts for 22%, and the relatively low SNDI country or region accounts for 83%; for the images corrected by PBPIF-based model, the low SNDI country or region only accounts for 52%, and the relatively low SNDI country or region accounts for 88%. The comparison results show that the NTL images corrected by PBPIF-based and the tPIF-based model greatly inhibited SNDI between countries or regions, but the PBPIF-based model performed better. Although the results of RSR-based model correction have been greatly improved compared with the raw image, the SNDI suppression is slightly inferior to the other two correction models.

Furthermore, from the SDNI distribution of the country or region, we find that the low-SDNI units are mainly distributed between latitudes of 10 to 50 degrees, while the SNDI in some countries near the equator is still greater than 0.5 after calibrating. These countries mainly include South Sudan, Uganda, Central African Republic, Congo, Liberia, Ivory Coast in Africa, Sri Lanka, Cambodia, Papua New Guinea in Asia, Costa Rica, Panama, Cuba and Haiti in Central America. Considering the special climatic conditions near the equator, the blocking effect of cloudiness on lighting may be an important cause of this phenomenon.

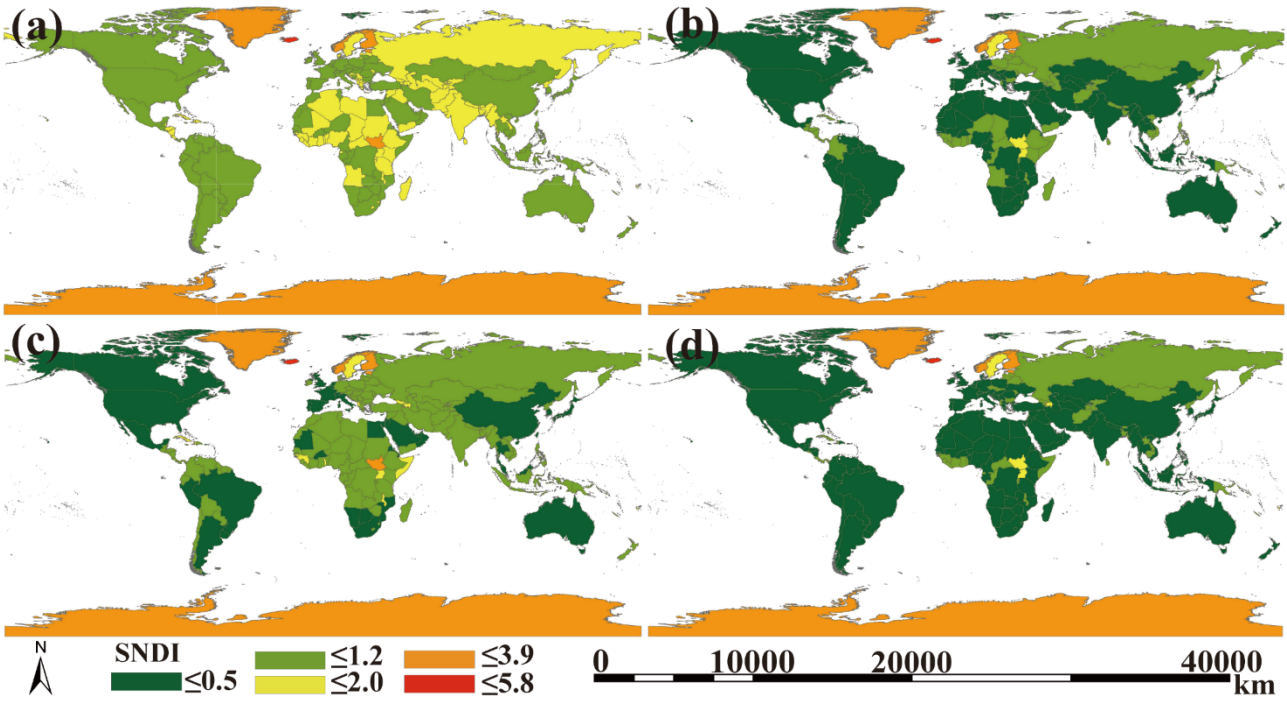

Figure 3.9. The SDNI of raw NTL and corrected NTL at national scale. Note: (a) raw NTL; (b) the NTL corrected by traditional PIF-based model; (c) the NTL corrected by RSR-based model; (d) the NTL corrected by PBPIF-based model.

3.5.3 Global Night Lighting Intensity Changes

(1) General Characteristics

Based on the pixel level OLS regression analysis of DMSP/OLS NTL images from 1992 to 2013, the 22-year global LICC in stable lighting areas were produced for the first time (Figure 3.10). The global LICC fluctuated between -3.65 and 4.27 for 22 years (mean value is 0.268), which indicates that despite the spatial heterogeneity of global nighttime LICC changes over 22 years, the overall LICC showing an upward trend, the DN value increases by 0.268 per year. In terms of the coefficient composition of global stable light pixels, about 30% of stable light pixels have experienced a light intensity decline in 22 years, while the intensity rising pixels accounted for the majority, reaching about 70%. Moreover, pixels with LICC below 0 are mainly distributed in North America and Eastern Europe, and pixels with LICC greater than 0 are more widely distributed, mainly including East Asia, South Asia, Western Europe, North America, and Eastern South America. Specifically, among the pixels with rising light intensity, the light pixels with a growth rate higher than the average value of 0.268 are mainly distributed in East Asia, Southeast Asia, West Asia, Europe, and

southeastern South America; the pixels whose growth rate is lower than the average are mainly concentrated in South Asia, Western Europe and southeastern North America.

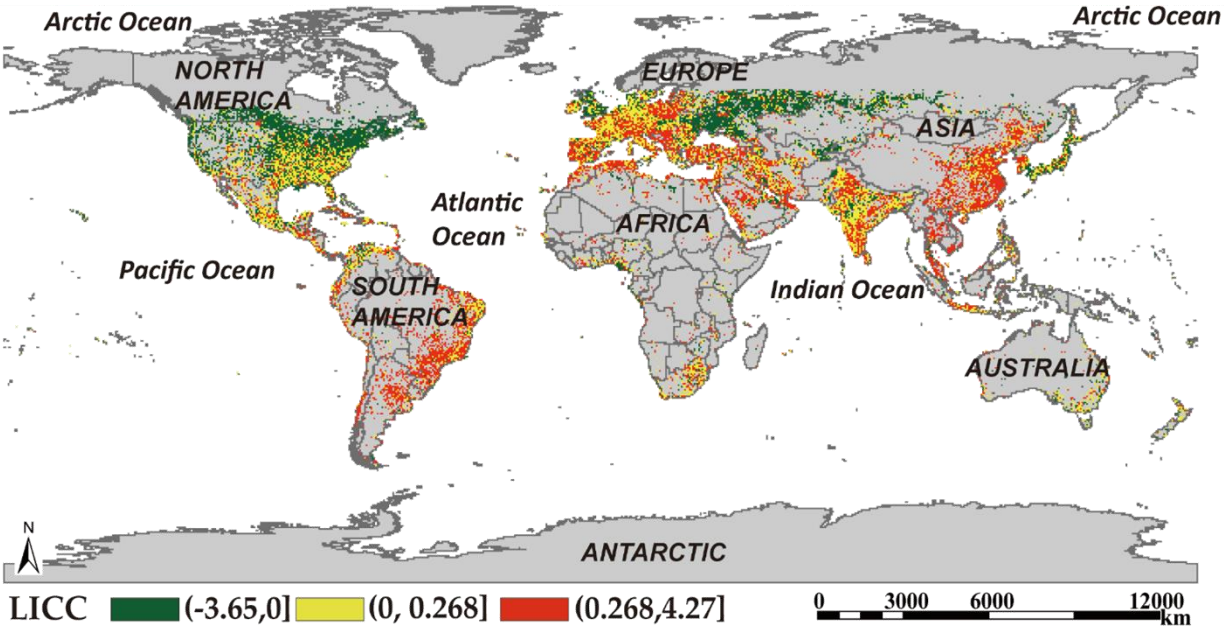

Figure 3.10. LICC of global stable lighting area from 1992 to 2013.

In addition, Figure 3.11 shows the average of LICC (avgLICC) with the nation as statistical unit. At the national level, 88.5% of countries or regions have avgLICC greater than 0, while only 11.5% of countries or regions have avgLICC lower than 0. Among the countries where avgLICC is below 0 (except for countries in high latitudes and near the equator that may be disturbed by clouds and other factors), Ukraine, Moldova, Uzbekistan, Tajikistan and Zimbabwe experienced a decline in GDP during the study period, which also coincided with the results of the fluctuation coefficient.

In fact, the amount of stable light pixels is neglected when the avgLICC is counted under the national statistical unit, which often results in higher avgLICC in developing countries with small pixel amount but high fluctuation coefficient. Therefore, we have calculated the sum of the LICC (sumLICC) by country or region on a global scale (Figure 3.12). The results show that on a global scale, the sumLICC in Canada is the lowest, while China has the highest sumLICC. For China, since the reform and development in the 1980s, economic and urbanization has continued to advance, and its economic volume and economic growth have remained stable at a high level. During the study period, China's GDP growth rate remained at an average annual rate of 10.27% (2.8% of the world average). Compared with 1992, the total GDP in 2013 increased by 22.5 times (3 times of the world average) and surpassed Japan as the world's second-largest economy in 2010. High-speed economic development and huge economic volume make it indisputable as the most representative country with positive fluctuation of night light intensity in 22 years. Correspondingly, the average annual GDP growth rate in Canada during the study period was only 2.58%, and the total GDP increased by about 3.1 times. The lower GDP growth rate and the special geographical location (located in high latitudes) make the sum of the LICC in the development process at a lower level.

The countries with the high level sumLICC include the United States and India. The United States, as the world's largest economy, is recognized as one of the most developed economies in the world. During 1992-2013, the average annual GDP growth rate was maintained at 2.59%, and the total GDP expanded by 2.6 times. India, BRICS Members, during the study period, their economic growth rate is second only to China, and the total domestic GDP has expanded by about 6.5 times, making it one of the fastest growing countries in the world. In addition, the number of countries where sumLICC is at a relatively high level has increased, including Mexico, Brazil, Spain, France, Italy, Germany, Poland, Egypt, Saudi Arabia and Iran. Among these countries, Brazil is a member of the BRICS, ranking first in South America in GDP, and Mexico's economic development has been developing rapidly since its entry into the North American Free Trade Area (NAFTA) in 1994. Spain, France, Italy, Germany and Poland, as traditional developed countries, maintained relatively stable GDP growth during 1992-2013, with an average annual GDP growth rate of 2%, and the total GDP increased by about 2.5 times compared with 1992. The average annual growth rate of GDP was 4.5%, 2.9% and 2.7% respectively, and the total GDP increased by 6.89 times, 5.44 times and 7.33 times respectively compared with 1992.

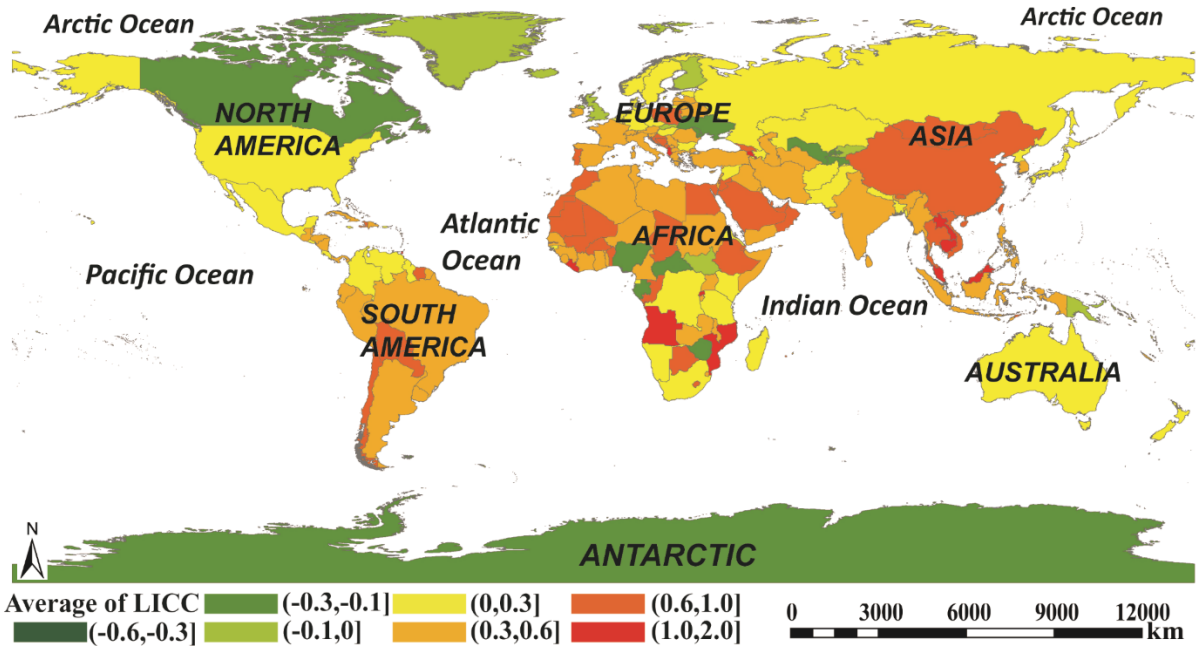

Figure 3.11. The avgLICC among the countries or regions.

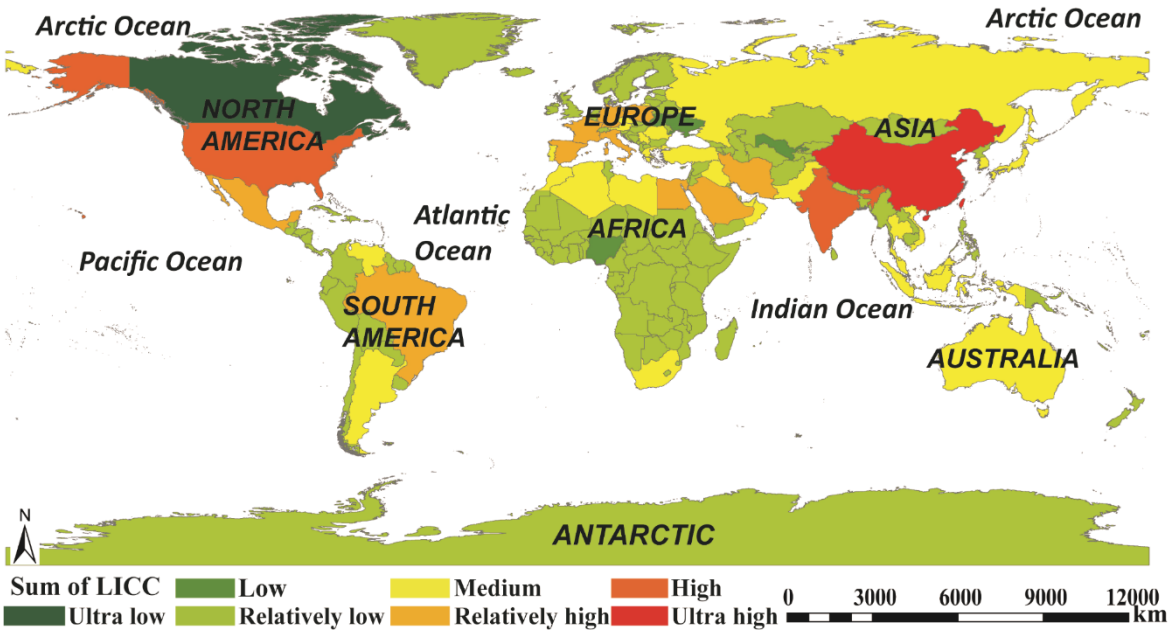

Figure 3.12. The sumLICC among the countries or regions.

(2) Regional Characteristics

Previous studies on time series NTL fluctuation mainly focused on national or regional scales, only revealing the overall change characteristics and trends of spatial units. To break through the limitation of space unit and maximize the utilization of NTL data, a global night light fluctuation analysis based on pixel-level is proposed in this paper. Figure 3.13 shows the LICC distribution in six typical regions around the world, which can reflect the fluctuation characteristics of NTL in the region. The area in Figure 3.13(a) is located in the southeastern part of the United States and is one of the areas where nighttime lights are densely distributed. The distribution of high-value LICC has a ring structure, such as Atlanta and Charlotte. The pixels with high-value coefficients are mostly around the periphery of the urban core area and stacked into a circular structure. For Figure 3.13(b), it is located in central Europe and includes Italy and its surrounding areas, with a high percentage of stable lighting coverage. Among them, the high-value LICC has formed an agglomeration belt from Venice in the east to Turin in the west in Italy. The agglomeration zone is located in the Po Plain in northern Italy, which is the most developed and densely populated area in Italy (Khawar, 2017). Figure 3.13(c) depicts the distribution of LICC in the Middle East, particularly in Egypt, Israel, Palestine, Saudi Arabia, Lebanon and Syria. The high-valued LICC pixels in the area formed two clusters, one along the Nile and the estuary delta in Egypt; the other was the Jerusalem and Amman provinces on both sides of the Jordan River. Compared with other areas, the climate in this area is dry and precipitations are limited. With tropical desert climate as the main climate, water resources play a decisive role in urban location and development (Richmond, 2019), and ultimately form a regional high-value LICC coordinated with the distribution of water resources.

In South America, this paper chooses cities in southeastern Brazil including Brasilia, Sao Paulo and Rio de Janeiro as case areas (Figure 3.13(d)). Although Brasilia is the capital of Brazil, its lighting area and amount of high-value LICC pixels are smaller than those in coastal areas of Sao Paulo and Rio de Janeiro. Sao Paulo

is Brazil's largest and most economically prosperous city in South America, with the largest lighting area and the largest number of high-value LICC in the region (Eigenheer and Somekh, 2019). For Rio de Janeiro, once the capital and the second largest city in Brazil, the LICC of Macae, the center of the coastal oil industry in the east of Rio de Janeiro, is higher than that of Sao Paulo. For Asia, this paper chooses South Asia and East Asia, which have the largest lighting area, as the case areas of LICC comparison (Figure 3.13(e, f)). In South Asia, India has the largest stable lighting area. India is one of the fastest growing economies in Asia (Tan et al., 2019). Its stable light pixels form the northern cluster centered on New Delhi, the central cluster centered on Mumbai and Hyderabad, and the southern cluster centered on Bangalore. The case areas in East Asia include eastern China, Taiwan and the Korean Peninsula. With the rapid development of economic globalization and regional economy, East Asia has gradually grown into the leader of global economic development, especially China. The eastern part of China not only has the largest number of high-value LICC pixels, but also has relatively aggregated distribution, which is quite different from that of other parts of the world. Specifically, in the process of urbanization, China's eastern region has gradually formed China's two largest urban agglomerations: the Yangtze River Delta urban agglomeration and the Pearl River Delta urban agglomeration. During the urbanization process, cities in the estuary delta are expanding with each other, and urban agglomerations with compact spatial organization and high degree of integration are gradually realized, which reflected on the LICC is the aggregation of high-value coefficients. Conversely, the distribution of high-value LICC in North China is discrete and presents a pattern of scatter distribution.

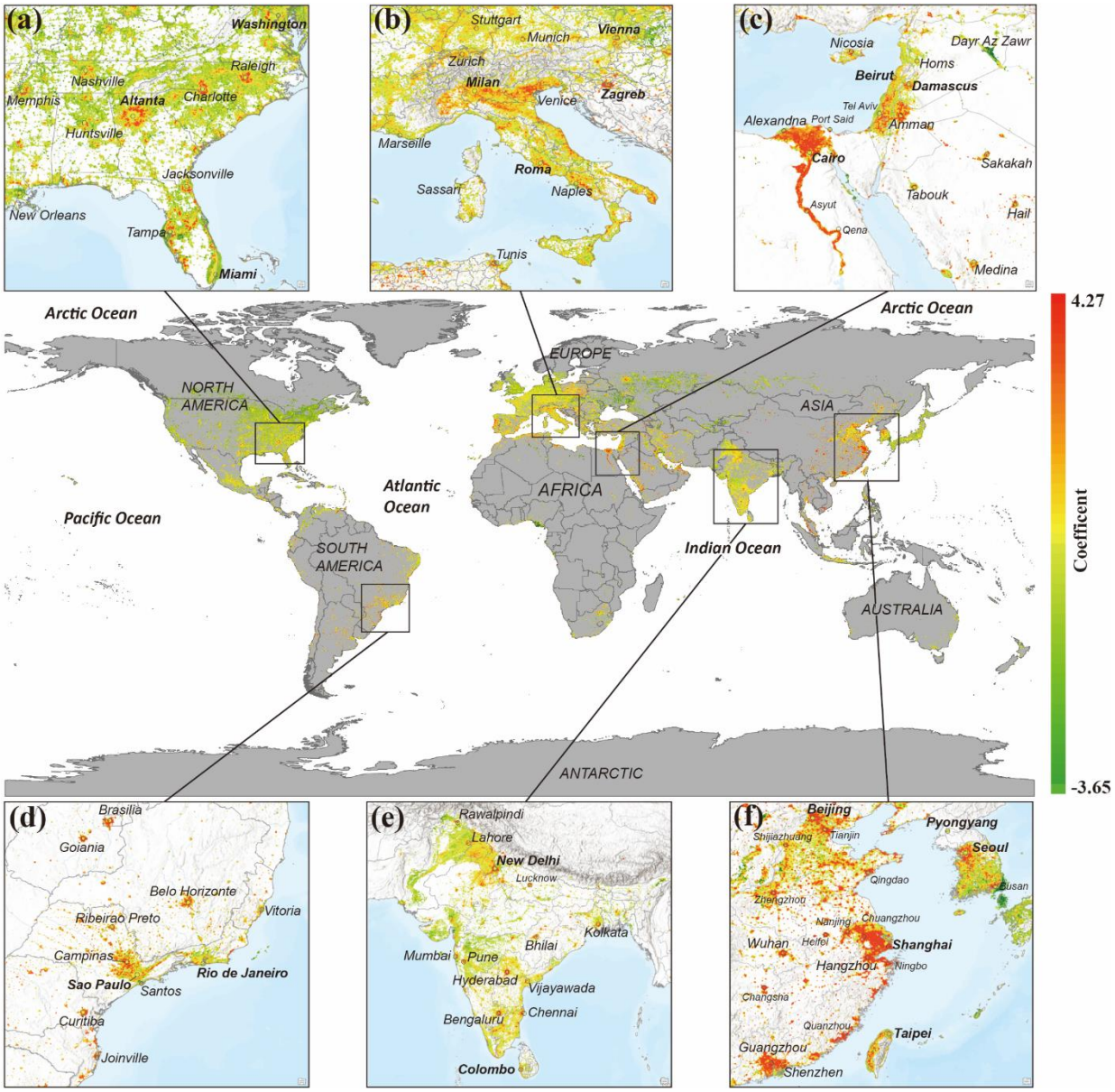

Figure 3.13. The LICC distribution in typical case areas worldwide.

3.6 Discussion

3.6.1 PBPIF-based Calibration Model and Comparison of Results

As mentioned above, the tPIF-based model assumes that the light intensity in a specific region is stable, and the global pixel correction is performed using the deviation characteristics of DN values in the region. The RSR-based model uses density scatter plot of image pair to extract ridgeline as conversion function between NTL images. The PBPIF-based model proposed in this paper synthesizes the advantages of tPIF-based and RSR-based models to achieve more efficient and automatic time series NTL calibration. The calibration procedures for the above three NTL interannual calibration methods are different. Among them, the tPIF-based model uses the prior knowledge to artificially select the constant area of the light intensity, and uses the deviation relationship between uncorrected images and reference images in the invariant region to correct the

time series NTL in the whole research area. The advantage of this calibration model is that the processing flow is simple, and the calculation amount is small, while the disadvantage includes strong subjective participation and low automation. The RSR-based model uses the density scatter plot of all pixels of the reference image and uncorrected image to extract ridgeline manually, and then determines the correction function by fitting ridgeline. The RSR-based model avoids the subjective error caused by PIF selection, reduces the degree of manual participation during the correction process, and makes up for the shortcomings of tPIF-based model. However, there are still some shortcomings in this method. On the one hand, the correction process needs to plot the density scatter plot of all the pixels (1.45×10^9 pixels of the two images), which greatly increases the difficulty of data processing. On the other hand, due to extremely dense pixel scatter, the ridgeline can only be extracted by manual screening, which reduces the degree of automation of the processing process. The PBPIF-based model proposed in this paper can automatically find PIF pixels on the global scale by using the fluctuation characteristics of the pixel itself, which greatly reduces the subjective participation. Meanwhile, the global selection of PIF pixels can avoid the errors caused by the use of local invariant target regions in the traditional PIF model to correct the global NTL. Compared with the raw NTL images, the number of PIF pixels identified decreases sharply, which makes it possible to automatically extract ridgelines, or to fit the distribution of scatters.

In addition, TSOL and SNDI at global and national scales were compared to assess the calibration benefit of PBPIF-based and the current common interannual correction models. The results show that RSR-based model and PBPIF-based model are better than tPIF-based model in eliminating the turbulence of NTL images in time series. The TSOL interannual curve of NTL corrected by RSR-based model and PBPIF-based model is smoother and more synergistic with the fluctuation curve of GDP (Figure 3.7). For SNDI, which measures the deviation between sensors, PBPIF-based works best, followed by tPIF-based and RSR-based models. In addition, the SNDI suppression results of the three calibration models for the national unit reflect that the correction performance of the three correction models is more effective at the mid-low latitudes, while at higher latitudes (Russia, Nordic countries, Greenland, etc.) the performance is general due to the known problems of high latitude NTL data. In the middle and low latitudes where most of the population and cities are concentrated, the number of light pixels accounts for about 80% of all NTL images, and the data is less disturbed by clouds, thus maintaining high quality. Therefore, profit by the wide range of PIF automatic screening at the pixel level, PBPIF-based model can obtain more PIF samples in low and middle latitudes to improve the effect of correction function. However, for countries with high latitudes and near the equator, the lighting data is disturbed by factors such as clouds, aurora and sunshine, which degrades the data quality, resulting in irregularities and differences in deviations from different sensors compared to mid-low latitudes. Therefore, the correction effect of the three correction models in high latitudes is gradually decreases. In fact, due to the natural conditions and climatic conditions of the high latitudes, the population density and urban density are lower than those in the middle and low latitudes. Although it is difficult to reduce the SNDI to the ideal level in the high latitudes for the three calibration models, the results of PBPIF-based calibration can still be used for time series analysis and vitality monitoring of urbanization worldwide considering the low population and

urban density in the region.

3.6.2 Fluctuation Characteristics of NTL

At present, the results of the change analysis based on the corrected time series NTL datasets are constantly enriched. However, these studies tend to focus on large unit scales such as countries and regions. During the study period, the change of average light intensity and the total amount of light was used to measure the fluctuation of light, which concealed the difference of light change in the interior space of the unit, and is not conducive to mining more detailed differences in lighting changes and urban development. With the rapid development of the economy and the continuous advancement of urbanization, the analysis of the lighting fluctuations within the spatial unit can help reveal the differences in urban development and a more comprehensive understanding of the urbanization process (Zheng et al., 2019a). The spatial resolution of the NTL images has reached about 1 km, which has great potential for developing more fine-scale characteristics of light intensity fluctuation. In this paper, the light fluctuation analysis based on pixel regression is implemented for corrected NTL images, which can release the information contained in NTL images and improve the precision of night light intensity fluctuation research.

From the LICC statistics of countries and regions worldwide, it can be found that the sumLICC on national or regional units can better reflect the real changes of lighting between countries than the avgLICC. In fact, there are significant differences in the distribution of global light pixels among countries, especially for stable light pixels. On the one hand, for countries with large territory, more light pixels will inevitably increase the dispersion of the overall pixel value. On the other hand, for developing countries with smaller territory, during the study period, most of the lights were concentrated in a few developed cities in the region and maintained rapid growth. Hence, the avgLICC ignores the significance of the pixel amount in light fluctuations, due to the huge difference in the number of light pixels between countries. Through the summarization of all stable lighting pixels LICC in the unit, the sumLICC can more accurately depict the lighting fluctuation characteristics of the global national scale for 22 years. The results of the national scale sumLICC show that the growth of light intensity in emerging economies represented by China in recent years is larger than that of traditional developed countries. According to data released by the International Monetary Fund (IMF), the economy of developed economies grew by only 2.7% in 2007, and the economy of emerging and developing economies grew by 8%, and gradually became a "source of world economic stability" in the context of economic globalization (Zhang and Tian, 2010).

In addition, there are substantial differences in LICC within the city between emerging economies represented by China and traditional developed countries represented by the United States. Figure 3.14 shows the distribution of LICC in four representative cities or regions in the United States and China. For a highly developed country like United States, the fluctuation coefficient of the city and its surrounding areas has the following characteristics: 1) the LICC of the urban core area is close to 0, and the fluctuation is weak; 2) there are ring-shaped high-valued LICC pixels around the core of the city, such as Las Vegas, Atlanta, and

Philadelphia; 3) for the periphery of the ring-shaped LICC, the LICC in the suburban area is much lower than the urban area. The LICC of Chinese cities or regions is obviously different from the above-mentioned cities or regions and has the following characteristics: 1) the LICC in the urban core area is higher than that in the United States, and the LICC of the Central Business District (CBD) is close to 0; 2) LICC in urban transition zone and suburban area is higher than the core area, and shows a growth and integration trend, which is different from the three-tier classification of the United States cities; 3) the development of urban integration has been strengthened and presented the development mode of urban agglomeration, and the overall lighting intensity of the region has increased rapidly. As mentioned earlier, the saturation defect of the DMSP/OLS sensor results in that the DN value of the lighting pixel exceeding 63 will not be recorded correctly (more than 63 is still recorded as 63). For the most intense urban core area of NTL, the DN value is limited to 63 for a long time, which in turn leads to a low LICC. It should be emphasized that the area and light intensity of urban core area in the United States were significantly higher than that of the Chinese city in 1992. Obviously, urban core areas in developed countries bear more problems caused by the saturation defects of OLS sensors than those in developing countries, which results in that the pixels of LICC approaching 0 in urban core areas in the United States are larger than those in developing countries.

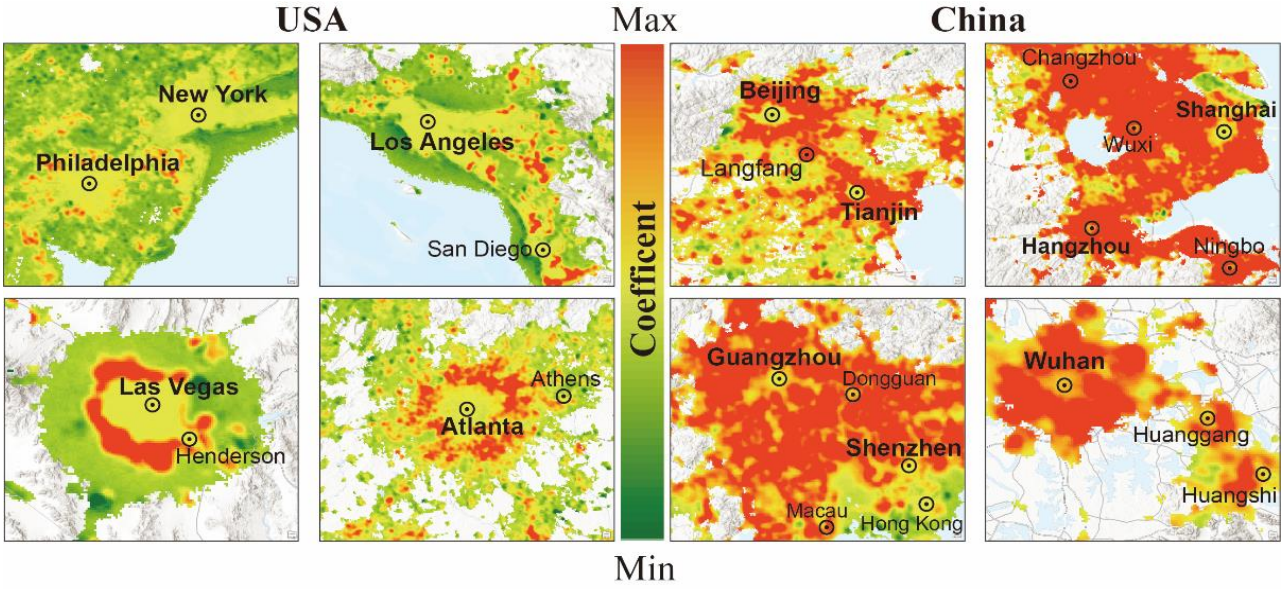

Figure 3.14. Comparison of LICC between Chinese and American Cities.

Another notable difference between Chinese and American cities is the difference of LICC in suburban areas. Specifically, LICC in urban transitional and suburban areas of China does not show a rapid decline trend, and the urban integration development model is more obvious. In the process of urban development in China, coordinated urban development and urban agglomeration have gradually become an important mode of urban development (Zheng et al., 2019b). Cities with close geographical location tend to present the pattern of cluster development, and the mutual expansion of cities makes the original suburban areas change dramatically with the development of urbanization. Generally, the differences in the initial development, growth rate and development mode between the traditional developed cities and the newly developing cities represented by China and the United States can be effectively captured by the pixel-based fluctuation analysis.

3.7 Conclusions

Rapid development of the global economy and the reality of regional differences in development have placed higher demands for time series analysis based on NTL. In recent years, with the no-longer-used collection of DMSP/OLS NTL data, the development of sensor technology and the rising demand for night lighting monitoring, a series of new lighting data (NPP/VIIRS and Luojia-1), were launched, expanding the research and application of night lighting data. Although the radiation sensitivity and spatial resolution of the new generation of night light data are greatly improved compared with NTL, the long-term historical NTL datasets is still an indispensable data source for scholars to carry out urbanization research. In order to remedy the interannual instability of NTL datasets and achieve more fine-scale global light fluctuation analysis, an interannual correction model (PBPIF-based model) based on pixel regression is proposed to calibrate the global time series NTL data. In addition, TSOL and SNDI at global and national scales are used to assess the reliability of interannual calibration results based on pixel regression. Finally, based on the corrected time series NTL datasets, this paper uses pixel regression to analyze the fluctuation characteristics of the global stable lighting pixels.

The results show that the PBPIF-based model proposed in this paper can minimize the participation of subjective factors and improve automation during the calibration process. The evaluation results of the calibration performance show that the calibration model can improve the continuity of time series NTL efficiently, reduce the deviation between sensors and improve the accuracy and reliability of NTL images for time series analysis. Meanwhile, the PBPIF-based model has also achieved better correction results in comparison with the existing two widely used calibration models. Although the wide selection of PIF pixels globally can best avoid PIF low variation and satellite observation interference (Coesfeld et al., 2018), the use of a strictly constant physical calibrator will be the key to the next phase of NTL interannual correction. Finally, based on the corrected time series NTL datasets, the global LICC is produce. Pixel-level LICC can maintain the resolution of light data and reveal the characteristics of economic development and urbanization process more precisely than traditional light data change analysis, which can be used as a new data for subsequent urbanization research.

Author Contributions: Conceptualization, Z. Z.; Data curation, Z. Z.; Formal analysis, Z. Z. and Z. Y.; Funding acquisition, Z. W.; Methodology, Z. Z.; Project administration, Z. W. and F. M.; Software, Z. Z. and Z. Y.; Supervision, F. M.; Validation, Z. Z.; Visualization, Z. Z.; Writing – original draft, Z. Z.; Writing – review & editing, Y. C. and F. M..

Acknowledgments: This research was funded by National Natural Science Foundation of China (41671430) and Natural Science Foundation of Guangdong Province (2018B030312004). We acknowledge the free use of DMSP/OLS NTL data collection from NCEI (National Centers for Environmental Information). We also want to express our sincere gratitude to the anonymous reviews and editors for their efforts in the improvement of the paper.

Conflicts of Interest: The authors declare no conflict of interest.

References

Bennett, M.M. & Smith, L.C. (2017) Advances in using multitemporal night-time lights satellite imagery to detect, estimate, and monitor socioeconomic dynamics. Remote Sensing of Environment 192, 176-197.

Bennie, J., Davies, T.W., Duffy, J.P., Inger, R. & Gaston, K.J. (2014) Contrasting trends in light pollution across Europe based on satellite observed night time lights. Scientific reports 4, 1-6.

Cao, Z., Wu, Z., Kuang, Y., Huang, N. & Wang, M. (2016) Coupling an intercalibration of radiance-calibrated nighttime light images and land use/cover data for modeling and analyzing the distribution of GDP in Guangdong, China. Sustainability 8, 108.

Cauwels, P., Pestalozzi, N. & Sornette, D. (2014) Dynamics and spatial distribution of global nighttime lights. EPJ Data Science 3, 1-26.

Chen, Z., Yu, B., Zhou, Y., Liu, H., Yang, C., Shi, K. & Wu, J. (2019) Mapping global urban areas from 2000 to 2012 using time-series nighttime light data and MODIS products. IEEE Journal of Selected Topics in Applied Earth Observations and Remote Sensing 12, 1143-1153.

Coesfeld, J., Anderson, S.J., Baugh, K., Elvidge, C.D., Schernthanner, H. & Kyba, C. (2018) Variation of individual location radiance in VIIRS DNB monthly composite images. Remote Sensing 10, 1964.

Croft, T.A. (1978) Nighttime images of the earth from space. Scientific American 239, 86-101.

de Miguel, A.S., Zamorano, J., Castaño, J.G. & Pascual, S. (2014) Evolution of the energy consumed by street lighting in Spain estimated with DMSP-OLS data. Journal of Quantitative Spectroscopy and Radiative Transfer 139, 109-117.

Eigenheer, D.M. & Somekh, N. (2019) Sao Paulo Metropolitan Transformations: Innovation or Reproduction. Urban and Regional Planning 4, 48.

Elvidge, C.D., Baugh, K.E., Zhizhin, M. & Hsu, F.-C. (2013) Why VIIRS data are superior to DMSP for mapping nighttime lights. Proceedings of the Asia-Pacific Advanced Network 35, 62.

Elvidge, C.D., Hsu, F.-C., Baugh, K.E. & Ghosh, T., (2014) National trends in satellite-observed lighting, Global urban monitoring and assessment through earth observation, pp. 97-118.

Elvidge, C.D., Ziskin, D., Baugh, K.E., Tuttle, B.T., Ghosh, T., Pack, D.W., . . . Zhizhin, M. (2009) A fifteen year record of global natural gas flaring derived from satellite data. Energies 2, 595-622.

Ghosh, T., Elvidge, C.D., Sutton, P.C., Baugh, K.E., Ziskin, D. & Tuttle, B.T. (2010) Creating a global grid of distributed fossil fuel CO2 emissions from nighttime satellite imagery. Energies 3, 1895-1913.

Hall, F.G., Strebel, D.E., Nickeson, J.E. & Goetz, S.J. (1991) Radiometric rectification: toward a common radiometric response among multidate, multisensor images. Remote Sensing of Environment 35, 11-27.

He, C., Shi, P., Li, J., Chen, J., Pan, Y., Li, J., . . . Ichinose, T. (2006) Restoring urbanization process in China in the 1990s by using non-radiance-calibrated DMSP/OLS nighttime light imagery and statistical data. Chinese Science Bulletin 51, 1614-1620.

Hsu, F.-C., Baugh, K.E., Ghosh, T., Zhizhin, M. & Elvidge, C.D. (2015) DMSP-OLS radiance calibrated nighttime lights time series with intercalibration. Remote Sensing 7, 1855-1876.

Huang, Q., Yang, X., Gao, B., Yang, Y. & Zhao, Y. (2014) Application of DMSP/OLS nighttime light images: A meta-analysis and a systematic literature review. Remote Sensing 6, 6844-6866.

Jensen, J.R., (1986) Introductory digital image processing: a remote sensing perspective. University of South Carolina, Columbus.

Ju, Y., Dronova, I., Ma, Q. & Zhang, X. (2017) Analysis of urbanization dynamics in mainland China using pixel-based night-time light trajectories from 1992 to 2013. International journal of remote sensing 38, 6047-6072.

Khawar, M., (2017) North Versus South–An Examination of Regional Comparative Development in Italy and Brazil, The Geography of Underdevelopment. Springer, pp. 25-34.

Kyba, C.C., Kuester, T., De Miguel, A.S., Baugh, K., Jechow, A., Hölker, F., . . . Guanter, L. (2017) Artificially lit surface of Earth at night increasing in radiance and extent. Science advances 3, e1701528.

Li, X., Chen, F. & Chen, X. (2013a) Satellite-observed nighttime light variation as evidence for global armed conflicts. IEEE Journal of Selected Topics in Applied Earth Observations and Remote Sensing 6, 2302-2315.

Li, X., Chen, X., Zhao, Y., Xu, J., Chen, F. & Li, H. (2013b) Automatic intercalibration of night-time light imagery using robust regression. Remote sensing letters 4, 45-54.

Li, X., Ge, L. & Chen, X. (2013c) Detecting Zimbabwe's decadal economic decline using nighttime light imagery. Remote Sensing 5, 4551-4570.

Liao, B., Wei, K. & Song, W. (2012) Assessment and app;ication of DMSP/OLS nighttime light data in the spatial structure of urban system-A case of Jiangxi Province in nearly 16 years. Resources and Environment in the Yangtze Basin 21, 1295-1300.

Liu, Z., He, C., Zhang, Q., Huang, Q. & Yang, Y. (2012) Extracting the dynamics of urban expansion in China using DMSP-OLS nighttime light data from 1992 to 2008. Landscape and urban planning 106, 62-72.

Lu, D., Tian, H., Zhou, G. & Ge, H. (2008) Regional mapping of human settlements in southeastern China with multisensor remotely sensed data. Remote Sensing of Environment 112, 3668-3679.

Ma, Q., He, C., Wu, J., Liu, Z., Zhang, Q. & Sun, Z. (2014) Quantifying spatiotemporal patterns of urban impervious surfaces in China: An improved assessment using nighttime light data. Landscape and urban planning 130, 36-49.

Ma, T., Zhou, C., Pei, T., Haynie, S. & Fan, J. (2012) Quantitative estimation of urbanization dynamics using time series of DMSP/OLS nighttime light data: A comparative case study from China's cities. Remote Sensing of Environment 124, 99-107.

Ma, T., Zhou, Y., Zhou, C., Haynie, S., Pei, T. & Xu, T. (2015) Night-time light derived estimation of spatio-temporal characteristics of urbanization dynamics using DMSP/OLS satellite data. Remote Sensing of Environment 158, 453-464.

Miller, S.D., Mills, S.P., Elvidge, C.D., Lindsey, D.T., Lee, T.F. & Hawkins, J.D. (2012) Suomi satellite brings to light a unique frontier of nighttime environmental sensing capabilities. Proceedings of the National Academy of Sciences 109, 15706-15711.

Pandey, B., Joshi, P. & Seto, K.C. (2013) Monitoring urbanization dynamics in India using DMSP/OLS night time lights and SPOT-VGT data. International Journal of Applied Earth Observation and Geoinformation 23, 49-61.

Pandey, B., Zhang, Q. & Seto, K.C. (2017) Comparative evaluation of relative calibration methods for DMSP/OLS nighttime lights. Remote Sensing of Environment 195, 67-78.

Pok, S., Matsushita, B. & Fukushima, T. (2017) An easily implemented method to estimate impervious surface area on a large scale from MODIS time-series and improved DMSP-OLS nighttime light data. ISPRS Journal of Photogrammetry and Remote Sensing 133, 104-115.

Richmond, A.K., (2019) Water, land, and governance: environmental security in dense Urban Areas in Sub-Saharan Africa, The Environment-Conflict Nexus. Springer, pp. 91-102.

Ryan, R.E., Pagnutti, M., Burch, K., Leigh, L., Ruggles, T., Cao, C., . . . Helder, D. (2019) The Terra Vega active light source: A first step in a new approach to perform nighttime absolute radiometric calibrations and early results calibrating the VIIRS DNB. Remote Sensing 11, 710.

Schott, J.R., Salvaggio, C. & Volchok, W.J. (1988) Radiometric scene normalization using pseudoinvariant features. Remote Sensing of Environment 26, 1-16.

Shao, Z. & Liu, C. (2014) The integrated use of DMSP-OLS nighttime light and MODIS data for monitoring large-scale impervious surface dynamics: A case study in the Yangtze River Delta. Remote Sensing 6, 9359-9378.

Song, C., Woodcock, C.E., Seto, K.C., Lenney, M.P. & Macomber, S.A. (2001) Classification and change detection using Landsat TM data: when and how to correct atmospheric effects? Remote Sensing of Environment 75, 230-244.

Sutton, P., Roberts, D., Elvidge, C. & Meij, H. (1997) A comparison of nighttime satellite imagery and population density

for the continental United States. Photogrammetric engineering and remote sensing 63, 1303-1313.

Sutton, P.C., (2003) Estimation of human population parameters using night-time satellite imagery, Remotely-Sensed Cities. Taylor and Francis, London, pp. 301-333.

Tan, K.G., Luu, N.T.D. & Cher, S.Y.W. (2019) Understanding growth slowdown dynamics in India's sub-national economies: An empirical investigation. International Journal of Social Economics.

Tuttle, B.T., Anderson, S., Elvidge, C., Ghosh, T., Baugh, K. & Sutton, P. (2014) Aladdin's magic lamp: Active target calibration of the DMSP OLS. Remote Sensing 6, 12708-12722.

Wu, J., He, S., Peng, J., Li, W. & Zhong, X. (2013a) Intercalibration of DMSP-OLS night-time light data by the invariant region method. International journal of remote sensing 34, 7356-7368.

Wu, J., Wang, Z., Li, W. & Peng, J. (2013b) Exploring factors affecting the relationship between light consumption and GDP based on DMSP/OLS nighttime satellite imagery. Remote Sensing of Environment 134, 111-119.

Wu, K. & Wang, X. (2019) Aligning pixel values of DMSP and VIIRS nighttime light images to evaluate urban dynamics. Remote Sensing 11, 1463.

Xie, Y. & Weng, Q. (2016) Detecting urban-scale dynamics of electricity consumption at Chinese cities using time-series DMSP-OLS (Defense Meteorological Satellite Program-Operational Linescan System) nighttime light imageries. Energy 100, 177-189.

Xie, Z., Ye, X., Zheng, Z., Li, D., Sun, L., Li, R. & Benya, S. (2019) Modeling polycentric urbanization using multisource big geospatial data. Remote Sensing 11, 310.

Yu, B., Shu, S., Liu, H., Song, W., Wu, J., Wang, L. & Chen, Z. (2014) Object-based spatial cluster analysis of urban landscape pattern using nighttime light satellite images: A case study of China. International Journal of Geographical Information Science 28, 2328-2355.

Zhang, Q., Pandey, B. & Seto, K.C. (2016) A robust method to generate a consistent time series from DMSP/OLS nighttime light data. IEEE Transactions on Geoscience and Remote Sensing 54, 5821-5831.

Zhang, Q. & Seto, K.C. (2011) Mapping urbanization dynamics at regional and global scales using multi-temporal DMSP/OLS nighttime light data. Remote Sensing of Environment 115, 2320-2329.

Zhang, X., Guo, S., Guan, Y., Cai, D., Zhang, C., Fraedrich, K., . . . Tian, Z. (2018) Urbanization and spillover effect for three megaregions in China: Evidence from DMSP/OLS nighttime lights. Remote Sensing 10, 1888.

Zhang, Y. & Tian, F. (2010) Definition of" Emerging Economies" and their Role in the Global Economic Landscape [J]. International Economic Review 4.

Zheng, Q., Weng, Q. & Wang, K. (2019a) Developing a new cross-sensor calibration model for DMSP-OLS and Suomi-NPP VIIRS night-light imageries. ISPRS Journal of Photogrammetry and Remote Sensing 153, 36-47.

Zheng, W., Xu, W.-l. & Chen, Y. (2019b) Dynamic evolution of economic network within inter-regional urban agglomerations: Based on the urban agglomerations of west coast of Taiwan Straits, Yangtze River Delta and Pearl River Delta. Economic Geography 39, 58-66.

Zheng, Z., Yang, Z., Wu, Z. & Marinello, F. (2019c) Spatial variation of NO2 and its impact factors in China: An application of sentinel-5P products. Remote Sensing 11, 1939.

Zhou, Y., Li, X., Asrar, G.R., Smith, S.J. & Imhoff, M. (2018) A global record of annual urban dynamics (1992–2013) from nighttime lights. Remote Sensing of Environment 219, 206-220.

4. A Simple Method for Near-Real-Time Monthly Nighttime Light Image Production [3]

4.1 Abstract

Compared with previous nighttime light (NTL) data, the Black Marble product developed by NASA in recent years is the most advanced NTL product, which plays an important role in regional activity monitoring and special events (process) tracking due to its excellent timeliness (near- real-time release) and global data coverage capability. Currently, among the Black Marble products, the VNP46A2 product is not updated in a timely manner and VN46AX is still under development. Thus, VNP46A1, which is released in near real time, has become a key product available to the public, although it is affected by cloud cover and moonlight. To obtain high-quality near-real-time monthly NTL images and reduce the data gaps before VNP46AX is released, a simple processing scheme based on VNP46A1 is proposed in this letter. The results show that the proposed processing chain can effectively filter cloud-polluted pixels and alleviate the interference of moonlight radiation. The near-real-time monthly NTL (NRTMNTL) data generated by the scheme achieve a higher correlation with VNP46A2 and present a better visual purity. The near-real-time data availability and parameter-free input make the proposed scheme more applicable for short-period events tracking.
Keywords: Black Marble; near real time; nighttime light (NTL); VNP46A1

4.2 Introduction

The Suomi National Polar-orbiting Platform/Visible Infrared Imaging Radiometer Suite (SNPP/VIIRS) Night- time light (NTL) products, with their excellent low-light detection capability, daily revisit cycle, and data availability, are becoming the core data sources for night light research, especially for human activity signature tracking (Levin et al., 2020). Based on SNPP/VIIRS Day/Night Band (DNB), NASA has developed a new standard product suite, the Black Marble product suit, which represents the latest in current technology for NTL applications (Román et al., 2018). The near-real-time processing of the product suite allows the data to support real-time monitoring of the ground surface (Wang et al., 2018). The product suite includes: the daily at-sensor top of atmosphere (TOA) nighttime radiance product (VNP46A1), the daily moonlight-adjusted NTL product (VNP46A2), Monthly/Annual moonlight-adjusted NTL product (VNP46AX), and Black Marble HD (Román et al., 2019).

Research on NTL applications based on the VNP46 product suite is currently advancing (Wang et al., 2016; Liu et al., 2020). However, scholars have to face several challenges, such as: 1) the near-real- time

[3] This Chapter relies on the paper "Zheng, Z., Wu, Z., Chen, Y., Guo, G., Yang, Z., & Marinello, F. (2021). A Simple Method for Near-Real-Time Monthly Nighttime Light Image Production. IEEE Geoscience and Remote Sensing Letters, 1–5.". https://doi.org/10.1109/LGRS.2021.3059799

released VNP46A1 is still interfered by clouds and moonlight and 2) the development algorithm of the improved VNP46A2 is overly complex. Thus, the monthly NTL image VNP46AX cannot be updated to the public. Therefore, there is an urgent need to develop a simple algorithm to pro- duce a cloud-free, low-moonlight interfered, near-real-time monthly NTL (NRTMNTL) composite product. In this letter, an efficient and simple processing chain was proposed to generate near-real-time monthly NTL images based on the multitemporal VNP46A1 images to fill the data gap before the availability of VNP46AX.

4.3 Data and study area

The main NTL data used in this study were derived from VIIRS Level 3 Black Marble products, including VNP46A1 and VNP46A2. These two light products pro- vide daily NTL monitoring results at 500-m resolution. VNP46A1 contains 26 scientific data sets (SDS) layers, including sensor radiation, cloud cover flags, brightness temperature, and so on, which are released in near real time (Román et al., 2019). VNP46A2 contains seven SDS layers, including DNB BRDF- Corrected NTL, Gap-Filled DNB BRDF-Corrected NTL, and so on. However, due to the complexity of the production algorithm, VNP46A2 is only available for a limited period.

In this letter, four tiles covering Italy were selected as the study area due to its diverse and representative surface types, as shown in Figure 4.1. Considering the availability of VNP46A2 images, all daily VNP46A1 and VNP46A2 images in 2017 were used.

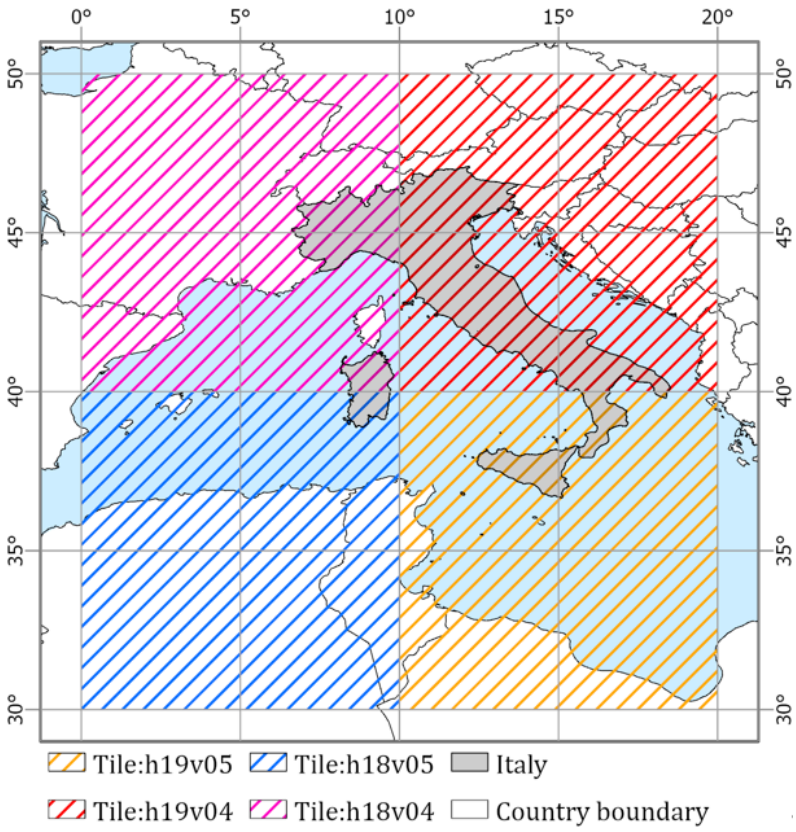

Figure. 4.1. Study area and selected tiles.

4.4 Method

4.4.1 Filtering of Cloud-Polluted Pixels

As with daytime satellite remote sensing, cloud obscuration of light pixels is the most prominent factor that limits the wide- spread use of VNP46A1 products (Figure 4.2). During the low- moonlight night, clouds attenuate or even obscure the upward radiation of surface light, so that the light radiation received by the sensor is much lower than the actual radiation. Moreover, they also introduce a blurring effect on the light pixels. Conversely, during the strong moonlight night, the clouds reflect the moon's radiation, and the sensor receives more light than actual surface light, resulting in an "overexposure" phenomenon in the generated NTL image.

Figure. 4.2. VNP46A1 images of the Italian region disturbed by cloud cover and moonlight.

Therefore, the accurate removal of cloud-contaminated pixels from the daily VNP46A1 image was the first step in the processing chain. The 26 SDS layers included in the VNP46A1 product provided a flag layer for the cloud mask state: the QF_Cloud_Mask. This layer was a 10-bit binary flag raster, and the key on each bit represented different surface and cloud information. Here, the bit flag sequences that were suitable for VNP46A1 cloud-polluted pixel removal are explicitly listed (Table 4.1). The flag sequences were determined based on a joint comparison of "QF_Cloud_Mask" and the light radiation layer, and a large number of samples were examined. In addition, partially filled pixels (65535) were also excluded since they marked low-quality pixels.

Table 4.1. Flag sequences for cloud-polluted pixel removal.

Flag				Decimal Value
Snow/Ice	Cirrus	⋯	Day/Night	
0	0		0	32
0	0		0	34
0	0		0	36
0	0		0	42
0	0	⋯	0	48
0	0		0	50
0	0		0	52
0	0		0	58
1	0		0	1056

1	0	0	1058
1	0	0	1060
1	0	0	1066
1	0	0	1072
1	0	0	1074
1	0	0	1076
1	0	0	1082

Figure 4.3 shows the raw NTL radiation layers and the filtered results of cloud-polluted pixels for VNP46A1 in the Italian region during January 2017. Generally, the QF_Cloud_Mask-based approach of cloud-polluted pixel filtration was efficient. It is worth noting that the efficiency of the strategy was still affected by the moonlight radiation and extreme weather. Typically, the method filtered cloud-contaminated pixels more precisely when the moonlight fraction was less than 50%–60%.

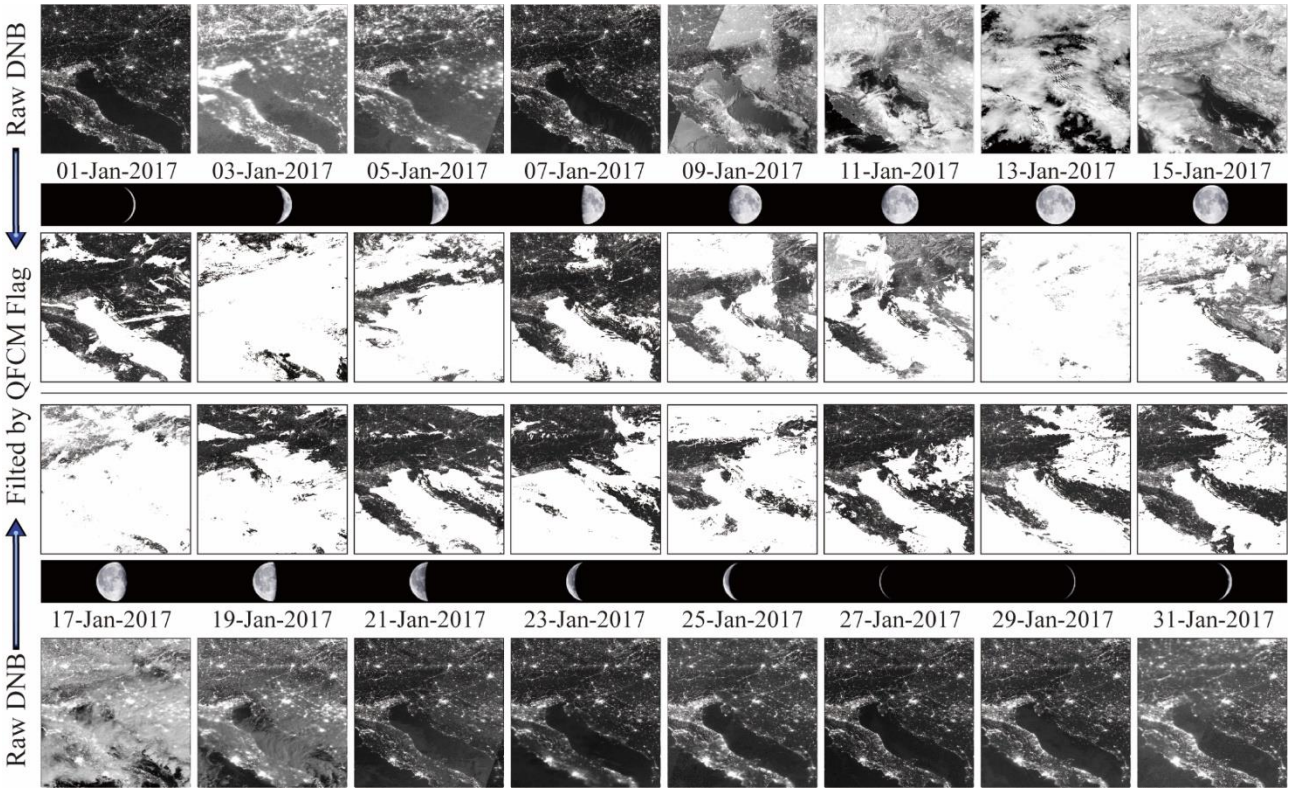

Figure 4.3. Comparison of the original light image with results after removal of cloud-contaminated pixels.

4.4.2 Reduces Moonlight Radiation

Through tracked moonlight radiation from multiple time- series tiles, it was found that high-intensity moonlight radiation caused two types of defects in the daily NTL image: 1) when there was no cloud cover, highly reflective surfaces, such as snowy mountains, deserts, and showed abnormally high values of light radiation, and the surface texture was imaged and 2) when there was thick cloud cover, the moonlight reflected from clouds interfered with the cloud mask flag, and caused few contaminated pixels that could not be filtered.

A pixel-mean analysis of the VNP46A1 images over a single lunar phase cycle was implemented to reveal the effect of the lunar fraction on the daily VNP46A1 light radiation (Figure 4.4). The results show that the daily mean light radiation from VNP46A1 during the lunar phase cycle showed a single-peaked structure and

reached the peak at the full-moon night. In addition, the dynamics of the mean radiation of VNP46A1 with the lunar phase was not limited to a single tile, but was also stable in multiple background tiles.

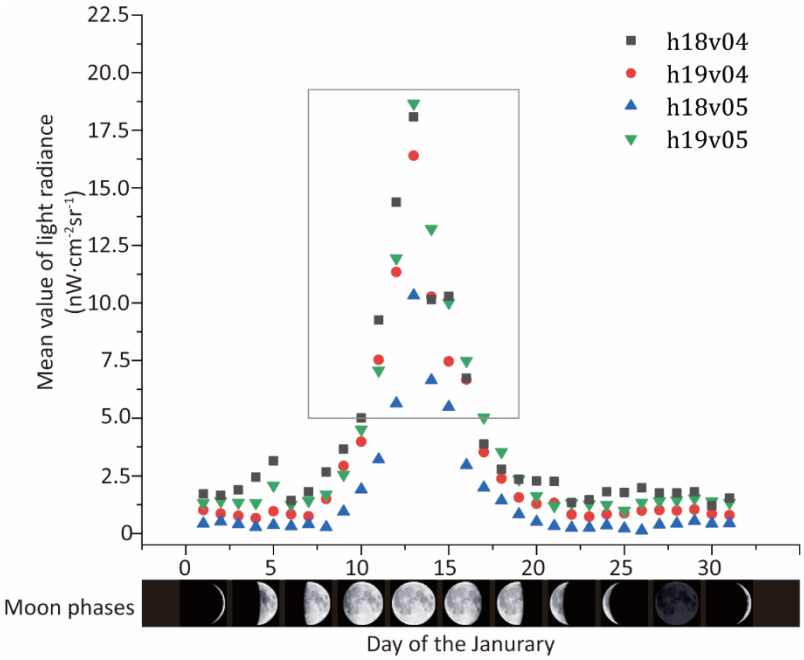

Figure 4.4. Results of pixel-mean analysis of multi-background tiles in January 2020.

Considering the high correlation between the moonlight fractions and the nighttime light radiation of the tiles (Figure 4.5(a)), the segmental coefficient of variation (CV) detection method was proposed to determine the threshold value of moonlight radiation interference. Theoretically, the light radiation of the tile will maintain a stable level over a single lunar phase period. Therefore, by dynamically com- paring the CV of the light radiation for the "front (low)-end (high)" moonlight fractions of a single lunar phase period, the mutation point of the light radiation change can be located. Specifically, the CV difference was calculated as

$$CV_{difference} = CV_{end} - CV_{front} \tag{4.1}$$

$$CV_{front} = S_{front}/m_{front} \tag{4.2}$$

$$CV_{end} = S_{end}/m_{end} \tag{4.3}$$

$$m_{end} = \sum_{i=k}^{i=1} u_i/N' \tag{4.4}$$

$$m_{front} = \sum_{i=0}^{i=k} u_i/N \tag{4.5}$$

$$S_{front} = \sqrt{\sum_{i=0}^{i=k} (u_i - m_{front})/(N-1)} \tag{4.6}$$

$$S_{end} = \sqrt{\sum_{i=k}^{i=1} (u_i - m_{end})/(N'-1)} \tag{4.7}$$

where μ_i is the NTL image's mean radiation values of the day with moonlight fraction i; k is the dynamic fraction threshold that divides the "front" and "end" parts; N and N' are the sample sizes (number of days) of the "front" and "end" parts, respectively; m_{front}, m_{end}, s_{front} and s_{end} are the mean and standard

deviation values of the “front” and “end” part parts, respectively.

The results in Figure 4.5(b) show that 1) as the group line moved to the right, the front part CV increased while the end part CV decreased; and 2) the CV difference between the front and end parts was positive when the moonlight fraction was no higher than 60% and negative when it exceeded 60%. When the moonlight fraction was over 60%, the high-intensity moonlight radiation caused strong reflection from features with a high surface reflectivity (especially snow/ice surfaces), and greatly increased the radiation at-sensor. In addition, high intensity moonlight radiation was also reflected by clouds and captured by the sensor, causing the “overexposure” phenomenon. Given the diversity and irregularity of feature types, and the unpredictability of regional meteorological conditions, it was concluded that daily VNP46A1 images with a moonlight fraction greater than 60% should be excluded from the NRTMNTL product. Although discarding samples with moonlight fractions over 60% to composite NRTMNTL images resulted in partial loss of light radiation, images with moonlight fractions below 60% (20-21 days) accounted for about 65%-70% of all samples, which were sufficient to reflect surface light emission characteristics. Furthermore, the parameter-free and robust performance of the processing scheme was an additional non-negligible advantage for near real-time monthly light data production.

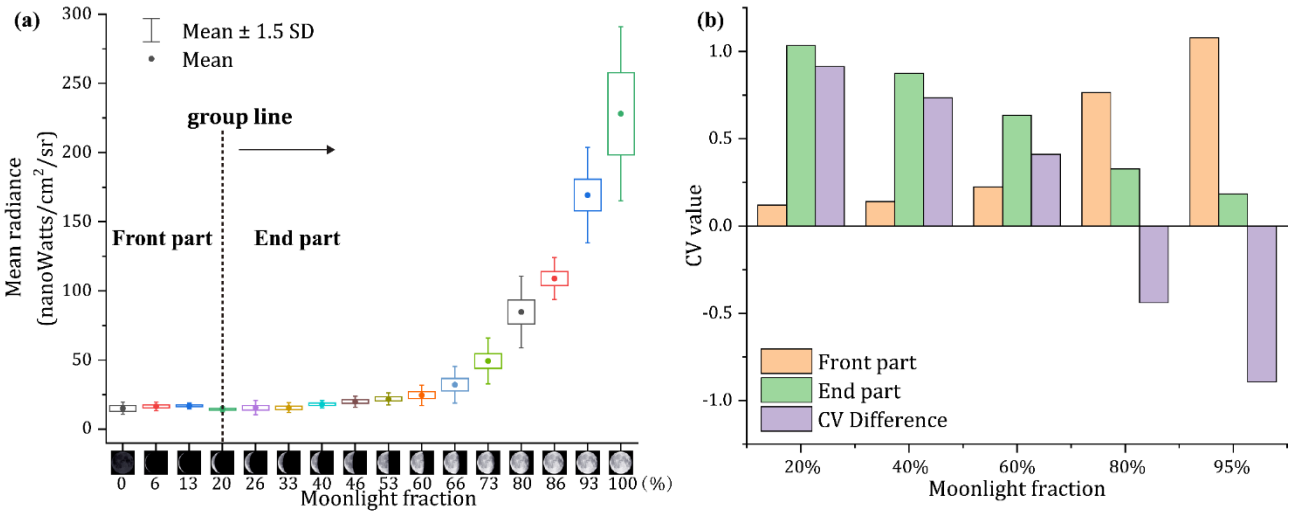

Figure 4.5. Dynamics of CV with lunar fraction during the lunar phase cycle.

4.5 Data validation

In this paper, NRTMNTL was compared with median shift corrected composite product (MedianSCP), minimum radiation composite product (MinCP) and raw composite product (RawCP) to evaluate the product performance. The median shift correction model, which was proposed by Stathakis et al. (2020), is characterized by its simplicity and user-friendliness. The method included 3 steps: 1) the median radiation of the light image on the new moon night after de-clouding was taken as the standard value; 2) the deviation between the median radiation of the remaining nights and the standard median was computed as the correction factor; 3) the correction factor was subtracted from the light images of each night. Hence, VNP46A1 images

of all scenes in January 2017 were selected and de-clouded, and then 1) mean composition analysis was performed based on samples below 60% of the moonlight fraction, 2) mean composition analysis was performed using the results after median shift correction, 3) minimum composition analysis was performed on all images, and 4) mean composition analysis was performed directly on all images, and four monthly composited NTL images were generated.

As mentioned before, VNP46A2 is the most advanced daily NTL product, which has been optimized for radiation correction and cloud shadow restoration. Therefore, in this paper, the monthly NTL image composited by the four approaches were linearly regressed at the pixel scale with the "Gap-Filled DNB BRDF-Corrected NTL" monthly composite image in VNP46A2 to assess their performance differences. Table 4.2 shows the fitting degree of the linear regression between the monthly light image synthesized by different approaches and the monthly composite image of VNP46A2. The results showed that the highest R^2 was achieved for NRTMNTL with VNP46A2 monthly synthesis images on all four tiles, followed by RawCP, MedianSCP and MinCP.

Table 4.2. Linear fit performance between the composited images and monthly VNP46A2 image.

Product	Tiles			
	h18v04	h18v05	h19v04	h19v05
NRTMNTL	0.91	0.87	0.85	0.94
MedianSCP	0.74	0.70	0.83	0.77
MinCP	0.59	0.26	0.72	0.57
RawCP	0.87	0.84	0.82	0.89

Next, a 10×10 grid was constructed on each tile and the R^2 of each grid was computed to reveal the performance differences between products in spatial scale. The product that achieved the highest R^2 on the grid is presented in Figure 4.6(a). It can be seen that NRTMNTL achieved a significant lead among the 400 grids evaluated, with 94.5% of all grids having the highest fit.

Furthermore, the performance differences of the above four composited images over 12 months in 2017 were calculated. The results show that the performance differences between the composite methods existed throughout the year and were relatively stable (Figure 4.6(b)). Among them, NRTMNTL achieved better performance in different months, while MedianSCP showed mediocre performance and only outperformed RawCP during the winter period. Overall, NRTMNTL achieved an average fit R^2 of 0.9 in the linear regression evaluation with VNP46A2, indicating that NRTMNTL has stable performance in both the spatial scale and the temporal dimension.

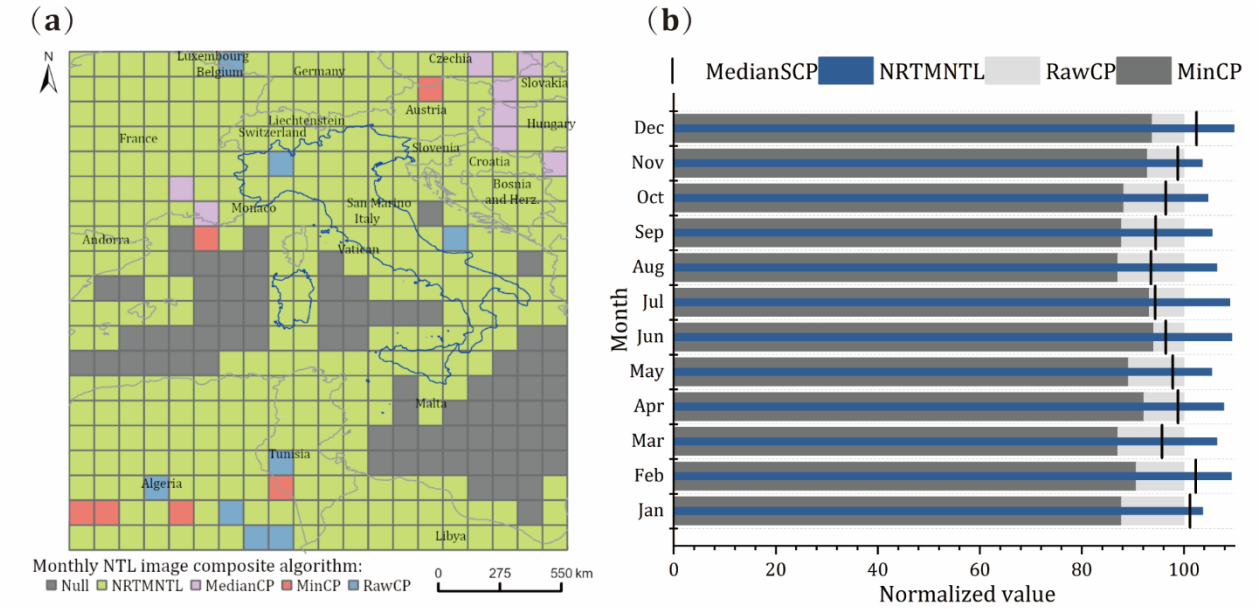

Figure 4.6. Performance evaluation of multiple composite products. note: (a) spatial differences in performance; (b) temporal differences in performance.

The data accuracy can be measured by the linear correlation of the composited image with VNP46A2. However, for the composite monthly image, especially the single-band NTL image, the visual purity of the image is also a key parameter for the image quality. Therefore, in this paper, the image purity of RawCP, MinCP, MedianSCP, NRTMNTL and VNP46A2 in four tiles was visually checked, as shown in Figure 4.7.

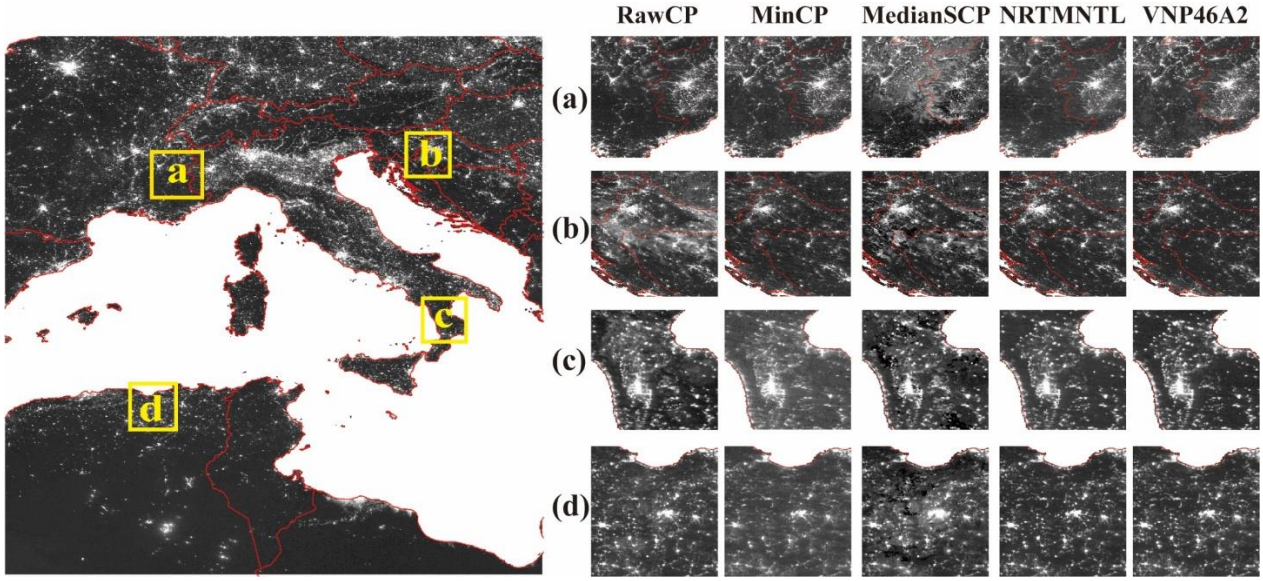

Figure 4.7. The visual purity differences of RawCP, MinCP, MedianSCP, NRTMNTL and VNP46A2.

It can be seen that the VNP46A2 image presented the highest contrast and the least amount of noise. The image purity of NRTMNTL was close to that of the VNP46A2, with slight radiation differences in the faint areas. Despite the favorable image contrast of MedianSCP and RawCP, the image quality still suffered from radiometric noise, especially the large amount of noise from the highly reflective features, such as snow/ice surface. For MinCP, although the radiation noise from the highly reflective surface was effectively eliminated, the minimum composition resulted in low-image contrast in the faint region.

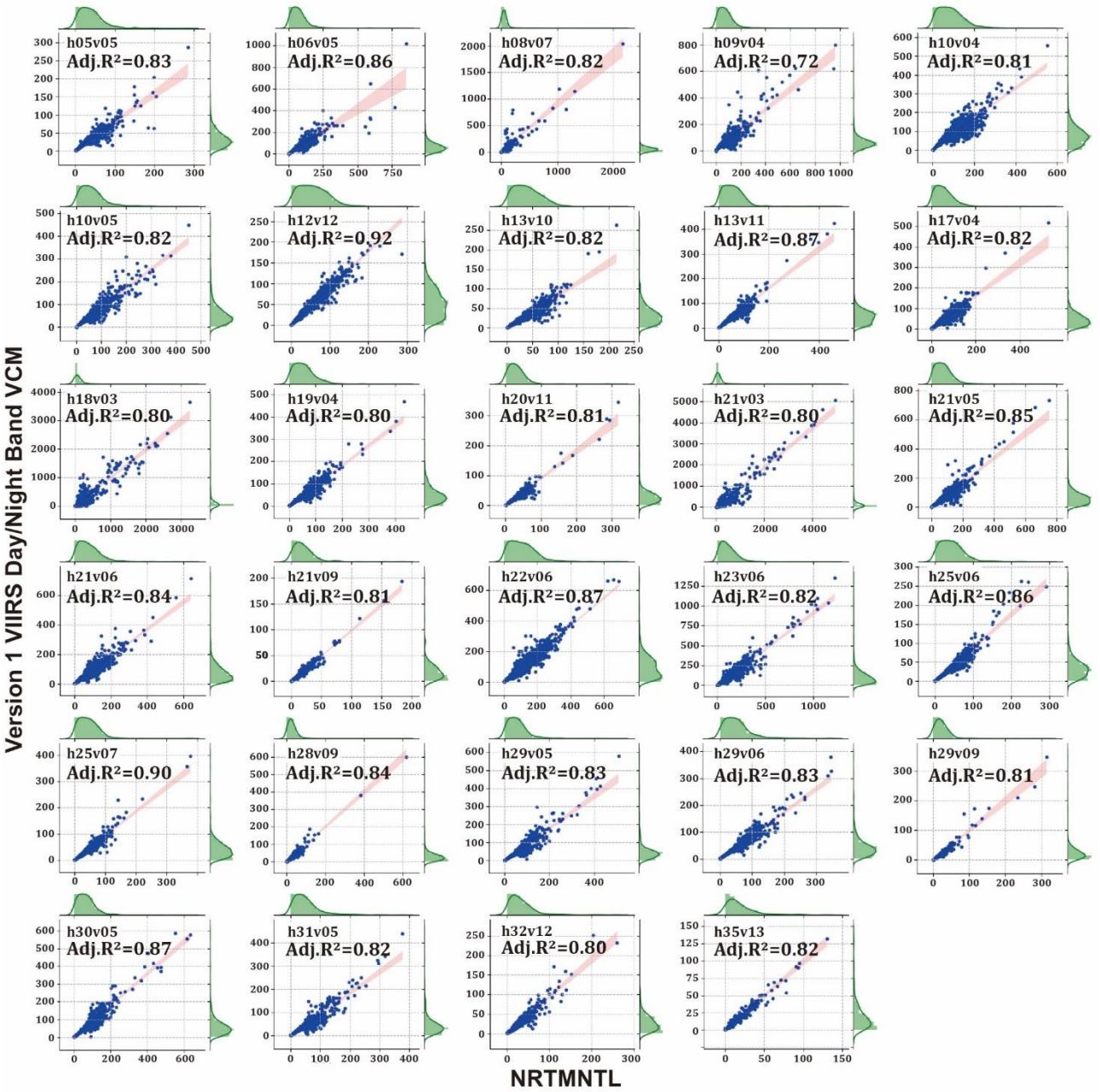

Figure 4.8. Pixel scatter plot between NRTMNTL and VCM for diverse background tiles globally (January 2017).

In addition, a correlation analysis was conducted between the produced NRTMNTL and Version 1 VIIRS Day/Night Band NTL Cloud Mask product (VCM). The VCM is produced and publicly distributed by the Earth Observation Group (EOG). It is the most widely known and used monthly synthetic light product due to its high accessibility and well-organized data structure (6 tiles global coverage). However, due to the complexity of the entire process, VCM cannot be released in near real-time (usually lags for more than six months). Hence, tiles with different levels of urbanization were selected for validation analysis at a global scale. The results of the pixel scatter plot with multiple background tiles (Figure 4.8) show that the NRTMNTL produced in this paper correlated well with the VCM produced by EOG (R^2>0.8) and was steady across varied light intensity backgrounds.

Finally, Wuhan city was selected as the application area in this paper to examine the potential of

NRTMNTL product for major event monitoring. The results (Figure 4.9) show that from January 2020 to June 2020, the light intensity in Wuhan experienced a decline and then a rebound, especially in the urban center area. As the earliest outbreak region of COVID-19, Wuhan became one of the most severely affected regions by this epidemic. To effectively prevent the spread of COVID-19, Wuhan was placed on lockdown on January 23, and nighttime activities were halted with a significant decrease in light radiation. As the epidemic was gradually brought under control and the number of infections declined rapidly, Wuhan was unlocked on April 8, and nighttime activities gradually returned to normal conditions. As seen from Figure 4.9, NRTMNTL effectively captured the dynamic changes of human activity intensity with control measures during the epidemic, which showed the excellent potential of NRTMNTL for monitoring significant surface events.

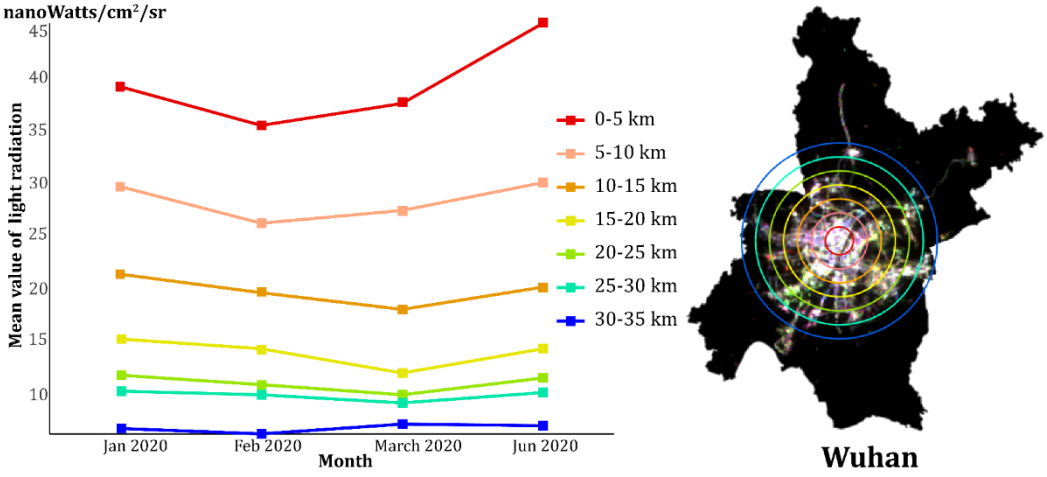

Figure 4.9. Wuhan's light intensity changes over the lockdown period.

4.6 Discussion

As the most advanced NTL product, VNP46A1 is one of the fundamental data sources for special event observation and regional assessment due to its global data coverage, near-real-time release, and easy access. Especially in 2020, which was ravaged by COVID-19 globally, VNP46A1 products were used by scholars to reveal the impact of COVID-19 on human social activities and economic conditions at different scales and regions. However, VNP46A1 suffers from the interference of clouds and moonlight radiation, while the improved products VNP46A2 and VNP46AX also cannot be released in a timely manner due to the complicated algorithm, which greatly limits the widespread application of near-real-time NTL data.

With the aim of exploiting the potential of VNP46A1 and alleviating existing data gaps, a simple and efficient processing chain was proposed in this paper to generate near-real-time monthly NTL image NRTMNTL. There are several advantages of the method proposed in this paper. First, the method is simple and efficient. In the processing chain, "QF_Cloud_Mask" and dynamics light radiation CV were used for fast removal of cloud and moonlight radiation interference. This parameter-free input processing chain was completely based on the layer and radiation characteristics of the VNP46A1 image itself and was suitable for batch processing with good productivity.

Second, the method showed good performance and robustness. The performance evaluation results all indicated that NRTMNTL achieved better correlation with VNP46A2 in both spatial and temporal dimensions and also had better visual purity and contrast. Also, the good correlation of NRTMNTL with the most commonly used monthly VCM data using tiles with different urbanization levels at a global scale indicated the positive performance of NRTMNTL. Previous schemes circumvented moonlight radiation by discarding light images near the full moon, which requires the measurement of natural light radiation at a specific time and place, making them complicated and low-migration methods (Baugh et al., 2013; Fan et al., 2019). The proposed dynamic CV difference method identified moonlight fraction thresholds to avoid moonlight radiation interference, which was robust and did not require field measurement.

Third, the proposed method provides near-real-time data and has high-potential applications. It is well-known that the near-real-time availability of NTL images is a fundamental condition for timely monitoring of short-period events. Although some scholars monitored short-period major events based on monthly VCM data, this approach tended to suffer from two issues: 1) the data could not be released timely, and typically lagged by more than half a year; 2) the intra-month light radiation dynamics was not accessible. Since NRTMNTL was developed based on VNP46A1, it can be updated simultaneously with VNP46A1 and has global coverage, which enables timely human activity monitoring worldwide. Further, the proposed scheme is essentially based on daily NTL images, so it is possible to adjust the composite time-window to capture the dynamic changes in light radiation intra-month.

However, the proposed processing chain in this paper still has some shortcomings. During the production of the NRTMNTL, daily light VNP46A1 images with a moonlight fraction of over 60% were excluded from the processing stream, which means that approximately 10 days of light images in a complete lunar phase cycle were not included in the composition. These 10-day light images were heavily influenced by high-intensity moonlight radiation, and the mean light radiation values of the images jumped abnormally. The absence of one-third of the daily light images during the lunar phase cycle will inevitably lead to some light radiation bias in NRNMNTL. However, given the high linear correlation between NRTMNTL and the standard products (VNP46A2 and VCM), it is still one of the promising products for human activity assessment. Besides, some additional error factors weren't considered (e.g., anisotropy (Li et al., 2019)) since the radiation errors caused by them were much smaller compared to moonlight and cloud.

4.7 Conclusion

With in-depth research based on NTL data worldwide, the availability of high-quality, fine-scale, near real-time NTL data is becoming critical, especially for tracking ground-specific events and processes. In this paper, based on the most advanced Black Marble product, a processing chain was proposed to produce cloud-free, low-lunar radiation disturbed, near-real-time composite image NRTMNTL. Compared with the composite light images produced by other schemes, the processing chain proposed in this paper effectively removed the cloud contaminated pixels and suppressed the interference of moonlight radiation without

additional parameters and data. As a result, the produced NRTMNTL achieved better accuracy and visual purity. Although the scheme was unable to collect all samples in a single lunar phase cycle, given the overall data precision and parameter-free characteristic, it can serve as an important alternative for near-real-time monthly NTL data before the release of VNP46AX.

References

Baugh, K., Hsu, F.-C., Elvidge, C.D. & Zhizhin, M. (2013) Nighttime lights compositing using the VIIRS day-night band: Preliminary results. Proceedings of the Asia-Pacific Advanced Network 35, 70-86.

Fan, X., Nie, G., Deng, Y., An, J., Zhou, J. & Li, H. (2019) Rapid detection of earthquake damage areas using VIIRS nearly constant contrast night-time light data. International journal of remote sensing 40, 2386-2409.

Levin, N., Kyba, C.C., Zhang, Q., de Miguel, A.S., Román, M.O., Li, X., . . . Miller, S.D. (2020) Remote sensing of night lights: A review and an outlook for the future. Remote Sensing of Environment 237, 111443.

Li, X., Ma, R., Zhang, Q., Li, D., Liu, S., He, T. & Zhao, L. (2019) Anisotropic characteristic of artificial light at night–Systematic investigation with VIIRS DNB multi-temporal observations. Remote Sensing of Environment 233, 111357.

Liu, Q., Sha, D., Liu, W., Houser, P., Zhang, L., Hou, R., . . . Hu, T. (2020) Spatiotemporal patterns of COVID-19 impact on human activities and environment in mainland China using nighttime light and air quality data. Remote Sensing 12, 1576.

Román, M.O., Wang, Z., Shrestha, R., Yao, T. & Kalb, V., (2019) Black marble user guide version 1.0, NASA: Washington, DC, USA.

Román, M.O., Wang, Z., Sun, Q., Kalb, V., Miller, S.D., Molthan, A., . . . Pandey, B. (2018) NASA's Black Marble nighttime lights product suite. Remote Sensing of Environment 210, 113-143.

Wang, J., Aegerter, C., Xu, X. & Szykman, J.J. (2016) Potential application of VIIRS Day/Night Band for monitoring nighttime surface PM2. 5 air quality from space. Atmospheric environment 124, 55-63.

Wang, Z., Román, M., Sun, Q., Molthan, A., Schultz, L. & Kalb, V., (2018) Monitoring disaster-related power outages using NASA black marble nighttime light product, The International Archives of the Photogrammetry, Remote Sensing and Spatial Information Sciences, pp. 1853-1856.

5. Pixel-level cross-sensor calibration quality identification method for extended nighttime light products [4]

5.1 Abstract

Nighttime light (NTL) satellite imagery has become an essential data source for urbanization studies because it is able to capture human activities. Thanks to imagery derived from the Defense Meteorological Satellite Program's Operational Linescan System (DMSP/OLS) and the Suomi National Polar-orbiting Partnership Visible Infrared Imaging Radiometer Suite (NPP/VIIRS), which are the two most widely used NTL data sources, long-term global light radiation dynamic analysis can be conducted by their cross-sensor calibration combinations. Although new cross-sensor calibration models for these two NTL products are constantly being proposed, methods for evaluating pixel continuity quality after calibration are still scarce and cursory. For instance, Total Sum of Light (TSOL) has been commonly used to assess light radiation continuity, whereas it can only qualitatively reflect continuity at the regional level, which conceals the amount of pseudo-continuous light radiation pixels being found. In order to achieve a more refined and quantitative extended NTL (ENTL) continuity quality assessment, a pixel-level continuity identification scheme based on Theil-Sen Median trend analysis and Mann-Kendall testing was developed in this paper. Based on this scheme, the two most representative ENTLs, derived from opposite production streams, were selected for quality identification. The results showed that our proposed scheme can automatically generate continuous quality labels of global light pixels with more detailed information compared to the previous TSOL. In addition, the Pixel Change Identification Standard ($PCI_{Standard}$) layer created in the process annotated significant changes in global light radiation between 1992-2018 and can be used for other ENTL detection and urbanization studies.
Keywords: Extended Nighttime Light (ENTL), DMSP/OLS, NPP/VIIRS, Pixel Change Identification (PCI)

5.2 Introduction

Satellited-based earth observations offer humans a unique perspective on the dynamics of the earth's surface. Compared to daytime optical remote sensing, nighttime light (NTL) remote sensing allows us to track the human footprint at local, regional and global scales by capturing artificial lights emitted by human activities. Due to the unique advantages of NTL in characterizing socio-economic activities and urban expansion, etc., NTL-based applications, such as urban boundary identification (Zhang and Seto, 2011; Li et al., 2018c; Zhao et al., 2020; Yang et al., 2021), population and GDP spatialization (Klomp, 2016; Stokes and Seto, 2019; Yu et al., 2019; Chen et al., 2021a), energy consumption assessment (Cao et al., 2014; Román et al., 2019; Shi et al., 2019), disaster impacts (Li et al., 2018b), human pressure (Mammides, 2020), air and

[4] This Chapter relies on the paper "Zheng, Z., Wu, Z., Chen, Y., Yang, Z., & Marinello, F. (2021). Pixel-level cross-sensor calibration quality identification method for extended nighttime light products. Submitted to IEEE Transactions on Geoscience and Remote Sensing.

light pollution assessment (Li et al., 2015; Jiang et al., 2017; Ji et al., 2019; Zheng et al., 2021), have expanded in recent years.

Presently, the most widely used and accessible NTL data are from the Defense Meteorological Satellite Program's Operational Linescan System (DMSP/OLS) and the Suomi National Polar-orbiting Partnership Visible Infrared Imaging Radiometer Suite (NPP/VIIRS). Specifically, version 4 DMSP/OLS stable NTL data provides annual synthetic products for the period 1992-2013, while the NPP/VIIRS cloud-free DNB (Day/Night Band) composite data provides monthly synthetic products after April 2012 (Levin et al., 2020). As upgraded NTL data, NPP/VIIRS products have higher radiometric and spatio-temporal resolutions, which are applicable for finer scale human activity tracking, especially in public safety arenas such as disasters (Cao et al., 2013; Li et al., 2018a; Zhao et al., 2018), health (Ghosh et al., 2020; Yin et al., 2021) and war (Li et al., 2017; Li et al., 2018b). With the expansion of NTL-based applications, single sensor-based studies are no longer able to meet the needs of human footprint tracking over longer timespans compared to optical remote sensing with good continuity, such as the Landsat and MODIS projects (Fensholt and Proud, 2012; Lyu et al., 2018). Therefore, the combination of DMSP/OLS and NPP/VIIRS NTL products naturally becomes a solution to worth considering.

One issue that first must be addressed is the alignment of NTL images from DMSP/OLS and NPP/VIIRS, as the two sensors have completely different performance parameters. DMSP/OLS NTL products record relative radiation intensity, which is stored as a digital number ranging from 0-63. NPP/VIIRS NTL products record absolute radiation intensity in nanoWatts/cm^2/sr. In addition, they have different spatial resolutions, e.g. the DMSP/OLS NTL image resolution is 30 arc second (~500m at the Equator), while the NPP/VIIRS NTL is 15 arc second (1000m at the Equator). Therefore, a number of cross-sensor calibration schemes and models have been proposed to generate aligned DMSP/OLS and NPP/VIIRS NTL products. For example, Li et al. (2017) used a pow function to convert VIIRS data into corresponding simulated DMSP/OLS images to assess changes in human activities during the Syrian war. Also, based on the pow function, Wu and Wang (2019) tracked the urban expansion of Beijing. Zheng et al. (2019a) used a residual-corrected GWR model to generate a DMSP-like VIIRS dataset considering seasonal effects, then applied and validated it in a highly developed city. Sahoo et al. (2020) employed machine learning schemes (multilayer perceptron and random forest) with multiple auxiliary data to produce VIIRS-like DMSP datasets and obtain long time-series light data products. In addition, the BiDoseResp model was applied by Ma et al. (2020) to capture the deformation of two types of NTL data and generate a DMSP-like VIIRS dataset. Although all of the above cross-sensor calibration methods have made some progress in specific local areas, it is worth advancing the development of global-scale cross-sensor calibration models considering the massive applications for NTL data in revealing the dynamics of human activities at large scales. Among the large scale aligned NTL data development solutions, the consistent extended NTL (ENTL) data developed and open-sourced by Li et al. (2020) and Chen et al. (2021b) are the most noteworthy cross-sensor calibration products today due to their full-time span and accessibility. Their release provides data support for other long-term NTL-based applications and is widely used in a variety of

scenarios for analysis, such as economic growth estimation (Du et al., 2021; Zhong et al., 2022), urbanization intensity (Li et al., 2021; Xu et al., 2021) and light pollution (Lian et al., 2021).

However, while calibration solutions and NTL alignment products continue to be released, the methods and metrics used to assess calibration performance and NTL data continuity have stagnated. In the studies described above, the most widespread metrics for performance evaluation (data continuity assessment) of calibration models have been limited to one-dimensional (Total Sum of Light, TSOL (Li and Zhou, 2017)) and two-dimensional (DN scatter plot and histogram (Zhang et al., 2016)). The performance of the calibration model and the quality of the calibrated ENTL products are examined by comparing the continuity of these metrics before and after calibration. It must be acknowledged that these assessment models and metrics can reflect overall data quality changes and have a positive contribution to aligning model improvements. However, these metrics are often extracted from subjectively selected regions, such as the sum, mean and median of light radiation of the whole region, and although the metrics maintain good consistency and variability across a timeline, they may conceal continuity anomalies within the regions, resulting in a pseudo-continuous phenomenon. Consequently, when fine-scale urbanization studies are conducted based on these data, they often lead to irregular and disordered light intensity variations. This quality risk of open-sourced data is fatal, as it may lead to completely opposite conclusions in time-series light radiation studies. Therefore, developing a quantitative assessment scheme specifically for aligned NTL data and generating finer data quality labels will not only improve the assessment performance of cross-sensor calibration model but also minimize the risks associated with pseudo-variable pixels.

To achieve this, we developed a pixel-level continuity anomaly detection model for light radiation change based on Theil-Sen Median trend analysis and Mann-Kendall testing. The core idea of the model is 1) to generate a full time series light radiation standard dynamic identification layer by associating the light change identification results of DMSP/OLS and NPP/VIIRS; 2) to compare this standard layer with the change identification results of the ENTL that is to be detected, so that the pixels with abnormal variations can be located quickly and efficiently. Our proposed scheme is able to more accurately pinpoint pixels with abnormal variation in the ENTL, which is not possible in previous ENTL continuity assessment schemes (metrics). In addition, by accurately indicating erroneous pixels in the ENTL, our solution enables cross-sensor calibration model developers to quantitatively evaluate the performance of their calibration models, quickly identify model deficiencies and make targeted improvements. The remainder of this paper describes the data sources (Section II), methodology (Section III), the ENTL quality identification results (Section IV), a discussion (Section V) and conclusions (Section VI).

5.3 Data sources

In this paper, the global ENTL products developed by Li et al. (2020) and Chen et al. (2021b) (referred to as LiNTL and ChenNTL, respectively) were selected to perform pixel-level continuous quality assessments due to their global coverage, high accessibility and widespread deployment. LiNTL offers continuous light

products from 1992-2018 globally. It's core production process includes: 1) employing a stepwise calibration approach to ensure good temporal consistency for DMSP/OLS NTL from 1992-2013; 2) applying a cloud weight synthesis scheme to generate annual VIIRS images for 2014-2018; and 3) generating DMSP-like VIIRS products through kernel density, logarithmic and sigmoid functions and combining them with the calibrated DMSP/OLS products. Comparatively, ChenNTL provides a continuous light product from 2000-2018, which is slightly different from LiNTL. Specifically, they used saturation-corrected EANTLI from 2013 (Zhuo et al., 2015) and annual VIIRS synthetic images to train the auto-encoder model, and the model was applied to EANTLI from 2000-2012 to generate VIIRS-like DMSP products. Finally, the VIIRS-like DMSP products were assembled with the NPP/VIIRS annual synthesis products and released as ENTL products. A detailed parameter comparison of these two ENTLs can be found in Table 5.1. In terms of the processing procedure of these two ENTLs, they are reversed in the generation direction; that is, LiNTL is organized as DMSP united DMSP-like data, while ChenNTL is VIIRS-like united VIIRS data. Therefore, compared to LiNTL, ChenNTL has a higher spatial resolution because it is derived from VIIRS data.

Table 5.1. Detailed parameters of LiNTL and ChenNTL.

ENTL	Data availability	Spatial resolution	Radiation unit	Production Stream
LiNTL	1992-2018	1000m	DN value	DMSP + DMSP-liked
ChenNTL	2000-2018	500m	$nWcm^{-2}sr^{-1}$	VIIRS-liked + VIIRS

In addition, since LiNTL and ChenNTL performed necessary pre-processing (e.g., noise removal and resampling) of the DMSP/OLS and NPP/VIIRS NTL products, respectively, we can extract the pre-processed DMSP/OLS and NPP/VIIRS annual products from each of them. Here, we extracted NTL products from LiNTL for 1992-2013, and from ChenNTL for 2013-2018, which were used to produce light radiation dynamics standard layer for subsequent ENTL quality assessments.

5.4 Methods

5.4.1 General procedures

As research into the DMSP/OLS and NPP/VIIRS products has intensified, calibration and correction methods for the two NTL products themselves are now relatively well established and the performance of both corrected NTL data has been significantly improved. Therefore, the key challenge in achieving cross-sensor calibration of DMSP/OLS and NPP/VIIRS is to align light radiation intensities with completely different performance parameters to form a continuous, comparable NTL product. It should be emphasized that this alignment of light radiation intensity is not only required for the regional scale, but also for each pixel, which has been neglected in previous studies. On this basis, we developed an automatic and efficient detection scheme specifically for highlighting possible errors in radiation alignment in ENTL. The prerequisite assumptions of this scheme are that 1) the actual light radiation changes at the surface are continuous and progressive over two adjacent time intervals (between 1992-2013 and 2013-2018), and 2) the radiation trends of the calibrated DMSP/OLS and NPP/VIIRS NTL products are real and accurate because they come from the

same type of sensors and are calibrated. According to the above assumptions, we can extract light radiation change trends based on DMSP/OLS and NPP/VIIRS light data products respectively, and make simple logical judgments to produce light radiation change layers for the period 1992-2018, which can be used as a standard to detect other ENTL products. Generally, the detection scheme can be divided into four steps: 1) Conduct a pixel-by-pixel light radiation trend analysis based on extracted LiNTL products from 1992-2013 (denoted as $DMSP/OLS_{1992\text{-}2013}$) to generate a global light radiation dynamic identification layer ($PCI_{DMSP/OLS}$); 2) Conduct a similar radiation trend analysis based on extracted ChenNTL products for the period 2013-2018 (denoted as $NPP/VIIRS_{2013\text{-}2018}$) to create another worldwide light radiation dynamic identification layer ($PCI_{NPP/VIIRS}$); 3) Associates $PCI_{DMSP/OLS}$ and $PCI_{NPP/VIIRS}$ and performs logical judgements to generate a full time-span global light radiation dynamic standard layer ($PCI_{Standard}$); 4) Perform light radiation trend analysis for LiNTL and ChenNTL products and cross-validate with $PCI_{Standard}$ separately to generate ENTL quality identification layers (denoted as $ENQI_{LiNTL}$ and $ENQI_{ChenNTL}$). The flowchart of the whole scheme is shown in Figure 5.1.

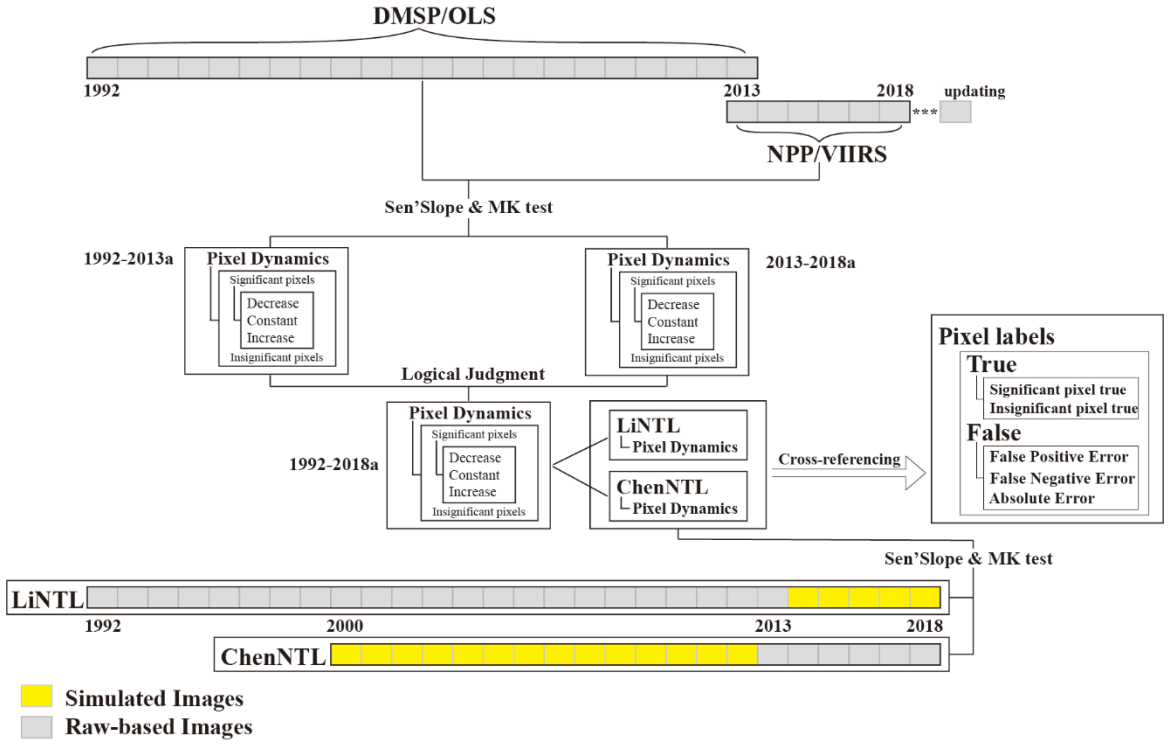

Figure 5.1. Flowchart of the joint DMSP/OLS and NPP/VIIRS NTL products for continuous quality identification of LiNTL and ChenNTL.

5.4.2 Pixel-level light radiation trend analysis

As described the steps above, one of the main tasks of the whole scheme is the light radiation trend analysis by pixels. It should be noted that "pixels" in this paper refer to the grid cells with a defined map projection for NTL and ENTL products. Through the trend analysis of the light radiation variation, its temporal variation features can be characterized as significant increase, significant decrease, no change and non-significant change, which is a refining of time-series radiation information.

In this paper, the Theil-Sen Median trend analysis and Mann-Kendall testing were used for global pixel-level light radiation trend detection, because they did not require the data to conform to a given distribution and were resistant to data outliers. As an effective method for trend analysis of time-series data, it has been widely used in the fields of vegetation dynamics (Jiang et al., 2015), precipitation detections (Narayanan et al., 2016), temperature changes (Panwar et al., 2018) and light trends (Xu et al., 2019). The Theil-Sen Median trend analysis formula is as follows:

$$slope_{NTL} = median(\frac{NTL_j - NTL_i}{j-i}) \quad 1992 \le i \le j \le 2018 \tag{5.1}$$

where NTL_j and NTL_i represent j-year and i-year pixel light DN values for NTL products, respectively; $slope_{NTL}$ represents the trend of the calculated light radiance value, and when $slope_{NTL} > 0$, it means that the pixel light radiance is increasing, and when vice versa, decreasing. The significance of this trend was then tested by Mann-Kendall, as:

$$Z = \begin{cases} (S-1)/\sqrt{Var(S)} & (S > 0) \\ 0 & (S = 0) \\ (S+1)/\sqrt{Var(S)} & (S < 0) \end{cases} \tag{5.2}$$

$$S = \sum_{i=1}^{n-1} \sum_{j=i+1}^{n} sgn(NTL_j - NTL_i) \tag{5.3}$$

$$sgn(NTL_j - NTL_i) = \begin{cases} 1 & (NTL_j - NTL_i > 0) \\ 0 & (NTL_j - NTL_i = 0) \\ -1 & (NTL_j - NTL_i < 0) \end{cases} \tag{5.4}$$

$$Var(S) = n(n-1)(2n+5)/18 \tag{5.5}$$

where, sgn is the sign function; n is the length of the time series; Z is the statistical value of the significance test of the time series with a value range of (-∞, +∞). At a confidence level of $\alpha = 0.05$, $|Z| \ge Z_{0.05/2} = 1.94$ indicates that there is a significant trend in the radiance value of the pixel lights.

Based on trend analysis and significance tests, the time-series light radiation variation characteristics of each pixel were identified in the following categories: 1) significant increased ($slope_{NTL} > 0$, $p \le 0.05$); 2) significant decreased ($slope_{NTL} < 0$, $p \le 0.05$); 3) no changed ($slope_{NTL} = 0$, $p \le 0.05$); 4) non-significant change ($p > 0.05$).

5.4.3 Pixel-level logical diagnostics

According to the methods in Section III-B, the pixels in the DMSP/OLS$_{1992\text{-}2013}$, NPP/VIIRS$_{2013\text{-}2018}$, LiNTL and ChenNTL were classified, labeled, and the dynamic identification layers PCI$_{DMSP/OLS}$, PCI$_{NPP/VIIRS}$, PCI$_{LiNTL}$ and PCI$_{ChenNTL}$ were generated, respectively. Since PCI$_{DMSP/OLS}$ and PCI$_{NPP/VIIRS}$ provide light radiation change characteristics for the periods 1992-2013 and 2013-2018 respectively, we can extract full time light radiation dynamics information as a standard dynamics layer (PCI$_{Standard}$) by associating them. Then,

the $PCI_{Standard}$ was used as a reference for the association and logical diagnosis of the PCI_{LiNTL} and $PCI_{ChenNTL}$ and the corresponding quality assessment product ENQIs were finally exported. Figure 5.2 shows the entire flow of the logical diagnosis, which consists mainly of the $PCI_{Standard}$ diagnosis in the left section and the ENQI diagnosis in the right section. For ease of explanation, we denoted significant increased pixels in the PCI by "+", significant decreased by "-", significant unchanged by "=" and non-significant changes by "~".

1) Logical diagnosis for $PCI_{Standard}$: Considering that there were four radiation dynamic types in each of $PCI_{DMSP/OLS}$ and $PCI_{NPP/VIIRS}$, sixteen combinations were generated. Hence, a set of logical diagnostic rules was designed to compute the $PCI_{Standard}$ layer. Details are as follows:

a) "+" and "+" leads to "+", which means that for a given pixel, if its light radiation is significantly increased between 1992-2013 (identified as "+" in the $PCI_{DMSP/OLS}$) and also between 2013-2018 (identified as "+" in the $PCI_{NPP/VIIRS}$), then we consider that the radiation of this pixel is also significantly increased for the full period (1992-2018).

b) "-" and "-" leads to "-", which means that for a given pixel, if its light radiation is significantly decreased between 1992-2013 and also between 2013-2018, then we consider that the radiation of this pixel is also significantly decreased for the full period (1992-2018).

c) "=" and "=" leads to "=", which means that for a given pixel, if its light radiation is not changed between 1992-2013 and also between 2013-2018, then we consider that the radiation of this pixel is also unchanged for the full period (1992-2018).

d) "+" and "=" or "=" and "+" leads to "+", which means that for a given pixel, if its light radiation is significantly increased between 1992-2013 and unchanged between 2013-2018 or vice versa, then for the full period (1992-2018) we conclude that the radiation of this pixel is significantly increased.

e) "-" and "=" or "=" and "-" leads to "-", which means that for a given pixel, if its light radiation is significantly decreased between 1992-2013 and unchanged between 2013-2018 or vice versa, then for the full period (1992-2018) we conclude that the radiation of this pixel is significantly decreased.

f) "~" with any type leads to "~", which is obvious because once there is a non-significant change in any one time period, the change after its combination with another time period will also become non-significant. This rule is prudent because we do not want to increase the risk of underestimation errors.

g) "+" and "-" or "-" and "+" leads to "*", which means that for a given pixel, if its light radiation is significantly increased between 1992-2013 and decreased between 2013-2018 or vice versa, then for the full period (1992-2018) we are unable to directly determine how the pixel changed. For two consecutive periods with completely opposite changes in light radiation, determining the final trend is difficult, especially as they have different radiation units.

2) Logical diagnosis for ENQI: Similar to the diagnostic rules above, $PCI_{Standard}$ was cross validated with PCI_{LiNTL} or $PCI_{ChenNTL}$, and twenty combinations were generated. The reason for the four extra combinations was that a few new unidentified pixels were introduced into the $PCI_{Standard}$.

Next, based on the twenty combinations generated by the cross-validation, we categorized them into six types according to the rules in Figure 5.2:

a) Significant-Significant correct (SSC): pixels are both identified as significant pixels in $PCI_{Standard}$ and PCI_{LiNTL} ($PCI_{ChenNTL}$) and shared the same change characteristics. Specifically, it includes three combinations, "++", "--" and "==". These are high quality pixels in the ENTL, as their trends are perfectly consistent with the $PCI_{Standard}$ markers and passed the significance test.

b) Nonsignificant-Nonsignificant correct (NNC): pixels are both identified as non-significant pixels in $PCI_{Standard}$ and PCI_{LiNTL} ($PCI_{ChenNTL}$). It only consists of "~~". These are the relatively high-quality pixels in the ENTL as they are not identified as a significant changes in either the ENTL or $PCI_{Standard}$.

c) Unidentified: pixels identifications in $PCI_{Standard}$ are uncertain. Since there are a few unidentified pixels in the $PCI_{Standard}$, it is not possible to give a valid quality judgement when associating them.

d) Nonsignificant-Significant error (NSE): pixels are identified as not significantly changed in $PCI_{Standard}$ while marked as significantly changed in the PCI_{LiNTL} ($PCI_{ChenNTL}$). It includes three combinations, "~+", "~-" and "~=". We consider these to be medium quality pixels in ENTL because their dynamic trends are not significant enough in $PCI_{Standard}$.

e) Significant-Nonsignificant error (SNE): pixels are identified as significantly changed in $PCI_{Standard}$ while marked as not significantly changed in the PCI_{LiNTL} ($PCI_{ChenNTL}$). It also includes three combinations, "+~", "-~" and "=~". They are relatively low-quality pixels in ENTL, as they do not detect those pixels that have significant changes in the $PCI_{Standard}$, which is an omission error.

f) Significant-Significant error (SSE): Pixels are identified as significant pixels in both $PCI_{Standard}$ and PCI_{LiNTL} ($PCI_{ChenNTL}$), however, with different variation characteristics. It consists of six combinations, as shown in Figure 5.2. These are the lowest quality pixels in the ENTL, as their significant trend is completely different from that of the $PCI_{Standard}$. Such errors will seriously induce wrong conclusions from quantitative analysis based on ENTL and need to be highlighted in ENTL urgently

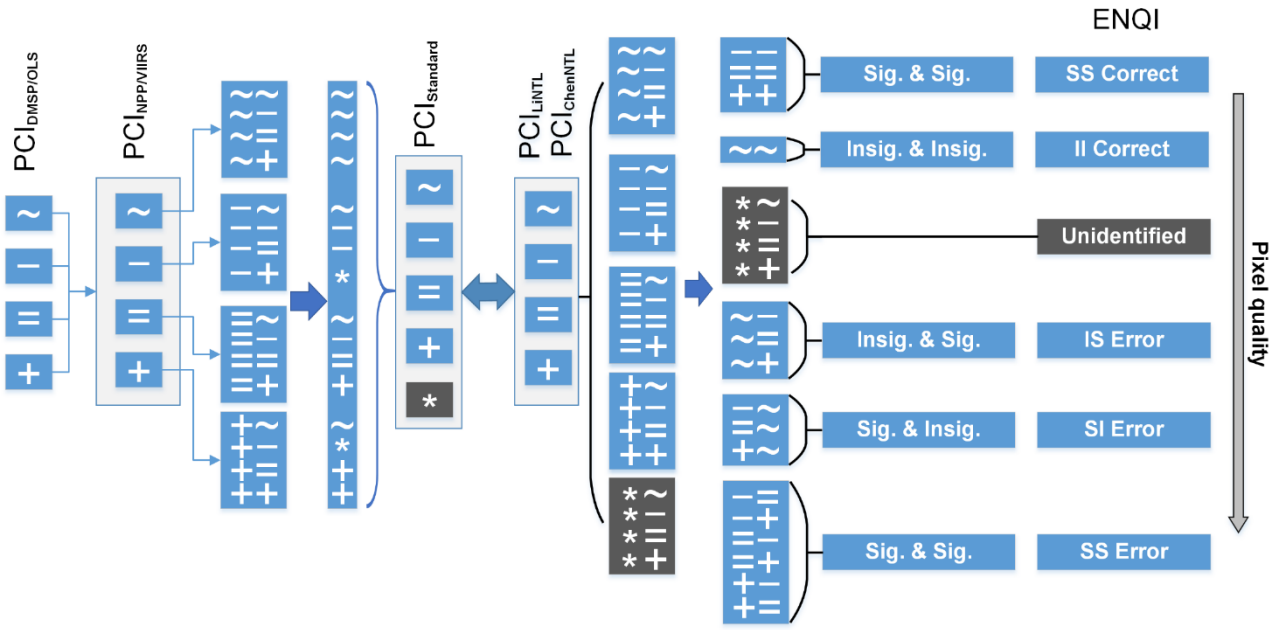

Figure 5.2. Logical flow for creating pixel change identification (PCI) and performing pixel quality assessment. Specifically, the symbol "~" represents non-significant pixel radiation changes, the symbol "=" represents constant radiation, and the symbols "-" and "+" represent significant radiation decrease and increase, respectively.

5.5 Results

5.5.1 Global light radiation $PCI_{Standard}$ layer

Based on the pre-processed $DMSP/OLS_{1992\text{-}2013}$ and $NPP/VIIRS_{2013\text{-}2018}$, $PCI_{DMSP/OLS}$ and $PCI_{NPP/VIIRS}$ were first produced by trend analysis, and the global light radiation dynamics standard layer, $PCI_{Standard}$, for the period 1992-2018 was derived by subsequent logical diagnosis, and the results were shown in Figure 5.3.

Globally, the light radiation dynamic detection results from $PCI_{DMSP/OLS}$ and $PCI_{NPP/VIIRS}$ showed that: 1) pixels with non-significant changes in light radiation (grey pixels) were concentrated at high latitudes in both the northern and southern hemispheres, especially for $PCI_{NPP/VIIRS}$. Although there were few traces of human activity and artificial light emission in the high latitudes due to the extreme climate and environmental conditions, the irregular light noise caused by the aurora leads to the conclusion of non-significant light radiation variations. 2) For pixels with significant signs, the proportion of unchanged pixels (black pixels) was the highest, accounting for 73.1% of $PCI_{DMSP/OLS}$ and 69.8% of $PCI_{NPP/VIIRS}$. These constant pixels were mostly distributed in regions without artificial illumination such as oceans, deserts, and inland areas. 3) Percentages of significantly decreased pixels (blue pixels) were the lowest in $PCI_{DMSP/OLS}$ and $PCI_{NPP/VIIRS}$, at 0.4% and 0.1%, respectively. For $PCI_{DMSP/OLS}$, blue pixels were concentrated in southeastern Russia, Ukraine, and the northeastern United States, while blue pixels for $PCI_{NPP/VIIRS}$ were mainly located in the east-central United States and the United Kingdom. 4) The percentage of pixels with significantly increased light radiation (red pixels) was approximately three times higher than blue pixels in $PCI_{DMSP/OLS}$ and $PCI_{NPP/VIIRS}$, at 1.7%

and 0.3% respectively. Specifically, in $PCI_{DMSP/OLS}$, red pixels were widely distributed in East Asia, South Asia, Europe, etc., while in $PCI_{NPP/VIIRS}$, the density of red pixels decreased dramatically and were mainly clustered in the built-up area.

Compared to $PCI_{DMSP/OLS}$ and $PCI_{NPP/VIIRS}$, which both reflect the dynamics of light radiation only for part of the time period, $PCI_{Standard}$ to reflect the dynamic characteristics of the full time period (1992-2018). The $PCI_{Standard}$ layer showed that on a global scale, about 9.7% of the pixels were labeled as non-significant changes in light radiation, while 68% were identified as significant pixels, with 1.06%, 66.6% and 0.34% of the increased, unchanged and decreased pixels, respectively. In addition, the percentage of pixels of unidentified type was almost negligible, only 0.05%. This also indicates that our proposed logical diagnosis scheme is feasible, as there are very few pixels that cannot be identified during logical diagnosis.

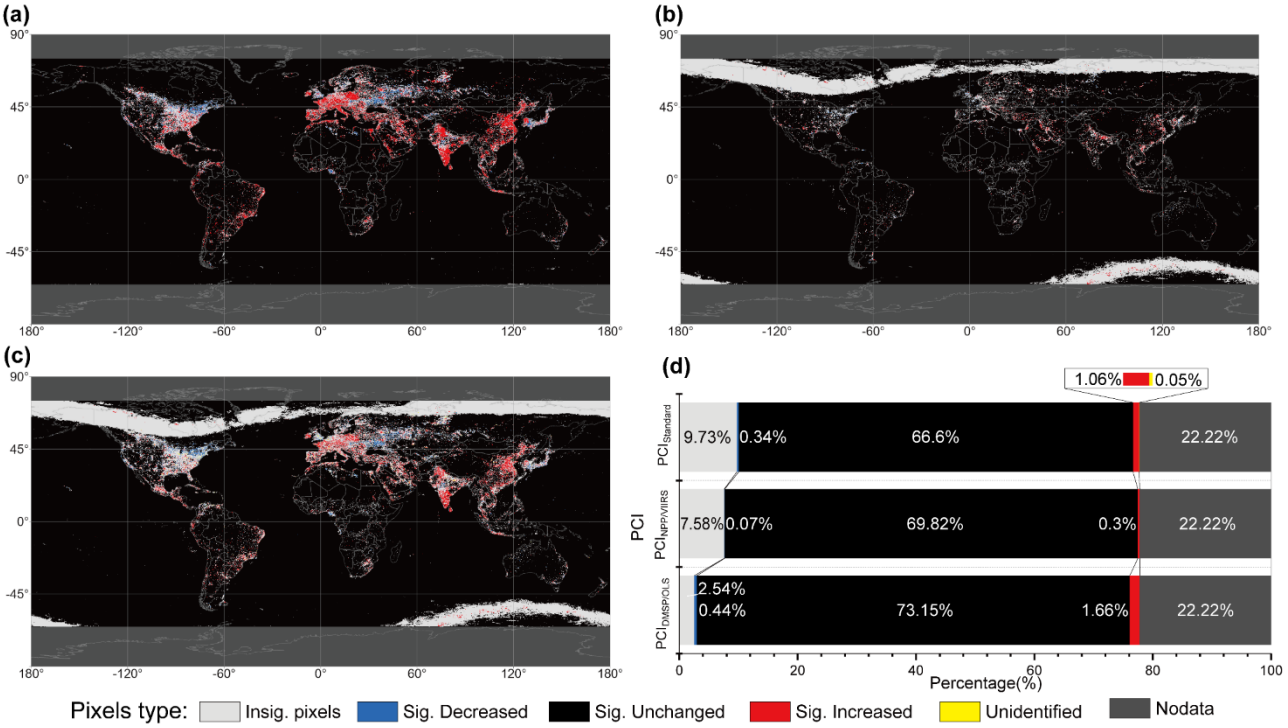

Figure 5.3. Global distribution of $PCI_{DMSP/OLS}$, $PCI_{NPP/VIIRS}$ and $PCI_{Standard}$ and its pixel percentages.

In addition, Figure 5.4 shows the three PCI identification layers for selected regions, including the Veneto Region (Europe), the Yangtze River Delta Region (Asia) and the New York Region (North America), which helps to compare the differences between them. The PCI identification results for the three regions had similar characteristics. Firstly, the significantly increased pixels marked as red in $PCI_{DMSP/OLS}$ were predominant and showed a contiguous distribution, while in $PCI_{NPP/VIIRS}$, there were clearly fewer red pixels, and they were clustered in urban areas. Secondly, percentages of red and blue pixels in $PCI_{Standard}$ were both between $PCI_{DMSP/OLS}$ and $PCI_{NPP/VIIRS}$, because according to the diagnostic rules (d) and (e), the combination of constant and significantly changed signs was redefined as significantly changed. Finally, the number of non-significantly changed pixels in the $PCI_{Standard}$ was higher than in $PCI_{DMSP/OLS}$ and $PCI_{NPP/VIIRS}$. The increase of non-significant pixels in $PCI_{Standard}$ was mainly stems from the diagnostic rule (f), whereby the combination of non-significant pixels with all other types were defined as non-significant. Meanwhile, unidentified pixels

recorded in regional $PCI_{Standard}$ were shown in yellow, and were especially prominent in the New York area. These yellow pixels experienced completely different trends in light radiation between 1992-2013 and 2013-2018. It must be acknowledged that economic development and urbanization have varied and shifted between regions over the last few decades, and the fact that some traditionally developed regions have indeed experienced a decline in light radiation in recent years compared to newly developing regions (Zheng et al., 2019b). Up to now, we have not been able to effectively distinguish between real light radiation mutations and mis-calibration caused mutations. For this reason, it is prudent to set them as unidentified.

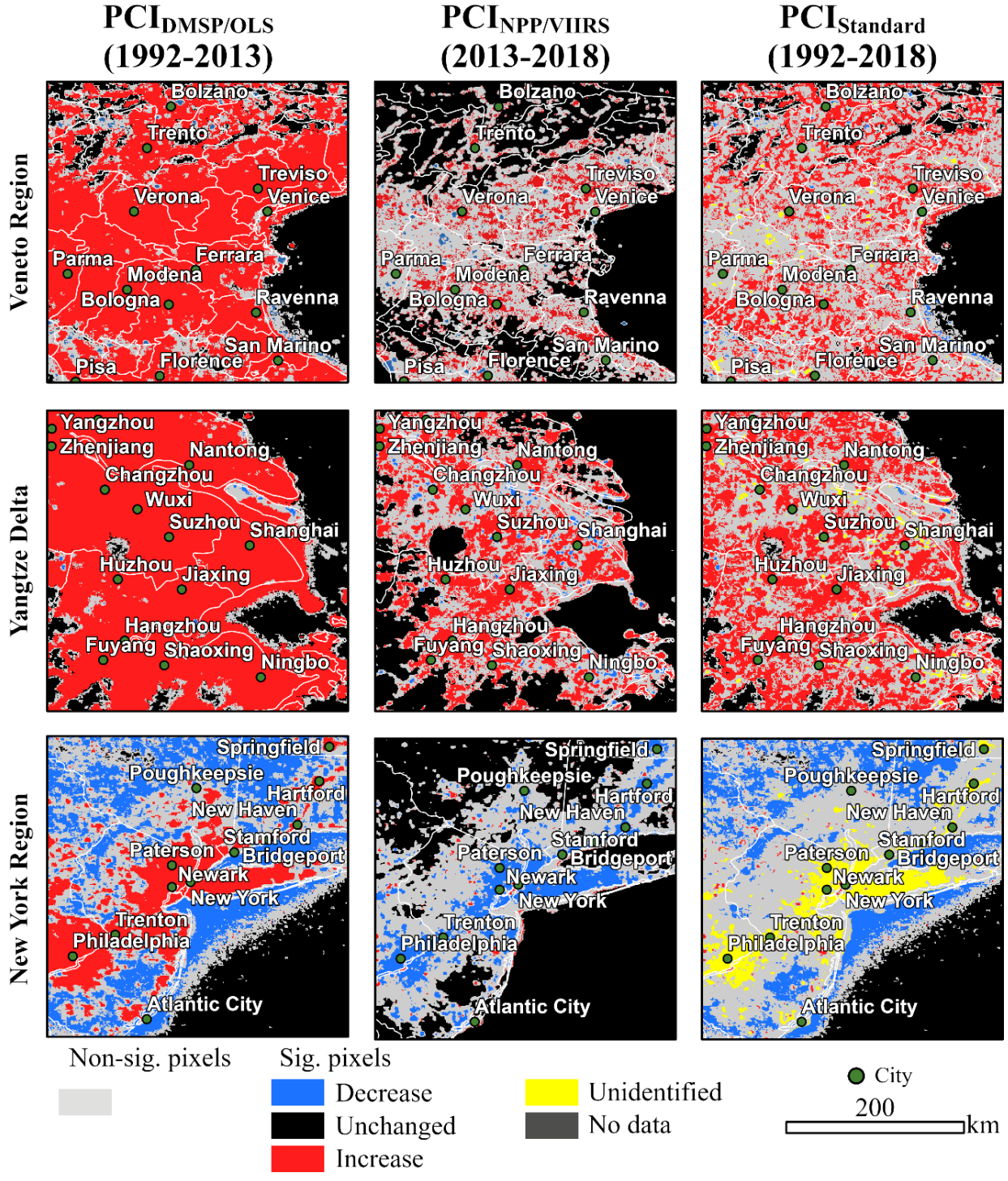

Figure 5.4. $PCI_{DMSP/OLS}$, $PCI_{NPP/VIIRS}$ and $PCI_{Standard}$ results in the US, Europe and China urban areas.

5.5.2 PCI Results of LiNTL and ChenNTL

As mentioned previously, LiNTL and ChenNTL are the most representative ENTL products from the two typical calibration schemes. We generated corresponding PCI layers using Theil-Sen Median trend analysis and Mann-Kendall testing. Figure 5.5 shows the PCI_{LiNTL} and $PCI_{ChenNTL}$ results at the global and regional scales.

Globally, the percentage of non-significant pixels (grey) in PCI_{LiNTL} was 30%, with a spatial distribution extending from high to mid-latitudes. The percentage of significantly decreased pixels (blue) was 0.4%, mainly concentrated between 45-60°N. The percentage of significantly increased pixels (red) was 2.6%, clearly higher than the $PCI_{Standard}$ 1.7%, and concentrated in the United States, China, India and Southern Europe. The percentage of grey pixels in $PCI_{ChenNTL}$ was only 23.2%, mainly distributed in high-latitude regions. The percentage of blue pixels was similar to $PCI_{NPP/VIIRS}$, only 0.1%, with a sporadic distribution. The percentage of red pixels was 0.4%, or about one-fourth of PCI_{LiNTL}, and widely distributed in small patches across East Asia, South Asia, Southern Europe and North America. Overall, the proportion of significant change pixels and non-significant pixels in PCI_{LiNTL} were higher than in $PCI_{ChenNTL}$, and the spatial distribution of pixels in PCI_{LiNTL} showed more pronounced anomalous clustering, for example there was a clear division line at 45°N.

Local-scale comparisons further support the above results, with a large number of pixels labelled blue and red in the PCI_{LiNTL} for the North American Great Lakes region, while these pixels were clearly reduced in $PCI_{ChenNTL}$. In Beijing, China, which experienced the most rapid urbanization in recent years, red pixels made up the majority of the PCI_{LiNTL}, indicating that the light radiation in this region increased from 1992-2018. Meanwhile, some differences were observed in $PCI_{ChenNTL}$, where the downtown was occupied by blue pixels and surrounded by red pixels, creating a "blue heart" phenomenon, and the extent of the red pixel marked had been also reduced. As previously mentioned for the division in PCI_{LiNTL}, in Eastern Europe, plenty of blue pixels appeared north of 45°N, while red pixels were almost exclusively found in the south. In the Tokyo area of Japan, PCI_{LiNTL} marked a large number of blue pixels and covered almost the entire Kanto and central Japan area, compared to $PCI_{ChenNTL}$, where the distribution of red and blue pixels was much smaller and concentrated in and around the Tokyo metropolitan area.

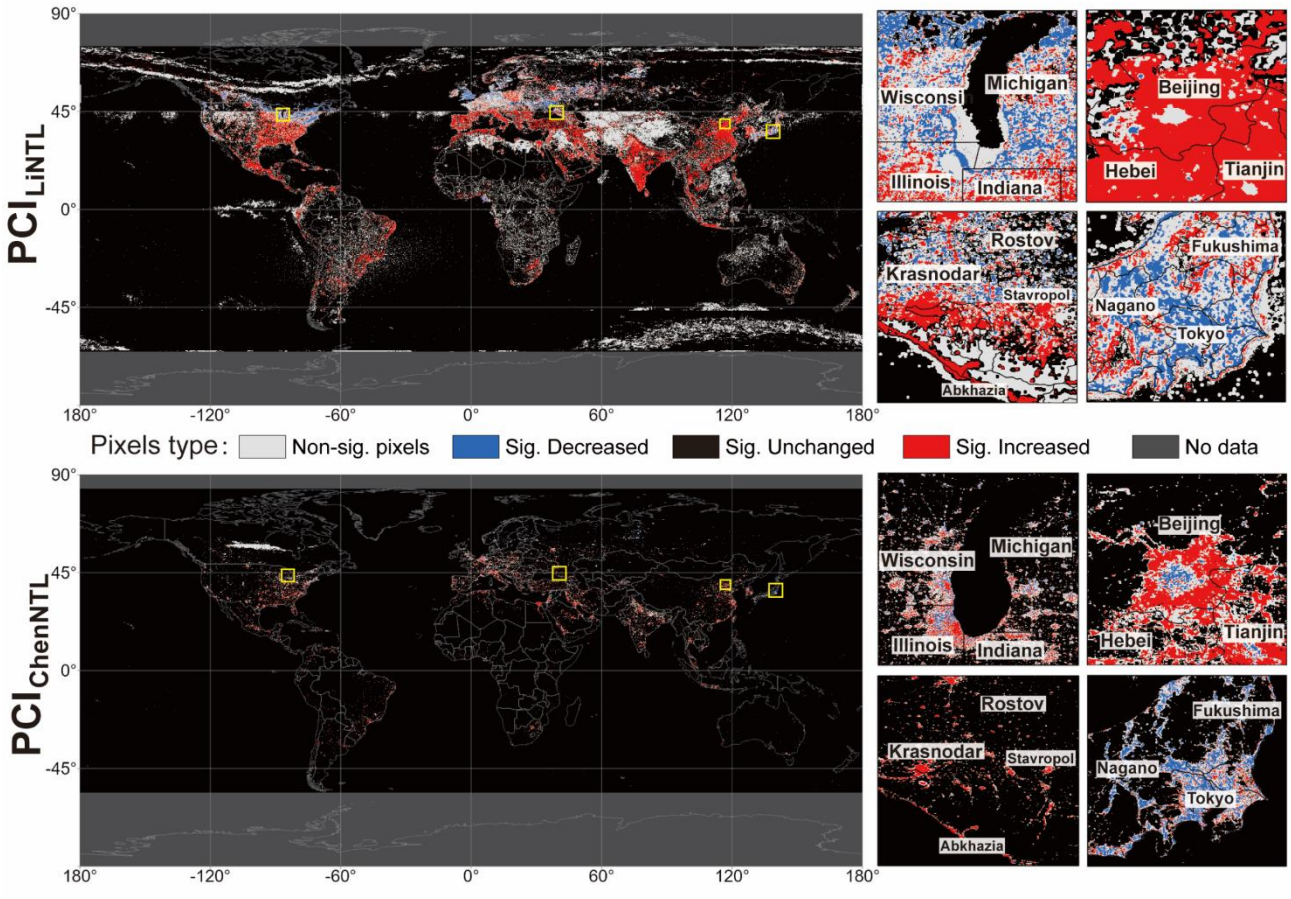

Figure 5.5. Global and local scales of PCI_{LiNTL} and $PCI_{ChenNTL}$.

5.5.3 Quality assessment of LiNTL and ChenNTL

PCI_{LiNTL} and $PCI_{ChenNTL}$ were associated, logical diagnostics with $PCI_{Standard}$ respectively, and the global light pixels were quickly and automatically quality-tagged with the corresponding ENQI layers generated. Figure 5.6(a) shows the global $ENQI_{LiNTL}$, where the percentage of correct pixels marked as SSC type was 63.5%, and 2.9% for NNC, with over 65% of all correct pixels. Pixel percentages for the three error types were 0.2%, 4.3%, and 6.8%. Among them, SSE, which PCI_{LiNTL} marked the exact opposite significant change from $PCI_{Standard}$, was the lowest quality pixel in the ENTL and accounted for only 0.2%. The pixel percentage of error type SNE was 4.3%, mainly distributed between 45°N and 45°S. Similarly, there was an especially sharp divide in SNE at 45°N that created a clear asymmetric distribution (S. Figure 5.1). The percentage of pixels of NSE error type was about 7%, and they were mainly distributed at higher latitudes of 45°N and 45°S.

The global $ENQI_{ChenNTL}$ distribution pattern was shown in Figure 5.6(b). Overall, the pixel percentage with the correct type was 63.2% and 9.4% for the error type. Specifically, for error-labeled pixels, the percentage of type SSE was 1.1%, mainly distributed in East Asia, South Asia and Europe; the extent of SNE types was considerably reduced to 0.2% compared to $ENQI_{LiNTL}$. The percentage of NSE pixels was 8.2%, mainly concentrated in the high latitudes of the northern and southern hemispheres, which was similar to

$ENQI_{LiNTL}$. The comparison of $ENQI_{LiNTL}$ and $ENQI_{ChenNTL}$ shows that while LiNTL has slightly more high quality pixels than ChenNTL, ChenNTL also has fewer low quality pixels than LiNTL.

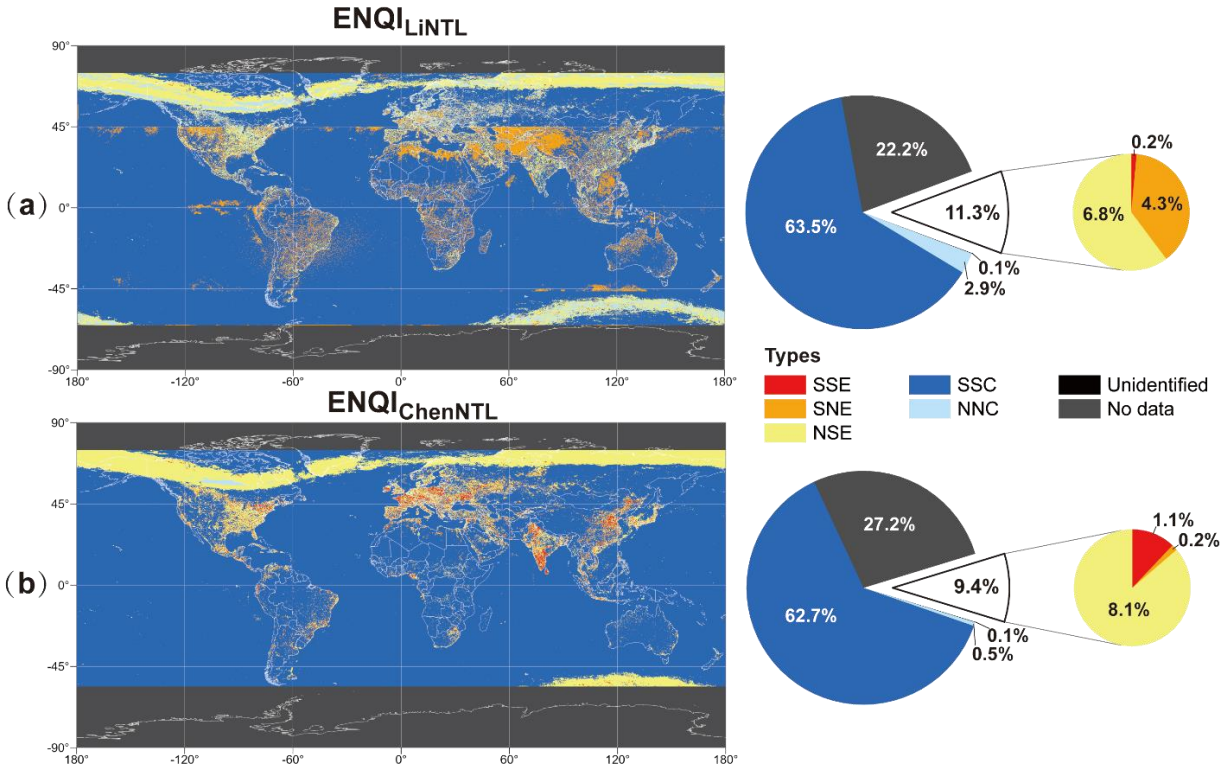

Figure 5.6. Global distribution of $ENQI_{LiNTL}$ and $ENQI_{ChenNTL}$ and their type percentages.

5.6 Discussion

5.6.1 Differences between $ENQI_{LiNTL}$ and $ENQI_{ChenNTL}$

As ENTL products, although both LiNTL and ChenNTL provide long-term collections of NTL images, they apply completely opposite "schemes" for image alignment and calibration that result in data quality differences. Therefore, evaluating data quality at the pixel scale for both datasets is crucial before conducting quantitative time-series light radiation dynamics studies.

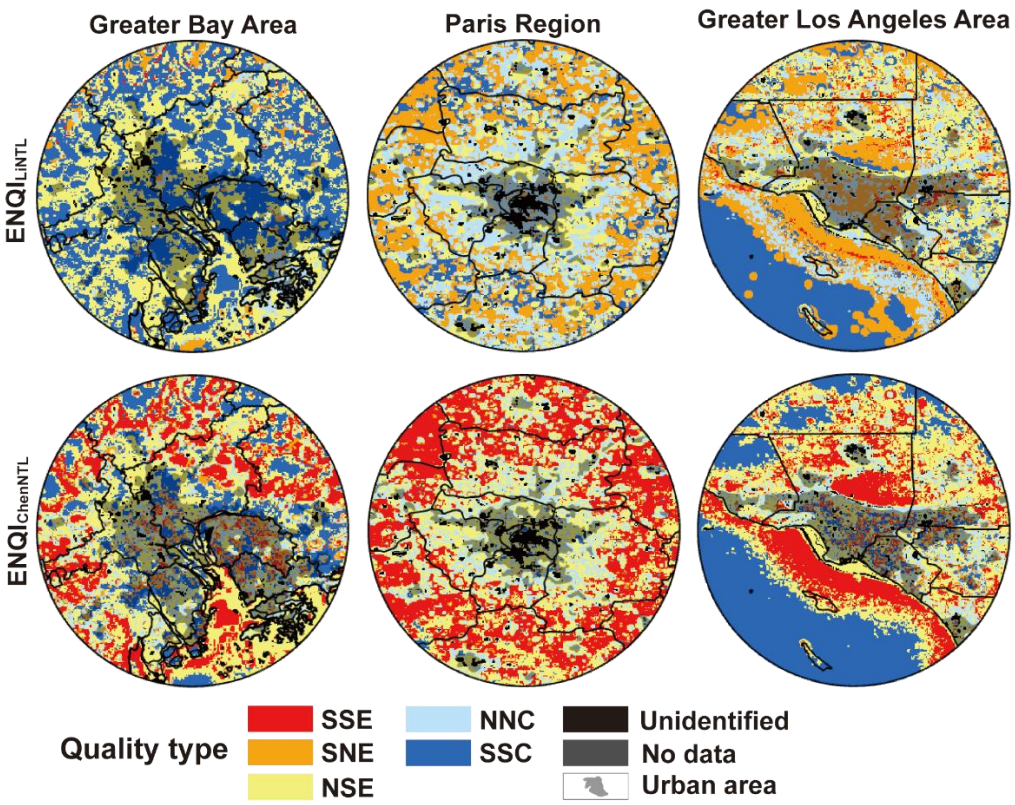

Figure 5.7. $ENQI_{LiNTL}$ and E $ENQI_{ChenNTL}$ for the Greater Bay Area (China), Paris Region (France), and Greater Los Angeles Area (USA).

Firstly, the percentage of pixels marked as errors in $ENQI_{ChenNTL}$ was slightly lower than in $ENQI_{LiNTL}$, which meant ChenNTL pixel quality was better globally, especially for non-urban areas. This can be clearly observed in Figure 5.7. In addition, among the error-marked pixels, SSE was the most noteworthy error type, as it indicated a significant mismatch between PCI_{LiNTL} ($PCI_{ChenNTL}$) and $PCI_{Standard}$. However, the percentage of SSE error types in $ENQI_{ChenNTL}$ was 1.1%, while it was only 0.2% in $ENQI_{LiNTL}$. Globally, SSE in $ENQI_{ChenNTL}$ was mainly concentrated in the regions of East Asia, South Asia and Europe. Compared with $ENQI_{LiNTL}$, the pattern of SSE pixels in $ENQI_{ChenNTL}$ demonstrated two main characteristics: 1) nearly 99% of the SSE pixels were distributed in suburban areas; 2) about 1% were distributed within the downtown area. By jointly checking $PCI_{ChenNTL}$ and $PCI_{Standard}$ we traced the source of SSE, and the results indicated that SSE in $ENQI_{ChenNTL}$ was mainly derived from the mismatch of significant increased signs in $PCI_{Standard}$ and significant unchanged signs in $PCI_{ChenNTL}$. We speculate that the reason for the percentage gap of SSE in $ENQI_{LiNTL}$ and $ENQI_{ChenNTL}$ was caused by the spatial and radiometric resolution differences between NPP/VIIRS and DMSP/OLS. Due to the improved spatial and radiometric resolution of the VIIRS sensor, the pixel explosion effect (Henderson et al., 2003; Abrahams et al., 2018; Zheng et al., 2020) in VIIRS data was much lighter than in OLS data, especially in suburban areas, which were the most clustered areas of SSE pixels. Furthermore, considering that the $PCI_{Standard}$ we used was generated based on $PCI_{DMSP/OLS}$ from 1992-2013, and ChenNTL only covered DMSP/OLS images after 2000, the amount of light radiation variability marked by $PCI_{ChenNTL}$ would theoretically be less than that of $PCI_{Standard}$. To eliminate the bias caused by differences in temporal cover, we recalculated $PCI_{Standard}$ based on DMSP/OLS from 2000-2013 and recalculated the $ENQI_{ChenNTL}$ (S.

Figure 5.2-5.4). The pixel share of SSE decreased from 1.1% to 0.9%, but the overall distribution was unchanged.

5.6.2 Advantages and potential compared to TSOL

Compared to the continuous developments in alignment or calibration algorithms, the methods for evaluating ENTL calibration performance are lagging behind. Currently, for time-series NTL products, annualized global (regional) TSOL dynamic curves are the most used assessment method. In addition, auxiliary indicators such as GDP are also frequently used to diagnose dynamic anomalies in TSOL, which is a more subjective judgment. To illustrate this bias, we have selected units for comparison at different scales. Figure 5.8 shows the dynamics of the four sets of TSOLs at the national, state provincial and municipal levels. At the national scale, TSOL showed a significant, continuous increase in all four countries with different levels of economic development. At the state and provincial scales, the TSOL curves fluctuated but remained generally increasing. At the city scale, which had the smallest spatial extent, we observed increased fluctuations in the TSOL curves for most. Although the existing ENTL showed a general increasing trend in light radiation on a global scale, anomalies still existed at local scales, which were captured as the observation area decreased. This meant that previous continuity assessments may have concealed data quality issues. The scheme proposed in this paper essentially sets the observation area at the pixel scale (S. Figure 5.5), which was unprecedented and allowed us to explicitly identify the locations where anomalies occurred.

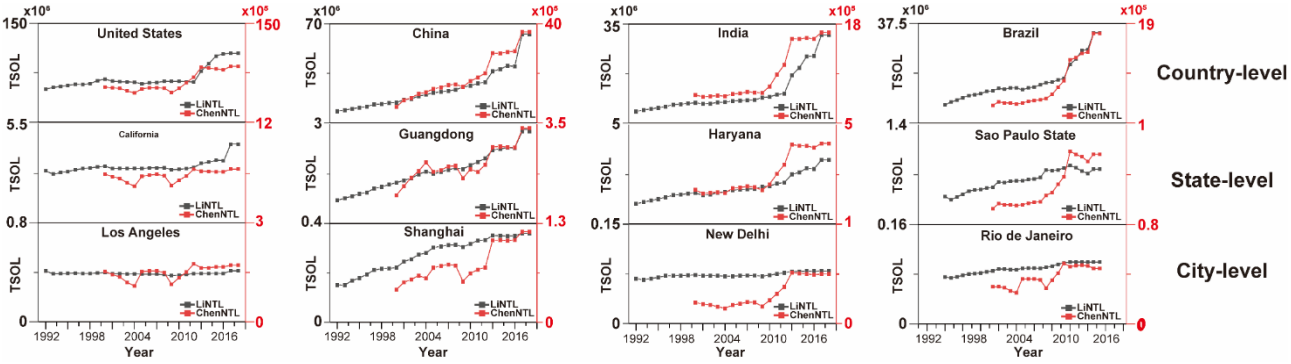

Figure 5.8. National, provincial and city-scale TSOL dynamic curves in LiNTL and ChenNTL.

Moreover, the $PCI_{Standard}$, used as a light radiation dynamics standard to identify continuity errors in ENTL in this paper, was also a good data source for global urbanization analysis. ENTL is an important dataset for long-term urbanization monitoring, but as our test results showed, both the most widely used LiNTL and ChenNTL suffered from pixel-scale continuity anomalies (especially SSE-type errors) that negatively impact urbanization studies. However, $PCI_{Standard}$ uses robust Theil-Sen Median trend analysis and Mann-Kendall testing to label light variation features based on DMSP/OLS and NPP/VIIRS datasets, providing dynamic light radiation results without continuous anomalies. For example, Figure 5.9 shows the sum of significantly increased and significantly decreased light radiation pixels in $PCI_{Standard}$ of different countries worldwide to assess the urbanization, anti-urbanization intensity. China and India had the highest number of significantly increased light pixels during the last 27 years, while the United States, Russia and

Ukraine recorded a considerable number of decreased light pixels.

Compared with existing ENTL continuity detection schemes such as TSOL, the proposed method in this paper achieved pixel-scale ENTL continuity identification. However, the scheme still has some shortcomings that deserve further advancement. First, as illustrated in Figure 5.2, some pixels were identified as significantly decreased (increased) in $PCI_{DMSP/OLS}$ and as significantly increased (decreased) in $PCI_{NPP/VIIRS}$. This means that pixels changed during the former phase in the exact opposite way to the latter phase, which made it impossible to directly identify the pixel's change type in $PCI_{Standard}$. Nevertheless, because the number of pixels that coincided with significant opposite changes was only 0.05%, it was acceptable to apply it to the existing ENTL quality identification. We will introduce additional metrics to support the identification the true variation of these pixels in future studies. Second, the spatial resolutions did not match. Because $PCI_{Standard}$ was created based on $PCI_{DMSP/OLS}$, its spatial resolution was limited to 30 arc seconds by the "barrel principle". However, through deep learning models, Chen et al. (2021b) generated the VIIRS-liked NTL dataset, which allowed ChenNTL to achieve a spatial resolution of 15 arc seconds. Therefore, the layers of $ENQI_{ChenNTL}$ generated in this paper were limited by the resolution of the $PCI_{Standard}$ and could be misidentified. Given that light radiation variability at the surface usually does not involve only individual pixels, the misidentification risk was acceptable, especially when compared to the original TSOL scheme.

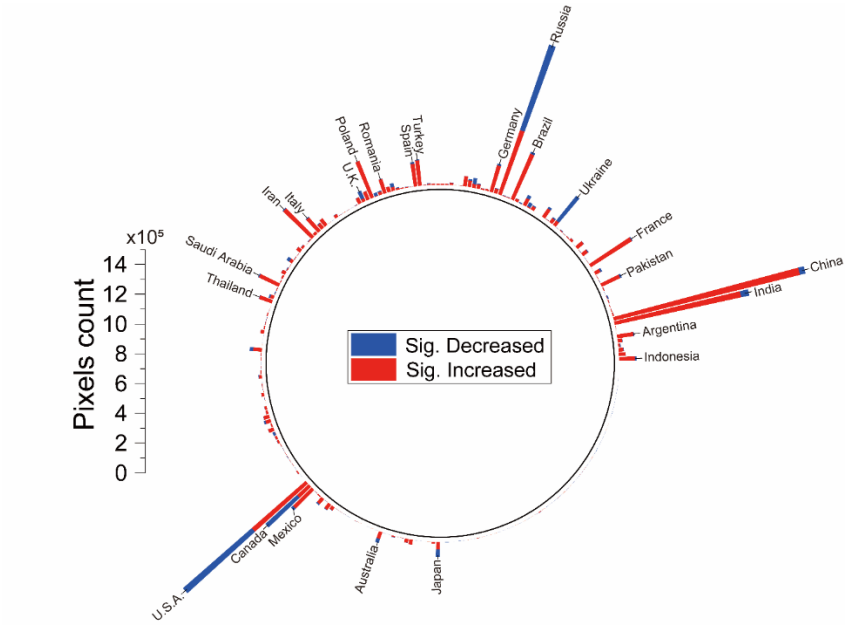

Figure 5.9. Significantly increased and decreased pixels of light radiation in each country of the world during 1992-2018.

5.7 Conclusion

Given the potential for night light remote sensing in tracking urbanization development and inversion of socio-economic parameters, abundant research based on NTL is being promoted. The integration of two heterogeneous sources, DMSP/OLS and NPP/VIIRS, has become an attractive way to carry out long-term global light radiation dynamics analysis. Although methods for aligning (calibrating) these two NTL data

sources continue to be proposed, methods for assessing the continuity quality of calibrated pixels are lacking. To address this challenge, we developed a pixel-level ENTL continuity quality identification scheme. Robust Theil-Sen Median trend analysis and Mann-Kendall testing were used to identify light change characteristics of global light pixels from 1992-2013 and 2013-2018, and a joint logistic judgment was used to generate a $PCI_{Standard}$ for light radiation change from 1992-2018 and assess the quality of the two most widely used ENTL products. The results showed that 1) LiNTL had 11.3% of error pixels, mainly type SNE, and only 0.2% of SSE; 2) ChenNTL had a slightly lower percentage of error pixels at 9.4%, but 0.9% were of SSE type, mainly concentrated in suburban areas. In addition, the $PCI_{Standard}$ was generated for a specific time period. The robust pixel increase or decrease can also be used for urbanization or anti-urbanization intensity analysis. In addition, we generated open-source PCI identification layers and ENQI results related to this paper, which will greatly facilitate their use in other studies (https://doi.org/10.6084/m9.figshare.14915268.v1).

Acknowledgment: The LiNTL image collection was downloaded from Figshare (https://doi.org/10.6084/m9.figshare.9828827) and ChenNTL image collection was downloaded from the Harvard Dataverse (https://doi.org/10.7910/DVN/YGIVCD). The authors thank them for their efforts in open-source data and knowledge sharing. Also, the authors would like to thank the anonymous reviewers and the editor for their constructive comments and suggestions.

References

Abrahams, A., Oram, C. & Lozano-Gracia, N. (2018) Deblurring DMSP nighttime lights: A new method using Gaussian filters and frequencies of illumination. Remote Sensing of Environment 210, 242-258.

Cao, C., Shao, X. & Uprety, S. (2013) Detecting light outages after severe storms using the S-NPP/VIIRS day/night band radiances. IEEE Geoscience and Remote Sensing Letters 10, 1582-1586.

Cao, X., Wang, J., Chen, J. & Shi, F. (2014) Spatialization of electricity consumption of China using saturation-corrected DMSP-OLS data. International Journal of Applied Earth Observation and Geoinformation 28, 193-200.

Chen, H., Wu, B., Yu, B., Chen, Z., Wu, Q., Lian, T., . . . Wu, J. (2021a) A New Method for Building-Level Population Estimation by Integrating LiDAR, Nighttime Light, and POI Data. Journal of Remote Sensing 2021.

Chen, Z., Yu, B., Yang, C., Zhou, Y., Yao, S., Qian, X., . . . Wu, J. (2021b) An extended time series (2000–2018) of global NPP-VIIRS-like nighttime light data from a cross-sensor calibration. Earth System Science Data 13, 889-906.

Du, X., Shen, L., Wong, S.W., Meng, C. & Yang, Z. (2021) Night-time light data based decoupling relationship analysis between economic growth and carbon emission in 289 Chinese cities. Sustainable cities and society 73, 103119.

Fensholt, R. & Proud, S.R. (2012) Evaluation of earth observation based global long term vegetation trends—Comparing GIMMS and MODIS global NDVI time series. Remote Sensing of Environment 119, 131-147.

Ghosh, T., Elvidge, C.D., Hsu, F.-C., Zhizhin, M. & Bazilian, M. (2020) The dimming of lights in india during the covid-19 pandemic. Remote Sensing 12, 3289.

Henderson, M., Yeh, E.T., Gong, P., Elvidge, C. & Baugh, K. (2003) Validation of urban boundaries derived from global night-time satellite imagery. International journal of remote sensing 24, 595-609.

Ji, G., Tian, L., Zhao, J., Yue, Y. & Wang, Z. (2019) Detecting spatiotemporal dynamics of PM2. 5 emission data in China using DMSP-OLS nighttime stable light data. Journal of Cleaner Production 209, 363-370.

Jiang, W., He, G., Long, T., Wang, C., Ni, Y. & Ma, R. (2017) Assessing light pollution in China based on nighttime light imagery. Remote Sensing 9, 135.

Jiang, W., Yuan, L., Wang, W., Cao, R., Zhang, Y. & Shen, W. (2015) Spatio-temporal analysis of vegetation variation in the Yellow River Basin. Ecological Indicators 51, 117-126.

Klomp, J. (2016) Economic development and natural disasters: A satellite data analysis. Global Environmental Change 36, 67-88.

Levin, N., Kyba, C.C., Zhang, Q., de Miguel, A.S., Román, M.O., Li, X., . . . Miller, S.D. (2020) Remote sensing of night lights: A review and an outlook for the future. Remote Sensing of Environment 237, 111443.

Li, R., Liu, X. & Li, X. (2015) Estimation of the PM2. 5 pollution levels in Beijing based on nighttime light data from the defense meteorological satellite program-operational linescan system. Atmosphere 6, 607-622.

Li, S., Sun, D., Goldberg, M.D., Sjoberg, B., Santek, D., Hoffman, J.P., . . . Holloway, E. (2018a) Automatic near real-time flood detection using Suomi-NPP/VIIRS data. Remote Sensing of Environment 204, 672-689.

Li, X., Li, D., Xu, H. & Wu, C. (2017) Intercalibration between DMSP/OLS and VIIRS night-time light images to evaluate city light dynamics of Syria's major human settlement during Syrian Civil War. International journal of remote sensing 38, 5934-5951.

Li, X., Liu, S., Jendryke, M., Li, D. & Wu, C. (2018b) Night-time light dynamics during the iraqi civil war. Remote Sensing 10, 858.

Li, X., Zhao, L., Li, D. & Xu, H. (2018c) Mapping urban extent using Luojia 1-01 nighttime light imagery. Sensors 18, 3665.

Li, X. & Zhou, Y. (2017) A stepwise calibration of global DMSP/OLS stable nighttime light data (1992–2013). Remote Sensing 9, 637.

Li, X., Zhou, Y., Zhao, M. & Zhao, X. (2020) A harmonized global nighttime light dataset 1992–2018. Scientific data 7,

1-9.

Li, Y., Ye, H., Gao, X., Sun, D., Li, Z., Zhang, N., . . . Zheng, J. (2021) Spatiotemporal Patterns of Urbanization in the Three Most Developed Urban Agglomerations in China Based on Continuous Nighttime Light Data (2000–2018). Remote Sensing 13, 2245.

Lian, X., Jiao, L., Zhong, J., Jia, Q., Liu, J. & Liu, Z. (2021) Artificial light pollution inhibits plant phenology advance induced by climate warming. Environmental Pollution 291, 118110.

Lyu, H., Lu, H., Mou, L., Li, W., Wright, J., Li, X., . . . Yu, L. (2018) Long-term annual mapping of four cities on different continents by applying a deep information learning method to landsat data. Remote Sensing 10, 471.

Ma, J., Guo, J., Ahmad, S., Li, Z. & Hong, J. (2020) Constructing a new inter-calibration method for DMSP-OLS and NPP-VIIRS nighttime light. Remote Sensing 12, 937.

Mammides, C. (2020) A global assessment of the human pressure on the world's lakes. Global Environmental Change 63, 102084.

Narayanan, P., Sarkar, S., Basistha, A. & Sachdeva, K. (2016) Trend analysis and forecast of pre-monsoon rainfall over India. Weather 71, 94-99.

Panwar, M., Agarwal, A. & Devadas, V. (2018) Analyzing land surface temperature trends using non-parametric approach: A case of Delhi, India. Urban Climate 24, 19-25.

Román, M.O., Stokes, E.C., Shrestha, R., Wang, Z., Schultz, L., Carlo, E.A.S., . . . Kalb, V. (2019) Satellite-based assessment of electricity restoration efforts in Puerto Rico after Hurricane Maria. PloS one 14, e0218883.

Sahoo, S., Gupta, P.K. & Srivastav, S. (2020) Inter-calibration of DMSP-OLS and SNPP-VIIRS-DNB annual nighttime light composites using machine learning. GIScience & Remote Sensing 57, 1144-1165.

Shi, K., Yang, Q., Fang, G., Yu, B., Chen, Z., Yang, C. & Wu, J. (2019) Evaluating spatiotemporal patterns of urban electricity consumption within different spatial boundaries: A case study of Chongqing, China. Energy 167, 641-653.

Stokes, E.C. & Seto, K.C. (2019) Characterizing urban infrastructural transitions for the Sustainable Development Goals using multi-temporal land, population, and nighttime light data. Remote Sensing of Environment 234, 111430.

Wu, K. & Wang, X. (2019) Aligning pixel values of DMSP and VIIRS nighttime light images to evaluate urban dynamics. Remote Sensing 11, 1463.

Xu, D., Yang, F., Yu, L., Zhou, Y., Li, H., Ma, J., . . . Zhang, C. (2021) Quantization of the coupling mechanism between eco-environmental quality and urbanization from multisource remote sensing data. Journal of Cleaner Production 321, 128948.

Xu, P., Wang, Q., Jin, J. & Jin, P. (2019) An increase in nighttime light detected for protected areas in mainland China based on VIIRS DNB data. Ecological Indicators 107, 105615.

Yang, Z., Chen, Y., Guo, G., Zheng, Z. & Wu, Z. (2021) Using nighttime light data to identify the structure of polycentric cities and evaluate urban centers. Science of the Total Environment 780, 146586.

Yin, R., He, G., Jiang, W., Peng, Y., Zhang, Z., Li, M. & Gong, C. (2021) Night-Time Light Imagery Reveals China's City Activity During the COVID-19 Pandemic Period in Early 2020. IEEE Journal of Selected Topics in Applied Earth Observations and Remote Sensing 14, 5111-5122.

Yu, B., Lian, T., Huang, Y., Yao, S., Ye, X., Chen, Z., . . . Wu, J. (2019) Integration of nighttime light remote sensing images and taxi GPS tracking data for population surface enhancement. International Journal of Geographical Information Science 33, 687-706.

Zhang, Q., Pandey, B. & Seto, K.C. (2016) A robust method to generate a consistent time series from DMSP/OLS nighttime light data. IEEE Transactions on Geoscience and Remote Sensing 54, 5821-5831.

Zhang, Q. & Seto, K.C. (2011) Mapping urbanization dynamics at regional and global scales using multi-temporal DMSP/OLS nighttime light data. Remote Sensing of Environment 115, 2320-2329.

Zhao, M., Zhou, Y., Li, X., Cheng, W., Zhou, C., Ma, T., . . . Huang, K. (2020) Mapping urban dynamics (1992–2018) in Southeast Asia using consistent nighttime light data from DMSP and VIIRS. Remote Sensing of Environment 248,

111980.

Zhao, X., Yu, B., Liu, Y., Yao, S., Lian, T., Chen, L., . . . Wu, J. (2018) NPP-VIIRS DNB daily data in natural disaster assessment: Evidence from selected case studies. Remote Sensing 10, 1526.

Zheng, Q., Weng, Q. & Wang, K. (2019a) Developing a new cross-sensor calibration model for DMSP-OLS and Suomi-NPP VIIRS night-light imageries. ISPRS Journal of Photogrammetry and Remote Sensing 153, 36-47.

Zheng, Q., Weng, Q. & Wang, K. (2020) Correcting the Pixel Blooming Effect (PiBE) of DMSP-OLS nighttime light imagery. Remote Sensing of Environment 240, 111707.

Zheng, Z., Wu, Z., Chen, Y., Guo, G., Cao, Z., Yang, Z. & Marinello, F. (2021) Africa's protected areas are brightening at night: A long-term light pollution monitor based on nighttime light imagery. Global Environmental Change 69, 102318.

Zheng, Z., Yang, Z., Chen, Y., Wu, Z. & Marinello, F. (2019b) The Interannual Calibration and Global Nighttime Light Fluctuation Assessment Based on Pixel-Level Linear Regression Analysis. Remote Sensing 11, 2185.

Zhong, L., Liu, X. & Ao, J. (2022) Spatiotemporal dynamics evaluation of pixel-level gross domestic product, electric power consumption, and carbon emissions in countries along the belt and road. Energy 239, 121841.

Zhuo, L., Zheng, J., Zhang, X., Li, J. & Liu, L. (2015) An improved method of night-time light saturation reduction based on EVI. International journal of remote sensing 36, 4114-4130.

Supplementary files

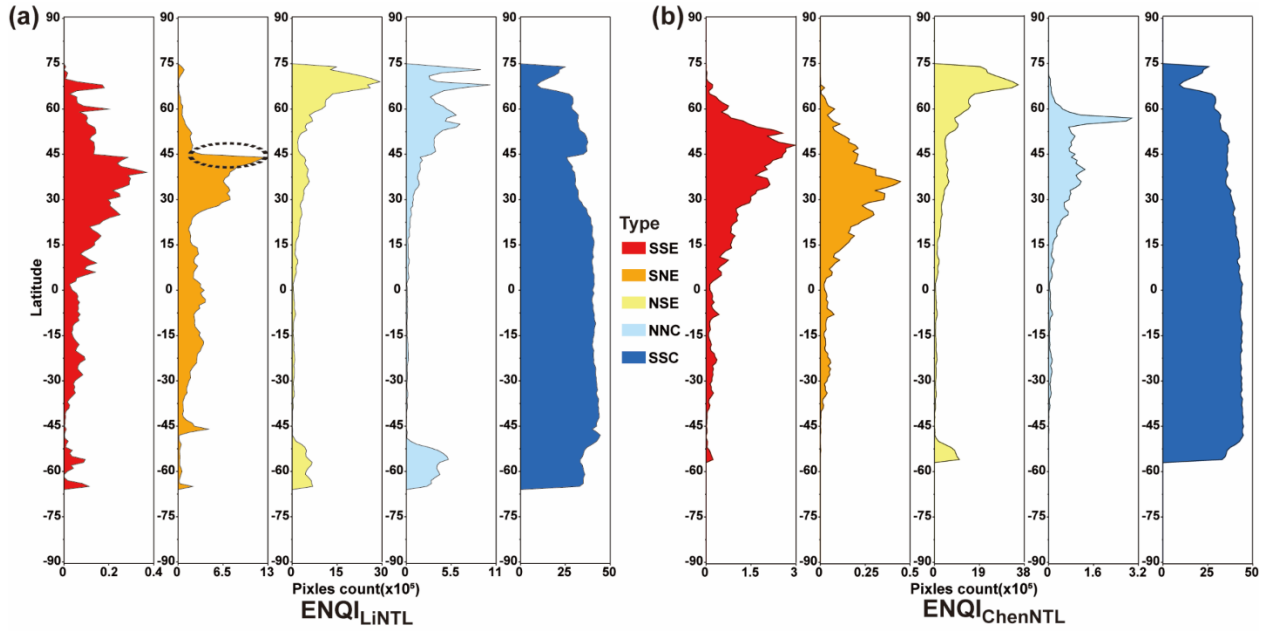

S. Figure 5.1. (a) The $ENQI_{LiNTL}$ pixel histogram along the latitude direction. (b) The $ENQI_{ChenNTL}$ pixel histogram along the latitude direction. The black dashed line highlights the amount surging in SNE-type pixels at 45°N.

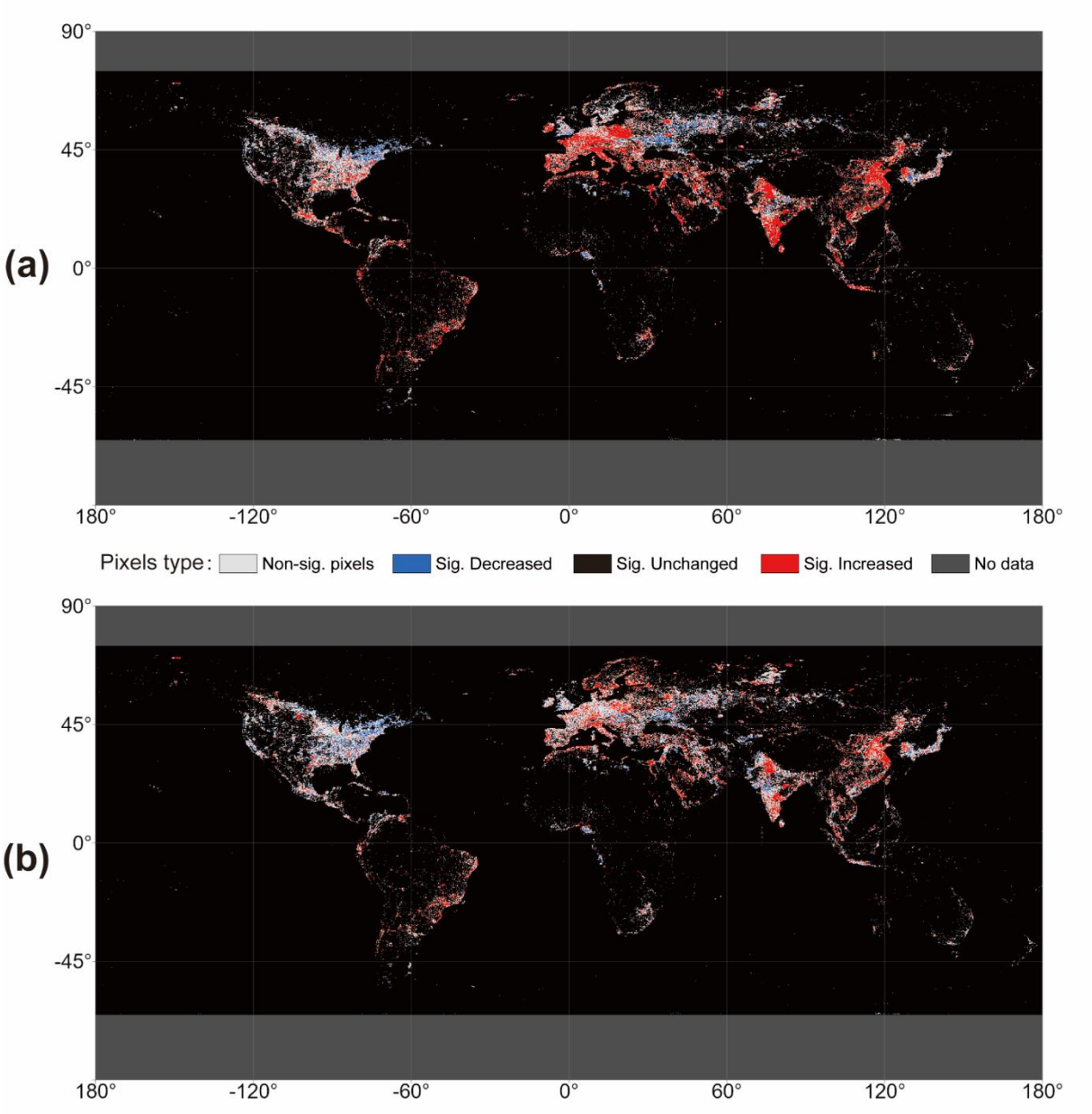

S. Figure 5.2. (a) The $PCI_{DMSP/OLS}$ layer calculated from the DMSP/OLS NTL collection over the period 1992-2013. (b) The $PCI_{DMSP/OLS}$ layer calculated from the DMSP/OLS NTL collection over the period 2000-2013.

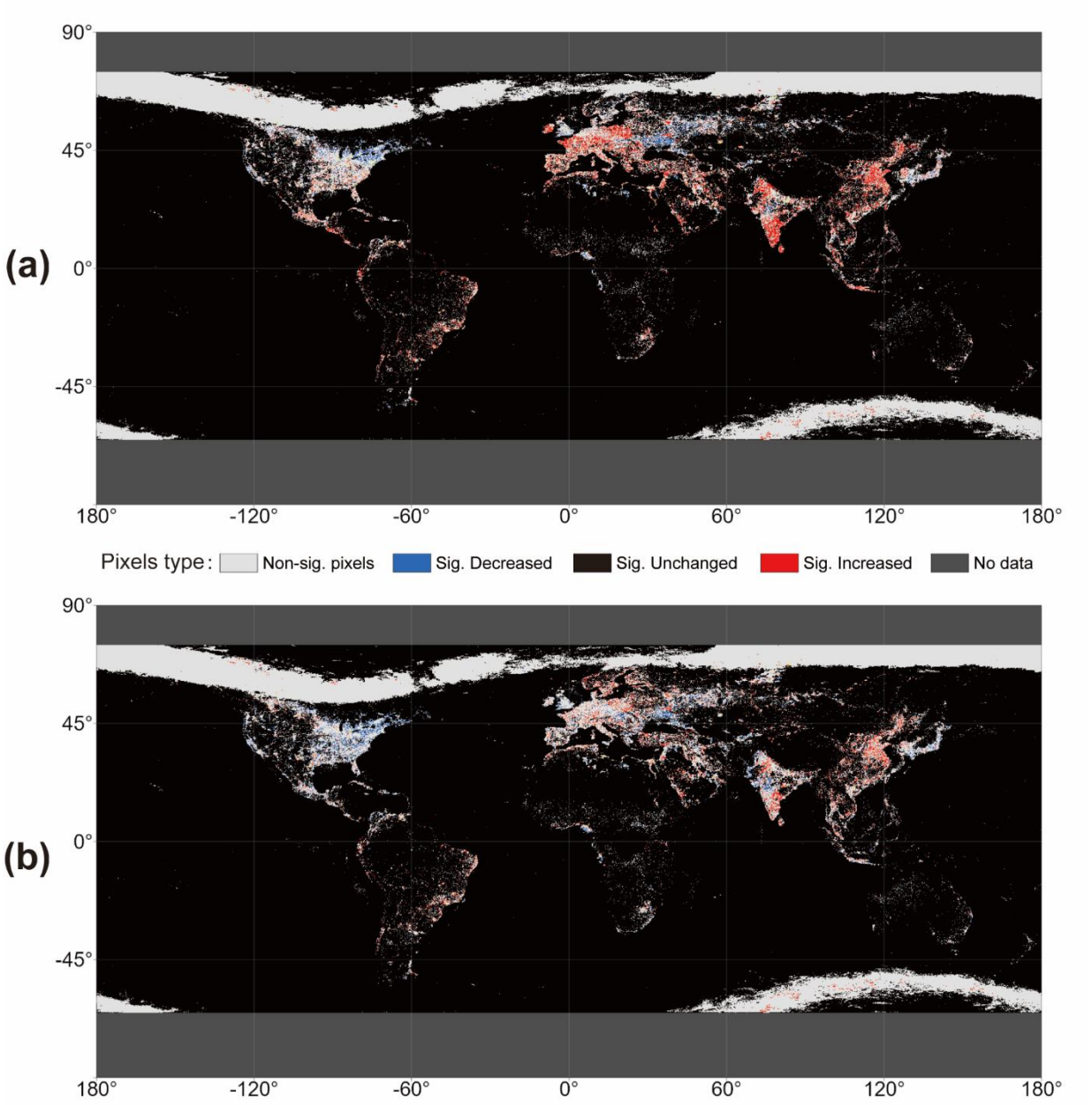

S. Figure 5.3. (a) The $PCI_{Standard}$ layer derived from on $PCI_{DMSP/OLS}$ for the period 1992-2013 and $PCI_{NPP/VIIRS}$ for the period 2013-2018. (b) The $PCI_{Standard}$ layer derived from on $PCI_{DMSP/OLS}$ for the period 2000-2013 and $PCI_{NPP/VIIRS}$ for the period 2013-2018.

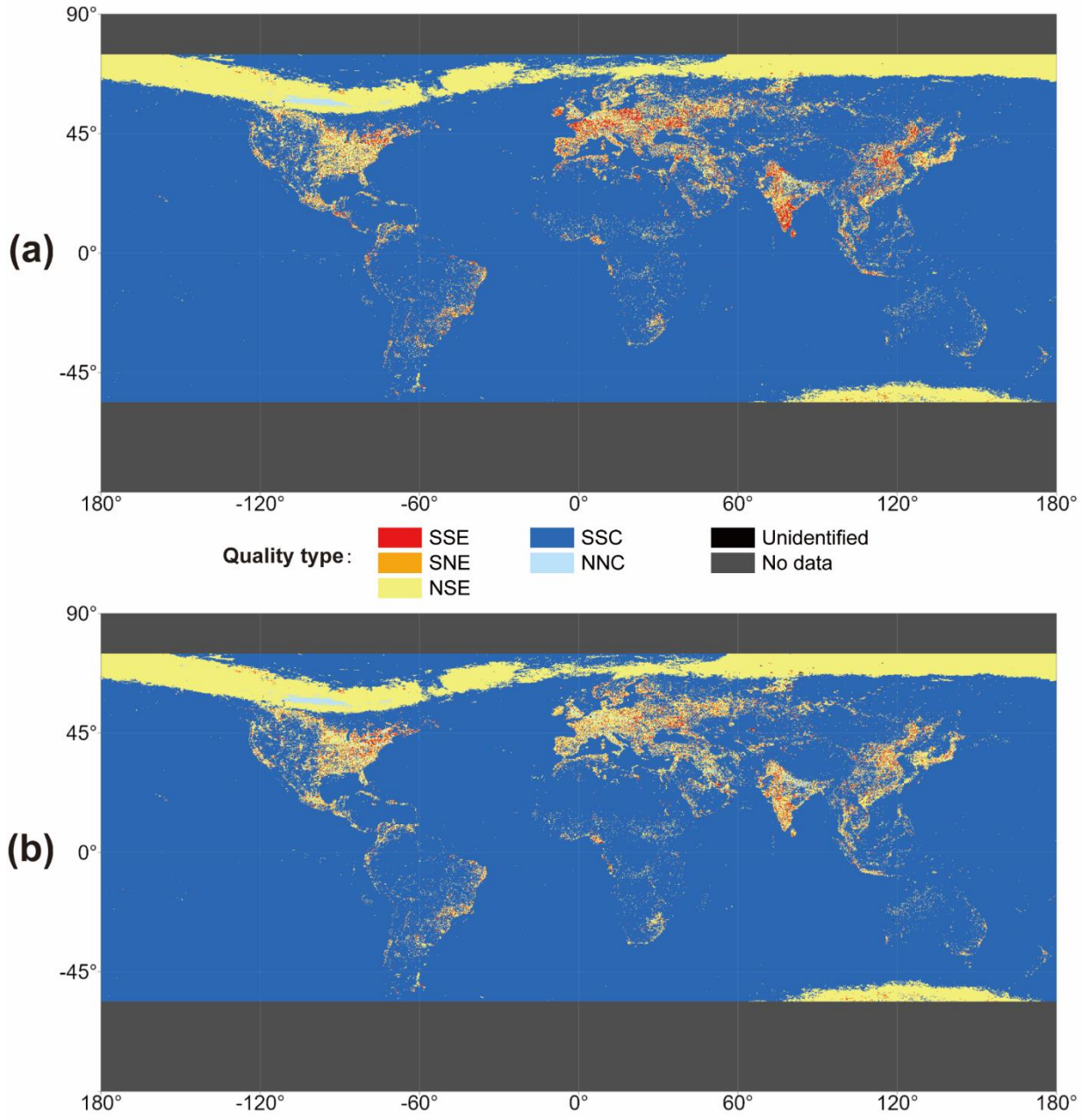

S. Figure 5.4. (a) The quality identification layer $ENQI_{ChenNTL}$ based on $PCI_{Standard}$ during 1992-2018. (b) The quality identification layer $ENQI_{ChenNTL}$ based on $PCI_{Standard}$ during 2000-2018.

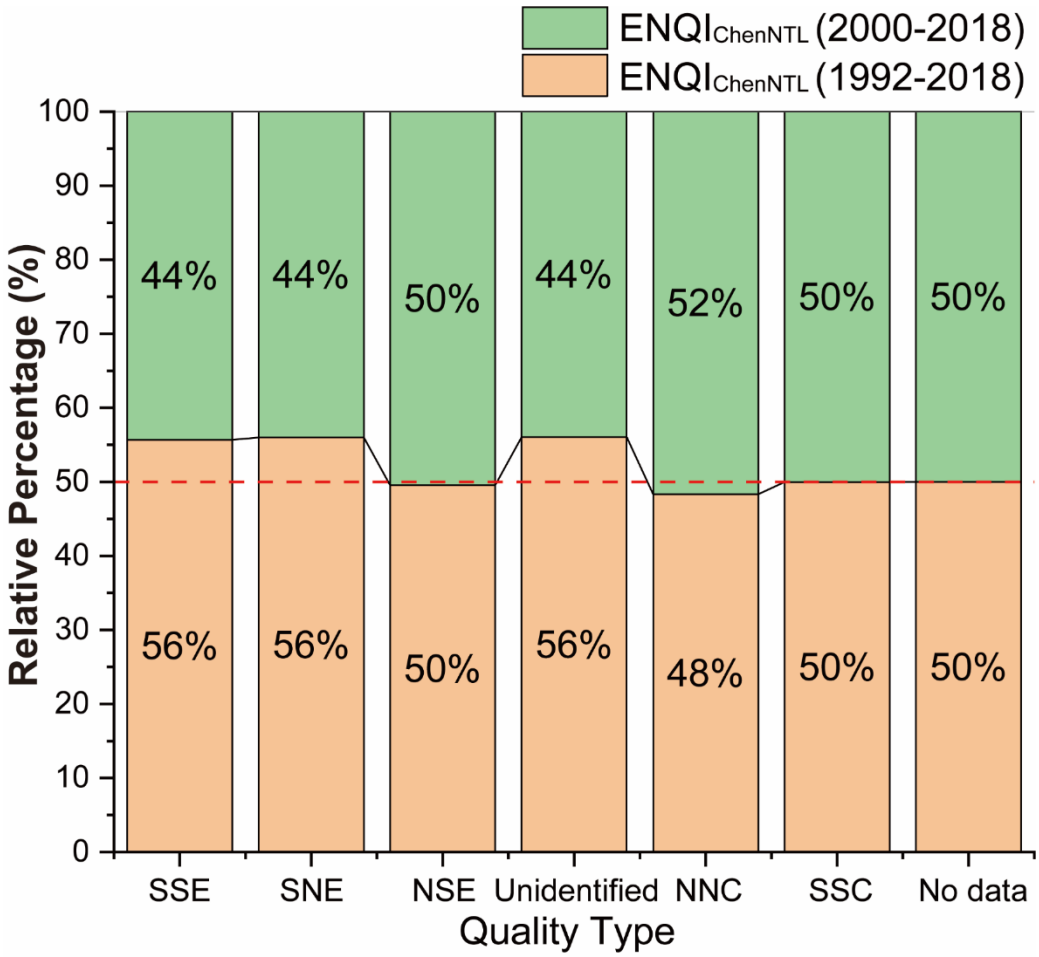

S. Figure 5.5. Comparison of the relative percentage of pixels for each quality identification type. $ENQI_{ChenNTL}$ (1992-2018) indicates that ENQI was performed based on the $PCI_{Standard}$ during 1992-2018, while $ENQI_{ChenNTL}$ (2000-2018) is based on the $PCI_{Standard}$ during 2000-2018. It can be found that the pixel quantity of SSE, SIE and Unidentified have all decreased in the updated $ENQI_{ChenNTL}$.

6. Africa's protected areas are brightening at night: a long-term light pollution monitor based on nighttime light imagery [5]

6.1 Abstract

As the cornerstone of biodiversity conservation, the core value of protected areas (PAs) is to maintain an area's natural conditions (both day and night) and to restrict human-caused disturbances to biology and the environment. Although the value of PAs has been universally recognized, light pollution within them is worsening as a result of the widespread use of artificial illumination devices. Previous studies have focused on light pollution in PAs and evaluated light radiation using nighttime light imagery. However, given the scale and span of these studies (national scale and over short periods), PA light pollution research should be advanced further. In this paper, we conducted long-term (1992-2018) monitoring and evaluation of light pollution in African PAs using aligned multi-sensor NTL data. The results showed that **1)** Africa PAs were impacted by increasingly severe artificial lights during 1992-2018, with all three light indices showing an accelerating increasing trend. **2)** The number of light-polluted PAs also rapidly increased, with more than 80% of PAs experiencing aggravated light pollution as of 2018. **3)** Different types of PAs had heterogeneous light pollution, which penetrates indiscriminately into all PA regulation levels. **4)** Light pollution in African PAs was divided into three types, including outside invasion, internal sources, and mixed pollution. **5)** Human activity intensity surrounding the PAs was highly correlated with light pollution within them, with a maximum effect distance of approximately 245 km. This paper provides new approaches for understanding the patterns of light pollution within PAs, and is a valuable reference for future PA planning.

Keywords: protected areas; light pollution; nighttime light; Africa; human activities

6.2 Introduction

Since 2015, countries around the world have made progress in promoting global ecological governance but are still far from the climate change reduction and sustainable development goals set out in the Paris Agreement. In particular, global wildlife populations have declined by about 68% due to population expansion, consumption growth, and agricultural reclamation, and there are deep threats and challenges to ecosystem diversity (Almond et al., 2020). As a positive response to the ecological crisis, the establishment of protected areas (PAs) of various types is a globally recognized conservation strategy that plays a fundamental role in biodiversity and species conservation (Joppa et al., 2008; Watson et al., 2018). PAs are set aside by protocol for special protection and management, such as land or maritime spaces that are representative natural ecosystems, have natural concentrations of rare and endangered species of wild animals and plants, and are

[5] This Chapter relies on the paper "Zheng, Z., Wu, Z., Chen, Y., Guo, G., Cao, Z., Yang, Z., & Marinello, F. (2021). Africa's protected areas are brightening at night: A long-term light pollution monitor based on nighttime light imagery. Global Environmental Change, 69, 102318.". https://doi.org/10.1016/j.gloenvcha.2021.102318.

natural heritage features of special value (Zhu et al., 2018). Currently, more than 260,000 PAs have been established globally, covering about 15.4% of the Earth's surface area, but this still falls short of the Aichi Biodiversity Targets, which require that at least 17% of the world's land and 10% of the world's oceans be included in PA systems (Cao et al., 2019; Buchanan et al., 2020).

As the cornerstone of biodiversity conservation, the core value of PAs is the maintenance of natural conditions within the area (both day and night) and to prevent and mitigate potential biological and environmental disturbances caused by human activities (Green et al., 2019). Although PA value has been recognized and their numbers are increasing worldwide, these areas still suffer from human interference, including settlement, education, resource development, and tourism activities. It has been reported that globally, more than 6,000,000 km^2 of PAs are exposed to intense human pressures, and more than 50% of PAs have experienced increased human pressures (Jones et al., 2018). Of these disturbances, severe nighttime light pollution has far-reaching biological impacts on species and the ecology, leading to increased attention to the ecological impacts of nighttime light in PAs (Aubrecht et al., 2008; Gaston et al., 2013).

In recent decades, urbanization, population growth, and economic development have led to a rapid and sustained increase in the density and extent of artificial lighting, which has shaped a new global nighttime light environment. The widespread use of artificial light at night has greatly improved human quality of life but also disrupts the natural cycle of light and darkness, which can be regarded as an environmental pressure (Longcore and Rich, 2004; Frank et al., 2006; Navara and Nelson, 2007; Perkin et al., 2011; Mammides, 2020). Ecology and species diversity threats from nighttime light pollution, especially in PAs, are broadly twofold: 1) nighttime lighting affects the abundance, distribution, and ecosystem function of photosensitive species, threatening biodiversity and accelerating species extinction (Aubrecht et al., 2010); 2) nighttime lighting in PAs is typically a sign of greater human activity, which poses a direct threat to the ecological balance and biodiversity (Xiang and Tan, 2017). Therefore, accurate information on the current and historical spatial distribution and intensity of artificial light in PAs is essential for monitoring human activities, assessing the impacts of anthropogenic lighting, and maintaining PA ecology.

Remote sensing, which has the advantages of rapid, macroscopic, and repeatable observations, has become an important technology for PA monitoring and assessments and is widely used worldwide (Dimobe et al., 2017; Green et al., 2019; Riggio et al., 2019; Akodéwou et al., 2020; Zhang et al., 2020). Night light (NTL) remote sensing has been used by scholars to monitor the intensity of human activities and light pollution in PAs because it can directly capture the distribution and intensity of surface artificial light sources on a global scale. Compared to traditional field survey methods, monitoring schemes based on nighttime light remote sensing allow for the quantitative assessment of light pollution and human activities in PAs without “contact” to ecologically sensitive areas (Yang and Xu, 2019). For example, the human stress (footprint) index commonly used by scholars to assess the intensity of anthropogenic disturbance within PAs references lighting data for selected years (Geldmann et al., 2014; Venter et al., 2016; Jones et al., 2018). For time-series monitoring of human activities in PAs, Xiang and Tan (2017) and Shi et al. (2018) used the Defense

Meteorological Satellite Program/Operational Linescan System (DMSP/OLS) NTL data to conduct temporal and spatial analyses of light pollution in China's PAs between 1992 and 2012. Xu et al. (2019) used data from a new Visible Infrared Imaging Radiometer Suite Day/Night band (VIIRS/DNB) source to detect NTL disturbance in PAs on mainland China.

In fact, the current widely used and easily accessible NTL products mainly include DMSP/OLS stable light data and NPP/VIIRS cloud-free monthly average composite data, which together comprise NTL observations over a long-time span (1992-present). These previous studies confirmed the potential of NTL data (DMSP/OLS and NPP/VIIRS) for monitoring light pollution in PAs, but to our knowledge, no prior work has joined multi-source NTL data to enable longer time span assessments. Therefore, in this paper, we focused on PAs in the African continent and conducted long-term monitoring and evaluation of light pollution in PAs using aligned multi-sensor NTL data.

6.3 Materials and methods

6.3.1 Study area

The African continent covers an area of about 30 million square kilometers (excluding nearby islands), accounting for about 20.2% of the world's total land area, making it the second largest continent in the world after Asia. Meanwhile, Africa is the second most populous continent (1.2 billion) and has an average annual population growth rate of 2.3%. The vast African continent also has a dense concentration of PAs: according to the World Database on Protected Areas (WDPA), there are currently 8,448 PAs in Africa, of which 14.23% and 12.23% are terrestrial and marine, respectively. Considering the size and type of PAs, a total of 2984 PAs, including national, regional, and international designations, were selected in this paper with reference to Xu et al. (2019), as listed in Table 6.1.

Table 6.1. Properties of African PAs selected in this paper.

PA Type	IUCN Categories	Count	Area (km^2)
Biosphere Reserve	I_a, II, IV, Not Applicable, Not Reported	44	405,645
Forest Reserve	I_b, II, III, IV, V, VI, Not Applicable, Not Assigned, Not Reported	1766	318,952
National Park	I_b, II, IV, V, VI, Not Assigned, Not Reported	251	725,835
Natural Reserve	I_a, I_b, II, IV, V, VI, Not Assigned, Not Reported	549	190,778
Scenic Site	Not Reported	37	5,237
Wetland Reserve	II, IV, V, VI, Not Reported	203	534,849
Wildlife Reserve	II, III, IV, VI, Not Assigned, Not Reported	92	294,681
World Heritage Site	II, Not Applicable, Not Reported	42	407,758
Total	I_a, I_b, II, III, IV, V, VI, Not Applicable, Not Assigned, Not Reported	2984	2,883,735

*PAs = Protected Areas; IUCN = International Union for Conservation of Nature.

The selected PAs covered all PA types in the IUCN classification system and had a combined area of about 2,880,000 km^2, which is about 10% of the total area of the African continent. PA vector boundaries were

derived from the updated database released by the WDPA in August 2020, and based on the original data we made topological corrections to ensure that each patch was as complete as possible and free from overlaps, overhanging points, and other errors. Their locations are shown in Figure 6.1.

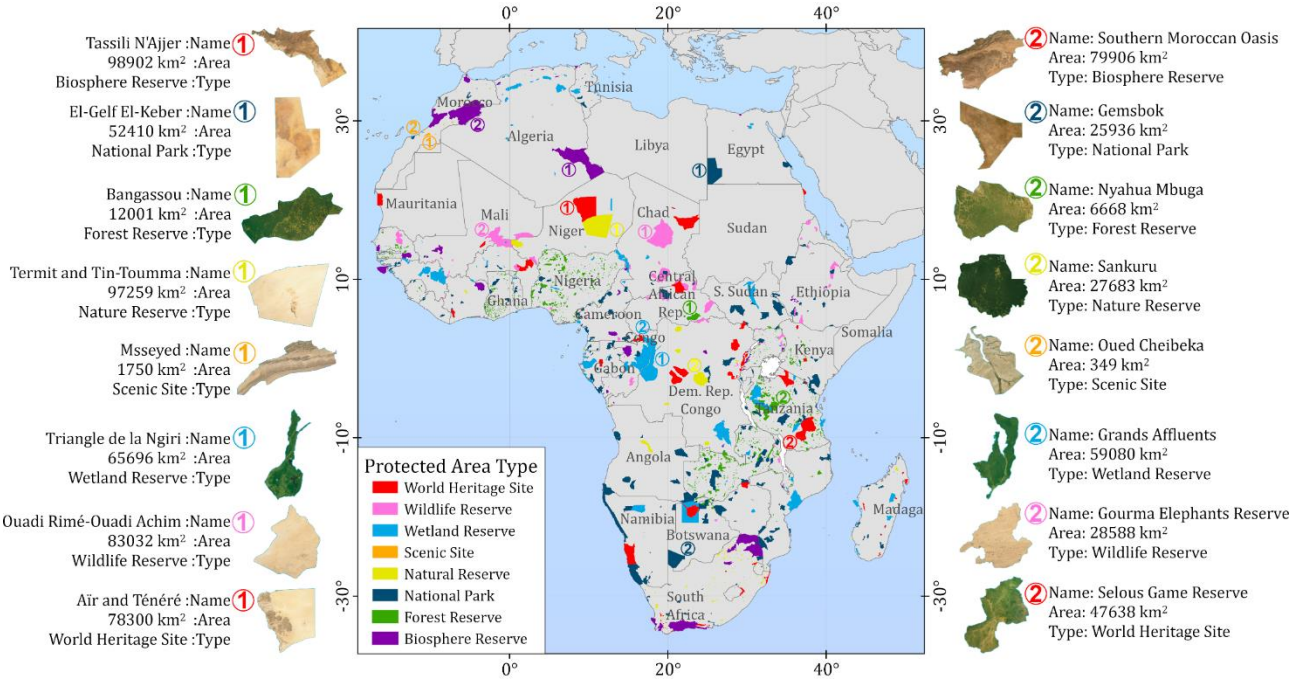

Figure 6.1. PA locations in Africa. The left and right panels show thumbnails and information about the top first and second PA within each type, respectively.

6.3.2 Data sources

As opposed to common daytime optical remote sensing, NTL remote sensing has been widely used for monitoring human activities on the ground by effectively capturing faint light emissions at night, including in: urban sprawl and urbanization studies (He et al., 2006; Lu et al., 2008; Yu et al., 2014), population spatial estimates (Sutton, 1997; Zhuo et al., 2009), the spatialization of economic parameters such as GDP (Sutton and Costanza, 2002; Chen and Nordhaus, 2011), electricity consumption and carbon emissions (Elvidge et al., 1997; Ghosh et al., 2010), and fisheries and oil and gas platform detection (Cho et al., 1999; Waluda et al., 2004). Generally, the most frequent and widely used NTL data used by scholars has included DMSP/OLS and NPP/VIIRS products. DMSP/OLS NTL data provide annual synthetic night lighting products from 1992-2013, while NPP/VIIRS are monthly synthetic lighting products from 2013 to present (Chen et al., 2019). Despite the differences in sensors and calibrations between the two NTL products, numerous studies have revealed the value and possibilities of using joint multi-source NTL data for surface human activity intensity detection (Li et al., 2017; Wu and Wang, 2019). In this paper, NTL data products from DMSP/OLS and NPP/VIIRS were aligned to enable light pollution detection in African PAs from 1992-2018.

Additionally, Sentinel-2 multispectral images were used to investigate the in-situ features of prominent surface light sources, which assisted in classifying the light pollution in Africa's PAs. Detailed parameters of the satellite images are shown in Table 6.2.

Table 6.2. Spatial and temporal resolution parameters of the satellite images.

Satellite	Sensor	Spatial resolution	Temporal resolution	Data available	Access link
DMSP	OLS	30 arc-second (around 1000m)	Annual	1992-2013	https://eogdata.mines.edu/products/dmsp/
NPP	VIIRS	15 arc-second (around 500m)	Monthly	April 2012-Present	https://eogdata.mines.edu/products/vnl/
Sentinel-2	MSI	10 m	5-10 days	June 2015-Present	https://scihub.copernicus.eu/

6.3.3 Methods

(1) Cross-sensor calibration of NTL data

As mentioned earlier, NTL data from DMSP/OLS and NPP/VIIRS differ significantly in terms of temporal coverage and resolution, spatial resolution, radiometric resolution, etc., so pre-processing of the light data is required when they are joined for long-term light pollution studies. In general, the generation of long-term, continuous NTL data includes the following steps: 1) inter-annual calibration of DMPS/OLS data, 2) synthesis of annual VIIRS NTL data, and 3) transformation of VIIRS annual NTL data to align with DMSP/OLS NTL data. Specifically:

a) Inter-annual calibration of DMPS/OLS NTL data. Annual NTL datasets for 1992-2013, published online by the National Geophysical Data Center (NGDC), are provided by six sensors: F10 (1992-1994), F12 (1994-1999), F14 (1997-2003), F15 (2000-2007), F16 (2004-2009), and F18 (2010-2013). Due to performance differences between sensors and the degradation of the sensors themselves, there is a problem of "light drift" in the time-series NTL dataset (Cao et al., 2015). To eliminate the discontinuity between annual NTL images from 1992-2013 and calibrate them, this paper adopted the PBPIF calibration model proposed by Zheng et al. (2019b). This method builds an inter-annual calibration model by automatically detecting the pseudo-invariant feature pixels, which can be efficiently applied to correct large-scale light radiation variability.

b) Synthesis of annual VIIRS NTL data. The monthly "VIIRS Cloud Mask" NTL product from VIIRS eliminates stray light; however, background noise and outliers still need to be removed. In this paper, we used the method of Zhao et al. (2020) to set thresholds for noise filtering and corrected outliers with the scheme proposed by Shi et al. (2014). Moreover, following the approach of Li et al. (2020), annual VIIRS NTL images were synthesized with reference to cloud-free coverage to set weights. Compared with the traditional simple mean composition, the post-weighted synthesis scheme greatly reduced the interference from clouds and solar illumination (Román et al., 2018) and improved data quality.

c) Align VIIRS annual NTL data to DMSP/OLS data. Aligning heterogenous NTL images has been proposed by several studies (Zheng et al., 2019a; Ma et al., 2020; Hu et al., 2021). Because the annual composite VIIRS NTL data had a better resolution than the OLS annual light data, it was more feasible to align the VIIRS NTL images to the OLS NTL images. Hence, the alignment scheme of Zhao et al. (2020) was used

in this paper due to its low input parameters, full-time span, and high robustness. Specifically, the scheme includes three steps: resolution reduction, data structure matching, and automatic pixel alignment. Firstly, the Kernel density (KD) approach was used to transform the resolution from fine to coarse and moderately restore the blurring effect of OLS NTL images. Next, a log-transform was used to aggregate the VIIRS NTL images, as in Eq.6.1. Finally, a sigmoid function was applied to align the log-transformed images to the OLS NTL images, as in Eq.6.2.

$$Log^{Y}_{VIIRS_{KD}} = ln(VIIRS^{Y}_{KD} + 1) \tag{6.1}$$

$$DMSP^{Y}_{liked} = a + b(1/1 + e^{-c(Log^{Y}_{VIIRS_{KD}} - d)}) \tag{6.2}$$

where $VIIRS_{KD}$ is aggregated VIIRS image of year Y; $Log^{Y}_{VIIRS_{KD}}$ is a log transformed image of $VIIRS_{KD}$; $DMSP^{Y}_{liked}$ is the NTL image for year Y after $Log^{Y}_{VIIRS_{KD}}$ aligned; a, b, c, d are constant values of 6.5, 57.4, 1.9, and 10.8, respectively (Li et al., 2020). In addition, to further optimize the interannual light trends, the moving average method was used to eliminate interannual irregular fluctuations in the synthetic light images. Specifically, this paper used a three-year time window to smooth the single-year light images.

(2) PA lighting change detection

With the advancement of NTL research, especially quantitative NTL remote sensing studies, several light indices have been widely used to measure surface light pollution and human activities (Ghosh et al., 2009; Jiang et al., 2017; Zheng et al., 2020b). In this paper, the total sum of light intensity (TSOL), the mean NTL intensity (MNTLI), and the proportion of lighted area (POLA) were used to measure the light pollution level within PAs. TSOL is defined as the sum of the radiation values for all light pixels in a PA, MNTLI is the mean value of light radiation, and POLA is the proportion of pixels with a digital number (DN) greater than 1.

Furthermore, Theil-Sen Median trend analysis and the Mann-Kendall test were used to examine trends in the long-term sequence of light intensity changes in PAs. Both methods have a strong tolerance for outliers and are important for conducting trend analysis of time series data. They have been widely used to analyze trends in vegetation, precipitation, air temperature, and other intermediate factors (Tucker et al., 1991; Liu et al., 2011). The Theil-Sen Median trend analysis formula is:

$$Slope_{NTL} = median\left(\frac{NTL_j - NTL_i}{j - i}\right) \quad 1992 \le i \le j \le 2018 \tag{6.3}$$

where NTL_i and NTL_j are pixel NTL values at year i and j, respectively. When $Slope_{NTL} > 0$, the light intensity is increasing at the pixel; otherwise, it is decreasing.

The Mann-Kendall test is calculated as:

$$Z = \begin{cases} (S-1)/\sqrt{Var(S)} & (S > 0) \\ 0 & (S = 0) \\ (S+1)/\sqrt{Var(S)} & (S < 0) \end{cases} \tag{6.4}$$

$$S = \sum_{i=1}^{n-1} \sum_{j=i+1}^{n} sgn(NTL_j - NTL_i) \tag{6.5}$$

$$sgn(NTL_j - NTL_i) = \begin{cases} 1 & (NTL_j - NTL_i > 0) \\ 0 & (NTL_j - NTL_i = 0) \\ -1 & (NTL_j - NTL_i < 0) \end{cases} \quad (6.6)$$

$$Var(S) = n(n-1)(2n+5)/18 \quad (6.7)$$

where sgn is symbolic function; n is the length of the time series; Z is the significance test statistic with a value range of $(-\infty, +\infty)$. At a confidence level of $\alpha = 0.05$, $|Z| \geq Z_{\frac{0.05}{2}} = 1.94$ indicates that there is a significant change in the light intensity.

6.4 Results

6.4.1 Light pollution dynamics of PAs

Time-series remote sensing monitoring is an effective way to track the dynamics of light pollution and anthropogenic disturbance within PAs. Hence, we used nighttime light remote sensing observations to assess the dynamics of light pollution in African PAs over the past 26 years at the general, PA, and pixel levels.

(1) Index dynamics at the general level

The results for tracking light pollution in African PAs based on NTL images from 1992-2018 are shown in Figure 6.2. It is worth noting that, despite the pre-processing procedures that were adopted in this paper to align the two light data sources, in faintly lighted PAs (as opposed to urban areas), the significant improvement in VIRS sensor radiance resolution allowed it to record more light radiation and resulted in a "jumping" phenomenon in 2013 (see further discussion in Section 5.1). Specifically, the three lighting indices (MNTLI, TSOL, and POLA) in Figure 6.2 all increased with time, although there was a clear break between 1992-2012 and 2013-2018. We eliminated this statistically unexpected shift by 1) assuming that PA light radiation in 2013 would continue the trend from 1992 to 2012, and 2) converting between observed and predicted light radiation values in 2013 to correct the light radiation in subsequent years. The green scatter plot in Figure 6.2 shows the adjusted PA light index values, which steadily increased from 1992-2018 in the African PAs. Generally, over the past 26 years, African PAs experienced a dramatic increase in nighttime light pollution, with TSOL spiking from 446010 to 2291253, MNTLI jumping from 0.15 to 0.78, and POLA increasing from 1.39% to 6.19% within PAs.

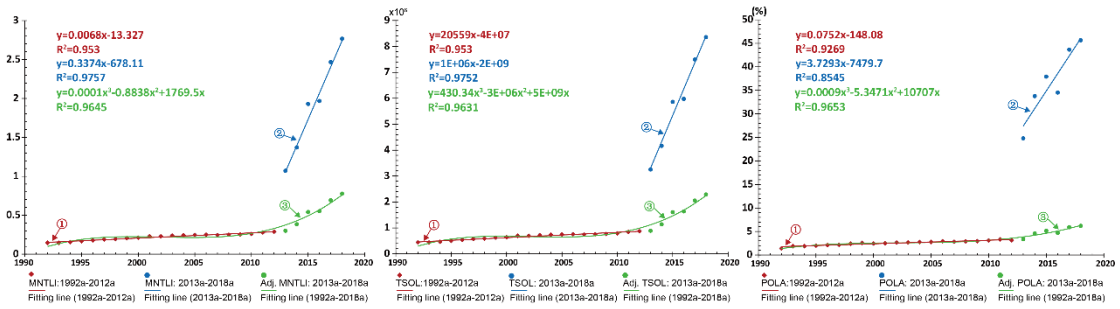

Figure 6.2. Dynamic changes in TSOL, MNTLI, and POLA values in the studied PAs. Red symbols represent OLS

observations, blue symbols represent VIIRS observations, and green symbols represent the corrected results.

(2) MNTL dynamics at the PA level

At the reserve level, the MNTLI of each PA was calculated annually because it better reflects the level of light pollution (Xu et al., 2019). The results in Table 6.3 show that only 0.87% of the PAs mitigated light pollution over the past 26 years, 18.06% had no change in light radiation, and 81.07% were under pressure to increased light pollution. Notably, of the 2,419 PAs that experienced increased light pollution, approximately 82% did not suffer from light pollution in 1992 but did have light pollution in 2018, which we referred to as primary pollution. About 18% of the PAs observed light radiation in 1992 and detected even higher light radiation in 2018, which we referred to as secondary pollution.

Table 6.3. Statistics of light radiation changes in African PAs.

Dynamics		Number of PAs			
		Count		Percent (%)	
Light decrease		26		0.87	
No-light increase		539		18.06	
Light increase	Primary pollution	1978	2419	66.29	81.07
	Secondary pollution	441		14.78	

In addition, to further reveal the spatial characteristics of light pollution dynamics in PAs, we analyzed spatial autocorrelation at the PA level. The results of Global Moran's I (0.21, $p<0.01$) indicated that there was a significant spatial clustering effect of light pollution dynamics over the past 26 years. More specifically, we found that PAs with high pollution increases were mainly concentrated along the Mediterranean coast, south of the Sahel and in the Great Lakes region, whereas low pollution increases were concentrated in the Sahara Desert, the Congo Basin, etc., where the environment was extremely harsh or pristine (Figure 6.3). We hypothesize that landscape habitability was one of the driving forces that shaped this distribution, as a more livable environment will lead to higher population density and human activity, and generate more artificial lighting that threatens the darkness of the reserve.

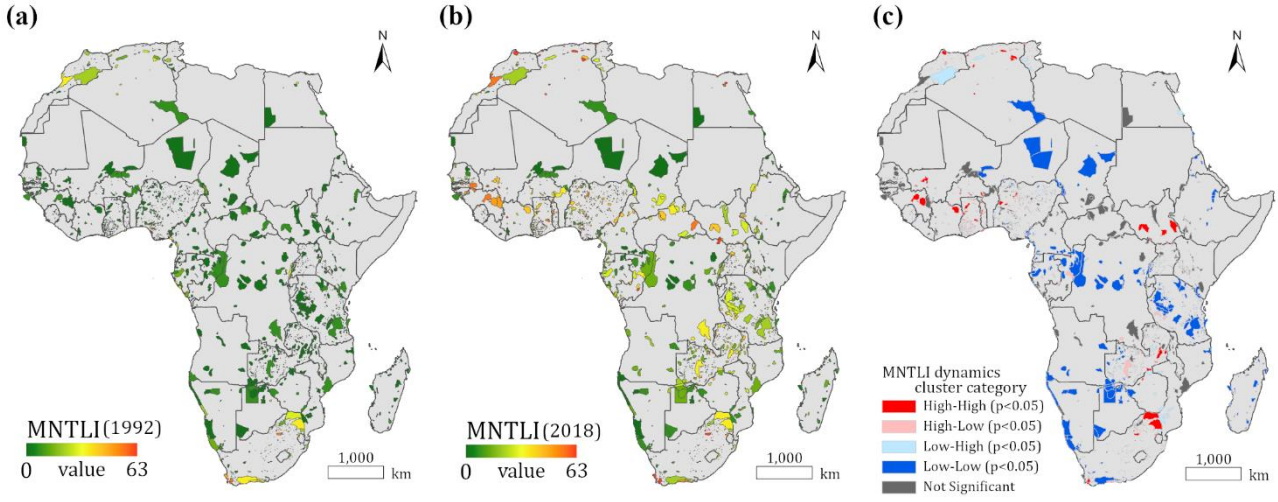

Figure 6.3. Spatial distribution and clustering characteristics of MNTLI in PAs.

(3) Light intensity dynamics at the pixel level

At the pixel level, we performed Theil-Sen Median trend analysis and Mann-Kendall tests to detect dynamic changes in light radiation for PA light pixels between 1992-2012 and 2013-2018 (Figure 6.4). From 1992-2012, 55421 and 14539 pixels had significant increases and decreases in light radiation, respectively, with a mean value of 0.23 for Sen's slope. From 2013-2018, respective increases and decreases were 971788 and 60195 with a significant mean value of 0.78 for Sen's slope. Although differences in sensor performance resulted in many more observed pixels with light radiation change from 2013-2018 than from 1992-2012, the sharp increase in pixels with more light radiation and Sen's slope values over the two periods confirmed that African PAs have experienced increasing light pollution over the last 26 years.

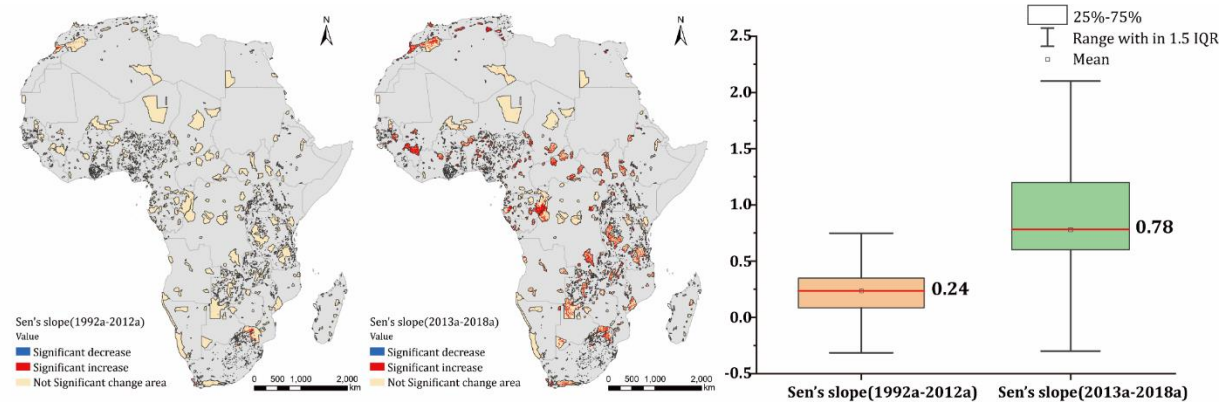

Figure 6.4. Sen's slope results during the OLS and VIIRS observation periods.

6.4.2 Categorized light pollution of PAs

(1) Categories for different design purposes

The PAs selected in this paper were divided into eight categories (Table 6.1) according to their design purpose, and analysis of the pollution differences between the types will help us to better understand the structural characteristics of light pollution. Figure 6.5 shows the MNTLI values for different PA types in 1992, 2012, 2013, and 2018. The results showed that 1) in 2018, forest reserves, biosphere reserves, wetland reserves, and scenic sites had substantially higher MNTLI values than the other reserve types, and there were significant differences in light radiation between them. 2) All types experienced an increase in light radiation during both OLS and VIIRS observations, and the most significant increases were observed at scenic sites and wetland reserves, with respective increases of 122% and 148% from 1992-2012, and 284% and 181% from 2013-2018. Meanwhile, the natural reserves and World Heritage Sites had the smallest increases of 82% and 23% from 1992-2012, and 98% and 117% from 2013-2018, respectively.

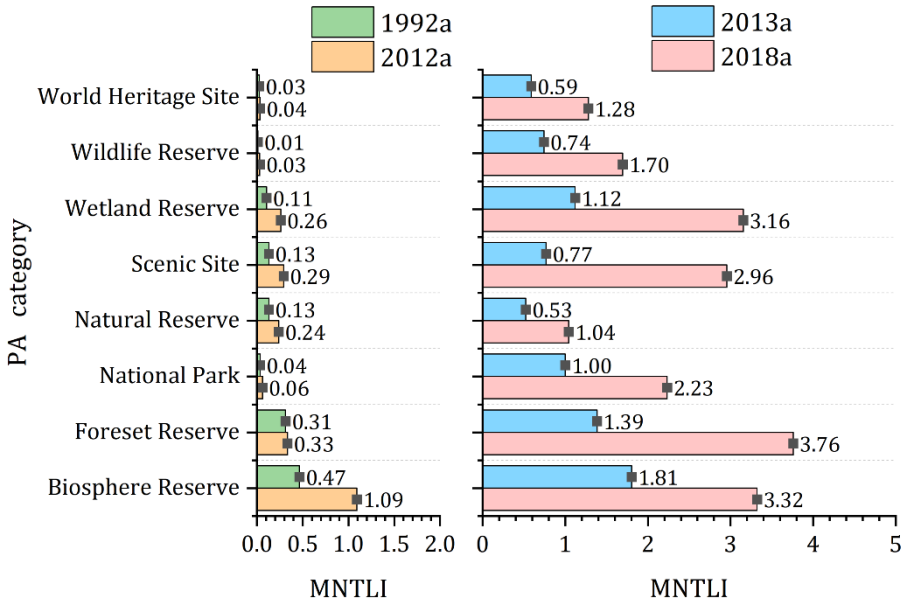

Figure 6.5. M*NTLI values for different PA types in 1992, 2012, 2013, and 2018.*

In addition, pixel-scale trend analyses and tests showed that the light radiation Sen's slope values for scenic sites, biosphere reserves, and wetland reserves exceeded 0.2 in the OLS observation period and 0.8 in the VIIRS observation period, further confirming that those types experienced dramatic light radiation growth over the past 26 years. In general, there were differences in light pollution between the different types of reserves, with scenic sites, biosphere reserves, and wetland reserves experiencing particularly severe light pollution and also faster increases in light radiation.

(2) Categories for different levels of regulation

The PA catalogue system developed by the International Union for Conservation of Nature (IUCN) classifies PAs according to their management objectives and has been endorsed by international agencies such as the United Nations and many national governments as the global standard for defining and documenting PAs. Currently, there are six types of IUCN catalogue systems, including: I_a (Strict Nature Reserve), I_b (Wilderness Area), II (National Park), III (Natural Monument or Feature), IV (Habitat/Species Management Area), V (Protected Landscape/Seascape) and VI (PA with sustainable use of natural resources). Previous studies have already identified a relationship between human activity intensity and PA control level, with strictly controlled PAs (IUCN categories I and II) generally experiencing lower human activity pressures (Jones et al., 2018).

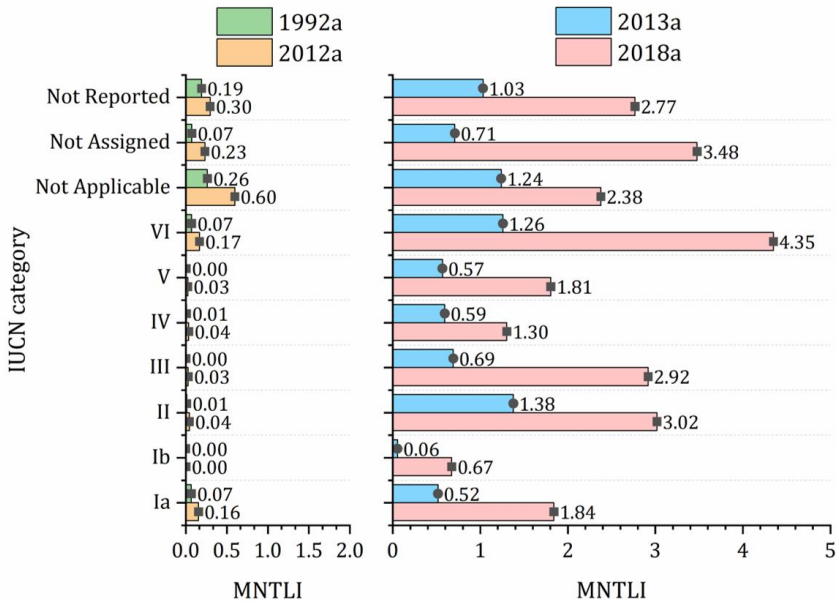

Figure 6.6. MNTLI values for different PA regulation levels in 1992, 2012, 2013, 2018.

Figure 6.6 shows MNTLI values for PAs in different years under the IUCN catalogue system. Firstly, during the period from 1992-2012, the overall level of light radiation in PAs was low and light radiation in IUCN-listed PAs was significantly lower than in PAs that were not included in the category (not applicable, not assigned, and not reported). Secondly, from 2013-2018, light radiation in PAs at all regulatory levels increased substantially, but the difference in light radiation between IUCN-listed and not-included PAs decreased.

Contrary to the well-known belief that human pressure on PAs decreases as control level increases, our monitoring of light pollution and Sen's slope (Table 6.4) under the IUCN catalogue showed that the current light pollution intensity was less correlated with control level and instead penetrated all PAs indiscriminately. For instance, I_a, as the most strictly regulated PA category, should theoretically be exposed to the lowest levels of human stress and light pollution, yet significant increases in MNTLI were observed during the study period and the light pollution problem was quite serious.

Table 6.4. Sen's slope under different PA types and IUCN categories.

PA Category	Sen's slope		IUCN Category	Sen's slope	
	1992-2012	2013-2018		1992-2012	2013-2018
Forest Reserve	-0.16	0.83	I_a	0.67	0.91
Wildlife Reserve	0.10	0.77	I_b	0.07	0.67
National Park	0.17	0.72	II	0.17	0.76
Natural Reserve	0.19	0.75	III	0.13	0.91
World Heritage Site	0.25	0.74	IV	0.20	0.74
Scenic Site	0.21	0.95	V	0.03	0.80
Biosphere Reserve	0.29	0.82	VI	0.23	0.96
Wetland Reserve	0.27	0.80	Not Applicable	0.29	0.80
			Not Assigned	0.26	0.73
			Not Reported	0.12	0.79

6.4.3 Links between human activity and light pollution in PAs

On the one hand, night light basically comes from artificial light sources associated with human activities, and on the other, most human activities tend to aggregate and expand. Therefore, exploring the relationship between human activities outside PAs and light pollution in them can help us better optimize PA planning strategies to minimize environmental disturbance.

To generate layers that characterized human activity level, this paper first synthesized an intensity map of human activity on the African continent in 2018 based on land use data and lighting data. Specifically: 1) built-up land intensity was extracted based on the land cover classification product CGLS-LC100 collection 3 (Buchanan et al., 2020) under Copernicus Global Land Service; 2) the mean values of the built-up land intensity layer and the 2018 NTL images were calculated and exported as the African continent human activity intensity map. The derived intensity map contained observations of human activities on the ground from daytime optical remote sensing and NTL remote sensing, which were able to accurately measure the human activity levels in the area. Based on the above layers, we carried out quantitative assessments of the human activity impact on PA light pollution.

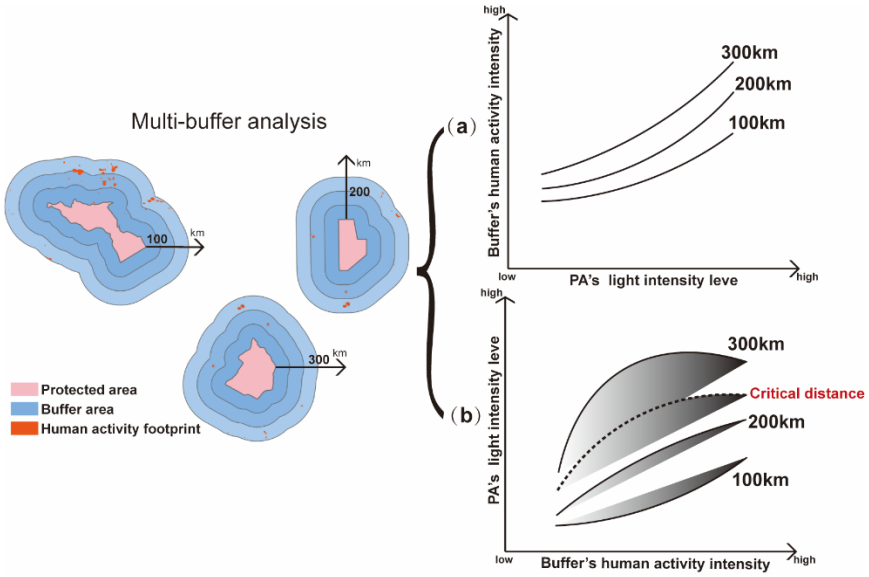

Figure 6.7. Diagram of the multiple buffer analysis conducted at PA peripheries.

PA perspective. According to the average size of the protected area and the human activity footprint, we constructed buffer zones around PAs at thresholds of 100 km, 200 km, and 300 km, and calculated the human activity intensity within them (Figure 6.7(a)). Then, average human activity intensity within different buffer distances under the light pollution gradient was calculated and the results are shown in Figure 6.8. The results showed that 1) more severe light pollution was associated with higher human activity intensity around the PAs, and this pattern was stable across multiple buffer distances; 2) for a PA with the same level of light pollution, the detected surrounding human activity intensity increased as the buffer zone expanded (100-300 km). One well-known phenomenon is that light has a serious halo effect, especially for high-intensity radiation sources at night (Abrahams et al., 2018; Zheng et al., 2020a). Therefore, compared to light sources inside the reserve, the afterglow from artificial light sources outside the reserve was another key source of PA light pollution that cannot be ignored.

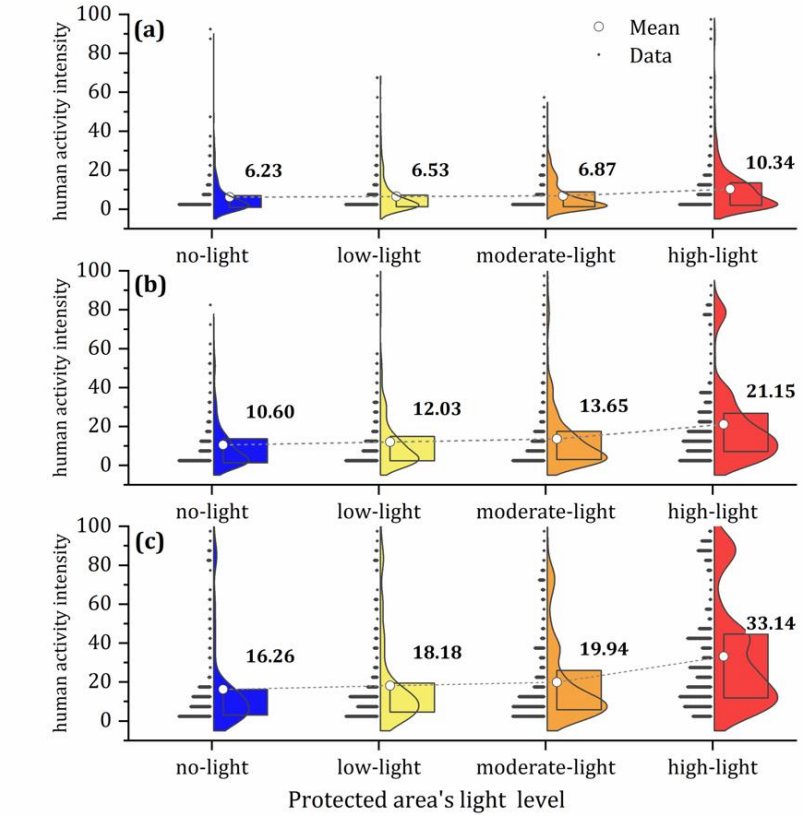

Figure 6.8. Human activity intensity under light pollution gradients in PAs at different buffer distances.

Human activity perspective. The PAs perspective was essentially a "results-conditions" perspective; that is, the differences in results were compared to differences in conditions, which revealed that external human activities were a key driver of light pollution in PAs. Hence, to compare the contribution of different conditions (human activity level outside the PAs) to results (light pollution inside the PAs), we designed a stepwise approximation strategy based on buffer distance. This identified the critical distance for the effect of external human activities on light pollution inside the PA (Figure 6.7(b)). Theoretically, within the scope of human activity, human activity intensity and light pollution of PAs should have a significant positive correlation, i.e., higher intensity human activities around the PA would cause more serious light pollution within it. Therefore, we created multiple buffers and computed light radiation values of PAs under the human activity intensity gradient until the positive correlation between them was unstable (Figure 6.9). The comparisons at different buffer distances showed that closer sources of high-intensity human activity led to stronger light emission in the PA. We also used stepwise approximation to determine that a positive correlation between external human activities and light pollution within the PA was not valid beyond a buffer distance of 245 km. Therefore, it can be assumed that a 245 km radius around the PA is a potential threshold for the disturbance effects that high-intensity human activity sources would cause in a PA.

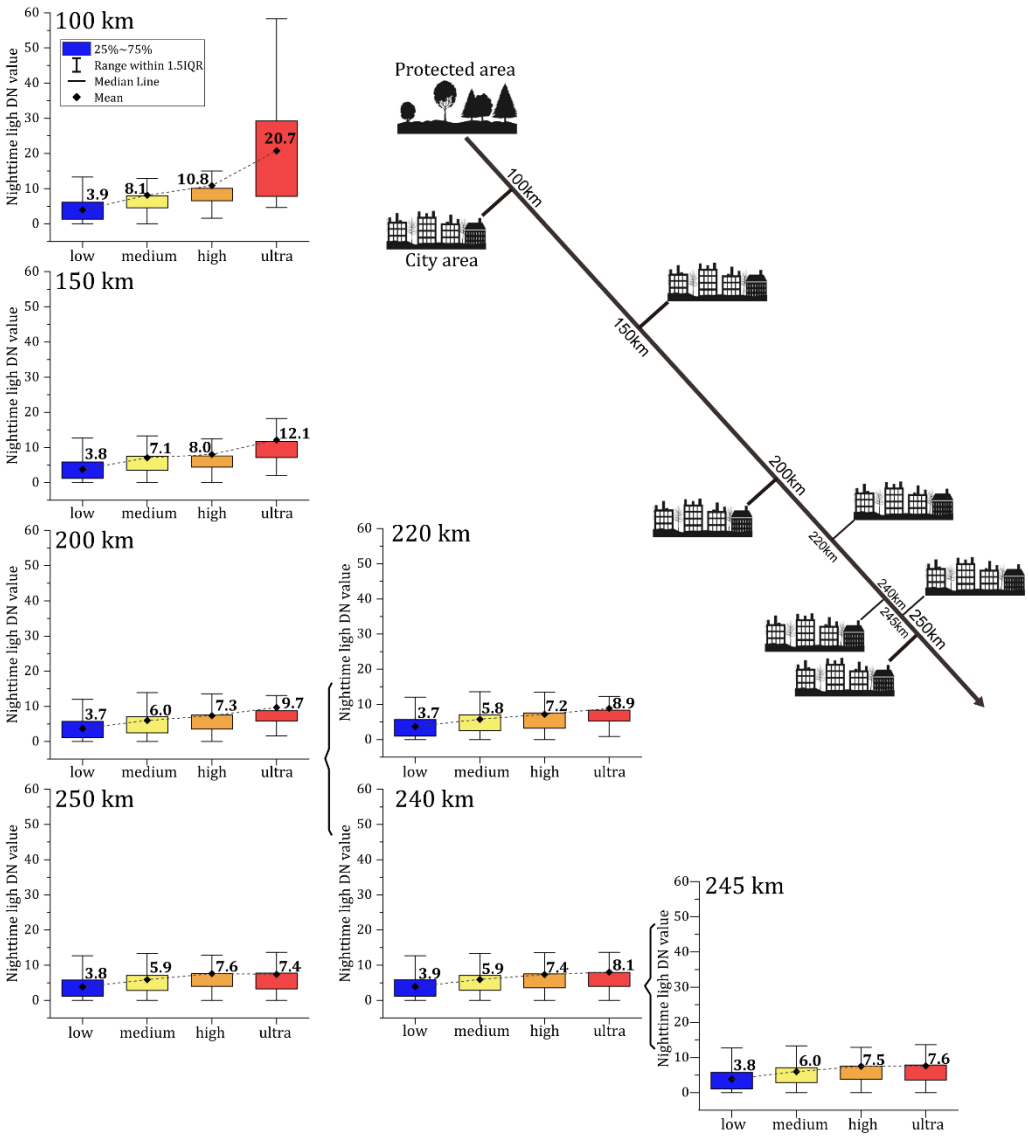

Figure 6.9. Correlations between human activities and light pollution in PAs within different distances. When the buffer distance is less than 250km, the higher the intensity of human activities, the larger the light DN values. When the buffer distance is 250 km, the light DN value under the ultra-high level of human activity intensity is less than that under high level of human activity intensity.

6.5 Discussion

6.5.1 Light pollution characteristics of PAs

As the immense value of PAs in maintaining natural habitats and conserving biodiversity has been recognized worldwide, the number of PAs has increased to 260,000. Nevertheless, there are still a considerable number of PAs that face intrusion from artificial light sources at night. All three light indices in our study confirmed that light pollution pressures on the African continent's PAs have been rising since 1992 at an increasing rate. It should be emphasized that this increase in light pollution in PAs has been comprehensive. On the one hand, light radiation values increased, with MNTLI surging from 0.15 to 0.78 between 1992 and

2018. On the other hand, the number of light-polluted PAs also climbed, with more than 80% of PAs suffering from varying degrees of light pollution in 2018. Meanwhile, according to World Bank statistics, sub-Saharan Africa's population and total GDP respectively increased approximately two and four times between 1992 and 2018. The population boom and dramatic economic growth have accelerated the intensity and scope of human activities in Africa, and threats to PAs are increasingly evident.

As a positive response to potential human activity disturbance in PAs, the IUCN catalogue system classified PAs into different regulation levels. The implementation of the IUCN classification system did appear to have a positive effect on restricting human activities and light pollution in PAs. Figure 6.6 clearly shows that from 1992-2012, light pollution in PAs under the IUCN control system was significantly lower than in non-regulated areas (one-way ANOVA $p<0.01$). However, this regulation appeared to be ineffective in more recent years ($p>0.1$), and increased slightly in PAs under the IUCN classification system, with some types even exceeding non-regulated PAs.

Although the high-performance photo-multiplier tube (PMT) used for nighttime remote sensing can detect faint light on the earth's surface, due to the single-band and coarse spatial resolution the NTL imagery still cannot accurately identify the in-situ light source characteristics. Also, since PMT was only sensitive to actively radiating light sources, a large number of non-actively radiating background features could not be recorded, whereas background information was crucial for identifying the characteristics and types of surface light emission sources. Considering these deficiencies of nighttime light remote sensing, joint daytime high-resolution optical observation for feature identification is a feasible solution. By comparing the spatial distribution between the surrounding background features (especially artificially modified surfaces) and the sources of light radiation at night in a PA, we can identify the light pollution sources. We used high-resolution Sentinel-2 imagery to conduct a visual inspection of PAs that were exposed to moderate and high-intensity light pollution (50%). According to the spatial locations of light emission sources within the PA, we found that the current light pollution intrusion could be roughly divided into three categories: 1) **Outside invasion type** (Figure 6.10(a)). For this type, PAs were usually located around (or even within) cities, where the human activity intensity within the PA was low; however, due to the halo and radiation effects of city lights, high levels of light pollution were observed within the PA. 2) **Internal Sources type** (Figure 6.10(b)). This type of PA was usually not surrounded by high light pollution sources represented by cities, but human activities within them (e.g., construction, agricultural facilities, etc.) contributed to light pollution. 3) **Mixed Pollution Type** (Figure 6.10(c)). This type included both forms of pollution described above, where the PA was subjected to high-intensity light pressure from the surrounding area and was also affected by internal human activities.

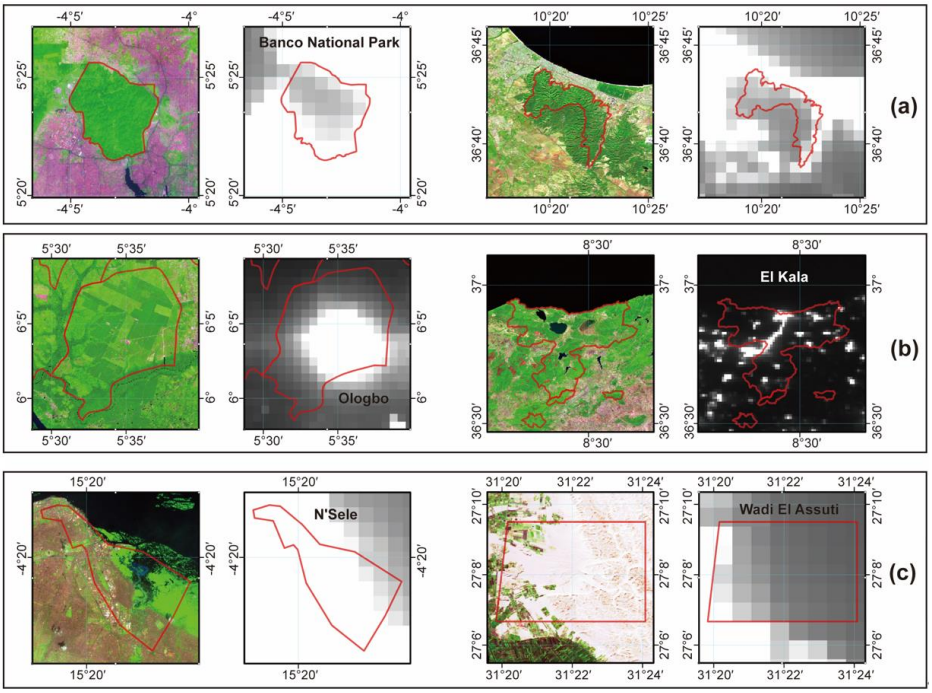

Figure 6.10. Three types of light intrusion in PAs.

In fact, we contend that the key factor that shaped the three different types of PA light intrusion described above was the distance from the PA to high-intensity anthropogenic areas (e.g., cities). PAs closer to cities were more susceptible to urban light radiation, even with the intrusion of urban land, which worsened the light pollution problem. For PAs far from cities, light pollution was mostly associated with partially built-up land and agricultural facility development. The subsequent multiple-buffer analysis also supported our view that human activity intensity surrounding PAs was positively correlated with light pollution, and this correlation stabilized at a radius of 245 km. This meant that human activities within 245 km of PAs had a strong impact on light pollution within PAs, but the impact did not increase beyond this threshold. The clarification of the distance threshold will allow us to better avoid the interference of human activities on the night ecology of PAs.

6.5.2 Potential and challenges of aligned NTL data for light pollution studies in PAs

Currently, the two main sources of light data are OLS and VIIRS sensors. These differ in both spatial and radiometric resolution, which has become one of the limitations in long-term PA light pollution studies. Therefore, to achieve long-term sequential light pollution monitoring, this paper adopted the time-continuous NTL dataset developed by Li et al. (2020) and further optimized it using a moving window. Although the dataset had good spatial continuity and stability (Li et al., 2020; Zhao et al., 2020), there are still several limitations that need to be addressed.

First, the radiation “drift” in low-light regions. Although increasing light pollution was detected in the PA, there was still a large light radiation gap compared to the urban areas. With the "faint" light background in PAs, the difference in sensor performance was further amplified, and numerous faint light pixels that were

not recorded by OLS sensors were captured by VIIRS. In addition, the S-function used to convert VIIRS to DMSP-liked data compressed pixel values in the low-light radiation interval, resulting in overestimation in the converted light image (Zhao et al., 2020). To confirm our speculations and measure light radiation dynamics, we selected four sample areas in the African region with different levels of development (Figure 6.11). In areas with strong background light radiation, such as Cairo and Lagos, the light radiation clearly increased throughout the study period, especially during 2012-2013 (the junction of the two light datasets) with a smooth shift. In areas without background light radiation, such as maritime space, the light radiation remained at zero over the study period. In PAs with low light radiation, the light radiation curve after moving window smoothing still jumped, especially in 2012-2013. For PA light pollution monitoring, although this spike in radiation resulted in higher light pollution levels in 2013-2018 than in 1992-2012, we considered this partial overestimation to be acceptable, especially since we used a segmented comparison strategy to circumvent possible overestimation.

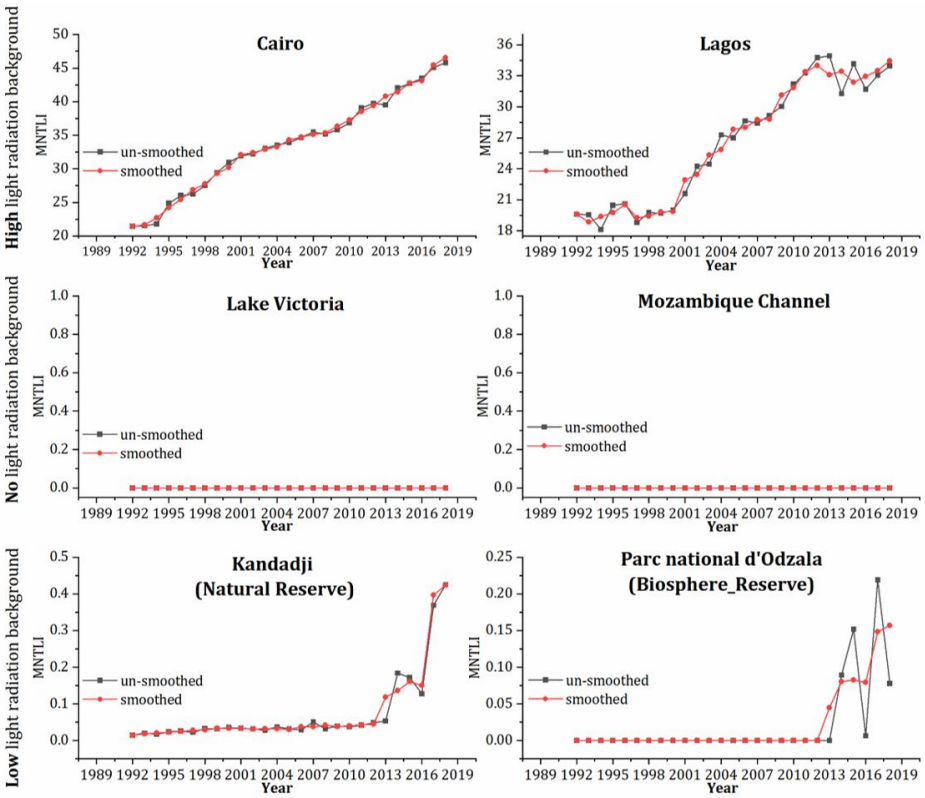

Figure 6.11. NTL radiance dynamics across multiple backgrounds.

Second, VIIRS data exhibit seasonal effects. As mentioned earlier, because the VIIRS lighting data products are distributed monthly, light radiation differences are observable every month. Previous studies have shown that there is a clear relationship between monthly light radiation changes and surface vegetation, as well as snow cover changes, especially in urban areas, which need to be considered when conducting a light radiation trend analysis using the VIIRS product (Levin, 2017; Zheng et al., 2019a). Considering the climatic conditions and geographical location of African PAs (more than 90% located at low latitudes, no snow cover, low monthly variation of vegetation, and far from urban areas), we believed that the weak seasonal effect of

VIIRS light radiation in PAs could be ignored. In addition, the post-weighted annual synthetic method we adopted could further reduce the seasonal effect and improve the stability of the model.

Third, there was a pixel blooming effect (PiBE). PiBE is a unique effect of nighttime light images, which negatively impacts NTL-based analyses (Henderson et al., 2003). In response, several scholars have proposed de-ambiguous, PiBE-free models to mitigate or even eliminate PiBE with good results (Abrahams et al., 2018). However, it should be noted that in this paper we did not adopt the corresponding methods to suppress PiBE manually due to the following considerations. The first was the specificity of the study area. The most prominent problem posed by PiBE in NTL-based analysis is the introduction of pseudo-light pixels in non-built-up areas, which typically causes the urban area being extracted to be overestimated. However, for African PAs, the impervious surface fraction (ISF) remained at quite low levels despite ongoing human intrusion, suggesting the absolute PiBE intensity of PAs was less than in high- ISF regions (Zheng et al., 2020a). Second, this study's core aim was to capture light pollution in PAs, which differed from the classical light-based urban area and urbanization index mapping. In fact, PA light pollution did not only come from internal radiation sources but also from many external artificial light facilities, whose halos still illuminated the night sky of the PA and disturbed the environment. Therefore, it is crucial to retain these PIBE generated halos to inform our results without underestimating the true light pollution levels in PAs. Third, this paper was a time-series study based on aligned NTL data and PiBE was observed every year, which meant that the disturbance caused by PiBE could be offset to a considerable extent during the trend analysis.

6.5.3 Further research

In this paper, we conducted a long-term monitoring study of light pollution in PAs on the African continent by combining light data from two sensors, DMSP/OLS and NPP/VIIRS. Although the results of the study contribute to the understanding of light pollution, types, and differences in PAs, there are still some aspects that deserve to be further understood and improved. First, to enable light pollution monitoring across long time spans, an aligned VIIRS to OLS conversion scheme was utilized. Although this scheme had good continuity in urban and non-lighted areas, there was still a "radiation jump" in PAs. Therefore, data continuity correction in a low light radiation background should be conducted to obtain more accurate and consistent light pollution monitoring. Second, we selected only PAs that were land-based and larger than 10 km^2 in Africa, which meant that our results ignored smaller, island- and marine-based PAs. Third, our study of disturbance distances to PAs considering surrounding human activities was a data-driven exploration that lacked mechanistic analysis. This prompts us to utilize more powerful spatial analytical models (like gravitational models) for mechanistic studies of representative PAs in future studies.

6.6 Conclusion

In this paper, we extracted a nighttime light image sequence for the period from 1992-2018 within African PAs using aligned DMPS/OLS and NPP/VIIRS NTL products, and carried out the first light pollution

assessment of PAs. Despite the spatial and radiometric domain uncertainties in current light data products, our qualitative and quantitative investigation confirmed the dynamics of light pollution in African PAs. The results of our study showed that African PAs have experienced increasing artificial light invasion from 1992-2018. On the one hand, the total amount of light radiation (three light indices) has steadily increased, and on the other hand, the extent of light pollution also expanded significantly, with more than 80% of PAs currently suffering from increased pressure from artificial lights. In addition, it was found that light pollution heterogeneity existed across different types of PAs, with scenic sites, biosphere reserves, and wetland reserves having particular exposure. Relatively speaking, the correlation between light pollution intensity and regulation levels in PAs was weakening, and light pollution penetrated indiscriminately into all levels. Finally, our assessment of the intensity of human activities around PAs and light radiation within them identified a strong positive correlation between human activities and light pollution that stabilized with distance, with a maximum effect at approximately 245 km. More generally, this study offers insights into the status and dynamics of light pollution in African PAs. Furthermore, distance thresholds for anthropogenic effects can be utilized in future PA planning and urban expansion.

Author Contributions: Zihao Zheng: Conceptualization, Methodology, Software, Validation, Investigation, Writing-original draft. Zhifeng Wu: Supervision, Project administration, Funding acquisition. Yingbiao Chen: Writing - review & editing. Guanhua Guo: Writing-review & editing. Zheng Cao: Writing-review & editing. Zhiwei Yang: Software, Validation. Francesco Marinello: Conceptualization, Supervision, Project administration, Writing-review & editing.

Declaration of Competing Interest: The authors declare that they have no known competing financial interests or personal relationships that could have appeared to influence the work reported in this paper.

Acknowledgments: The authors appreciate constructive comments by the associate editor and anonymous reviewers. This research was financially supported by the National key R&D Program of China (No. 2018YFB2100702), Key Special Project for Introduced Talents Team of Southern Marine Science and Engineering Guangdong Laboratory (Guangzhou) (No. GML2019ZD0301) and NSFC-Guangdong Joint Fund (No. U1901219).

References

Abrahams, A., Oram, C. & Lozano-Gracia, N. (2018) Deblurring DMSP nighttime lights: A new method using Gaussian filters and frequencies of illumination. Remote Sensing of Environment 210, 242-258.

Akodéwou, A., Oszwald, J., Saïdi, S., Gazull, L., Akpavi, S., Akpagana, K. & Gond, V. (2020) Land use and land cover dynamics analysis of the togodo protected area and its surroundings in Southeastern Togo, West Africa. Sustainability 12, 5439.

Almond, R., Grooten, M. & Peterson, T. (2020) Living Planet Report 2020-Bending the curve of biodiversity loss. World Wildlife Fund.

Aubrecht, C., Elvidge, C., Ziskin, D., Longcore, T. & Rich, C., (2008) 'When the Lights Stay On'–A Novel Approach to Assessing Human Impact on the Environment.

Aubrecht, C., Jaiteh, M. & De Sherbinin, A., (2010) Global Assesment of Light Pollution Impact on Protected Areas. CIESIN.

Buchanan, G.M., Butchart, S.H., Chandler, G. & Gregory, R.D. (2020) Assessment of national-level progress towards elements of the Aichi Biodiversity Targets. Ecological Indicators 116, 106497.

Cao, W., Huang, L., Xiao, T. & Wu, D. (2019) Effects of human activities on the ecosystems of China's National Nature Reserves. Acta Ecologica Sinica 39, 1338-1350.

Cao, Z., Wu, Z., Kuang, Y.-q. & Huang, N. (2015) Correction of DMSP/OLS night-time light images and its application in China. Journal of Geo-Information Science 17, 1092-1102.

Chen, X. & Nordhaus, W.D. (2011) Using luminosity data as a proxy for economic statistics. Proceedings of the National Academy of Sciences 108, 8589-8594.

Chen, Y., Zheng, Z., Wu, Z.F. & Qian, Q. (2019) Review and prospect of application of nighttime light remote sensing data. Progress in Geography 38, 205-223.

Cho, K., Ito, R., Shimoda, H. & Sakata, T. (1999) Technical note and cover fishing fleet lights and sea surface temperature distribution observed by DMSP/OLS sensor. International journal of remote sensing 20, 3-9.

Dimobe, K., Goetze, D., Ouédraogo, A., Forkuor, G., Wala, K., Porembski, S. & Thiombiano, A. (2017) Spatio-temporal dynamics in land use and habitat fragmentation within a protected area dedicated to tourism in a Sudanian savanna of West Africa. Journal of Landscape Ecology 10, 75-95.

Elvidge, C.D., Baugh, K.E., Kihn, E.A., Kroehl, H.W., Davis, E.R. & Davis, C.W. (1997) Relation between satellite observed visible-near infrared emissions, population, economic activity and electric power consumption. International journal of remote sensing 18, 1373-1379.

Frank, K.D., Rich, C. & Longcore, T. (2006) Effects of artificial night lighting on moths. Ecological consequences of artificial night lighting, 305-344.

Gaston, K.J., Bennie, J., Davies, T.W. & Hopkins, J. (2013) The ecological impacts of nighttime light pollution: a mechanistic appraisal. Biological reviews 88, 912-927.

Geldmann, J., Joppa, L.N. & Burgess, N.D. (2014) Mapping change in human pressure globally on land and within protected areas. Conservation Biology 28, 1604-1616.

Ghosh, T., Anderson, S., Powell, R.L., Sutton, P.C. & Elvidge, C.D. (2009) Estimation of Mexico's informal economy and remittances using nighttime imagery. Remote Sensing 1, 418-444.

Ghosh, T., Elvidge, C.D., Sutton, P.C., Baugh, K.E., Ziskin, D. & Tuttle, B.T. (2010) Creating a global grid of distributed fossil fuel CO2 emissions from nighttime satellite imagery. Energies 3, 1895-1913.

Green, D.S., Zipkin, E.F., Incorvaia, D.C. & Holekamp, K.E. (2019) Long-term ecological changes influence herbivore diversity and abundance inside a protected area in the Mara-Serengeti ecosystem. Global ecology and conservation 20, e00697.

He, C., Shi, P., Li, J., Chen, J., Pan, Y., Li, J., . . . Ichinose, T. (2006) Restoring urbanization process in China in the 1990s by using non-radiance-calibrated DMSP/OLS nighttime light imagery and statistical data. Chinese Science Bulletin 51, 1614-1620.

Henderson, M., Yeh, E.T., Gong, P., Elvidge, C. & Baugh, K. (2003) Validation of urban boundaries derived from global night-time satellite imagery. International journal of remote sensing 24, 595-609.

Hu, Y., Chen, J., Cao, X., Chen, X., Cui, X. & Gan, L. (2021) Correcting the Saturation Effect in DMSP/OLS Stable Nighttime Light Products Based on Radiance-Calibrated Data. IEEE Transactions on Geoscience and Remote Sensing.

Jiang, W., He, G., Long, T., Wang, C., Ni, Y. & Ma, R. (2017) Assessing light pollution in China based on nighttime light imagery. Remote Sensing 9, 135.

Jones, K.R., Venter, O., Fuller, R.A., Allan, J.R., Maxwell, S.L., Negret, P.J. & Watson, J.E. (2018) One-third of global protected land is under intense human pressure. Science 360, 788-791.

Joppa, L.N., Loarie, S.R. & Pimm, S.L. (2008) On the protection of "protected areas". Proceedings of the National Academy of Sciences 105, 6673-6678.

Levin, N. (2017) The impact of seasonal changes on observed nighttime brightness from 2014 to 2015 monthly VIIRS DNB composites. Remote Sensing of Environment 193, 150-164.

Li, X., Li, D., Xu, H. & Wu, C. (2017) Intercalibration between DMSP/OLS and VIIRS night-time light images to evaluate city light dynamics of Syria's major human settlement during Syrian Civil War. International journal of remote sensing 38, 5934-5951.

Li, X., Zhou, Y., Zhao, M. & Zhao, X. (2020) A harmonized global nighttime light dataset 1992–2018. Scientific data 7, 1-9.

Liu, Z., Wang, Y., Yao, Z. & Kang, H. (2011) Trend and periodicity of precipitation, air temperature and runoff in the Taihu Lake Basin. Journal of Natural Resources 26, 1575-1584.

Longcore, T. & Rich, C. (2004) Ecological light pollution. Frontiers in Ecology and the Environment 2, 191-198.

Lu, D., Tian, H., Zhou, G. & Ge, H. (2008) Regional mapping of human settlements in southeastern China with multisensor remotely sensed data. Remote Sensing of Environment 112, 3668-3679.

Ma, J., Guo, J., Ahmad, S., Li, Z. & Hong, J. (2020) Constructing a new inter-calibration method for DMSP-OLS and NPP-VIIRS nighttime light. Remote Sensing 12, 937.

Mammides, C. (2020) A global assessment of the human pressure on the world's lakes. Global Environmental Change 63, 102084.

Navara, K.J. & Nelson, R.J. (2007) The dark side of light at night: physiological, epidemiological, and ecological consequences. Journal of pineal research 43, 215-224.

Perkin, E.K., Hölker, F., Richardson, J.S., Sadler, J.P., Wolter, C. & Tockner, K. (2011) The influence of artificial light on stream and riparian ecosystems: questions, challenges, and perspectives. Ecosphere 2, 1-16.

Riggio, J., Jacobson, A.P., Hijmans, R.J. & Caro, T. (2019) How effective are the protected areas of East Africa? Global ecology and conservation 17, e00573.

Román, M.O., Wang, Z., Sun, Q., Kalb, V., Miller, S.D., Molthan, A., . . . Pandey, B. (2018) NASA's Black Marble nighttime lights product suite. Remote Sensing of Environment 210, 113-143.

Shi, K., Huang, C., Chen, Y. & Li, L. (2018) Remotely sensed nighttime lights reveal increasing human activities in protected areas of China mainland. Remote sensing letters 9, 467-476.

Shi, K., Yu, B., Huang, Y., Hu, Y., Yin, B., Chen, Z., . . . Wu, J. (2014) Evaluating the ability of NPP-VIIRS nighttime light data to estimate the gross domestic product and the electric power consumption of China at multiple scales: A comparison with DMSP-OLS data. Remote Sensing 6, 1705-1724.

Sutton, P. (1997) Modeling population density with night-time satellite imagery and GIS. Computers, Environment and Urban Systems 21, 227-244.

Sutton, P.C. & Costanza, R. (2002) Global estimates of market and non-market values derived from nighttime satellite imagery, land cover, and ecosystem service valuation. Ecological Economics 41, 509-527.

Tucker, C., Newcomb, W., Los, S. & Prince, S. (1991) Mean and inter-year variation of growing-season normalized difference vegetation index for the Sahel 1981-1989. International journal of remote sensing 12, 1133-1135.

Venter, O., Sanderson, E.W., Magrach, A., Allan, J.R., Beher, J., Jones, K.R., . . . Fekete, B.M. (2016) Sixteen years of change in the global terrestrial human footprint and implications for biodiversity conservation. Nature communications 7, 1-11.

Waluda, C., Yamashiro, C., Elvidge, C., Hobson, V. & Rodhouse, P. (2004) Quantifying light-fishing for Dosidicus gigas in the eastern Pacific using satellite remote sensing. Remote Sensing of Environment 91, 129-133.

Watson, J.E., Venter, O., Lee, J., Jones, K.R., Robinson, J.G., Possingham, H.P. & Allan, J.R. (2018) Protect the last of the wild. Nature.

Wu, K. & Wang, X. (2019) Aligning pixel values of DMSP and VIIRS nighttime light images to evaluate urban dynamics. Remote Sensing 11, 1463.

Xiang, W. & Tan, M. (2017) Changes in light pollution and the causing factors in china's protected areas, 1992–2012. Remote Sensing 9, 1026.

Xu, P., Wang, Q., Jin, J. & Jin, P. (2019) An increase in nighttime light detected for protected areas in mainland China based on VIIRS DNB data. Ecological Indicators 107, 105615.

Yang, H. & Xu, H. (2019) Assessing fractional vegetation cover changes and ecological quality of the Wuyi Mountain National Nature Reserve based on remote sensing spatial information. Chinese Journal of Applied Ecology 31, 533-542.

Yu, B., Shu, S., Liu, H., Song, W., Wu, J., Wang, L. & Chen, Z. (2014) Object-based spatial cluster analysis of urban landscape pattern using nighttime light satellite images: A case study of China. International Journal of Geographical Information Science 28, 2328-2355.

Zhang, M., Liu, Q., Wang, J., Cai, Y., Bai, Z. & Ye, J. (2020) Monitoring human activities in Jiaozi Mountain nature reserve based on remote sensing during 1992-2018. Journal of Ecology and Rural Environment 36, 1097-1105.

Zhao, M., Zhou, Y., Li, X., Cheng, W., Zhou, C., Ma, T., . . . Huang, K. (2020) Mapping urban dynamics (1992–2018) in Southeast Asia using consistent nighttime light data from DMSP and VIIRS. Remote Sensing of Environment 248, 111980.

Zheng, Q., Weng, Q. & Wang, K. (2019a) Developing a new cross-sensor calibration model for DMSP-OLS and Suomi-NPP VIIRS night-light imageries. ISPRS Journal of Photogrammetry and Remote Sensing 153, 36-47.

Zheng, Q., Weng, Q. & Wang, K. (2020a) Correcting the Pixel Blooming Effect (PiBE) of DMSP-OLS nighttime light imagery. Remote Sensing of Environment 240, 111707.

Zheng, Z., Wu, Z., Chen, Y., Yang, Z. & Marinello, F. (2020b) Exploration of eco-environment and urbanization changes in coastal zones: A case study in China over the past 20 years. Ecological Indicators 119, 106847.

Zheng, Z., Yang, Z., Chen, Y., Wu, Z. & Marinello, F. (2019b) The Interannual Calibration and Global Nighttime Light Fluctuation Assessment Based on Pixel-Level Linear Regression Analysis. Remote Sensing 11, 2185.

Zhu, P., Huang, L., Xiao, T. & Wang, J. (2018) Dynamic changes of habitats in China's typical national nature reserves on spatial and temporal scales. Journal of Geographical Sciences 28, 778-790.

Zhuo, L., Ichinose, T., Zheng, J., Chen, J., Shi, P. & Li, X. (2009) Modelling the population density of China at the pixel level based on DMSP/OLS non-radiance-calibrated night-time light images. International journal of remote sensing 30, 1003-1018.

7. Exploration of eco-environment and urbanization changes in coastal zones: A case study in China over the past 20 years [6]

7.1 Abstract

With the rapid development of urbanization and population migration, since the 20th century, the natural and eco-environment of coastal areas have been under tremendous pressure due to the strong interference of human response. To objectively evaluate the coastal eco-environment condition and explore the impact from the urbanization process, this paper, by integrating daytime remote sensing and nighttime remote sensing, carried out a quantitative assessment of the coastal zone of China in 2000–2019 based on Remote Sensing Ecological Index (RSEI) and Comprehensive Nighttime Light Index (CNLI) respectively. The results showed that: 1) the overall eco-environmental conditions in China's coastal zone have shown a trend of improvement, but regional differences still exist; 2) during the study period, the urbanization process of cities continued to advance, especially in seaside cities and prefecture-level cities in Jiangsu and Shandong, which were much higher than the average growth rate; 3) the Coupling Coordination Degree (CCD) between the urbanization and eco-environment in coastal cities is constantly increasing, but the main contribution of environmental improvement comes from non- urbanized areas, and the eco-environment pressure in urbanized areas is still not optimistic. As a large-scale, long-term series of eco-environment and urbanization process change analysis, this study can provide theoretical support for mesoscale development planning, eco-environment condition monitoring and environmental protection policies from decision-makers.

Keywords: Coastal zone; Eco-environment; Urbanization; RSEI; CNLI; Satellite imagery

7.2 Introduction

As a special geographical area connecting the marine and land systems, the coastal zone is not only the most active natural area on the earth's surface, with the most concentrated human activities and the most developed economy, but also the area with the most superior resources and environmental conditions (Crossland et al., 2005). Currently, nearly 60% of the world's population lives in coastal areas, and environmental changes in coastal areas are closely related to human survival and development (Chen and Wang, 2003; Fan et al., 2010). However, since the 20th century, with the development of coastal economy and urbanization, the large-scale population continues to concentrate in coastal areas, the regional environment is increasingly disturbed by human activities, and the natural and eco-environment are facing great pressure (Zhang and Zhu, 1997; Weston et al., 2009; Zhai et al., 2020). Facing increasing ecological disturbances, effective models are increasingly needed to detect the temporal and spatial changes of ecological environment

[6] This Chapter relies on the paper "Zheng, Z., Wu, Z., Chen, Y., Yang, Z., & Marinello, F. (2020). Exploration of eco-environment and urbanization changes in coastal zones: A case study in China over the past 20 years. Ecological Indicators, 119, 106847.". https://doi.org/10.1016/j.ecolind.2020.106847.

conditions to ensure the sustainable development of the coastal zone.

The rapid development of remote sensing technology provides data sources and technical support for regional eco-environment monitoring and evaluation, which can effectively reflect the ecological status at different scales (Ivits et al., 2009; Caccamo et al., 2011; de Araujo Barbosa et al., 2015; Willis, 2015). In particular, the frequent application of remote sensing based ecological assessment makes it an important means to monitor the coastal environment, and plays an important role in the global coastal ecological assessment research (Arnous and Green, 2011; Sririrwardane et al., 2015; Wang et al., 2018). In general, remote sensing-based coastal ecological research mainly focuses on landuse/ cover change (Zoran et al., 2010; Bui et al., 2014; Vatseva, 2015), landscape pattern analysis (Feng and Han, 2011; Hepcan, 2013; Chu et al., 2015; Li et al., 2015; Vorovencii, 2015; Xu et al., 2015), coastline change detection (Lo and Gunasiri, 2014; Guneroglu, 2015; Chen et al., 2016; Wang et al., 2016), vegetation change monitoring (Bird et al., 2004; Stanley et al., 2005; Alatorre et al., 2011; Shibly and Takewaka, 2013; Anwar and Takewaka, 2014; Aslan et al., 2016) and habitat change identification based on indicator system (Qin et al., 2008; Gong et al., 2011; Ning et al., 2016).

In fact, in an ecosystem, the interaction between each environmental indicator affects the whole ecosystem, and they are inseparable (Xu, 2013). However, most of these remote sensing-based coastal eco- logical environment assessments are based on a single index, such as vegetation index to describe vegetation change (Maselli, 2004; Gillespie et al., 2018) and water body index to represent coastline change (Wicaksono and Wicaksono, 2019). Due to the insufficient ability of these assessment models to reveal the comprehensive ecological status of the region, the detection of ecological change based on the aggregate remote sensing index is still a challenge (Behling et al., 2015). Gradually, some indicators or models that aggregate multiple indicators to monitor ecological conditions have been proposed, such as forest disturbance index (DI) which combines three components of tasseled cap transformation, MODIS global disturbance index (MGDI) which com- bines the enhanced vegetation index (EVI) and land surface temperature, Ecological Niche Modeling (ENM) which combines the red index, EVI and normalized difference water index (NDWI).

It is worth noting that a recent study on the remote sensing-based ecological index (RSEI) has brought new hope for the realization of long-span and large-scale ecological assessment (Xu, 2013). RSEI is completely based on remote sensing images and can integrate multiple index factors to evaluate regional ecological quality objectively and quickly. It selects four indicators, such as greenness, humidity, heat, and dryness, which can be directly felt by the human body, comprehensively reflects the regional ecological environment, and integrates various indicators through principal component transformation (PCA). RSEI overcomes the shortcomings of a single indicator, makes the aggregation of sub-indicators more reasonable, and has been successfully applied to many regions to provide support for the analysis, modeling and prediction of regional ecological characteristics (Zhang et al., 2015; Song and Xue, 2016; Hu and Xu, 2018; Zhang et al., 2018; Yue et al., 2019).

The continuous urbanization process has caused great changes in the natural ecological environment in

China's coastal areas since the 1980s. Under the premise of ensuring the sustainable development of the coastal zone, it is of great significance to explore the interaction between the eco-environment and human activities in China's coastal areas in the past few decades. Therefore, based on daytime and nighttime remote sensing images, the interaction between eco-environment and urbanization process in China's coastal areas are explored in this paper. The specific objectives of this study were: **1)** monitoring the long-term dynamics of eco-environment in the coastal zone of China under the background of rapid urbanization processes; **2)** evaluating the spatiotemporal differences in the intensity of human activity and the level of urbanization in the coastal zone over the last 20 years; **3)** assessing the coupling coordination level between the eco- environment and the urbanization level in coastal area, and recognizing the impact of continuous urbanization on local environmental.

7.3 Study area and data sources

7.3.1 Study area

Generally, the coastal zone is a belt area that extends to the land and sea sides of the coastline, involving land areas and near-shore waters (He, 2017). In fact, the coastal zone is commonly defined according to management purposes and research needs, leading to a diversity of coastal zone extent definitions. For example, the United Nations Millennium Ecosystem Assessment project defines coastal zones as lowlands extending 100 km from the coast to the mainland, while scholars usually conduct research based on administrative units (Agardy and Alder, 2005; Hou et al., 2018).

China's coastal zone is in the intersection of Eurasia and the Pacific Ocean, with a total length of the continental coastline is more than 18000 km (Cao and Wong, 2007). There are 14 provincial administrative units in the coastal zone, including Liaoning, Hebei, Tianjin, Shandong, Jiangsu, Shanghai, Zhejiang, Fujian, Guangdong, Guangxi, Hainan, Hongkong, Macao and Taiwan (Figure 7.1). Although the coastal provincial units cover only 13% of China's area, they are concentrated in more than 50% of China's large cities, 40% of its small and medium-sized cities, more than 40% of its population, and more than 60% of its GDP (Luo, 2016). The diversified urban scale and intensity of human activities in the coastal provinces make them an important "window" for recognizing the impact of urbanization on the environment (Di et al., 2014). Besides, considering the higher priority and independence of provincial administrative units in the formulation and implementation of environmental protection and urban development policies, this paper defines the coastal provincial unit as the study area to implement the time-series analysis. Due to the special geographical location of Beijing, it is also included in the study area.

Figure 7.1. The location map of coastal zone of China.

7.3.2 Data and Pre-processing

(1) Daytime remote sensing data

Four ecological components will be involved in the process of constructing RSEI, namely Greenness, Wetness, Heat and Dryness. Accordingly, this paper selects the corresponding standard products from the MODIS product library as the data source based on these four components. The Land Processes Distributed Active Archive Center (LPDAAC) Collections in the USGS United States Geological Survey (USGS, https://earthexplorer.usgs.gov) provides standard data collection for different application scenarios based on level 1B data, including land surface reflectance (LSR), land surface temperature and emission (LST&E), vegetation indices (VI), which can be directly applied to construct RSEI in this paper. For the study area of this paper, we use remote sensing image processing platform to preprocess the tiles images of different components, such as images mosaicing, clipping, resampling and projecting. Also, to reduce the interference caused by the difference of image acquisition time to the ecological components and improve the image quality under the cloud interference, this paper uses the adjacent month as the image acquisition time window for each component (Table 7.1).

Table 7.1. The data source of four ecological components.

Component	MODIS Data collection	Date layer	Spatial/temporal resolution	Data time	Image amount
Greenness	MOD13A1 V6	Enhanced Vegetation Index (EVI)	500m/16-days	August	85
Heat	MOD11A2 V6	Daytime Land Surface	1km/8-days	September	45

		Temperature (DLST)			
Wetness	MOD09A1	Corrected surface spectral reflectance for bands 1 to 7	500m/8-days	October	63
Dryness	MOD09A1	Corrected surface spectral reflectance for bands 1 to 7	500m/8-days	October	63

(2) Nighttime remote sensing data

Unlike traditional daytime remote sensing, the nighttime remote sensing can effectively detect the distribution and intensity of artificial light sources. Its image set has been confirmed to be highly correlated with surface human social activities and is widely used in urbanization (Ju et al., 2017; Zhou et al., 2018; Xie et al., 2019), population distribution (Li and Zhou, 2018; Yu et al., 2019), GDP (Ji et al., 2019) and energy consumption (Shi et al., 2019a). Considering the time span of this study, the nighttime light image for 2000, 2005 and 2010 were derived from the Stable Light (STL) of Defense Meteorological Satellite Program/Operational Linescan System (DMSP/OLS), while the light image for 2015 and 2019 were derived from the Day/Night Band (DNB) of National Polar-Orbiting Partnership/Visible Infrared Imaging Radiometer Suite (NPP/VIIRS). The detailed parameters of the two types of lighting data used in the paper are shown in Table 7.2. To avoid the deviations caused by abnormal data fluctuation and sensor difference, in-sensor calibration and sensor-cross calibration is performed referring to the model proposed by Zheng et al. (2019a) and Wu and Wang (2019).

Table 7.2. Data parameters of DMSP/OLS and NPP/VIIRS.

NTL data	Sensors	Spatial resolution	Temporal resolution	Data available interval	Unit
Stable Light (STL)	OLS	Annual	30 arc second (around 1km at equator)	1992-2013	DN (unitless)
Day/Night Band (DNB)	VIIRS	Monthly	15 arc second (around 500m at equator)	April 2012-Present	nanoWatts/cm^2/Sr

7.4 Methods

7.4.1 Construction of RSEI

The RSEI consists of four components: Greenness, Heat, Wetness and Dryness, which is often used for ecological assessment (Yuan and Bauer, 2007; Ivits et al., 2009; Li et al., 2017).

Although existing RSEI-based studies use NDVI as the green component, considering the NDVI's saturation problem in high vegetation coverage area, EVI was used as the green component. Since the MOD13A1 V6 image set contains the EVI layer, there was no need to calculate the EVI according to the formula (DataBase, 2019).

Different from Landsat image for small scale LST inversion, MODIS thermal infrared image with high temporal resolution (8-days) and medium spatial resolution (1 km) has become an indispensable data source

for large-scale regional LST inversion. As listed in Table 7.1, the heat component was derived from the DLST layer of MOD11A2 V6 Dataset.

Previous studies have confirmed that Kauth-Thomas (K-T) transformation is an effective data compression and de-redundancy technique, and its luminance, greenness, and wet components are directly related to surface physical parameters (Crist, 1985; Huang et al., 2002; Baig et al., 2014) and is widely used for wetness monitoring in eco-environmental assessment (Todd and Hoffer, 1998). As previous studies, the third component of K-T-transformed multispectral image is used to characterize the wetness component of RSEI. The formula is defined as:

$$Wet = c_1\rho_{red} + c_2\rho_{nir1} + c_3\rho_{blue} + c_4\rho_{green} + c_5\rho_{nir2} + c_6\rho_{swir1} + c_7\rho_{swir2} \quad (7.1)$$

where $\rho_{red}, \rho_{nir1}, \rho_{blue}, \rho_{green}, \rho_{nir2}, \rho_{swir1}$ and ρ_{swir2} represent the reflectance of the 7 bands of the MOD09A1 images, respectively (Zhang et al., 2002). For MODIS multi-band images, the coefficient of each band is: $c_1 = 0.1147$, $c_2 = 0.2489$, $c_3 = 0.2408$, $c_4 = 0.3132$, $c_5 = -0.3122$, $c_6 = -0.6416$, $c_7 = -0.5087$ (Xu et al., 2019).

As surface drying will have a huge impact on living conditions and biological richness, and become an important indicator of the level of eco-environment (Xu, 2008). To quantify the dryness component, the Normalized Difference Build-up and Soil Index (NDBSI) was constructed based on Bare-soil Index (BI) (Rikimaru et al., 2002) and Index-based Built-up Index (IBI) (Xu, 2008). The formula is as follows:

$$NDBSI = \frac{IBI + BI}{2} \quad (7.2)$$

$$IBI = \frac{\frac{2\rho_{swir1}}{\rho_{swir1} + \rho_{nir1}} - [\frac{\rho_{nir1}}{\rho_{nir1} + \rho_{red}} + \rho_{green}/(\rho_{green} + \rho_{swir1})]}{\frac{2\rho_{swir1}}{\rho_{swir1} + \rho_{nir1}} + [\frac{\rho_{nir1}}{\rho_{nir1} + \rho_{red}} + \rho_{green}/(\rho_{green} + \rho_{swir1})]} \quad (7.3)$$

$$BI = \frac{[(\rho_{swir1} + \rho_{red}) - (\rho_{nir1} + \rho_{blue})]}{[(\rho_{swir1} + \rho_{red}) + (\rho_{nir1} + \rho_{blue})]} \quad (7.4)$$

where ρ_{red}, ρ_{blue}, ρ_{green}, ρ_{nir1} and ρ_{swir1} are the surface reflectance of the corresponding bands in the MOD09A1 V6 images, respectively.

To compress the information on multidimensional variables and effectively reduce the number of variables, the principal component analysis (PCA) method is used to integrate the above four components. PCA determines the weight of each index manually, but automatically and objectively according to the contribution degree of each index to each principal component, thus avoiding the result deviation caused by the subjective setting of weight in the calculation process (Xu, 2013; Seddon et al., 2016). Specifically, 1) standardize each component; 2) perform PCA analysis based on ArcGIS Pro platform to obtain the first principal component as original value of RSEI; 3) standardize the original values to ensure the comparability of RSEI in different periods.

7.4.2 Construction of the nighttime light index

Based on the calibrated nighttime light image, this paper utilizes a comprehensive nighttime light index (CNLI) to reflect the level of urbanization and the intensity of human activities on the surface, which can effectively monitor the development of regional urbanization (Chen et al., 2003). CNLI is defined as the product of the light area proportion (LAP) and the mean light intensity (MLI) in a specific area. The formula is:

$$CNLI = LAP \times MLI \tag{7.5}$$

$$MLI = \frac{\sum_{i=1}^{63} C_i \times DN_i}{\sum_{i=1}^{63} C_i \times 63} \tag{7.6}$$

$$LAP = \frac{Area_{light}}{Area} \tag{7.7}$$

where DN_i is the light value of the light pixel and C_i is the number of pixels with a value of DN_i; $Area_{light}$ and $Area$ are the total area of the light patch and the total area of the study area, respectively.

7.4.3 Coupling coordination model

The coupling and coordination between the eco-environment and the development of urbanization (human activity) are important factors affecting the sustainable development of coastal areas. Based on the capacity coupling system model in physics, a coupling coordination model of urbanization and eco-environment was introduced in this paper (Liu et al., 2005). Firstly, the coupling model is constructed as:

$$CD = 2 \times \sqrt{(U \times E)/(U + E)^2} \tag{7.8}$$

where U represents CNLI and E represents RSEI; CD is the coupling degree between CNLI and RSEI. The larger the value of CD, the more coordinated the eco-environment and urbanization development.

Secondly, to avoid the "false coordination" of the two systems, the coupling coordination model is introduced to objectively reflect the coordinated development level. The formula is:

$$CCD = \sqrt{(\alpha U + \beta E) \times CD} \tag{7.9}$$

where CCD is the coupling coordination degree, the higher the value is, the higher the level of coupled and coordinated development of the system. α and β are weight coefficients. Considering that urbanization is the key factor leading to the change of eco-environment, and the impact of eco-environment on urbanization is quite limited, so the urbanization system should be given greater weight ($\alpha = 0.65; \beta = 0.35$ (Liao et al., 2018)).

7.5 Results

7.5.1 Eco-environment in the coastal zone

(1) Coastal zone RSEI and its changes

Figure 7.2 shows the distribution of the RSEI index in 2000, 2005, 2010, 2015, and 2019. The results

indicate that the RSEI in China's coastal regions showed a significant upward trend from 2000 to 2019. The RSEI mean-value of the coastal zone in 2000 was the lowest, only 0.492, while the RSEI mean-value of 2019 increased by about 17% from 2000 to 0.575. The increase in RSEI over the past 2 decades indicates that the ecological environment in China's coastal zones has improved to some extent. For the 2000 RSEI, the number of low-value RSEI pixels (poor eco-environment status) is large and mainly distributed in the north of the coastal zone. For 2019, the number of low-value RSEI pixels is significantly reduced, and most of them are concentrated in built-up areas and estuarine deltas, such as Pearl River Delta, Yangtze River Delta and Beijing-Tianjin areas. Through comparison, it can be found that the change characteristics of RSEI in coastal areas during the past almost 20 years can be summarized as follows: 1) the overall RSEI value shows an increasing trend, especially in the northern coastal zone; 2) the low-value RSEI pixels in urban areas, especially in urban agglomerations, shows an expanding trend. This change characteristic has a close relationship with the ecological civilization construction and green development road that China has continuously promoted in recent years under the development of high-speed urbanization. According to data from the World Bank, China's forest cover increased by 328,630 km^2 between 2000 and 2016, making it the country with the largest increase in forest area in the world (Bank, 2019).

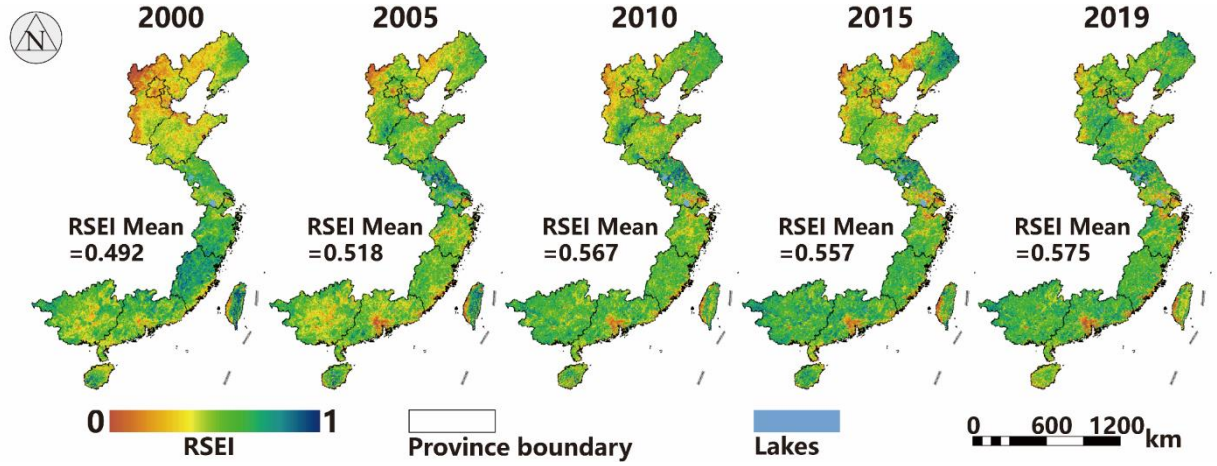

Figure 7.2. The RSEI map of China's coastal zone in 2000, 2005, 2010, 2015 and 2019.

To better reveal the RSEI changes in the past 2 decades, referring to the ecological classification methods provided by Hu and Xu (2018), the RSEI values of China's coastal areas are divided into 5 grades according to the equal interval of 0.2 to represent 5 different ecological conditions (Table 7.3). The results show that the area with ecological status of "Very Bad" has decreased by about 38.56% in the past 19 years, and the reduced area has reached over 4300 km^2. The area with the ecological status of 'Bad' decreased about 132800 km^2, more than 50% compared with that in 2000. The areas with "Good" and "Natural" ecological status increased significantly, with the growth rate reaching 198.6% and 1511% respectively. In the past almost 20 years, the conversion of RSEI has focused on three levels: Bad, Medium and Good. In year 2000, the ecological conditions of "Bad" and "Good" are relatively close, accounting for about 16% of the coastal area, while the area of 'Medium' accounts for about 66%. In year 2019, the proportion of regions in "Bad", "Medium" and "Good" is 7%, 45% and 45% respectively, which has changed significantly compared to 2000. Changes in the proportion structure indicate that in the past 19 years, about 20%-30% of the areas in the "Medium" have risen

to ‘Good’, and about 10% of the ‘Bad’ areas have improved.

Table 7.3. Area and percentage statistics of the five RSEI levels in different years.

RSEI Level	Very Bad (0~0.2) ($\times 10^2$ km^2)	Bad (0.2~0.4) ($\times 10^2$ km^2)	Medium (0.4~0.6) ($\times 10^2$ km^2)	Good (0.6~0.8) ($\times 10^2$ km^2)	Natural (0.8~1.0) ($\times 10^2$ km^2)
2000	111.6(0.83%)	2324.5(17.2%)	8977.7(66.6%)	2064.2(15.3%)	5.1(0.04%)
2005	53.1(0.39%)	1360.1(10.1%)	9731.0(72.2%)	2328.1(17.3%)	10.8(0.08%)
2010	49.6(0.37%)	896.2(6.70%)	6970.8(51.7%)	5483.0(40.7%)	83.4(0.62%)
2015	45.6(0.34%)	1218.9(9.04%)	7032.9(52.2%)	5146.4(38.2%)	39.2(0.29%)
2019	68.5(0.51%)	996.2(7.4%)	6172.9(45.8%)	6163.4(45.7%)	82.0(0.61%)
Change (2000-2019)	-43.1(-38.6%)	-1328.3(-57.1%)	-2804.8(-31.2%)	4099.2(198.6%)	76.9(1511%)

(2) Spatial heterogeneity of RSEI

As in most countries, China's administrative divisions have a spatial hierarchy. The social and economic policies formulated or promulgated by the central government can be conveyed through the governments at the provincial, city, county, town, and village levels (Zheng et al., 2019b). In the process of regional development and policy implementation, the prefecture-level administrative units have gradually become the core and basic spatial units (Shi et al., 2019b). Therefore, based on ArcGIS Pro platform, this paper performed the spatial autocorrelation analysis of RSEI values at prefecture-level cities to reveal the changes and spatial distribution characteristics of coastal eco-environment over the past 20 years.

Figure 7.3 shows the RSEI mean-value distribution of urban units and the Local Moran’s I of the change-value of RSEI during the past 20 years. In year 2000, there were 14 RSEI municipal units with lower than 0.4, which were mainly distributed in north-central of Hebei (Shijiazhuang, Zhangjiakou, Chengde, Langfang, etc.), Beijing, Tianjin, western Liaoning (Chaoyang and Jinzhou) and northern Shandong (Dongying). After 19 years of development, the number of RSEI municipal units lower than 0.4 has been significantly reduced, with only 6 remaining, and mainly distributed in the Pearl River Delta (Zhongshan, Dongguan, Foshan, etc.) and southwest Taiwan (Yunlin and Changhua). Meanwhile, the number of RSEI municipal units higher than 0.55 increased from 37 in 2000 to 69 in 2019, with a large increase.

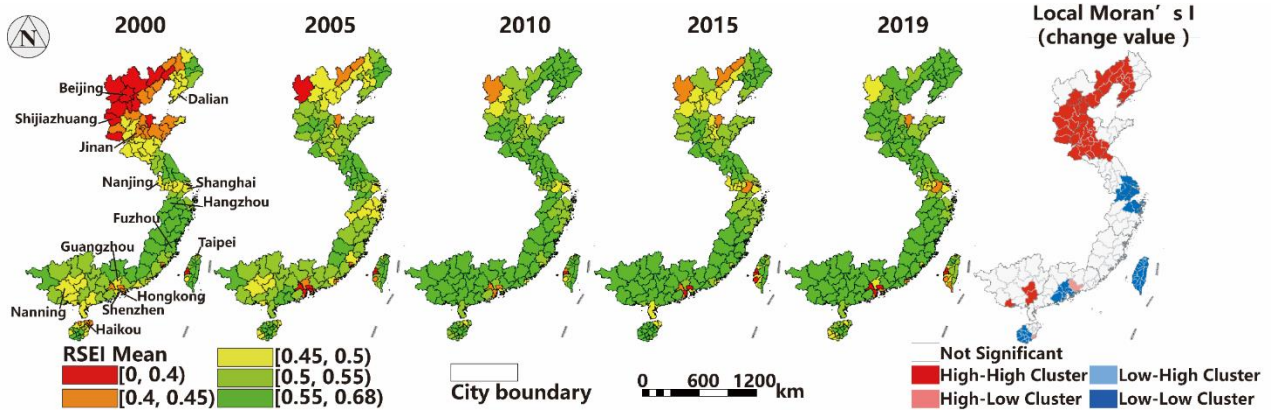

Figure 7.3. The RSEI mean-value distribution and local Moran’s I map of municipal units.

Although the overall ecological status of the coastal zone shows a trend of improvement, it still has spatial heterogeneity. According to the local Moran's I map, the RSEI rising units (eco-environment has improved) are mainly distributed in Shandong, Hebei, Tianjin and Beijing, the north-central part of the coastal zone. Since these areas are located in northern China and dominated by plains, the vegetation coverage, especially forest resources, is insufficient, unevenly distributed and low quality compared to the southern China. However, after 2000, with the promotion of "Ecological Civilization Construction" and the strengthening of environmental protection awareness, the vegetation coverage in this area has increased significantly (Li et al., 2017; Yan et al., 2019). Then, considering the contribution of EVI to RSEI, the improvement in vegetation coverage has driven the rise of RSEI. Conversely, the number of units that have experienced RSEI attenuation (ecological deterioration) over the past 19 years has been significantly reduced and scattered, including the Yangtze River Delta, the Pearl River Delta, southwestern Hainan, and Taiwan. Due to the better climatic and hydrological conditions, the initial ecological conditions in the above areas are better than those in the northern coastal zone. However, in the past 19 years, with the rapid development of economy and urban expansion, on the urban scale, the impervious surface has occupied more and more ecological land and resulting in the decline of vegetation coverage and ultimately affecting the regional RSEI.

7.5.2 Nighttime light in coastal areas

(1) Nighttime light intensity distribution and its changes

It is universally acknowledged that the light image after necessary preprocessing and calibration can directly reflect the surface vitality and urbanization intensity. Figure 7.4(a-e) shows the nighttime light images after calibration in China's coastal zone from 2000 to 2019. Obviously, in the past 20 years, the nighttime light in the coastal zone has increased substantially, both from the lighting area and the number of high-intensity light pixels. According to the statistical results of MLI and LAP of coastal light images in different years, the MLI of the light pixel was only 0.26 in 2000, and then it has increased year by year and reached 0.4 in 2019, with a growth rate of 53.8%. Meanwhile, the lighting area has also increased from 33.5×10^4 km^2 in 2000 to 86.9×10^4 km^2 in 2019, expanding by about 53.4×10^4 km^2 (the expansion rate is about 160%), and the LAP has also increased from less than 25% in 2000 to 63% in 2019.

For the spatial distribution of light pixels, it can be found that high brightness light pixels are mainly distributed in coastal cities, especially in the Yangtze River Delta and Pearl River Delta. Another noteworthy feature is that during the study period, the nighttime light pixels continued to expand from the coast to the inland. In year 2000, most of the light pixels were concentrated in coastal cities, while in 2019, the number of light pixels in non-coastal cities increased significantly, especially in North China in the middle and north of the coastal zone. Through comparison, we find that the main feature of the light change in coastal cities is the rapid increase of high brightness light pixels, while the main feature of non-coastal cities is the expansion of lighting area and the proliferation of light pixels.

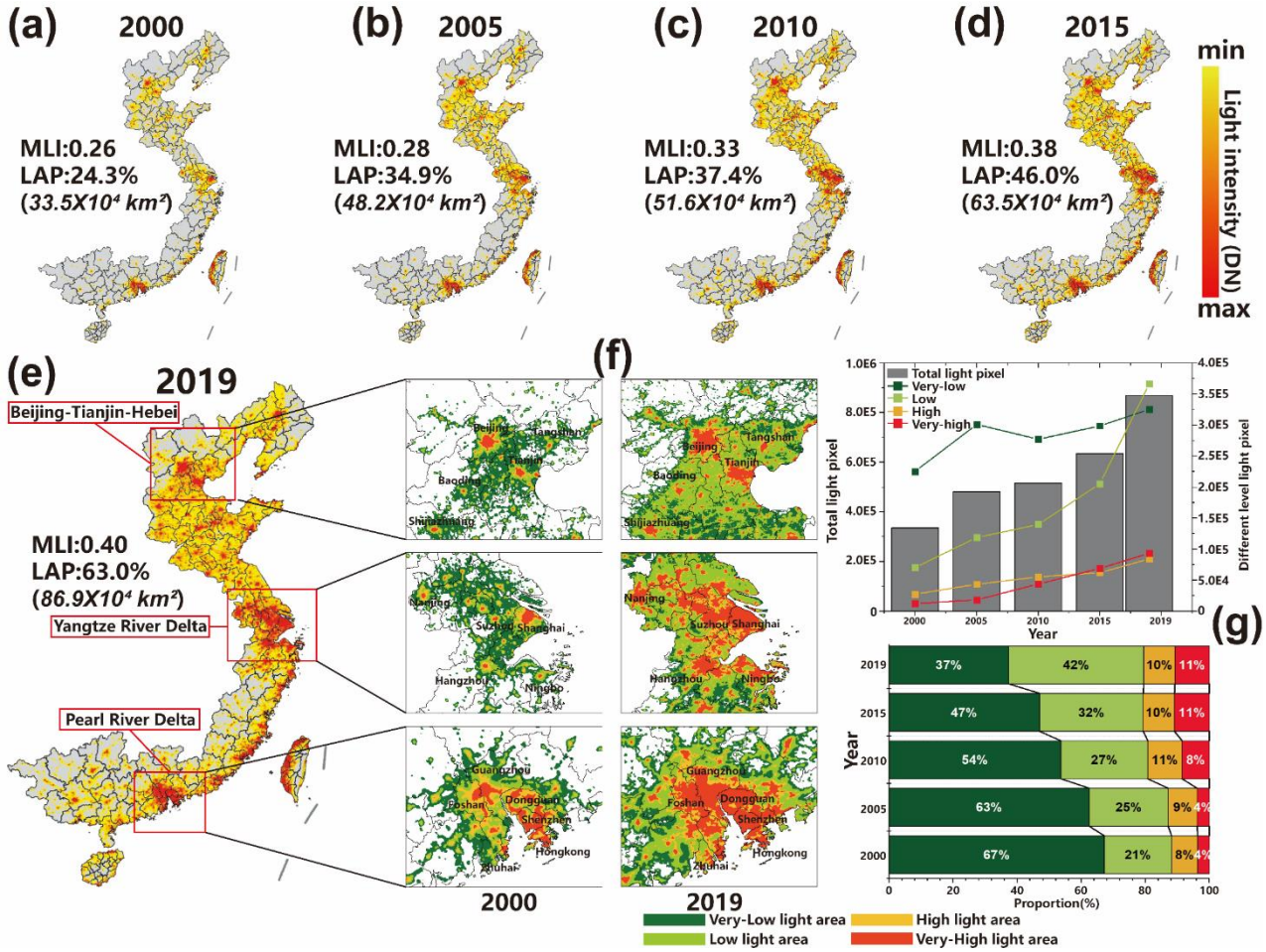

Figure 7.4. Coastal zone light images and its changes from 2000 to 2019.

Besides, to reveal the internal differences of light intensity changes in the past 20 years, this paper divides the DN value of light image into four levels: Very-low light, Low light, High light and Very-high light. Figure 7.4(f) shows the distribution of different levels of light intensity in 2000 and 2019 for the three largest urban agglomerations (the largest light pixel gathering area) in the coastal zone of China. During the study period, the Very-high light area continued to expand outward from the center of the core city, and connected with the center of the surrounding cities, with remarkable area expansion. At the same time, the light intensity in the Very-low light area keeps rising and transforms into Low light on a large scale, continuously extending to the surroundings and shaping the new boundaries of the light area. To quantitatively evaluate the difference in the expansion of light pixels, the number and proportion of light pixels under four levels are counted in this paper (Figure 7.4(g)). The results show that the number of light pixels in the four levels keeps substantial growth, of which the growth of Low light pixels is the most prominent, and for the first time exceeds the number of Very-low light pixels in 2019. In terms of the proportion of the light pixels, except the proportion of Very-low light continues to decrease (by 30%), the proportion of the remaining three levels of pixels has increased. It is worth pointing out that the proportion of pixels in Low light and Very-high light has increased markedly (by 21% and 7%, respectively), while the proportion of pixels in High light intensity has increased slightly, only 2%.

(2) CNLI changes in prefecture-level cities

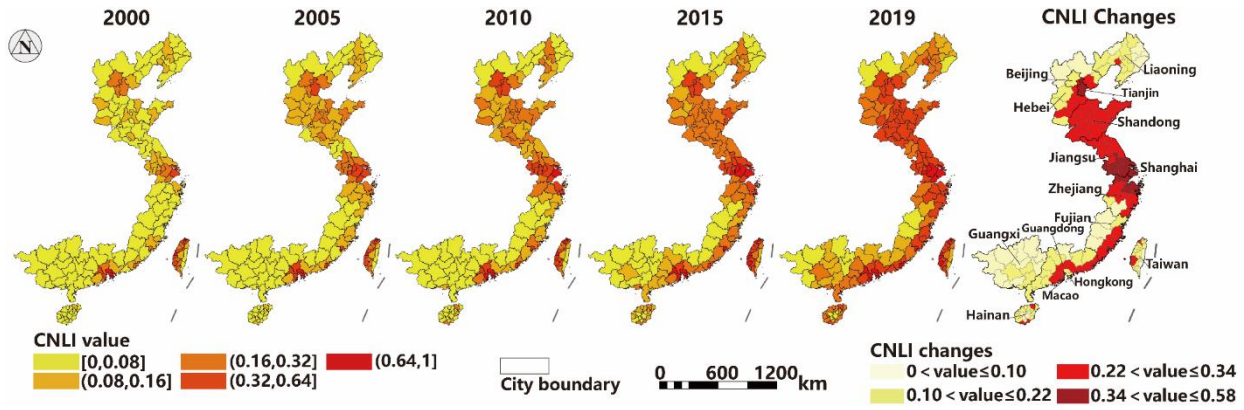

Figure 7.5. CNLI in prefecture-level cities and its changes.

According to the constructed CNLI model, the CNLI of each unit and its changes on the scale of the prefecture-level city are calculated, as shown in Figure 7.5. Compared with 2000, after 20 years of rapid urban development, CNLI in all coastal cities has increased. The CNLI change gradient of the city units shows that there are 28 CNLI lowest-growth cities (0 <increased CNLI≤0.1), accounting for 18.5% of all cities; 51 CNLI low-growth cities (0.1 <increased CNLI≤0.22), accounting for 33.8% of all cities; 55 cities with high-increase of CNLI (0.22 <increased CNLI≤0.34), accounting for approximately 36.4%; 17 cities with highest-increase of CNLI (0.34 <increased CNLI≤0.1), accounting for 11.3% of all units. According to the spatial distribution of four types of cities, the highest and high-growth cities, which growth rate exceeds the average level can be divided into two types, one is coastal cities of each province, and the other is Shandong and Jiangsu Prefecture-level cities. Coastal cities are mostly regional central cities or administrative centers, which have attracted many migrants and investment in the past 20 years, bringing motivation and resources for urbanization. The accelerated urbanization process and the expansion of impervious surfaces cause the rise of CNLI in the region. For Jiangsu Province and Shandong Province, according to the data released by the China Statistics Bureau, Guangdong Province, Jiangsu Province and Shandong Province were the top three provinces in terms of GDP and regional electricity consumption between 2000 and 2018. However, considering the differences in the size of provinces, Jiangsu and Shandong show a faster growth rate of GDP and electricity consumption. The sound economic foundation and geographical advantages have enabled Shandong and Jiangsu provinces to rapidly develop into China's most dynamic regions with close economic levels in the past 20 years (Guo et al., 2016; Liu et al., 2019), which has shown a higher growth rate in CNLI.

7.5.3 Interaction between eco-environment and urbanization

(1) CCD changes in the coastal zone

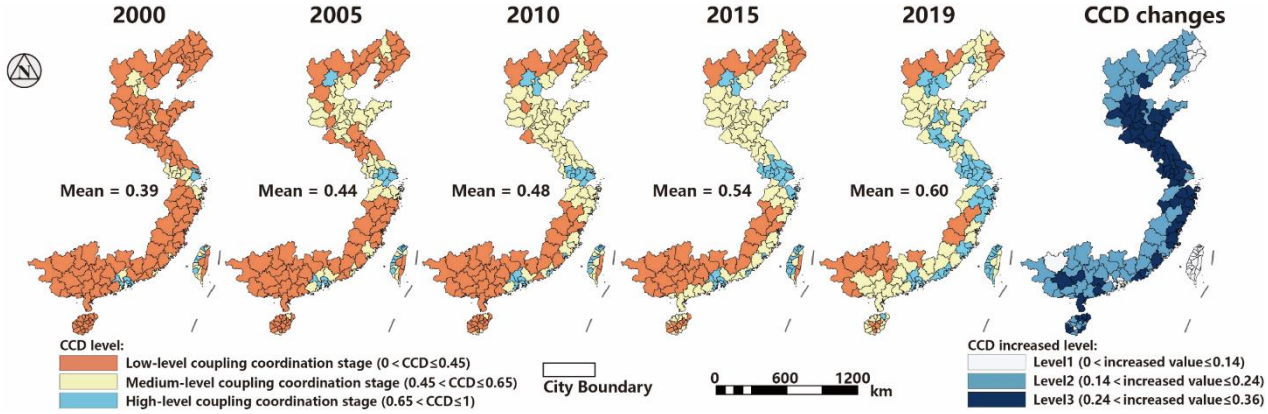

Figure 7.6. The CCD and its changes in the coastal zone.

Based on the calculated RSEI and urbanization characterization factors CNLI of each city, this paper generates CCD of prefecture-level cities in the coastal zone of China according to Eq. 7.8-7.9, as shown in Figure 7.6. In general, from 2000 to 2019, the CCD between RSEI and CNLI showed an upward trend, which means that the coupled and coordinated development of the ecological environment and urbanization of coastal zones has improved. Specifically, CDD continued to rise at a rate of approximately 0.01 per year, from 0.39 in 2000 to 0.6 in 2019, an increase of more than 50%. The continuous and steady rise of CCD indicates that the eco-environment and urbanization of coastal cities are undergoing a healthy development process.

To facilitate the analysis of the coupling coordination characteristics of the urban RSEI and CNLI, similarly, we divided the CCD of the prefecture-level city into three levels, namely the Low-level coupling coordination stage, which CCD is lower than 0.45; the Medium-level coupling coordination stage, which CCD is between 0.45 and 0.65; the High-level coupling coordination stage, which CCD is higher than 0.65. In year 2000, there are only 13 cities (9%) in the stage of High-level coupling, while the cities in the stage of Low-level coupling dominated, reaching 76% (Figure 7.7). In year 2005, the number of cities in the Low-level coupling stage decreased to 80, accounting for more than 50%, and the number of cities in the Medium-level coupling stage reached 51, an increase of more than double. In year 2010, the number of Low-level coupling cities continued to decline, accounting for less than 50% for the first time, and the Medium-level coupling cities continued to rise and exceeded the Low-level coupling cities for the first time. In year 2019, the portion of High-level coupling cities has increased significantly, accounting for nearly 40%, while the Low-level coupling cities have continued to decrease, less than 20%, and the Middle-level coupling cities has stabilized at about 45%.

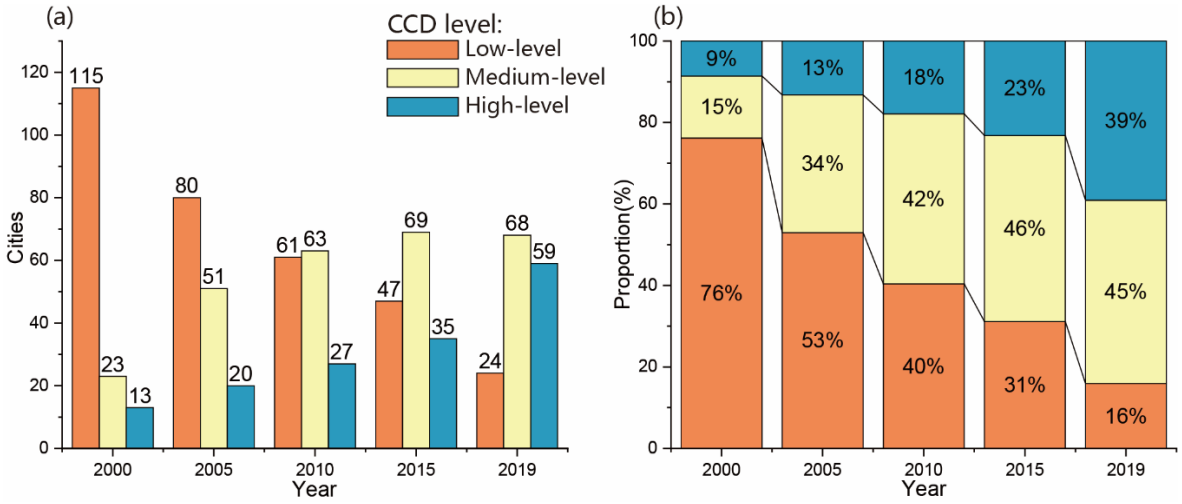

Figure 7.7. The quantity and proportion change of graded CCD.

In the past 20 years, the city's CCD has not only changed in absolute value and proportion, but also have differences in their spatial distribution. In year 2000, the Low-level coupling of coastal cities accounted for the vast majority, while the number of High-level coupling cities was small and mainly distributed in the Yangtze River Delta, Pearl River Delta and Taiwan. In year 2019, the High-level coupling cities reached about 40%, and the distribution area has expanded significantly, including the Pearl River Delta, Yangtze River Delta, Beijing-Tianjin-Hebei, Zhejiang-Fujian, and western Taiwan, while the Low-coupling cities that account for only 16% are mainly distributed on the west side (far-seaside) of the coastal zone, including northwestern Guangxi, western Fujian, and northern Hebei Province. Furthermore, the distribution of CCD change values shows that there is a significant spatial concentration of CCD growth values between cities, that is, areas with substantial growth (Level 3) are concentrated in Jiangsu, Shandong, Zhejiang and Fujian, while the low slight growth (Level 1) cities are mainly located in Liaoning and Taiwan Province.

(2) Response of RSEI to nighttime light change

This paper analyzes the characteristics of the RSEI and its components with the light intensity gradient to explore the impact of urbanization on eco-environment in coastal areas. Figure 7.8(a- e) shows the fluctuation of the mean values of RSEI and environmental components under different light intensity in 2000, 2005, 2010, 2015 and 2019. The results show that: 1) the average values of RSEI and EVI have the same fluctuation characteristics under the light gradient, that is: with the increase of light intensity, the regional eco-environment conditions and vegetation coverage have a downward trend; 2) with the increase of light intensity, LST, NDBSI and Wetness all show a synchronous upward trend. Furthermore, Figure 7.8(f) shows the R^2 and absolute coefficients of RSEI and its components linearly varying with the intensity gradient from 2000 to 2019. On the one hand, the results of R^2 indicate that RSEI, EVI, and LST are highly linearly correlated with light intensity (both above 0.8), followed by humidity (about 0.7), and the correlation between NDBSI and light intensity is increasing during the study period. On the other hand, the upward trend of the absolute value of the coefficient indicates that the influence of human activities on the composition and RSEI has deepened during the study period.

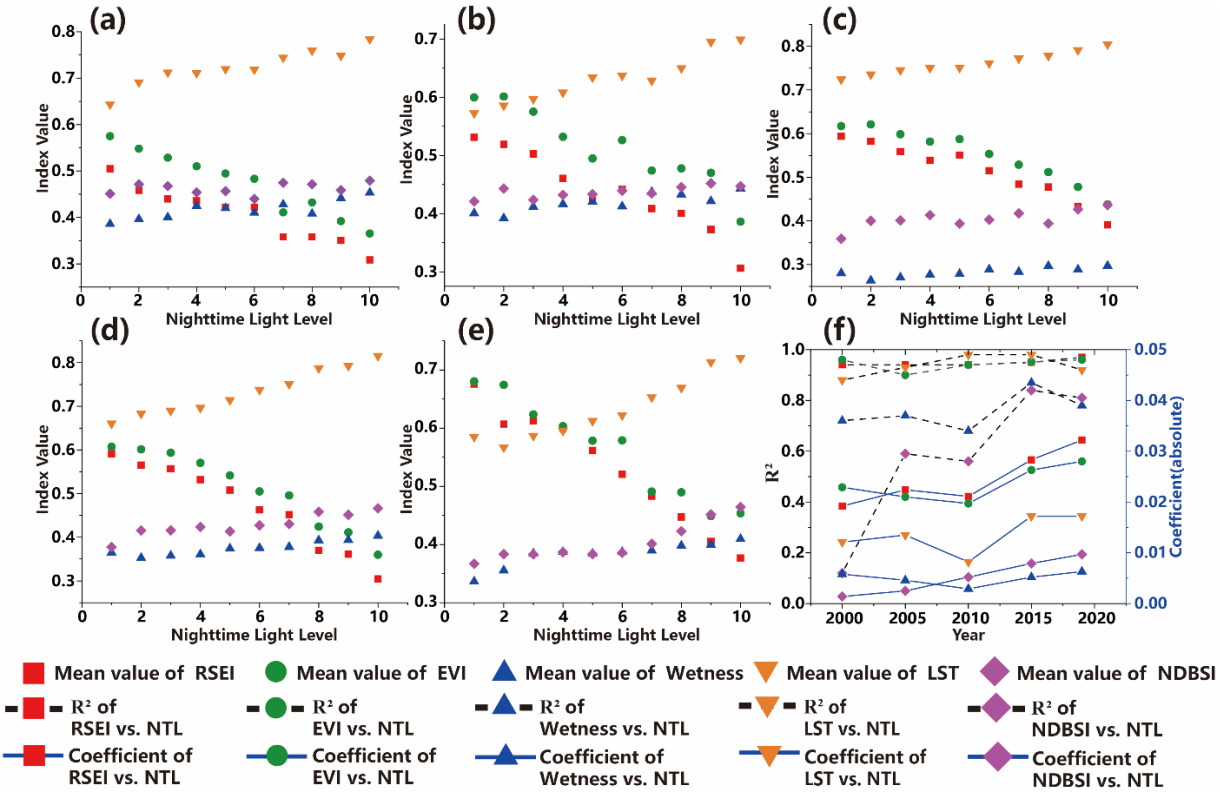

Figure 7.8. The mean value of RSEI and 4 factors at nighttime light intensity gradient.

In addition, this paper further compares the mean value and change of RSEI under the light gradient in the study period to reveal the interference of different urbanization levels on the eco-environment (RSEI). Figure 7.9(a) compares the mean value of RSEI under light gradient in 2000 and 2019, and the result shows that although the RSEI in 2019 is higher than that in 2000, the growth of RSEI decreases with the increase of light intensity. Figure 7.9(b) depicts the RSEI changes in the weakest and strongest light intensity regions in different years, indicating that during the study period, the RSEI in the region with the weakest light intensity increased relatively steadily, while the region with the highest light intensity changed slightly. In general, the results of RSEI and its components changes with the light gradient can reflect the impact of urbanization level on the eco-environment. Especially for RSEI, which represents the comprehensive ecological situation of the region, although the overall ecological environment of the coastal zone has been improved in recent 2 decades, the inhibition of urbanization process on the eco-environment still exists, which is not optimistic.

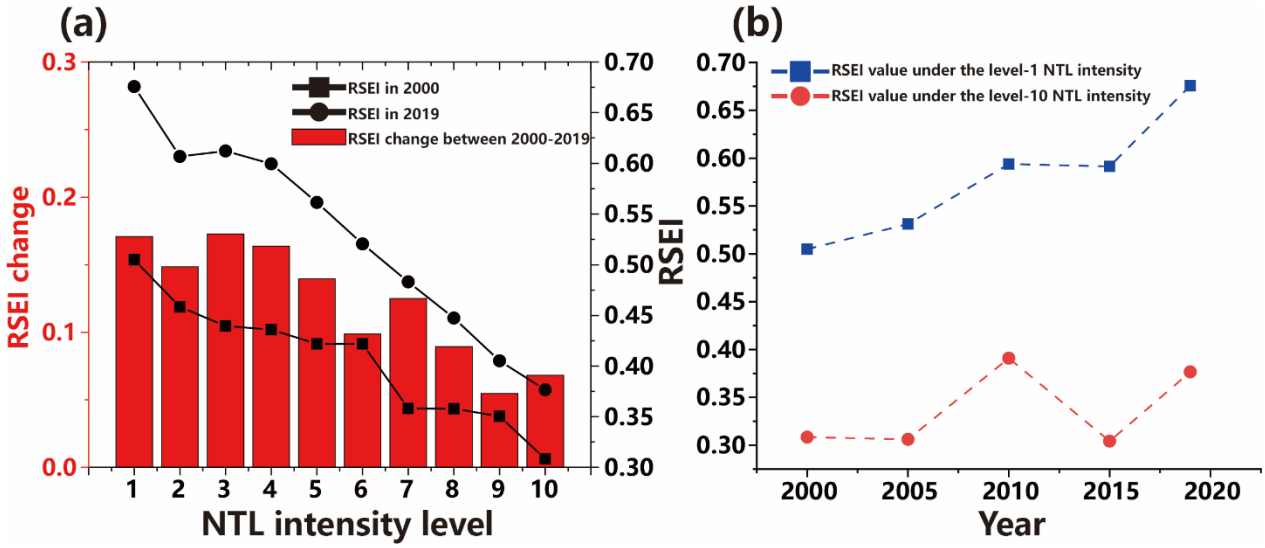

Figure 7.9. Comparison of RSEI changes under different light intensity.

7.6 Discussion

7.6.1 Improvement of coastal ecological environment

Through the statistics of the average RSEI of the provinces and cities in the past 2 decades, it is an indisputable fact that the overall eco-environment of the coastal zone of China is gradually improving. During the study period, the average RSEI value has increased by 17%, and the area with the ecological status of "Good" and "Natural" has increased by nearly 200% and 1500%, respectively. The negative effects that urbanization and the expansion of impervious surfaces will have on regional ecosystems have been well documented in numerous studies (Chithra et al., 2015; Du and Huang, 2017). However, the results of this paper show that the coastal zone, as one of the most rapidly urbanizing areas in the world, is showing some improvement in ecological conditions with urbanization, which is a deviation from the previous perception. Generally, the relationship between human activities (urbanization) and eco-environment is not always a simple negative correlation, but there is a complex interaction when human intervention is involved (Ariken et al., 2020). As urbanization and environmental pressures rise worldwide, sustainability development has become one of the key themes around the world. The successive formulation of the Millennium Development Goals (MDGs) and the Sustainable Development Goals (SDGs) has prompted efforts to balance regional development and environmental protection, especially for rapidly developing and emerging developing countries (Griggs et al., 2013; Hickel, 2019). As the largest developing country and a fast-growing economy, China promulgated a series of guidelines and policies after the millennium to protect and restore the eco-environment affected by the rapid urbanization process (Wang et al., 2013; Naustdalslid, 2014; Zhao et al., 2016). Therefore, we speculate that the intervention of anthropogenic regulatory measures has fairly reversed the natural trend of regional ecological degradation (with urbanization) and has shaped the upward trend of RSEI in the coastal zone. Also, according to statistics, China's total investment in environmental pollution control is 953.9 billion yuan, 7.2 times higher than that in 2001, with an average annual growth rate of 14.0%,

which also supports the above speculation.

Although the overall ecological status of the coastal zone shows a trend of improvement, it still has spatial heterogeneity. The RSEI rising units (eco-environment has improved) are mainly distributed in Shandong, Hebei, Tianjin and Beijing in the north-central part of the coastal zone. Since these areas are located in northern China and dominated by plains, the vegetation coverage, especially forest resources, is insufficient, unevenly distributed and low quality compared to southern China. However, after 2000, with the promotion of "Ecological Civilization Construction" and the strengthening of environmental protection awareness, the vegetation coverage in this area has increased significantly (Li et al., 2017; Yan et al., 2019). Then, considering the contribution of EVI to RSEI, the improvement in vegetation coverage has driven the rise of RSEI. Conversely, the number of units that have experienced RSEI attenuation (ecological deterioration) over the past 2 decades has been significantly reduced and scattered, including the Yangtze River Delta, the Pearl River Delta, southwestern Hainan, and Taiwan. Due to the better climatic and hydrological conditions, the initial ecological conditions in the above areas are better than those in the northern coastal zone. However, during the study period, with the rapid development of economy and urban expansion, on the urban scale, the impervious surface has occupied more and more ecological land and resulting in the decline of vegetation coverage and ultimately affecting the regional RSEI.

7.6.2 Urbanization process of coastal cities

As the pioneer area of China's reform and opening-up policy, the coastal cities of China have been expanding in recent decades, and the transportation network and communication network have developed rapidly (Duan et al., 2018; Xu et al., 2018b). According to the CNLI statistics of the coastal zone, the rapid increase in the area and intensity of nighttime lights is a side reflection of eastern China's rapid urbanization process and economic development in the past 20 years. Since the 21st century, China has set up nearly 20 national development strategies in coastal areas, and now the coastal zone has become the "golden zone" of regional social and economic development. Under the one belt, one road development strategy, the coastal zone is the first marine economic zone, which has become a new engine to promote the economic development of our country.

Although the urbanization level of coastal cities is constantly improving, the imbalance of urbanization level among regions is still prominent. An interesting comparison is from Guangdong Province and Jiangsu Province. Since 1989, Guangdong's GDP has consistently ranked first in the country and has become China's largest economic province, with the total economic output accounting for 1/8 of the country (Zhang et al., 2008). Jiangsu is located in the Yangtze River Economic Belt, and has been closely following Guangdong in the GDP ranking since 2000, ranking second. However, the growth rate of Jiangsu's CNLI and the area of the lighting area are obviously higher than those of Guangdong Province in the past 20 years. Although Guangdong has the highest GDP, its contribution mainly comes from the core areas (Guangzhou and Shenzhen). The urbanization level in the north, west and east of Guangdong Province is low, and the urban development is

unbalanced. For Jiangsu Province, profit by the topographical advantages, multiple urban agglomerations can be formed in the south. Cities can not only be linked in economic ties, but also maintain independence in economic volume, population and geographical space. Compared with Guangdong Province, the level of urbanization in Jiangsu is more balanced, and there is no absolutely dominant area.

7.6.3 Interaction between urbanization and eco-environment

With the rapid development of the economy, the impact and pressure of urbanization on eco-environment are more obvious, and the constraint and restriction of eco-environment on urbanization are more prominent (Liu and Wang, 2015). Especially for the coastal zone, the excellent economic development foundation and huge employment market have greatly attracted the employment-population from the inland areas of China. It is worth acknowledging that the findings of this paper show that the coupling and coordinated development level between urbanization and eco-environment in China's coastal zone is constantly improving. At present, the sustainable development of cities has become the mainstream. As mentioned earlier, governments at all levels have continuously introduced new policies and measures to strengthen the protection of the ecological environment.

It is worth noting that although the ecological environment quality of the whole coastal zone shows a trend of improvement, our research confirms that the contribution of this improvement is mostly from non-urbanized areas rather than urbanized areas. The decline effect of the increase of RSEI on the light intensity gradient reflects the limitations of the current environmental protection measures in coastal areas. For the urbanized areas, the pressure of population and economic development causes the ecological land to be occupied by impervious surfaces, and gradually leads to a series of urban ecological environment problems including heat island effect, air pollution. For the non-urbanized areas, due to the loss of population, the establishment of ecological protection zones and afforestation, the ecological conditions in areas with low human activity have been gradually restored in recent years.

At present, China’s urbanization has entered a period of accelerated development, and the agglomeration of population and industry has put forward greater demand for urban land area, making China one of the countries with the fastest expansion of urban land in the world. Considering the long-term existence of urban-rural differences in China, the urban resource concentration-effect continues to maintain, and spatial expansion is still one of the main trends in the future development of coastal cities. The demand for land in the urban development process is still severe, and the coercive effect of construction land on the eco-environment will not disappear in the short term. Therefore, how to optimize the allocation of limited land resources and realize the coordinated development of urban expansion and urban ecology will be the severe challenges facing land use in China. To realize the sustainable development of the city and construct the ecological city, it is necessary to improve the overall ecological environment while paying more attention to the improvement of the ecological environment within the city, and rationally allocate and optimize the green space within the city (parks, water bodies, greenways, etc.) to coordinated eco-environment and human activities.

7.6.4 Potentials and limitations

Since RSEI was proposed by Xu (2013), application analysis based on RSEI is being enriched. Due to the advantages in data accessibility and model robustness, RSEI has been steadily applied across a wide range of temperature zones and climatic conditions, such as subtropical monsoon climate (Wen et al., 2020), temperate monsoon climate (Xu et al., 2018a), temperate continental climate (Jing et al., 2020). Although the climatic conditions and geographical locations of the above study area are diverse, the studies are mostly focused on small-scale studies due to the resolution of the selected satellite images (Landsat TM/OLI, Sentinel-2). Therefore, the development of new satellite data sources for RSEI-based environmental assessment studies deserves to be further promoted. As a representative of medium resolution satellite imagery, MODIS imagery has good data quality and short revisit intervals, making it the preferred data source for medium scale RSEI-based environmental assessments. This paper validates the stability and feasibility of the RSEI model in a medium-scale environmental assessment scenario by integrating multiple MODIS standard data products for a long time series of ecological and environmental assessments of China's coastal zone.

The RSEI model used in this paper is completely based on remote sensing images and can comprehensively represent the ecological environment of the region by integrating a variety of ecological factors (green, humidity, temperature, dryness). However, the model is completely based on the satellite image, which means that remote sensing images will also produce systematic errors due to different sensors and transit time. Although, to ensure the comparability of the inverted RSEI in different years, the image selection time window is reduced as much as possible to avoid cloud interference, but it still cannot completely guarantee that the acquisition time of images in different years is completely the same.

Although RSEI and CNLI have been widely used in regional eco-environment detection and urbanization research by many scholars, the interaction between urbanization and eco-environment still cannot be explained in essence due to the limited spatial resolution of data and model parameters. We believe that introducing multi-dimensional parameters (including economy, population, environmental protection policies, etc.) to improve the indicator system of ecological environment and urbanization level, which can more comprehensively reveal the relationship between environment and urban development will be the next breakthrough point.

7.7 Conclusion

Remote sensing technology is of great value to the detection of eco-environment, and has been widely used in recent years. However, long-term large-scale analysis and assessment of ecological-urbanization interactions remain a challenge due to the limitations of data and analytical models. Therefore, this study proposes a detection scheme that combines daytime remote sensing and nighttime remote sensing, which can effectively characterize the regional eco-environment conditions, the intensity of urbanization, and the coupling and interaction between them. Specifically, this paper assesses the ecological condition and

urbanization intensity of the coastal zone of China over the past 20 years based on nighttime light data (DMSP/OLS and NPP/VIIRS) and MODIS images, and recognizes the intensity and characteristics of the impact of human activities on the ecological environment through a coupled model. Compared with other ecological evaluation models, the most prominent advantage of this scheme is the diversity of data sources and the less subjective intervention, which is suitable for large-scale time series analysis.

The results of this study show that: **1)** in the past 2 decades, the RSEI value of China's coastal areas has increased year by year, and the eco-environment has improved, especially for the cities in the north; **2)** the city maintained a high rate of urbanization during the study period, especially for seaside cities and prefecture-level cities in Jiangsu and Shandong, which were much higher than the average growth rate; **3)** although the coupling degree of urbanization and eco-environment of coastal cities is constantly improving, the main contribution of environmental improvement comes from the non-urbanization areas with low light intensity, while the eco-environment pressure of urbanization areas with high human activity intensity is still not optimistic.

Acknowledgments: This research was financially supported by the National Natural Science Foundation of China (No.41671430), Key Special Project for Introduced Talents Team of Southern Marine Science and Engineering Guangdong Laboratory (Guangzhou) (No. GML2019ZD0301) and NSFC-Guangdong Joint Fund (No. U1901219).

References

Agardy, T. & Alder, J., (2005) Coastal Systems, in: R., in: Hassan, R.S., Ash, N. (Eds.), Ecosystems and Human Well-being: Current State and Trends. ISLANDPRESS, Washington, pp. 513-549.

Alatorre, L.C., Sánchez-Andrés, R., Cirujano, S., Beguería, S. & Sánchez-Carrillo, S. (2011) Identification of mangrove areas by remote sensing: The ROC curve technique applied to the northwestern Mexico coastal zone using Landsat imagery. Remote Sensing 3, 1568-1583.

Anwar, M.S. & Takewaka, S. (2014) Analyses on phenological and morphological variations of mangrove forests along the southwest coast of Bangladesh. Journal of Coastal Conservation 18, 339-357.

Ariken, M., Zhang, F., Liu, K., Fang, C. & Kung, H.-T. (2020) Coupling coordination analysis of urbanization and eco-environment in Yanqi Basin based on multi-source remote sensing data. Ecological Indicators 114, 106331.

Arnous, M.O. & Green, D.R. (2011) GIS and remote sensing as tools for conducting geo-hazards risk assessment along Gulf of Aqaba coastal zone, Egypt. Journal of Coastal Conservation 15, 457-475.

Aslan, A., Rahman, A.F., Warren, M.W. & Robeson, S.M. (2016) Mapping spatial distribution and biomass of coastal wetland vegetation in Indonesian Papua by combining active and passive remotely sensed data. Remote Sensing of Environment 183, 65-81.

Baig, M.H.A., Zhang, L., Shuai, T. & Tong, Q. (2014) Derivation of a tasselled cap transformation based on Landsat 8 at-satellite reflectance. Remote sensing letters 5, 423-431.

Bank, W., (2019) Forest area (sq.km)-China, pp. 18-20.

Behling, R., Bochow, M., Foerster, S., Roessner, S. & Kaufmann, H. (2015) Automated GIS-based derivation of urban ecological indicators using hyperspectral remote sensing and height information. Ecological Indicators 48, 218-234.

Bird, M., Chua, S., Fifield, L.K., Teh, T.S. & Lai, J. (2004) Evolution of the Sungei Buloh–Kranji mangrove coast, Singapore. Applied Geography 24, 181-198.

Bui, T.D., Maier, S.W. & Austin, C.M. (2014) Land cover and land use change related to shrimp farming in coastal areas of Quang Ninh, Vietnam using remotely sensed data. Environmental earth sciences 72, 441-455.

Caccamo, G., Chisholm, L., Bradstock, R.A. & Puotinen, M. (2011) Assessing the sensitivity of MODIS to monitor drought in high biomass ecosystems. Remote Sensing of Environment 115, 2626-2639.

Cao, W. & Wong, M. (2007) Current status of coastal zone issues and management in China: a review. Environment International 33, 985-992.

Chen, G. & Wang, Y. (2003) Some Issues in the Integrated Coastal Management [J]. Marine Science Bulletin 3.

Chen, J., Zhuo, L., Shi, P.-J. & Toshiaki, I. (2003) The study on urbanization process in China based on DMSP/OLS data: Development of a light index for urbanization level estimation. Journal of Remote Sensing 7, 168-175.

Chen, Y., Wu, Z., Qian, Q., Zheng, Z. & Han, F., (2016) Dynamic monitoring and spatiotemporal evolution of the coastline in Pearl River estuary in recent fifty years, 2016 4th International Workshop on Earth Observation and Remote Sensing Applications (EORSA). IEEE, pp. 87-91.

Chithra, S., Nair, M.H., Amarnath, A. & Anjana, N. (2015) Impacts of impervious surfaces on the environment. International Journal of Engineering Science Invention 4, 27-31.

Chu, L., Huang, C., Liu, Q. & Liu, G. (2015) Changes of coastal zone landscape spatial patterns and ecological quality in Liaoning Province from 2000 to 2010. Resources Science 37, 1962-1972.

Crist, E.P. (1985) A TM tasseled cap equivalent transformation for reflectance factor data. Remote Sensing of Environment 17, 301-306.

Crossland, C.J., Baird, D., Ducrotoy, J.-P., Lindeboom, H., Buddemeier, R.W., Dennison, W.C., . . . Swaney, D.P., (2005) The coastal zone—a domain of global interactions, Coastal fluxes in the Anthropocene. Springer, pp. 1-37.

DataBase, I., (2019) Enhanced Vegetation Index. Island Press, Washington, Covelo, London.

de Araujo Barbosa, C.C., Atkinson, P.M. & Dearing, J.A. (2015) Remote sensing of ecosystem services: A systematic review. Ecological Indicators 52, 430-443.

Di, X., Hou, X. & Wu, L. (2014) Land use classification system for China's coastal zone based on remote sensing. Resources Science 36, 463-472.

Du, X. & Huang, Z. (2017) Ecological and environmental effects of land use change in rapid urbanization: The case of hangzhou, China. Ecological Indicators 81, 243-251.

Duan, P., Liu, S., Yin, P. & Zhang, H. (2018) Spatial-temporal coupling coordination relationship between development strength and resource environmental bearing capacity of coastal cities in China. Economic Geography 35, 60-67.

Fan, X., Yuan, L., Zhang, L. & Zou, W. (2010) The integrated coastal zone management (ICZM) and its progress. Acta Ecologica Sinica 30, 2756-2765.

Feng, Y. & Han, Z. (2011) RS and GIS derived spatio-temporal evolution of water landscape in coastal areas: a case study of Shanghai section on the northern bank of Hangzhou Bay. Remote Sens Land Resour 22, 123-127.

Gillespie, T.W., Ostermann-Kelm, S., Dong, C., Willis, K.S., Okin, G.S. & MacDonald, G.M. (2018) Monitoring changes of NDVI in protected areas of southern California. Ecological Indicators 88, 485-494.

Gong, C., Chen, Q., Yin, Q., Kuang, D. & Wang, J. (2011) Evaluation of eco-environment basic quality in coastal zone by remote sensing technique-case study of Nanhui east tidal flat. Marine Environmental Science 30, 711-714.

Griggs, D., Stafford-Smith, M., Gaffney, O., Rockström, J., Öhman, M.C., Shyamsundar, P., . . . Noble, I. (2013) Sustainable development goals for people and planet. Nature 495, 305-307.

Guneroglu, A. (2015) Coastal changes and land use alteration on Northeastern part of Turkey. Ocean & Coastal Management 118, 225-233.

Guo, X., Yan, Q., Tan, X. & Liu, S. (2016) Spatial distribution of carbon emissions based on DMSP/OLS nighttime light data and NDVI in Jiangsu province. World Regional Studies 25, 102-110.

He, P. (2017) Discussion on system improvement of coastal wetland conservation. Environmental Protection 45, 18-20.

Hepcan, C.C. (2013) Quantifying landscape pattern and connectivity in a Mediterranean coastal settlement: the case of the Urla district, Turkey. Environmental monitoring and assessment 185, 143-155.

Hickel, J. (2019) The contradiction of the sustainable development goals: Growth versus ecology on a finite planet. Sustainable Development 27, 873-884.

Hou, X., Di, X., Hou, W., Wu, L., Liu, J., Wang, J., . . . Yu, X. (2018) Accuracy evaluation of land use mapping using remote sensing techniques in coastal zone of China. Journal of Geo-Information Science 20, 1478-1488.

Hu, X. & Xu, H. (2018) A new remote sensing index for assessing the spatial heterogeneity in urban ecological quality: A case from Fuzhou City, China. Ecological Indicators 89, 11-21.

Huang, C., Wylie, B., Yang, L., Homer, C. & Zylstra, G. (2002) Derivation of a tasselled cap transformation based on Landsat 7 at-satellite reflectance. International journal of remote sensing 23, 1741-1748.

Ivits, E., Cherlet, M., Mehl, W. & Sommer, S. (2009) Estimating the ecological status and change of riparian zones in Andalusia assessed by multi-temporal AVHHR datasets. Ecological Indicators 9, 422-431.

Ji, X., Li, X., He, Y. & Liu, X. (2019) A simple method to improve estimates of county-level economics in China using nighttime light data and GDP growth rate. ISPRS International Journal of Geo-Information 8, 419.

Jing, Y., Zhang, F., He, Y., Johnson, V.C. & Arikena, M. (2020) Assessment of spatial and temporal variation of ecological environment quality in Ebinur Lake Wetland National Nature Reserve, Xinjiang, China. Ecological Indicators 110, 105874.

Ju, Y., Dronova, I., Ma, Q. & Zhang, X. (2017) Analysis of urbanization dynamics in mainland China using pixel-based night-time light trajectories from 1992 to 2013. International journal of remote sensing 38, 6047-6072.

Li, X., Wang, F., Yao, Y., Wen, H. & Xue, Z. (2015) An analysis on landscape pattern changes and its driving forces of coastal wetland in Zhuanghe city based on GIS. Bulletin of Soil and Water Conservation 35, 159-162.

Li, X. & Zhou, W. (2018) Dasymetric mapping of urban population in China based on radiance corrected DMSP-OLS

nighttime light and land cover data. Science of the Total Environment 643, 1248-1256.

Li, Z., Sun, R., Zhang, J. & Zhang, C. (2017) Temporal-spatial analysis of vegetation coverage dynamics in Beijing-Tianjin-Hebei metropolitan regions. Acta Ecologica Sinica 37, 7418-7426.

Liao, L., Dai, W., Huang, F. & Hu, Q. (2018) Coupling coordination analysis of urbanization and eco-environment system in Jinjiang using Landsat series data and DMSP/OLS nighttime light data. Journal of Fujian Normal University (Natural Science Edition) 34, 94-103.

Liu, Y., Li, R. & Song, X. (2005) Analysis of coupling degrees of urbanization and ecological environment in China. Journal of Natural Resources 20, 105-112.

Liu, Y. & Wang, S. (2015) Coupling coordinative degree and interactive coercing relationship between urbanization and eco-environment in Pearl River Delta. Human Geography 30, 64-71.

Liu, Z., Liu, L. & Zou, J. (2019) Hierarchical spatial modeling of county GDP in Shandong province based on NPP-VIIRS data. Bulletin of Surveying and Mapping, 114.

Lo, K.F.A. & Gunasiri, C.W. (2014) Impact of coastal land use change on shoreline dynamics in Yunlin County, Taiwan. Environments 1, 124-136.

Luo, Y. (2016) Sustainability associated coastal eco-environmental problems and coastal science development in China. Bulletin of Chinese Academy of Sciences 31, 1133-1142.

Maselli, F. (2004) Monitoring forest conditions in a protected Mediterranean coastal area by the analysis of multiyear NDVI data. Remote Sensing of Environment 89, 423-433.

Naustdalslid, J. (2014) Circular economy in China–the environmental dimension of the harmonious society. International Journal of Sustainable Development & World Ecology 21, 303-313.

Ning, L., Ma, L., Zhou, Y. & Bai, X. (2016) Spatiotemporal variations of ecosystem health of the coastal zone in Jiangsu Province based on the PSR model. China environment science 36, 534-543.

Qin, Q., Zhu, L., Ghulam, A., Li, Z. & Nan, P. (2008) Satellite monitoring of spatio-temporal dynamics of China's coastal zone eco-environments: preliminary analysis on the relationship between the environment, climate change and human behavior. Environmental geology 55, 1687-1698.

Rikimaru, A., Roy, P. & Miyatake, S. (2002) Tropical forest cover density mapping. Tropical ecology 43, 39-47.

Seddon, A.W., Macias-Fauria, M., Long, P.R., Benz, D. & Willis, K.J. (2016) Sensitivity of global terrestrial ecosystems to climate variability. Nature 531, 229-232.

Shi, K., Yang, Q., Fang, G., Yu, B., Chen, Z., Yang, C. & Wu, J. (2019a) Evaluating spatiotemporal patterns of urban electricity consumption within different spatial boundaries: A case study of Chongqing, China. Energy 167, 641-653.

Shi, K., Yu, B., Zhou, Y., Chen, Y., Yang, C., Chen, Z. & Wu, J. (2019b) Spatiotemporal variations of CO2 emissions and their impact factors in China: A comparative analysis between the provincial and prefectural levels. Applied Energy 233, 170-181.

Shibly, A.M. & Takewaka, S., (2013) Morphological changes and vegetation index variation along the western coastal zone of Bangladesh, Proceedings of the 7th International Conference on Asian and Pacific Coasts (APAC 2013) Bali, Indonesia.

Sirirwardane, M., Samanmali, M. & Rathnayake, R. (2015) Cloud based GIS approach for monitoring environmental pollution in the coastal zone of Kalutara, Sri Lanka. Journal of Tropical Forestry and Environment 5.

Song, H.M. & Xue, L. (2016) Dynamic monitoring and analysis of ecological environment in Weinan City, Northwest China based on RSEI model. Chinese Journal of Applied Ecology 27, 3913-3919.

Stanley, K.E., Murphy, P.G., Prince, H.H. & Burton, T.M. (2005) Long-term ecological consequences of anthropogenic disturbance on Saginaw Bay coastal wet meadow vegetation. Journal of Great Lakes Research 31, 147-159.

Todd, S.W. & Hoffer, R.M. (1998) Responses of spectral indices to variations in vegetation cover and soil background. Photogrammetric engineering and remote sensing 64, 915-922.

Vatseva, R. (2015) Mapping urban land use and land cover change in the Black Sea coastal zone in Bulgaria for the period

1977-2011 using remote sensing and GIS. Comptes rendus de l'Académie bulgare des Sciences 68, 903-913.
Vorovencii, I. (2015) Quantifying landscape pattern and assessing the land cover changes in Piatra Craiului National Park and Bucegi Natural Park, Romania, using satellite imagery and landscape metrics. Environmental monitoring and assessment 187, 1-22.
Wang, C., Hao, Z., Sun, X., Ren, B. & Yao, S. (2013) Study on the Urbanization Mode and its Path in China Based on the Scientific Development Concept. Urban Development, 01.
Wang, C., Li, W., Chen, S., Li, D., Wang, D. & Liu, J. (2018) The spatial and temporal variation of total suspended solid concentration in Pearl River Estuary during 1987–2015 based on remote sensing. Science of the Total Environment 618, 1125-1138.
Wang, J., Wu, Z., Li, S., Wang, S., Zhang, X. & Gao, Q. (2016) Coastline and land use change detection and analysis with remote sensing in the Pearl River estuary gulf. Scientia Geographica Sinica 36, 1903-1911.
Wen, X., Ming, Y., Gao, Y. & Hu, X. (2020) Dynamic monitoring and analysis of ecological quality of pingtan comprehensive experimental zone, a new type of sea island city, based on RSEI. Sustainability 12, 21.
Weston, N.B., Hollibaugh, J.T. & Joye, S.B. (2009) Population growth away from the coastal zone: Thirty years of land use change and nutrient export in the Altamaha River, GA. Science of the Total Environment 407, 3347-3356.
Wicaksono, A. & Wicaksono, P. (2019) Geometric accuracy assessment for shoreline derived from NDWI, MNDWI, and AWEI transformation on various coastal physical typology in Jepara Regency using Landsat 8 OLI imagery in 2018. Geoplanning Journal of Geomatics and Planning 6, 55-72.
Willis, K.S. (2015) Remote sensing change detection for ecological monitoring in United States protected areas. Biological Conservation 182, 233-242.
Wu, K. & Wang, X. (2019) Aligning pixel values of DMSP and VIIRS nighttime light images to evaluate urban dynamics. Remote Sensing 11, 1463.
Xie, Z., Ye, X., Zheng, Z., Li, D., Sun, L., Li, R. & Benya, S. (2019) Modeling polycentric urbanization using multisource big geospatial data. Remote Sensing 11, 310.
Xu, H. (2008) A new index for delineating built-up land features in satellite imagery. International journal of remote sensing 29, 4269-4276.
Xu, H. (2013) A remote sensing urban ecological index and its application. Acta Ecologica Sinica 33, 7853-7862.
Xu, H., Wang, M., Shi, T., Guan, H., Fang, C. & Lin, Z. (2018a) Prediction of ecological effects of potential population and impervious surface increases using a remote sensing based ecological index (RSEI). Ecological Indicators 93, 730-740.
Xu, H., Wang, Y., Guan, H., Shi, T. & Hu, X. (2019) Detecting ecological changes with a remote sensing based ecological index (RSEI) produced time series and change vector analysis. Remote Sensing 11, 2345.
Xu, L., Li, J., Yuan, Q., Wang, M., Lu, X. & Yang, L. (2015) Landscape pattern evolution of coastal zone around the Xiangshangang Bay. Journal of Marine Sciences 33, 47-56.
Xu, W., Dong, Y., Teng, X. & Zhang, P. (2018b) Evaluation of the development intensity of China's coastal area. Ocean & Coastal Management 157, 124-129.
Yan, S., Wang, H. & Jiao, K. (2019) Spatiotemporal dynamics of NDVI in the Beijing-Tianjin-Hebei region based on MODIS data and quantitative attribution. Journal of Geo-information Science 21, 767-780.
Yu, B., Lian, T., Huang, Y., Yao, S., Ye, X., Chen, Z., . . . Wu, J. (2019) Integration of nighttime light remote sensing images and taxi GPS tracking data for population surface enhancement. International Journal of Geographical Information Science 33, 687-706.
Yuan, F. & Bauer, M.E. (2007) Comparison of impervious surface area and normalized difference vegetation index as indicators of surface urban heat island effects in Landsat imagery. Remote Sensing of Environment 106, 375-386.
Yue, H., Liu, Y., Li, Y. & Lu, Y. (2019) Eco-environmental quality assessment in China's 35 major cities based on remote sensing ecological index. Ieee Access 7, 51295-51311.

Zhai, T., Wang, J., Fang, Y., Qin, Y., Huang, L. & Chen, Y. (2020) Assessing ecological risks caused by human activities in rapid urbanization coastal areas: Towards an integrated approach to determining key areas of terrestrial-oceanic ecosystems preservation and restoration. Science of the Total Environment 708, 135153.

Zhang, C., Xu, H., Zhang, H., Tang, F. & Lin, Z. (2015) Fractional vegetation cover change and its ecological effect assessment in a typical reddish soil region of Southeastern China: Changting County, Fujian Province. Journal of Natural Resources 30, 917-928.

Zhang, H., Ye, Y., Yang, L. & Wu, Q. (2008) Construction land expansion and its contribution to economic growth since reform and opening up in Guangdong province. Economic Geography 28, 904-908.

Zhang, L., Zhang, Y. & Huang, C. (2018) Remote Sensing Index Analysis on Ecological Environment Changes in the Recent 20 Years of City Belt in Wanjiang. Resources and Environment in the Yangtze Basin 27, 126-135.

Zhang, X., Schaaf, C.B., Friedl, M.A., Strahler, A.H., Gao, F. & Hodges, J.C., (2002) MODIS tasseled cap transformation and its utility, IEEE International Geoscience and Remote Sensing Symposium. IEEE, pp. 1063-1065.

Zhang, Y. & Zhu, D. (1997) Coastal zone: the key area of the global change research. Marine Science Bulletin 3, 69-80.

Zhao, Q., Huang, G. & Ma, Y. (2016) The ecological environment conditions and construction of an ecological civilization in China. Acta Ecologica Sinica 36, 6328-6335.

Zheng, Z., Yang, Z., Chen, Y., Wu, Z. & Marinello, F. (2019a) The Interannual Calibration and Global Nighttime Light Fluctuation Assessment Based on Pixel-Level Linear Regression Analysis. Remote Sensing 11, 2185.

Zheng, Z., Yang, Z., Wu, Z. & Marinello, F. (2019b) Spatial variation of NO2 and its impact factors in China: An application of sentinel-5P products. Remote Sensing 11, 1939.

Zhou, Y., Li, X., Asrar, G.R., Smith, S.J. & Imhoff, M. (2018) A global record of annual urban dynamics (1992–2013) from nighttime lights. Remote Sensing of Environment 219, 206-220.

Zoran, M., Zoran, L.F. & Golovanov, C.I., (2010) Opto-Spectral Assessment of North-Western Black Sea Coastal Zone Changes by Satellite Imagery, AIP Conference Proceedings. American Institute of Physics, pp. 1131-1136.

8. Spatial and temporal characteristics of NO_2 pollution in China based on satellite observation platform [7]

8.1 Abstract

As an important tropospheric trace gas and precursor of photochemical smog, the accumulation of NO_2 will cause serious air pollution. China, as the largest developing country in the world, has experienced a large amount of NO_2 emissions in recent decades due to the rapid economic growth. Compared with the traditional air pollution monitoring technology, the rapid development of the remote sensing monitoring method of atmospheric satellite has gradually become the critical technical means of global atmospheric environmental monitoring. To reveal the NO_2 pollution situation in China, based on the latest NO_2 products from Sentinel-5P TROPOMI, the spatial-temporal characteristics and impact factors of troposphere NO_2 column concentration of mainland China in the past year (February 2018 to January 2019) were analyzed on two administrative levels for the first time. Results show that the monthly fluctuation of tropospheric NO_2 column concentration has obvious characteristics of "high in winter and low in summer", while the spatial distribution forms a "high in East and low in west" pattern, bounded by Hu Line. The comparison of Coefficient of Variation (CV) and spatial autocorrelation models at two kinds of administrative scales indicates that although the spatial heterogeneity of NO_2 column concentration is less affected by the observed scale, there is a "delayed effect" of about one month in the process of NO_2 column concentration fluctuation. Besides, the impact factors analysis based on Spatial Lag Model (SLM) and Geographic Weighted Regression (GWR) reveals that there is a positive correlation between nighttime light intensity, the secondary and tertiary industries proportion and NO_2 column concentration. Furthermore, for regions with serious NO_2 pollution in North China Plain, the whole society electricity consumption and vehicle ownership also play a positive role in increasing the NO_2 column concentration. This study will enlighten the government and policy makers to formulate policies tailored to local conditions, to more effectively implement NO_2 emission reduction and air pollution prevention.

Keywords: NO_2; Sentinel-5P; air pollution; spatial autocorrelation; impact factor; China

8.2 Introduction

In the past decades, concomitant with the rapid process of industrialization and urbanization, China's urban construction and socioeconomic development have made remarkable achievements (Guan et al., 2018). At present, China has become the world's most populous country with the second largest economy in the world, especially for eastern China, which has become one of the areas with the most intensive and intense human

[7] This Chapter relies on the paper "Zheng, Z., Yang, Z., Wu, Z., & Marinello, F. (2019). Spatial variation of NO_2 and its impact factors in China: An application of sentinel-5P products. Remote Sensing, 11(16), 1939.". https://doi.org/10.3390/rs11161939.

activities. However, the large-scale urban construction, urban population aggregation, and the rapid growth of the number of motor vehicles accompanied by urban development have led to the deterioration of air quality in urban areas of China, which not only reduces the visibility of the urban atmosphere, but also causes great harm to human health, thus threatening the sustainable development of economy and society. Among the various atmospheric pollutants, the large-scale emission of NO_X (mainly including NO_2 and NO) in China makes the concentration and growth rate of NO_2 in the troposphere at a higher level, which is much higher than other countries and regions (Richter et al., 2005; Van Der A et al., 2006; Schneider et al., 2015; Duncan et al., 2016; Georgoulias et al., 2019). As an important trace gas, NO_2 is mainly distributed in the troposphere and stratosphere, and plays an important role in the stratospheric and tropospheric atmospheric chemistry. NO_2 is not only the main air pollution gas, but also an important precursor of ozone, acid rain, and photochemical smog. The nitrate aerosols produced by NO_2 have significant radiation forcing, which makes NO_2 an important factor in climate change (Steinfeld, 1998). Especially, since the middle of the 20th century, the emission of NO_2 has increased dramatically, and the concentration of NO_2 in the atmosphere has also increased continuously, which has a great negative impact on human health, ecological environment, biochemical cycle, tropospheric atmospheric composition, and air quality (Crutzen, 1979; Crutzen and Schmailzl, 1983; Lee et al., 1997; Change, 2007).

Generally, the sources of NO_2 in the atmosphere mainly include natural and anthropogenic emissions (Steinfeld, 1998). Among them, the natural emission sources mainly include natural combustion of biomass, atmospheric lightning process, and nitrates of microbial action; while artificial emission sources mainly include agricultural burning, burning of fossil fuels, industrial production, and vehicle exhaust emissions (Beirle et al., 2003; Van Der A et al., 2008; Tian et al., 2011; Huang et al., 2017). However, with the development of human society, industrial thermal power and motor vehicle emissions have gradually become the main sources of nitrogen oxides, accounting for 90% of the total emissions (Diao et al., 2016). At present, the anthropogenic emission of NO_2 is mainly in the troposphere, and the concentration and fluctuation trend of NO_2 in the stratosphere is smaller than that of the troposphere (Hendrick et al., 2016), mainly from the conversion of N_2O and the direct emission of supersonic aircraft (Velders et al., 2001). Hence, the higher the regional human activity intensity, the more drastic the change of tropospheric NO_2 column concentration (Zhang and Chen, 2007; Xiao et al., 2011; Sun et al., 2018). For years, the emission of NO_X in China's atmosphere has increased significantly, and the pollution of NO_X has been deteriorating due to excessive coal combustion, lack of emission reduction measures, and the sharp increase of motor vehicle emissions.

Nowadays, the concentration of NO_2 in the atmosphere has become one of the common indicators to measure the intensity of air pollution (Liu et al., 2016). The study of temporal and spatial variations of NO_2 and its influencing factors has become a hot topic in the study of atmospheric composition and trace gases. Since satellite remote sensing can efficiently and dynamically monitor the trend and distribution characteristics of gas pollutants, it has gradually become the key means for long-term large-scale monitoring of atmospheric changes in recent years (Tømmervik et al., 1995; Emeis and Schäfer, 2006; Gupta et al., 2006; Peng et al.,

2016; Marinello, 2017; Xue et al., 2017). The study of atmospheric trace gases by using remote sensing monitoring technology of atmospheric satellite began in the 1970s. In 1978, the United States carried a Total Ozone Mapping Spectrometer (TOMS) sensor on the Nimbus-7 satellite to monitor the total ozone change, marking the beginning of the formal study of tropospheric trace gases by satellite remote sensing (Stolarski et al., 1991). Then, the ERS-2 satellite launched by European Space Agency (ESA) in 1995 was loaded with Global Ozone Monitoring Experiment (GOME), which was used to monitor the global distribution of trace gases (Burrows et al., 1999). In 2002, ENVISAT-1, launched by ESA, was loaded with three detectors Global Ozone Monitoring by Occultation of Stars (GOMOS), Moderate Resolution Imaging Spectroradiometer (MODIS), and SCanning Imaging Absorption SpectroMeter for Atmospheric CHartographY (SCIAMACHY), which were used to study the composition changes of HNO_3, CH_4, H_2, N_2O, Chlorofluorocarbon (CFC) and to detect the concentration distribution of aerosol and ozone layer (Desnos et al., 2000). In 2004, the Ozone Monitor (OMI) on NASA's Earth Observation System (EOS) satellite Aura was able to obtain the global distribution of trace gases such as O_3, NO_2, and SO_2 (Krotkov et al., 2016). Subsequently, as the new-generation European instruments carried on MetOp series satellites, the Global Ozone Monitoring Experiment-2 (GOME-2) provides unique and long data sets for Atmospheric Research and application by measuring ozone, trace gases, and ultraviolet radiation (Hassinen et al., 2016; Munro et al., 2016).

However, the in-depth study of NO_2 monitoring and analysis has prompted scholars to put forward higher requirements for the quality and resolution of satellite monitoring data. Meanwhile, in order to compensate for the data gap between the existing SCIAMACHY detector and the subsequent launch of Sentinel-5, the new Tropospheric Monitoring Instrument (TROPOMI) was loaded onboard the Sentinel-5 satellite for fine gas monitoring (Showstack, 2014). The core mission of the project is to monitor global-scale air quality, climate, and ozone layer from 2017 to 2023, providing better data support for scholars' research on NO_2 (Berger et al., 2012). As a first imaging spectrometer to provide global data in medium spatial resolution, TROPOMI has a significant advantage over the previous sensor in spatial resolution (7×3.5 km) and number of clear-sky observations per day (Guanter et al., 2015). Considering that the application and analysis of data products for Sentinel-5P are constantly improving, this paper selects the latest Sentinel-5P NO_2 data product as data source, and synthesizes the distribution data of tropospheric NO_2 column concentration in China. Moreover, based on the spatial statistical analysis model, the distribution characteristics and impact factors of NO_2 column concentration in the troposphere of China are analyzed and modeled, which can reveal the variation characteristics of NO_2 and the source of pollutants, and provide suggestions for the designation of air quality control policies.

8.3 Study area

The economic and urban development of China, as the largest and most representative developing country in the world, has achieved remarkable results since the 1980s with the implementation of the market economy and the reform of the economic system. In 2018, China's Gross Domestic Product (GDP) reached 90.03 trillion

yuan, which has become the second largest economy in the world after the United States and one of the fastest growing economies in the world. Meanwhile, the rapid development of China's economy, the surge of urban population, and the increase of car ownership have led to a sharp increase in NO_2 emissions, and the growth rate is much higher than that of other countries (Guan et al., 2008; Georgoulias et al., 2019; Li and Bai, 2019).

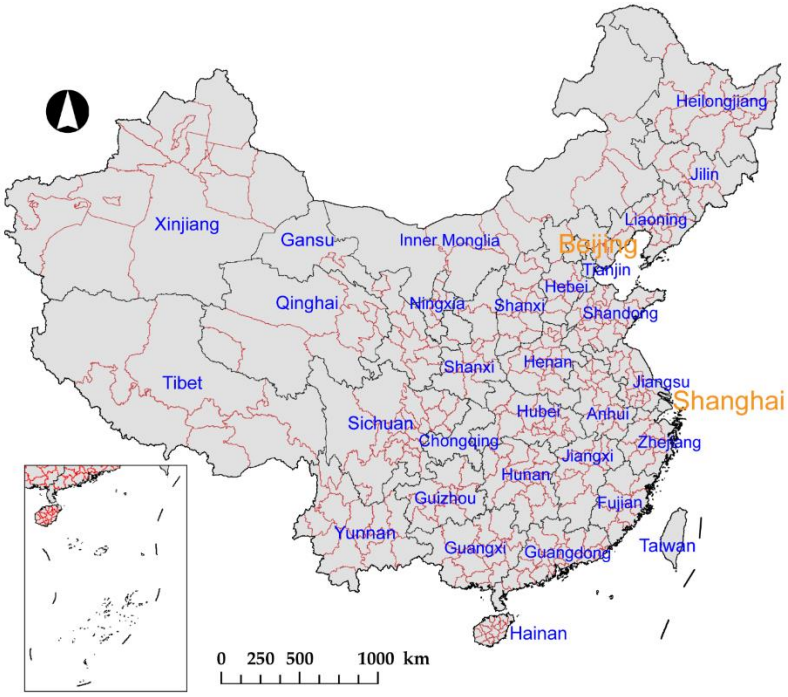

Figure 8.1. The administrative levels of China. Note: red and black lines are provincial and prefectural boundaries, respectively.

Due to its large population and vast territory, the administrative regionalization of China has a spatial stratification structure. The social and economic policies formulated or promulgated by the central government can be conveyed through the governments at the provincial, state, county, town, and village levels (Li and Wei, 2010). Since the 21st century, the number of prefecture level units in mainland China has gradually stabilized. As of October 2017, there are 334 prefecture-level administrative units in China, including: prefecture-level cities (294), autonomous prefectures (30), regions (7), and alliances (3). Since the provincial and prefectural units are the most representative and basic administrative units in China's policy implementation, this paper selects them as the spatial units for NO_2 spatial differentiation analysis (Figure 8.1). In addition, the statistics released by the Chinese government, including GDP, population, energy consumption, etc., are published on the basis of administrative divisions. Therefore, the spatial analysis with these two levels was carried out, which minimized the difficulty of collecting and sorting multidimensional socioeconomic data.

8.4 Materials and methods

8.4.1 Data collection

(1) Remote sensing images

The tropospheric NO_2 column concentration data used in this paper are produced by a TROPOMI instrument on a Sentinel-5 precursor (also known as Sentinel-5P). Sentinel-5P is the first Copernicus mission to monitor the atmosphere, with the aim of reducing the data gap between Envisat satellites (especially SCIAMACHY instruments) and the launch of Sentinel-5 (Veefkind et al., 2012). The satellite carries the most advanced TROPOMI instrument for measuring ultraviolet-visible (270–500 nm), near-infrared (675–775 nm) and short-wave infrared (2305–2385 nm) spectral bands, which means it can image various air pollutants such as NO_2, O_3, CH_2O, SO_2, CH_4, and CO more accurately than ever before (Galli et al., 2012). Since Sentinel-5P Level-2 data products provide atmospheric geophysical parameters and the total column of trace gases, the monthly tropospheric NO_2 column concentration data (February 2018–January 2019) from the Royal Netherlands Meteorological Research Institute (KNMI) are used in this paper. Following the technical route (Figure 8.2), the TOMS format files of tropospheric NO_2 columns released by KNMI are rasterized to generate a time-series raster dataset. Besides, for the TROPOMI NO_2 column products, a quality band (*qa_value* ranging from 0 (poor) to 1 (excellent)) for performing pixel filtering is also provided to eliminate cloud interference and ensure data quality. Since the research area of this paper is vast, and the weather changes significantly during the research period, the monthly NO_2 columns used in this paper have the problem of pixel loss in some areas (*qa_value* < 0.75). Therefore, based on the Kriging algorithm, the tropospheric NO_2 column concentration in the pixel-loss region is interpolated (Figure 8.2).

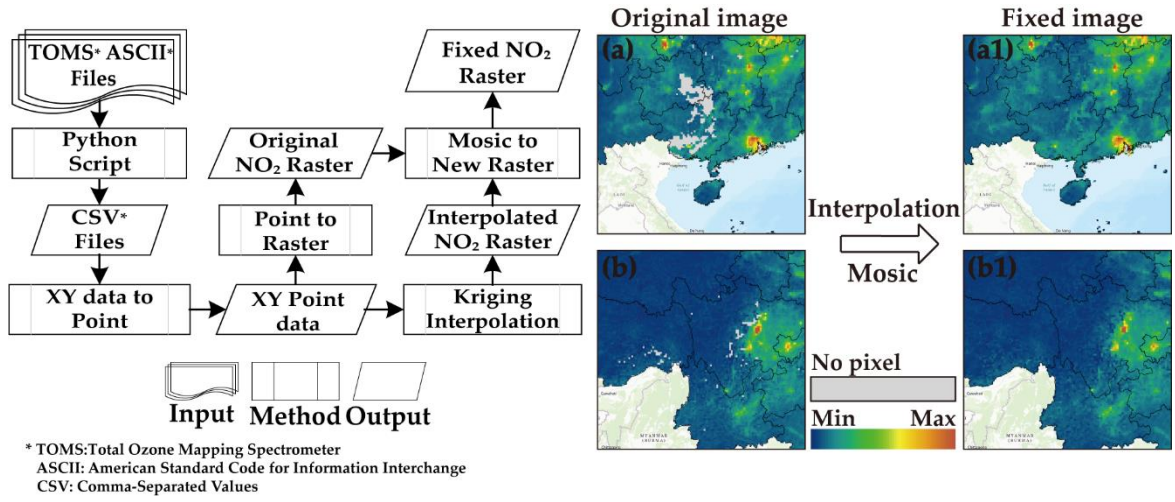

Figure 8.2. The flowchart of image preprocessing and restoration in pixel-missing areas. Note: (a) and (b) are the original images from February and September of 2018, respectively; (a1) and (b1) are the images restored using an interpolation algorithm.

The Suomi National Polar Orbiting Partnership (NPP), a near-polar geosynchronous orbit satellite with an orbital altitude of 824 km, carries a total of five sensors, and the Visible Infrared Imaging Radiometer Suite (VIIRS) is the most important of these (Cao et al., 2013). VIIRS has 22 spectral bands with a spectral range of "0.3~14 μm". Among them, the Day/Night Band (DNB) operates in the visible and near-infrared spectrum, between 500 and 900 nm, to collect low-light imaging data. This paper uses the NPP/VIIRS DNB dataset to characterize surface dynamics in the analysis of the impact factor of NO_2 columns in China. Specifically, we used the DNB images from February 2018 to January 2019 and eliminated the image background noise, based

on the method proposed by Li et al. (2016).

(2) Statistical bulletin data

During the process of exploring the influencing factors of tropospheric NO_2 column concentration, we also selected a series of socio-economic statistical indicators as potential impact factors, including population, GDP, industrial GDP and its proportion, social power consumption, total energy consumption, and motor vehicle ownership. These data (except for Hong Kong, Macao, and Taiwan) were mainly collected from national statistical databases, and provincial and prefectural Statistical Yearbooks of 2018. Moreover, the "China Urban Air Quality Monthly Report" published by the Ministry of Ecology and Environment of China was used to test coherence between NO_2 tropospheric column concentration of Sentinel-5P and surface NO_2 monitoring concentration. The monthly report published the ranking of the average surface concentrations of major air pollutants in major cities in China, including the average surface concentrations of NO_2 pollutants.

8.4.2 Spatial–temporal variation models

Based on the preprocessed monthly NO_2 tropospheric column concentration images of China, the spatial–temporal variation of NO_2 tropospheric column concentration in provincial and prefectural administrative units was further explored. In this part, three models were applied to evaluate the spatial distribution characteristics of NO_2 column concentration, aggregated by two kinds of administrative units, including coefficient of variation, and global and local spatial autocorrelation.

(1) Coefficient of variation of tropospheric NO_2 columns

In statistics, the coefficient of variation (CV) is a normalized measure of the degree of dispersion of probability distribution (Abdi, 2010). Since CV can eliminate the influence of measurement scale and dimension when measuring data dispersion, it is widely used in geoscience and social statistics research (Reed et al., 2002). CV is defined as the ratio of standard deviation to mean of data:

$$CV = SD/\mu = \sqrt{\frac{\sum_i^n (x_i - \bar{x})^2}{n}} \Big/ \bar{x} \tag{8.1}$$

where x_i represents the concentration of tropospheric NO_2 column of administrative unit i; n is the number of all administrative units; $\bar{x}$ is the average tropospheric NO_2 column concentration of all administrative units.

(2) Spatial autocorrelation of troposphere NO_2 columns

As an important method in the study of spatial statistics, spatial autocorrelation reflects the spatial dependence between geographical attributes and adjacent units on a regional unit, including global spatial autocorrelation and local spatial autocorrelation (Zhang and Chen, 2007). As the most well-known and widely used global spatial autocorrelation evaluation index, Global Moran's I is usually used to describe the overall

distribution of a geographical phenomenon or attribute value and to determine whether it has spatial aggregation characteristics (Boots and Tiefelsdorf, 2000). The specific formula is as follows:

$$I = \frac{n\sum_{i=1}^{n}\sum_{j=1}^{n} W_{ij}(x_i - \bar{x})(x_j - \bar{x})}{\sum_{i=1}^{n}\sum_{j=1}^{n} W_{ij}\sum_{i=1}^{n}(x_i - \bar{x})^2} \quad (8.2)$$

where n represents the total number of administrative units; x_i and x_j represent the tropospheric NO_2 column concentration of administrative unit i and j; $\bar{x}$ is the mean concentration of tropospheric NO_2 column of all administrative units; and W_{ij} is the weight matrix of binary inverse distance space, which can be defined as the inverse of the distance among units i and j. At a given level of significance, the closer I value approaches 1, the more significant the spatial aggregation of object attributes is and the closer I value approaches -1, the more significant the spatial divergence of object attributes is.

Unlike global spatial autocorrelation, local spatial autocorrelation is used to reflect the degree of correlation between a certain geographic phenomenon or attribute value on a local small-area unit and an adjacent local small-area unit (Zhang and Chen, 2007). To reveal the spatial heterogeneity of the tropospheric NO_2 columns, we used the local spatial autocorrelation index Local Moran's I to estimate the local autocorrelation (Premo, 2004). The Local Moran's I of spatial unit i is defined as:

$$I_i = \frac{(x_i - \bar{x})\sum_{j=1,j\neq i}^{n}\left[w_{ij}(x_j - \bar{x})\right]}{\sigma^2} \quad (8.3)$$

where σ^2 is the variance of tropospheric NO_2 column concentration. Under a specific level of significance, the administrative units can be divided into the following four categories on the basis of the results of Local Moran's I: (a) High-High (HH) accumulation, where both administrative unit i and neighboring units have higher observations; (b) Low-Low (LL) aggregation, where both unit i and neighboring units have lower observations; (c) High-Low (HL) dispersion, where observations of adjacent units are lower than unit i; (d) Low-High (LH) dispersion, where observations of adjacent units are higher than unit i.

8.4.3 Impact factors analysis

(1) Filtration of impact factors

As mentioned above, NO_2 emissions in the troposphere are mainly man-made, mainly affected by population, urban economic development level, motor vehicle exhaust, and so on. Based on the references and prior knowledge, we collected statistical yearbooks and bulletins of various administrative units, and selected 10 socio-economic indicators including permanent population, GDP, secondary industry GDP and its proportion, tertiary industry GDP and its proportion, urbanization rate, whole society electricity consumption, total energy consumption, and vehicle ownership as potential NO_2 column concentration impact factors. In addition, the light intensity mean and Digital Elevation Model (DEM) mean in each unit were extracted from NPP/VIIRS and SRTM3 Terrain Data to supplement the potential indicators. Parts of the indicators are explained as follows: (1) As anthropogenic emissions are the main source of tropospheric NO_2, more people

will probably bring more demand for emissions. (2) GDP is a key indicator of the economic situation of a country or region, while the secondary and tertiary industry GDP and its proportion can reflect the characteristics of China's industrial structure. Previous studies have pointed out that industrial production is an important source of tropospheric NO_2 emissions, so industrial restructuring will likely affect regional NO_2 column concentrations. (3) Urbanization rate is the proportion of urban permanent residents in the region at the end of the year to the total resident population in the region, which is an indicator of the urbanization process. Therefore, the different levels of urbanization will cause differences in NO_2 emissions. (4) Vehicle ownership is the stock of civil vehicles in the whole society of the region. Many literatures point out that automobile exhaust has become the main source of urban air pollution. (5) Nighttime light intensity is monitored by VIIRS sensor, which can effectively reflect the real vitality of the surface. Areas with high surface vitality tend to exchange more intense energy streams and produce more NO_2 emissions. (6) For DEM, different terrain conditions (elevation) inevitably affect the intensity of human activity and the level of NO_2 emissions (Yang et al., 2017). Besides, since the economic statistics are published on an annual basis, the NO_2 column concentration and monthly nighttime light data are synthesized annually in the impact factors analysis.

These potential impact factors and dependent variable (NO_2 column concentration) may have multiple collinearities, so redundant variables need to be removed. Based on the spatial analysis module of ArcGIS, the Ordinary Least Square (OLS) was used to evaluate the degree of redundancy between variables, and the results showed that: (1) At the provincial units level, the Variance Inflation Factors (VIF) of population, GDP, secondary industry GDP, tertiary industry GDP, urbanization rate, total energy consumption, and vehicle ownership are greater than 7.5, indicating that there are obvious multiple collinearities among these variables (Burridge, 1980). Therefore, the indicators of nighttime light intensity, DEM, whole society electricity consumption, and the proportion of GDP in the secondary industry and tertiary industry are retained to evaluate the mechanisms of NO_2 column concentration distribution in troposphere at the provincial unit scale. (2) At the prefectural unit level, especially the cities in the underdeveloped western regions, due to the serious incomplete records of socio-economic indicators, such as the whole society electricity consumption, total energy consumption, and the vehicle ownership, the Multicollinearity testing was performed only with a complete record. Finally, the indicators including the nighttime light intensity, DEM, population, and the proportion of secondary and tertiary industry GDP were selected to reveal the NO_2 column concentration distribution mechanism at the prefecture unit level.

(2) Spatial econometric model

Compared with the classical OLS linear model, the spatial economic model considers the spatial dependence effect of variables, which is the inheritance and development of traditional statistical methods. Generally, spatial economic models mainly include Spatial Lag Model (SLM) and Spatial Error Model (SEM) (Anselin, 1988). These two models are applicable to the spatial correlation of different spatial effects: 1) SLM is applied when there is significant spatial dependence between dependent variables; 2) SEM is applied when

the error terms of the model are spatially correlated. The Lagrange multiplier test (LM) constructed by Burridge (Wang et al., 2013; Xie and Liao, 2015) and Anelin (Yang et al., 2017) is widely used in the selection of spatial econometric models because it can effectively detect the types of spatial effects. Hence, in this paper, Lagrange Multiplier (LM) test and Robust LM test are used to determine the appropriate spatial economic model for provincial units (Xie and Liao, 2015). The results showed that LM-lag and Robust LM-lag have passed the significance test, while LM-Error and Robust LM-Error failed, so SLM was used to evaluate the impact factors of NO_2 column concentration at the provincial unit level. The formula of the SLM model is as follows:

$$y = \rho W y + X\beta + \varepsilon \tag{8.4}$$

where y is the $n \times 1$ vector of dependent variable (NO_2 column concentration); X is a $n \times k$ data matrix of selected independent variables (impact factors, such as permanent population, GDP, etc.); β is a $k \times 1$ vector of regression coefficient, which reflects the influence of independent variable on dependent variable y; W is the spatial weight matrix, and ρ is the coefficient of spatial lag variable Wy; ε is the random errors term.

(3) Geographically weighted regression

The results of multiple collinear tests of prefectural administrative units show that the Koenker (BP) statistic of the model is significant, which means that the model has significant heteroscedasticity or instability in statistics. Regression models with statistically significant instability state are often well suited for performing Geographic Weighted Regression (GWR) analysis. The GWR Model Based on the first law of geography (Tobler, 2004) extends the framework of the traditional OLS model, adds geographic location to regression parameters, and considers the spatial weights of adjacent points to allow local parameter estimation (Wheeler and Calder, 2007). The calculation formula of the GWR model is as follows:

$$y_i = \beta_0(u_i, v_i) + \sum_k \beta_k(u_i, v_i) x_{ik} + \varepsilon_i \tag{8.5}$$

where y_i is the dependent variable, the NO_2 column concentration at point I; (u_i, v_i) is the spatial coordinate of point i; $\beta_k(u_i, v_i)$ is the regression coefficient of the independent variable k at point (u_i, v_i); x_{ik} is the impact factors, and ε_i is the random errors terms.

8.5 Results

8.5.1 Coherence of NO_2 surface concentration and tropospheric columns

Until now, a series of ground experiments have shown that the NO_2 column concentration based on remote sensing interpretation has a strong correlation with ground-based data, and the correlation coefficients are mostly above 0.8, which well reflects the characteristics of atmospheric NO_2 concentration (Bucsela et al., 2008; Kramer et al., 2008; Huijnen et al., 2009). It is worth emphasizing that as the latest tropospheric NO_2

column concentration inversion results, the coherence analysis of Sentinel-5P TROPOMI's NO_2 data and surface monitoring data is still insufficient, so it is useful to carry out a coherence analysis of NO_2 surface monitoring concentration and tropospheric column concentration in China.

The China Urban Air Quality Monthly Report was used as the data source of NO_2 surface monitoring concentration. The monthly report provides monthly averages of NO_2 concentrations at surface monitoring stations in major cities in China (a total of 169 cities, accounting for 60% of all prefecture-level cities). In addition, based on the monthly air quality report data, we selected multiperiod data (9 months available for public access) for mean processing, to reduce the interference of data occasional fluctuations and weather factors. The results of coherence analysis between NO_2 monitoring concentration on urban surface and TROPOMI tropospheric column concentration are shown in Figure 8.3. The results show that the NO_2 column concentration retrieved by TROPOMI is highly correlated with the surface monitoring concentration of NO_2 on urban area ($p < 0.05$, Adj.$R^2 = 0.72$).

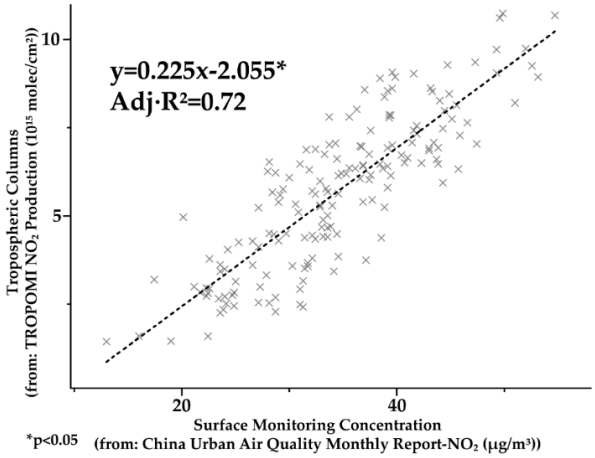

Figure 8.3. The linear regression between surface NO_2 monitoring concentration and TROPOMI tropospheric NO_2 column concentration. TROPOMI: TROPOspheric Monitoring Instrument.

8.5.2 Spatial–temporal characteristics of tropospheric NO_2 columns

(1) General characteristics

Figure 8.4 presents the monthly means maps of tropospheric NO_2 columns from February 2018 to January 2019. The most significant feature of the tropospheric NO_2 column concentration in China is that it is high in the east and low in the west. For western China, the NO_2 column concentration in most areas is less than 1×10^{15} molec./cm^2, while the areas with columns more than 2×10^{15} molec./cm^2 are mainly concentrated in Junggar Basin (Urumqi) and Turpan Basin (Turpan). For eastern China, the tropospheric NO_2 column concentration above 16×10^{15} molec./cm^2 is mainly concentrated in the North China Plain (Hebei Province), Shandong Peninsula (Shandong Province), and the middle and middle-lower Yangtze Plain (Hubei, Anhui, Jiangsu Province, Shanghai). The North China Plain, with warm temperate monsoon climate, has insufficient precipitation and large seasonal variations in temperature. During winter, the decrease of temperature has greatly increased the demand for regional heating, and the consumption of coal has increased sharply. Besides, with abundant coal, iron, and petroleum deposits in the plain, the heavy industries such as coal, electricity,

petroleum, chemical industry, and iron and steel occupy an important position in the region's economic system. The special geographical conditions and socio-economic development background have led to the high concentration of tropospheric NO_2 columns in the region, which has become the core of NO_2 pollution areas in China. Another notable tropospheric NO_2 column high-concentration agglomeration zone is the Middle-Lower Yangtze Plain, an important industrial base in China, with developed land and water transportation. Within the plain, there are two "peaks" of NO_2 column concentration, which are the Yangtze River Delta Plain in the East and the Jianghan Plain in the west. The Yangtze River Delta Plain is one of the world's famous estuary deltas. The advantageous geographical conditions have nurtured the Yangtze River Delta Urban Agglomeration (YRDUA), one of the six largest urban agglomerations in the world. As the most developed region in China, YRDUA is an important engine of China's economic development, a 2.1% land area that concentrates 1/4 of the total economic output and industrial-added value of the whole country. The Jianghan Plain, located in the south-central part of Hubei Province, is one of the lowest elevations in China. The NO_2 column concentration in Jianghan Plain shows a decreasing distribution from Wuhan City to the surrounding area. Wuhan is the capital of Hubei Province, the only sub-provincial city and mega-city in middle-China. As an important industrial base and core transportation hub in China, Wuhan has made remarkable achievements in urban construction and economic development in the recent ten years, but at the same time, it has also brought tremendous pressure to the environment and causes serious air pollution (Qiu et al., 2018).

Besides, there are also several small-scale high-concentration NO_2 distribution areas centered on the regional central cities. These small-scale NO_2 column concentration distribution areas mainly include Guangzhou and Shenzhen in South China, Chengdu and Chongqing in southwest China, Xi'an, Lanzhou, and Urumqi in western China, Anshan and Shenyang in northeast China. Most of the above cities are provincial capitals and regional central cities, where economic development level and human activity intensity are significantly higher than the local average level. The rapid development of economy and the increase of external population have increased NO_2 anthropogenic emission sources, aggravated atmospheric pollution, and led to the sharp increase of NO_2 column concentration in the troposphere around urban areas (Zheng et al., 2014; Ma et al., 2016; Sun et al., 2018).

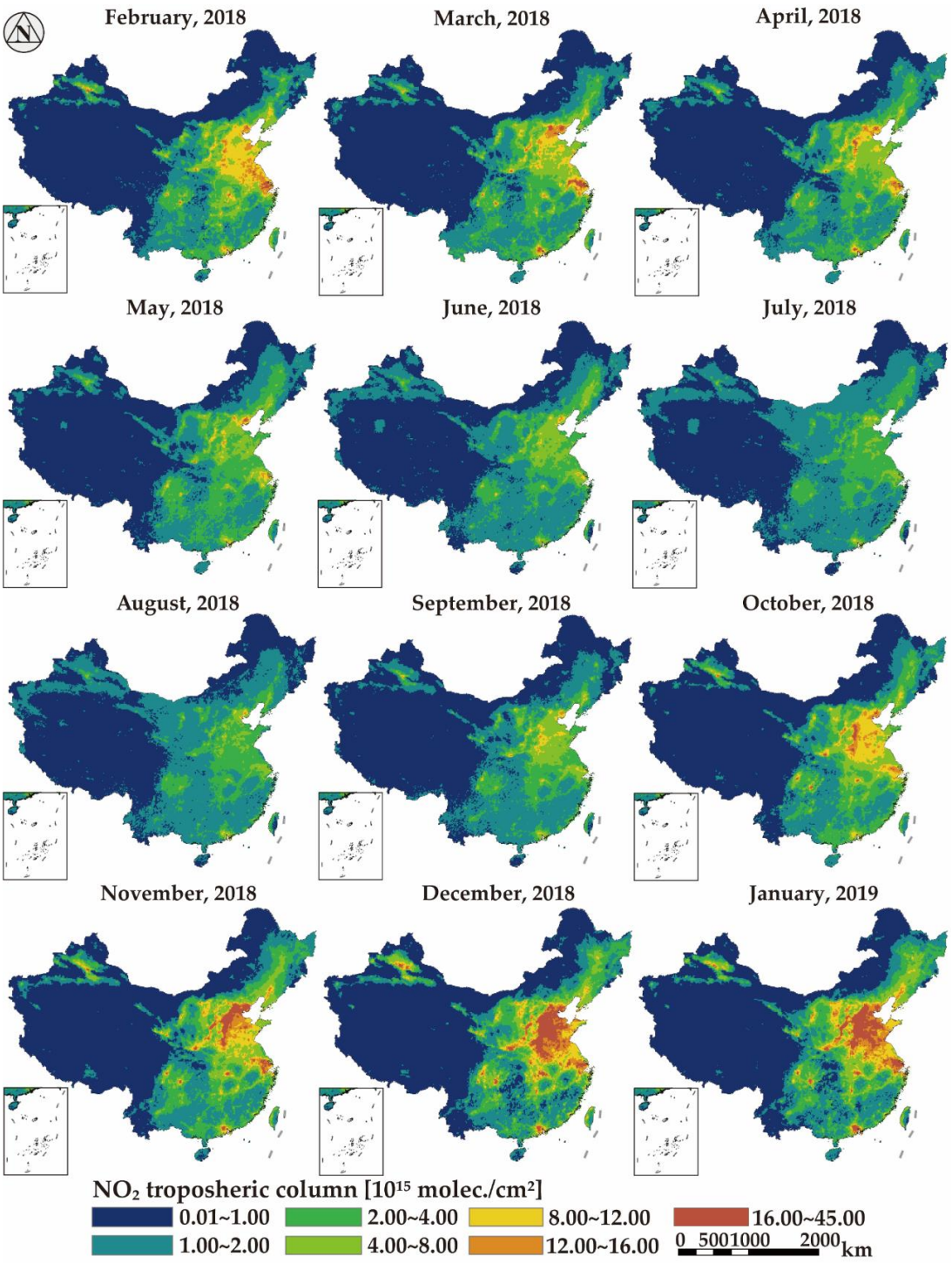

Figure 8.4. The monthly fixed images of tropospheric NO2 column concentration in China.

In this paper, the concentration data of tropospheric NO_2 column from February 2018 to January 2019 were used for monthly statistics, and the results show that there was a significant seasonal variation of the tropospheric NO_2 column concentration in China during the past year (Table 8.1). The minimum concentration of NO_2 column in each month was relatively stable, with only slight fluctuation in June and August of 2018. The maximum of NO_2 column concentration in each month had a significant difference, and the maximum value decreased from February 2018 to June 2018, and then rebounded to the highest level in January 2019. The monthly mean of NO_2 column concentration was high in winter, low in summer, and transitional in spring

and autumn, which is consistent with the observations of previous atmospheric monitoring satellites. Specifically, the mean concentration of NO_2 in July and August of 2018 was the lowest (1.35×10^{15} molec/cm^2), while the mean value in December 2018 and January 2019 was the highest (about 2.60×10^{15} molec/cm^2).

At the national scale, the significant negative correlation between NO_2 column concentration and temperature once again confirms that temperature is an important inducement for seasonal variation of NO_2 column concentration. Except for the northwest China and Qinghai-Tibet Plateau, most of China is affected by the monsoon climate, with low temperature in winter and high temperature in summer. As a trace gas, the concentration of NO_2 is determined not only by the total amount of emissions, but also by the intensity of solar radiation and other factors. Every winter, with the decrease of temperature, urban heating demand and coal consumption also increase rapidly, greatly increasing the NO_2 emissions in the troposphere. Moreover, frequent cold, fog, snow, and frost weather in winter lead to weak solar radiation and a thick inversion layer in the troposphere, which is not conducive to the dissipation of NO_2 and aggravates the concentration of NO_2 column in the troposphere. Correspondingly, every summer, with the increase of solar radiation, rainwater, and the decrease of coal consumption, the decomposition of light and rainwater and the wet deposition will further reduce the concentration of pollutants in the atmosphere.

Table 8.1. The monthly statistic results of tropospheric NO_2 column concentration and temperature (℃).

Year	2018						2019					
Month	Feb	Mar	Apr	May	Jun	Jul	Aug	Sep	Oct	Nov	Dec	Jan
Min	0.01	0.01	0.01	0.01	0.03	0.01	0.02	0.01	0.01	0.01	0.01	0.01
Max	29.01	27.99	23.54	22.65	14.33	11.19	15.86	16.01	37.96	38.41	34.40	41.52
Mean	1.90	1.84	1.68	1.52	1.45	1.35	1.35	1.47	1.94	2.24	2.60	2.61
Std	2.71	2.47	2.06	1.56	1.24	0.90	0.98	1.52	2.66	3.40	4.13	4.23
Temperature	−2.0	7.0	12.3	17.0	20.7	22.9	21.9	16.7	9.8	3.1	−3.8	−4.1

(2) The spatial heterogeneity of NO_2 columns at provincial units

Figure 8.5 shows the monthly CV and Global Moran's I of the tropospheric NO_2 column concentration on the provincial units from February 2018 to January 2019. At the provincial unit level, the CV of NO_2 column concentration fluctuated significantly, which indicated that there is a significant difference in the dispersion of the monthly tropospheric NO_2 column concentration in China. Specifically, we found that the value of CV dropped rapidly from 0.9 in February to 0.56 in July, a drop of about 38%, and then increased month by month and returned to above 0.9 after November. In fact, the fluctuation characteristics of CV were similar to the mean fluctuation of NO_2 column concentration, showing an obvious trend of "high in winter and low in summer". The seasonal variations in NO_2 emissions between different provinces are the possible causes of CV fluctuations. Although China has made remarkable achievements in social and economic development since its reform and development in 1978, the difference in regional development level has been further widened. The eastern coastal provinces benefit from the advantages of location and policy, and become the "first rich" area, while the inland provinces in the central and western regions, due to the limitations of natural conditions

and other factors, make the region become the "second rich" area. Differences in economy, population, and urban development between eastern and western provinces will inevitably lead to differences in NO_2 emissions. This difference will fluctuate regularly and periodically with the seasonal change. For example, during winter, the heating demand of eastern and northern provinces is significantly higher than that of southern and western provinces, which aggravates the emission of NO_2 and other atmospheric pollutants, while in summer, the difference of NO_2 emission between provinces decreases, and the NO_2 column concentration CV of provincial units also drops to the lowest.

From the results of Global Moran's I ($p < 0.05$), it clearly increased with a small fluctuation during the past year. Specifically, after the Global Moran's I rose from 0.45 in February to 0.57, it fluctuated around 0.55 in the next few months, until September. Since October, the Global Moran's I has increased significantly, and then reached its highest value in November, then fell back to about 0.65. Generally, the Global Moran's I in autumn and winter is higher than that in spring and summer, which indicates that the aggregation distribution pattern of the tropospheric NO_2 column concentration of the provincial units in the autumn and winter is more significant. In addition, we also found that the Global Moran's I and CV fluctuations were synergistic for most of the time, except for June to July. In fact, CV measures the dispersion of data as a whole, while the Global Moran's I measures the level of data aggregation after considering spatial location. Therefore, it can be considered that from May to July, although the dispersion degree of NO_2 column concentration between provinces decreased, the aggregation degree of high and low values between provinces increased.

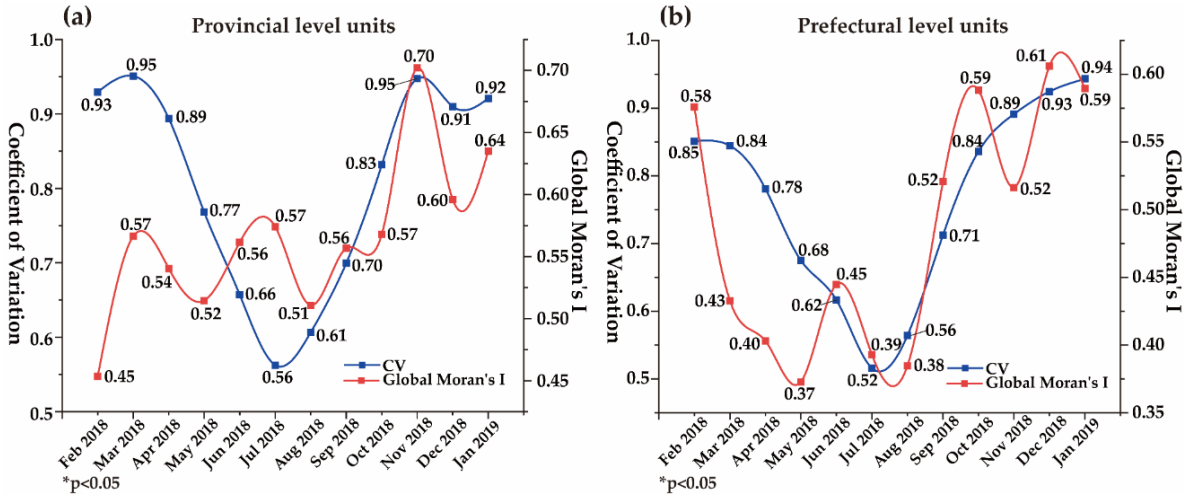

Figure 8.5. The monthly Coefficient of Variation (CV) and Global Moran's I at provincial and prefectural units. (Note: (a) shows the CV and Global Moran's I under the Provincial level unit; (b) shows the CV and Global Moran's I under the Prefectural level unit.)

As shown by the results of local spatial autocorrelation (Figure 8.6), the four-month concentration data were used to explore Local Moran's I change in different seasons. The results showed that in spring, the aggregation units of HH and LL in NO_2 column concentration accounted for 95.0% of all significant units; in summer, the aggregation units accounted for 85.0% of all significant units; in autumn, the aggregation units of HH and LL accounted for 84.2% of all significant units; in winter, the aggregation units accounted for 86.4% of all significant units. The HH and LL aggregated units accounted for the majority of the significant units in

the whole year, which indicated that the distribution of troposphere NO_2 column concentration was mainly under the aggregation effect. From the spatial distribution HH and LL units, the LL aggregation was mainly distributed in western provinces including Qinghai, Tibet, Yunnan, Sichuan, Guangxi, and Guizhou, while the HH aggregation was concentrated in eastern provinces including Beijing, Hebei, Henan, Shandong, Shanxi, Anhui, Jiangsu, and Shanghai. Moreover, there were also provinces with low concentration of NO_2 column such as Inner Mongolia, Hubei, Zhejiang, and so on around HH concentration provinces, which show as LH outlier.

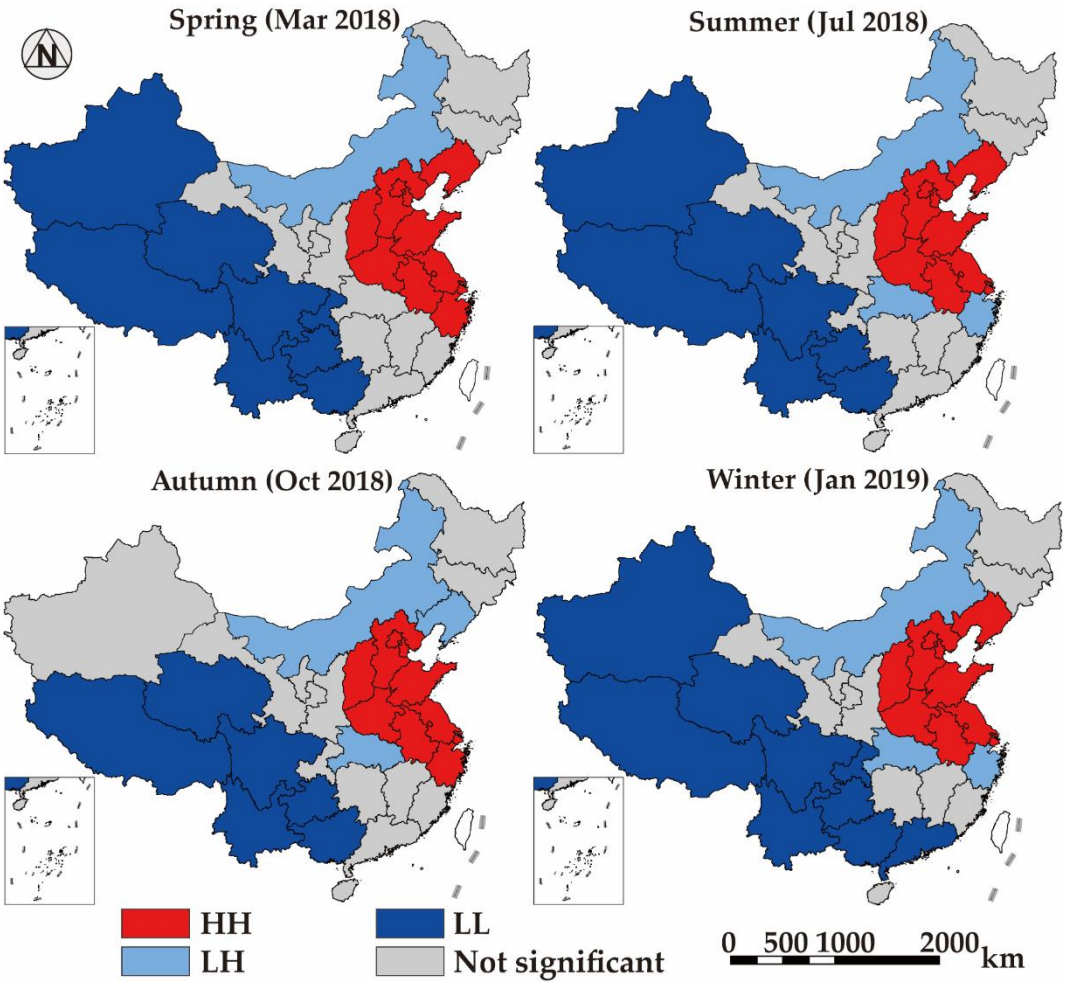

Figure 8.6. The Local Moran's I results of provincial units in one month per season.

(3) The spatial heterogeneity of NO_2 columns at prefectural units

The CV fluctuations on prefectural units showed a typical "V" shape, that is, high in autumn, winter, and spring, but low in summer. Specifically, from February to July 2018, CV continued to decline from 0.85 to 0.52 (minimum), and then began to rise to 0.94 in January 2019 (Figure 8.5(b)). According to the fluctuation stage of CV, during the transition period from spring to summer, CV maintained a rapid decline of 38.8%, while in autumn and winter, CV continued to rise rapidly, with an increase of 80.8%. The variation of CV reflects that there are also significant differences in the dispersion degree of NO_2 column concentration at prefectural units: during the summer, especially July and August, the difference of NO_2 column concentration between cities is shrinking; in spring and autumn, the NO_2 column concentration differences between cities is

increasing, and reaches the maximum in winter. The periodic variation characteristics of the Global Moran's I at prefectural units are similar to that of the provincial units, with only differences between February and March.

In addition, according to the Local Moran's I of tropospheric NO_2 column concentration in prefectural level, the units with spatial autocorrelation occupy the majority (Figure 8.7). The significant spatial autocorrelation units decreased from 283 in spring to 279 in summer, and then increased to 289 in autumn and 296 in winter. Besides, the proportion of HH and LL units in significant units in the four seasons also showed similar characteristics of "first falling then rising, high in winter and low in summer" (83.75%, 80.65%, 84.08%, and 85.47%). The high-value agglomeration units represented by HH mainly concentrated in eastern China, while the low-value agglomeration represented by LL mainly distributed in southwest and northeast China. The high-value discrete (high value surrounded by low value) units represented by HL are concentrated in Sichuan, China. The special topographic structure and development history of Sichuan Basin have resulted in a large number of people gathering, and a high concentration NO_2 distribution area centered on Chengdu has been formed. Compared to the HL units, the number of low-value discrete units of LH is significantly more and mostly located in the transition zone between the LL aggregation and HH aggregation. In general, the spatial agglomeration of the tropospheric NO_2 column concentration in the prefecture level has significant seasonal differences (high in winter and low in summer), and the distribution pattern of spatial agglomeration units is relatively stable.

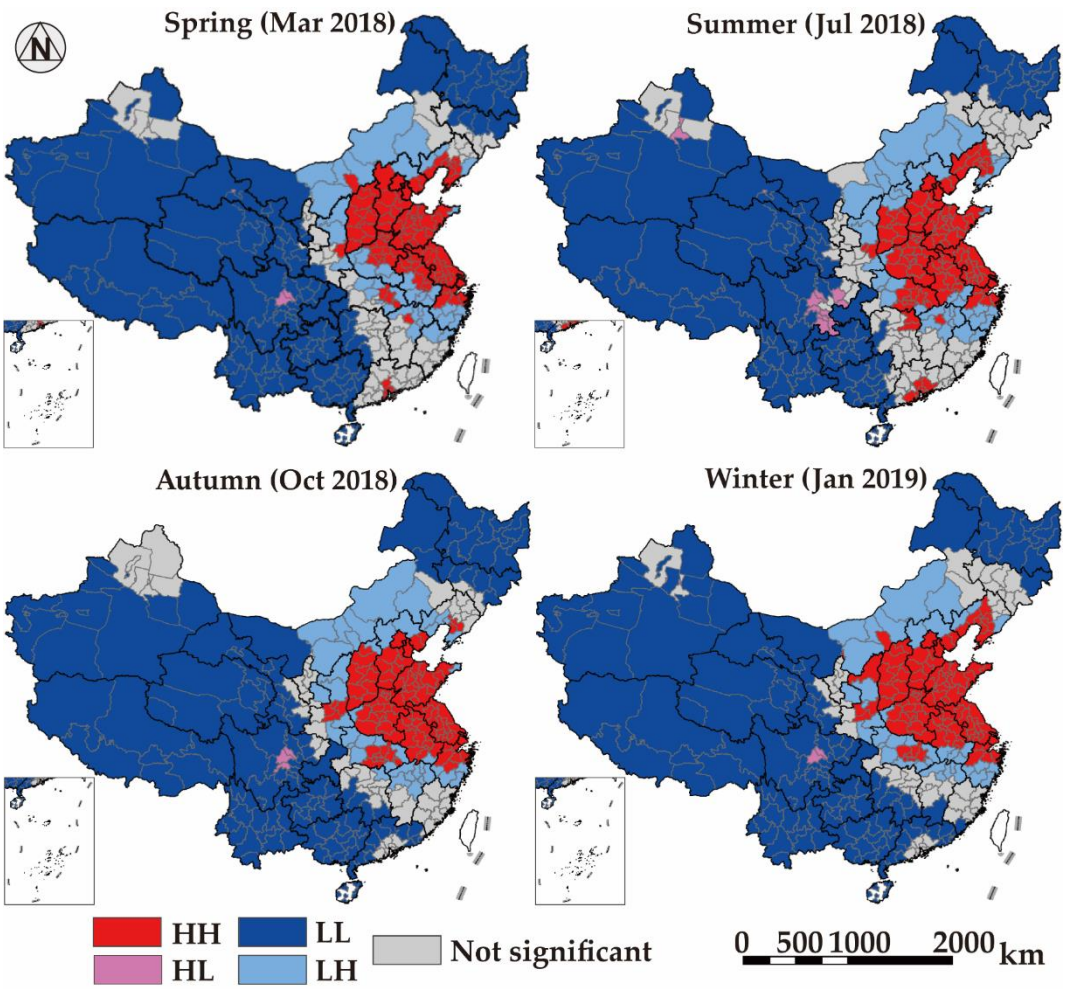

Figure 8.7. The Local Moran's I results of prefectural unit in one month per season.

8.5.3 Impact factors of tropospheric NO_2 columns

(1) Impacts factor analysis at provincial units

Considering the availability of data, SLM was used to implement impact factors analysis, with NO_2 column concentration in troposphere as dependent variable, nighttime light intensity, DEM, whole society electricity consumption, and the proportion of secondary and tertiary industries GDP as independent variables. The model performance indicators of R^2, Log Likelihood, Akaike Info Criterion (AIC), and Schwarz Criterion are listed in Table 8.2, respectively. In this paper, the R^2 and Log Likelihood of SLM were larger than OLS, while AIC and Schwarz Criterion were smaller than OLS. This showed that after consideration of the spatial effect, SLM effectively eliminates the spatial autocorrelation and improves the goodness of fit of the model, which is superior to the classical linear regression OLS model. Besides, according to the factor coefficients listed in Table 8.2, the nighttime light intensity, proportion of secondary and tertiary industries GDP are significant at provincial unit level. It is worth noting that the coefficients for the 3 factors are positive, which indicated that the human activity intensity and industrial structure can promote the regional concentration of NO_2.

Nighttime light intensity has been proved to be effective and accurate in reflecting the difference of human activity intensity and material energy distribution on the earth's surface (Zheng et al., 2019). The regional higher nighttime light intensity means higher land development intensity and is usually accompanied by severe environmental pollution, especially for China, which is developing rapidly (Yang et al., 2014; Misra and Takeuchi, 2016). The regression coefficients of the secondary and tertiary industries GDP proportion reflect the contribution of industrial production, transportation, and services to regional NO_2 column concentration.

Table 8.2. Results of Spatial Lag Model at provincial unit.

Impact Factor	Coefficient	Std.Error	z-value	Probability
W_NO_2	0.454	0.174	2.614	0.009
CONSTANT	−12.337	5.668	−2.176	0.030
Nighttime light intensity	0.451	0.128	3.527	0.000
Digital Elevation Model (DEM)	−0.038	0.028	−1.323	0.186
Proportion of second industry	0.146	0.064	2.275	0.023
Proportion of third industry	0.156	0.071	2.194	0.028
R-squared	0.781(0.722)		Log Likelihood	−54.212(−57.268)
Akaike Info Criterion	120.423(124.536)		Prob	0.01342
Schwarz Criterion	129.027(131.706)			

* Ordinary Least Square (OLS) indicators are list in parentheses.

(2) Impact factors analysis at prefectural units

As mentioned above, through VIF and coefficient significance test in OLS model, we selected the independent variables from the ensemble of available variables, including nighttime light intensity, DEM, population, and the proportion secondary and tertiary industries GDP. Since bandwidth is a key parameter in GWR, the AIC method was used to determine the most bandwidth to ensure the fit and smoothness of the model. The model performance evaluation indicators of the GWR and OLS at the prefecture level (Table 8.3) showed that the R^2 rises from 0.505 for OLS to 0.643 for GWR, and AICc (corrected AIC) also drops from 1488 to 1395, which indicates that the performance of the GWR model with local parameter estimation is better than OLS.

Table 8.3. The model indicator difference between Geographic Weighted Regression (GWR) and OLS at prefectural unit.

Model		GWR	OLS
Model indicator	R^2	0.643	0.505
	Adj.R^2	0.620	0.497
	Akaike Info Criterion corrected (AICc)	1395	1488
	Sigma-Squared	3.040	4.025
	Sigma-square Maximum Likelihood (Sigma-square ML)	2.855	3.956
	P-value	0.000	0.000

Meanwhile, we made statistics on the independent variable coefficients of prefecture units. The results showed that among the selected independent variables, the coefficients of nighttime light intensity, the proportion of secondary and tertiary industries, and the population were positive, which indicated that these

factors have a positive correlation with the NO_2 column concentration; the coefficient of DEM was negative, which means that the higher the terrain, the lower the concentration of NO_2. Unlike OLS, GWR model provides local model results for predicted variables and gives Adj.R^2 and each independent variable coefficient for each prefectural unit. Although the entirety R^2 of GWR reached 0.643, there were still significant differences in R^2 of each prefecture unit. As shown in Figure 8.8, the Local R^2 increased gradually from east to west, and the independent variables of the eastern coastal cities can only explain about 50% of the dependent variables, while the model explanatory power of the western inland cities can reach more than 75%.

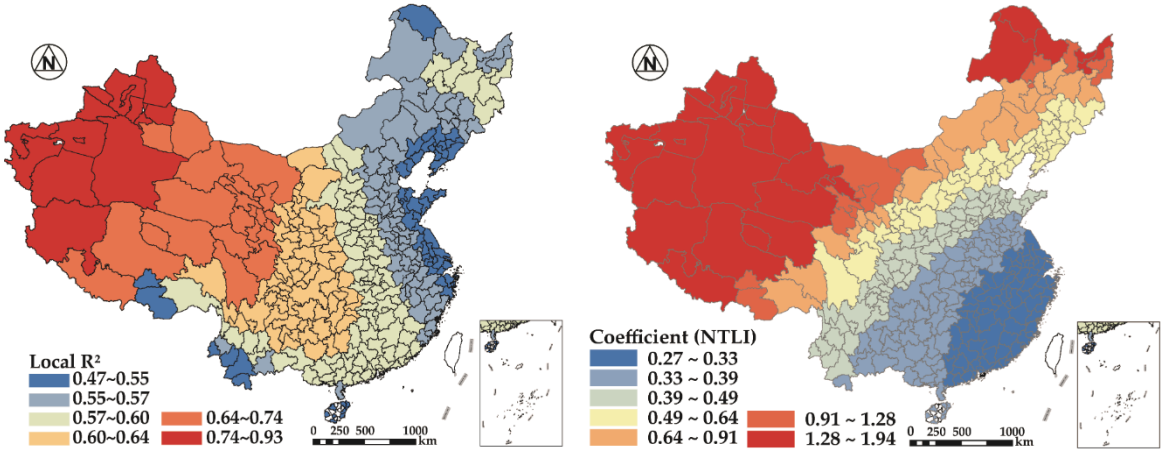

Figure 8.8. The Local R^2 of GWR and coefficient of Nighttime light intensity at prefectural unit level. (Note: all the coefficients are statistically significant).

Similarly, the coefficients of the independent variables between regions are also differences. For example, the coefficient of nighttime light intensity increased from southeast to northwest, indicating that the effect of light intensity on NO_2 column concentration increases from southeast to northwest (Figure 8.8). The reason for this phenomenon may be the difference of regional economic development level. The southeast of China is the most economically developed and populous region in China due to geographical conditions, policy conditions, and historical development, while the northwest of China is less developed due to the restrictions of natural conditions and transportation. Compared with the northwestern region, the nighttime light intensity between cities in southeastern China was relatively close, which cannot effectively reveal the difference in nitrogen dioxide concentration in the region.

8.6 Discussion

8.6.1 Division line of tropospheric NO_2 columns

Generally, the areas with high NO_2 column concentration are located in the southeast of China, while the low value areas are mostly located in the Northwest inland. By extracting the high and low boundary lines of NO_2 column concentration, we generated a NO_2 column concentration division line (Figure 8.9). This division line is mainly composed of a series of mountains, including Lesser Khingan, Great Khingan, Yin Mountains, Helan Mountains, Qilian Mountains, Laji Mountains, Min Mountains, and Hengduan Mountains. To a certain extent, the division line, which consists of the series of mountains, restricts the westward diffusion of NO_2 in

the eastern developed areas and gradually forms the spatial distribution pattern of NO_2 column concentration in China, which is an east-high and west-low pattern.

It is worth noting that the NO_2 column concentration division line is quite similar to the Hu Line. Hu Line, also known as Heihe-Tengchong Line, was proposed in 1935 by Hu Huanyong, a Chinese geographer (Chen et al., 2016). In addition, the Hu Line coincides with the 400 ml precipitation line and the demarcation line between monsoon and non-monsoon climate. This line has even become the dividing line of China's urbanization level. Most cities on the southeast side of the line have higher urbanization levels than the national average, while the cities on the northwest side of the line are usually lower than the average. The differences in natural geographical conditions, economic development levels, and population aggregation on both sides of the Hu Line led to significant differences in tropospheric NO_2 emissions and gradually shaped the NO_2 column concentration distribution pattern in China. Therefore, to simplify the division line, we can roughly assume that Hu Line is not only the boundary line between population density and urbanization level, but also the division line of tropospheric NO_2 column concentration in China. It must be emphasized that this is the first report on a similar dividing line between the Hu line and the NO_2 column concentration.

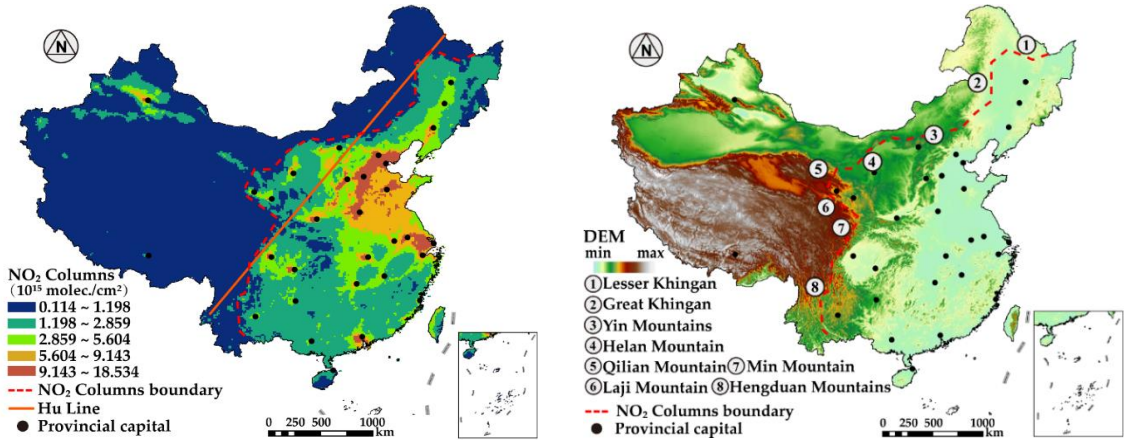

Figure 8.9. The division line of tropospheric NO_2 column concentration in China.

8.6.2 Spatial−temporal characteristics comparison at different administrative units level

The comparison of CV fluctuations between provincial and prefectural units from February 2018 to January 2019 showed a similar fluctuation evolution. For both administrative units levels, the highest CV in winter was around 0.9; the lowest CV in summer was between 0.5 and 0.6; the spring (autumn) season is the transition period of CV and showed a trend of decreasing (increasing) month by month. Although the seasonal fluctuation trend of CV between the levels was similar, there were still some differences in the fluctuation of CV during winter. As can be seen from Figure 8.10(a), during the winter (Nov 2018–Jan 2019), the CV of the provincial units showed slight fluctuations around 0.9, while the CV of the prefecture-level units maintained a relatively stable growth. We believe that there are two main reasons for this difference: on the one hand, there are 34 provincial units in China, while 333 prefectural administrative units. Provincial units with less NO_2 column concentration samples increase the instability and discreteness of data, resulting in higher CV. On the other hand, provincial units are composed of several prefectural units, which will lead the provincial

units to "amplify" or "narrow" the range of NO_2 change of prefectural units in the region, resulting in prominent differences between provincial units.

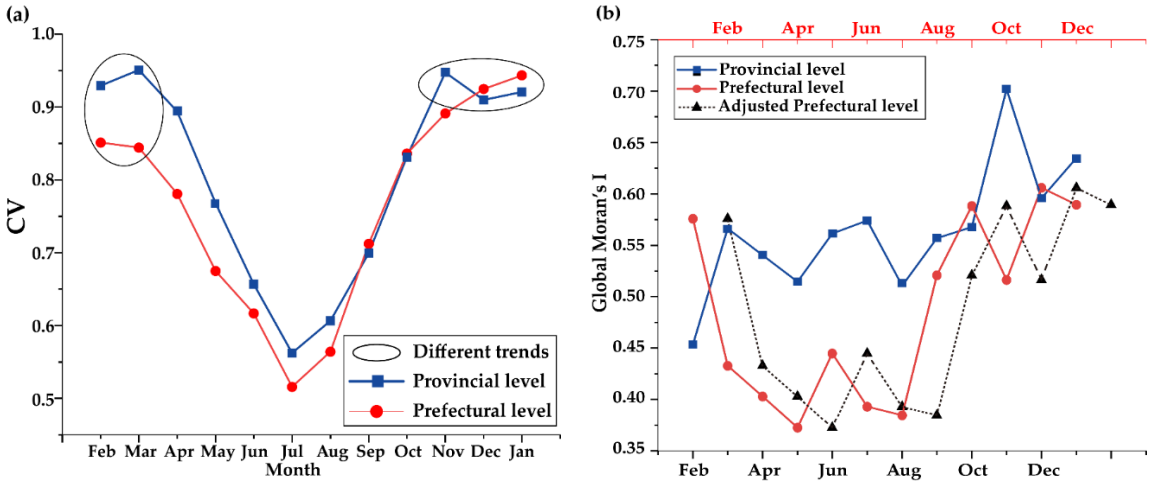

Figure 8.10. The comparison of CV and Global Moran's I of provincial and prefectural units.

Unlike the high similarity of fluctuation trend between two levels of CV, the fluctuation of Global Moran's I appears significant differences at different levels of administrative units. First, the provincial-level Global Moran's I was higher than the prefectural-level units; second, there were inconsistencies in the direction of data fluctuations in some months. For example, from February to March, the Global Moran's I showed an upward trend in provincial units and a downward trend in prefectural units; from October to December, the Global Moran's I of provincial units rose first and then decreased, while the Global Moran's I of prefectural units showed the opposite trend. We speculate that the main reason for this difference is the "delayed effect" caused by different observational scales in the process of concentration and dispersion of NO_2. From February to March, the NO_2 emission decreased as the temperature rose, and the column concentration of tropospheric NO_2decreased accordingly. The reduction of NO_2 column concentration is more obvious in cities with high NO_2 concentration, which leads to the reduction of high value agglomeration and the decrease of Global Moran's I. For provincial units, the larger space scales with multiple prefecture-level cities serve as a "buffer" when NO_2 begins to decline, which delays the change of the Global Moran's I caused by the change of NO_2 column concentration. From September to November, with the decrease of temperature, the NO_2 emission of prefecture-level cities increased, the NO_2 column concentration in the troposphere increased, and the Global Moran's I of prefectural units rose rapidly. Similarly, the rise of the Global Moran's I was delayed due to the delayed effect at the provincial level. In Figure 8.10(b), the fluctuation trend of the adjusted Global Moran's I of prefecture-level cities is highly similar to that of the provincial-level Global Moran's I, which further confirms that the provincial units with a larger spatial range have a one-month "delayed effect" of the fluctuation.

From the analysis of Local Moran's I, the distribution of HH agglomeration units in provincial and prefectural units is similar, that is, HH agglomeration is mainly concentrated in North China Plain and the middle-lower Yangtze Plain. For LL agglomeration, the LL agglomeration units number of prefectural level

has been expanded compared with provincial level, and LL agglomeration have also appeared in northeast China. In addition, another noteworthy difference is HL distribution. The NO_2 column concentration of provincial units is the average value of the cities under the jurisdiction, thus ignoring the discrete situation within provincial units. Conversely, because of the small spatial scale of prefectural units, there are also differences in NO_2 column concentration between cities in the province, which affects the evaluation level of high-value aggregation and low-value aggregation.

8.6.3 The impact factors analysis at different administrator units level

By comparing the impact factors at different administrative levels, we can find that the light intensity and the proportion of secondary and tertiary industries are always the positive factors affecting the distribution of NO_2 column concentration, while DEM is the negative factor. The difference is that population also plays a positive role in promoting the distribution of NO_2 column concentration in prefecture-level cities. In fact, the CV of population and NO_2 column concentration in provincial units are quite different (Population: 0.45; NO_2: 0.812), while those in prefectural units are relatively close (Population: 0.86; NO_2: 0.77). This indicates that the discrete degree of population and NO_2 column concentration at the prefectural level is closer compare with provincial units, so it can be selected as an effective independent variable to participate in the regression model.

Besides, the goodness of fit of GWR model with local regression at prefectural level is higher than SLM model in provincial units. With the reduction of spatial scale of spatial evaluation units and the increase of the number of units, the difference of NO_2 column concentration between cities is highlighted. In the case of the statistically significant unsteady regression model, the GWR model based on local regression can restore the local characteristics of variables and better fit the distribution of NO_2 column concentration than the provincial SLM model.

Although GWR performs well in overall fitting performance, the significant aggregation of standardized residuals reflects the absence of key variables in high concentration NO_2 agglomeration areas, especially in North China and East China (Figure 8.11). Therefore, we re-executed GWR modeling in cities with higher than 1.5 times standardized residuals in North and East China. For East China and North China, due to the close relationship and social-economic development between cities, the statistical data is more robust than the western cities. Hence, in the sub-region, the whole society electricity consumption and vehicle ownership are supplemented as new independent variables to participate in the construction of the model. The results showed that the Adj.R^2 of the new model with independent variables reaches 0.685 (previous model: 0.62), and the distribution of the standardized residuals of the new model presents random distribution (Global Moran's I = 0.04, $p < 0.05$). At present, many scholars have shown that with the rapid increase in the number of urban motor vehicles and the rising energy consumption, the proportion of NO_2 from coal-fired emissions and motor vehicle exhaust in tropospheric NO_2 is also increasing, and the problem of NO_2 pollution is more serious than ever (Chen and Xie, 2010; Memmesheimer et al., 2010; Fu et al., 2016). Moreover, due to the flat terrain and

the leading economic level between cities in North China and East China, the NO_2 pollutants in the region transfer and influence each other among cities, forming a huge "North China-East China NO_2 pollution system".

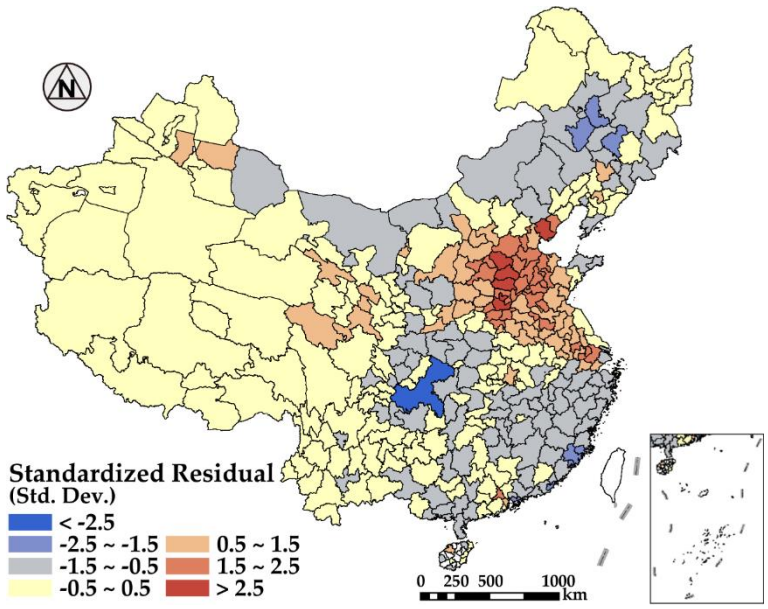

Figure 8.11. The standardized residual of GWR at prefectural level.

8.7 Conclusions

Based on the NO_2 data products of Sentinel-5P with TROPOMI, the spatial−temporal characteristics and impact factors of tropospheric NO_2 column concentration in China in 2018 were analyzed at provincial and prefectural levels in this paper. It is an application of NO_2 data products based on the Sentinel-5P TROPOMI sensor in China. The results of the study clarify the seasonal effect and agglomeration effect of the NO_2 column concentration distribution in China, which could help us better understand the distribution pattern of tropospheric NO_2 pollutants in China and its potential impact factors. The coherence analysis with the NO_2 surface monitoring concentration released by China Urban Air Quality Monthly Report reflects the high correlation between the NO_2 column concentration inverted by TROPOMI and the measured surface concentration, which reveals the great potential of the TROPOMI NO_2 column concentration in indicating urban surface air pollution conditions. The analysis of the spatial-temporal characteristics of the tropospheric NO_2 column concentration shows that: 1) the monthly fluctuation of the tropospheric NO_2 column concentration has a significant "winter high summer low" cycle characteristic; 2) the spatial distribution pattern of NO_2 column concentration in troposphere shows a general pattern of "east-high and west-low", and the division line between the eastern high-value area and the western low-value area of NO_2 column concentration is close to the Hu Line; 3) the results of CV and spatial autocorrelation models at two kinds of administrative scales show that although the spatial heterogeneity of NO_2 column concentration does not differ significantly with the scale change, NO_2 column concentration has a certain degree of "delayed effect" during the fluctuation process. Furthermore, the results of modelling and impact factors analysis of NO_2 column concentration at different levels show that: 4) nighttime light intensity, the proportion of secondary and tertiary industries GDP,

and tropospheric NO_2 column concentration are positively correlated at two administrative levels; while population is positively correlated with NO_2 only at the prefecture level; 5) within the areas with high concentration of NO_2 pollution in North China and East China, the whole social electricity consumption and vehicle ownership also play a positive role in promoting the column concentration of NO_2.

The results of the present study have implications for governments and policymakers to develop effective NO_2 emissions reduction and air pollution prevention policies. Firstly, the tropospheric NO_2 pollution in China has serious spatial differences, which requires us to adopt "local measures" to deal with NO_2 pollution. Among them, North China and East China, as the most serious and concentrated areas of NO_2 pollution in China, should take measures to optimize industrial integration and limit the number and total emissions of enterprises with high pollution and energy consumption. Meanwhile, the government should urge enterprises to increase investment in research and development of emission reduction technology to minimize the direct emission of NO_2 pollutants. For the underdeveloped areas in Western China, the column concentration of NO_2 is still in a low state, and the overall pollution situation can be neglected. Therefore, for the western region, the government should also take economic development as its main goal while controlling NO_2 emissions. Furthermore, considering the seasonal variation of NO_2 pollution, it is necessary and effective to adjust the NO_2 emission strategy seasonally.

Although the spatial-temporal characteristics and impact factors of NO_2 column concentration distribution in China are analyzed, there are still some limitations and shortcomings in this paper. For example, the incompleteness and partial absence of socio-economic statistics in prefectural units greatly limit the analysis of influential factors of NO_2 pollution. Therefore, the next stage of research should focus on exploring the impact mechanism of NO_2 pollutants at the local scale to guide the formulation of fine-scale NO_2 pollution control policies. Besides, since Sentinel-5P's NO_2 data monthly products are only available after February 2018, the longer time-scale fluctuation studies, such as the annual variation of NO_2 column concentration in China, cannot be implemented. As TROPOMI atmospheric monitoring data is being produced continuously, the available datasets are expanding. Therefore, collecting dynamically updated NO_2 column concentration data and carrying out long-span fluctuation analysis of air pollutants will also be our next focus.

Author Contributions: Conceptualization, Z.Z and F.M.; Funding acquisition, Z.W. and F.M.; Methodology, Z.Z.; Project administration, Z.W.; Software, Z.Z. and Z.Y.; Supervision, Z.W. and F.M.; Validation, Z.Z. and Z.Y.; Writing-original draft, Z.Z.; Writing-review & editing, F.M..

Funding: This study has been supported by National Social Science Foundation of China (41671430) and Natural Science Foundation of Guangdong Province (2018B030312004).

Acknowledgments: We acknowledge the free use of tropospheric NO_2 column data from the TROPOMI (Sentinel-5P) sensor from www.temis.nl. We also want to express our sincere gratitude to the anonymous reviews and editors for their efforts in the improvement of the paper.

Conflicts of Interest: The authors declare no conflict of interest.

References

Abdi, H., (2010) Coefficient of variation, in: Salkind, N. (Ed.), Encyclopedia of research design. Sage, Thousand Oaks, CA, 169-171.

Anselin, L. (1988) Lagrange multiplier test diagnostics for spatial dependence and spatial heterogeneity. Geographical analysis 20, 1-17.

Beirle, S., Platt, U., Wenig, M. & Wagner, T. (2003) Weekly cycle of NO_2 by GOME measurements: a signature of anthropogenic sources. Atmospheric Chemistry and Physics 3, 2225-2232.

Berger, M., Moreno, J., Johannessen, J.A., Levelt, P.F. & Hanssen, R.F. (2012) ESA's sentinel missions in support of Earth system science. Remote Sensing of Environment 120, 84-90.

Boots, B. & Tiefelsdorf, M. (2000) Global and local spatial autocorrelation in bounded regular tessellations. Journal of Geographical Systems 2, 319-348.

Bucsela, E., Perring, A., Cohen, R., Boersma, K., Celarier, E., Gleason, J., . . . Dirksen, R. (2008) Comparison of tropospheric NO_2 from in situ aircraft measurements with near-real-time and standard product data from OMI. Journal of Geophysical Research: Atmospheres 113.

Burridge, P. (1980) On the Cliff-Ord test for spatial correlation. Journal of the Royal Statistical Society: Series B (Methodological) 42, 107-108.

Burrows, J.P., Weber, M., Buchwitz, M., Rozanov, V., Ladstätter-Weißenmayer, A., Richter, A., . . . Eichmann, K.-U. (1999) The global ozone monitoring experiment (GOME): Mission concept and first scientific results. Journal of the Atmospheric Sciences 56, 151-175.

Cao, C., Xiong, J., Blonski, S., Liu, Q., Uprety, S., Shao, X., . . . Weng, F. (2013) Suomi NPP VIIRS sensor data record verification, validation, and long-term performance monitoring. Journal of Geophysical Research: Atmospheres 118, 11,664-611,678.

Change, I.C., (2007) The physical science basis, Contribution of working group I to the Fourth Assessment Report of the Intergovernmental Panel on Climate Change.

Chen, M., Gong, Y., Li, Y., Lu, D. & Zhang, H. (2016) Population distribution and urbanization on both sides of the Hu Huanyong Line: Answering the Premier's question. Journal of Geographical Sciences 26, 1593-1610.

Chen, Z.-m. & Xie, W., (2010) Notice of Retraction: Relations between traffic vehicles and environmental pollution, 2010 Second IITA International Conference on Geoscience and Remote Sensing. IEEE, 388-390.

Crutzen, P.J. (1979) The role of NO and NO_2 in the chemistry of the troposphere and stratosphere. Annual review of earth and planetary sciences 7, 443-472.

Crutzen, P.J. & Schmailzl, U. (1983) Chemical budgets of the stratosphere. Planetary and Space Science 31, 1009-1032.

Desnos, Y.L., Buck, C., Guijarro, J., Levrini, G., Suchail, J.-L., Torres, R., . . . Rosich, B., (2000) The ENVISAT advanced synthetic aperture radar system, IGARSS 2000. IEEE 2000 International Geoscience and Remote Sensing Symposium. Taking the Pulse of the Planet: The Role of Remote Sensing in Managing the Environment. Proceedings (Cat. No. 00CH37120). IEEE, 1171-1173.

Diao, B., Zeng, K., Su, P., Ding, L. & Liu, C. (2016) Temporal-spatial distribution characteristics of provincial industrial NO_x emissions and driving factors in China from 2006 to 2013. Resources Science 38, 1768-1779.

Duncan, B.N., Lamsal, L.N., Thompson, A.M., Yoshida, Y., Lu, Z., Streets, D.G., . . . Pickering, K.E. (2016) A space-based, high-resolution view of notable changes in urban NO_x pollution around the world (2005–2014). Journal of Geophysical Research: Atmospheres 121, 976-996.

Emeis, S. & Schäfer, K. (2006) Remote sensing methods to investigate boundary-layer structures relevant to air pollution in cities. Boundary-layer meteorology 121, 377-385.

Fu, C., Tang, J., Dan, L. & Xue, Y. (2016) Satellite-based long-term trends analysis in TroNO_2 over Hainan Island and its

possible reason. Acta Scientiae Circumstantiae 36, 1402-1410.

Galli, A., Butz, A., Scheepmaker, R., Hasekamp, O., Landgraf, J., Tol, P., . . . Wennberg, P. (2012) CH_4, CO, and H_2O spectroscopy for the Sentinel-5 Precursor mission: an assessment with the Total Carbon Column Observing Network measurements. Atmospheric Measurement Techniques 5, 1387-1398.

Georgoulias, A.K., van der A, R.J., Stammes, P., Boersma, K.F. & Eskes, H.J. (2019) Trends and trend reversal detection in 2 decades of tropospheric NO_2 satellite observations. Atmospheric Chemistry and Physics 19, 6269-6294.

Guan, D., Hubacek, K., Weber, C.L., Peters, G.P. & Reiner, D.M. (2008) The drivers of Chinese CO_2 emissions from 1980 to 2030. Global Environmental Change 18, 626-634.

Guan, X., Wei, H., Lu, S., Dai, Q. & Su, H. (2018) Assessment on the urbanization strategy in China: Achievements, challenges and reflections. Habitat International 71, 97-109.

Guanter, L., Aben, I., Tol, P., Krijger, J., Hollstein, A., Köhler, P., . . . Landgraf, J. (2015) Potential of the TROPOspheric Monitoring Instrument (TROPOMI) onboard the Sentinel-5 Precursor for the monitoring of terrestrial chlorophyll fluorescence. Atmospheric Measurement Techniques 8, 1337-1352.

Gupta, P., Christopher, S.A., Wang, J., Gehrig, R., Lee, Y. & Kumar, N. (2006) Satellite remote sensing of particulate matter and air quality assessment over global cities. Atmospheric environment 40, 5880-5892.

Hassinen, S., Balis, D., Bauer, H., Begoin, M., Delcloo, A., Eleftheratos, K., . . . Hao, N. (2016) Overview of the O3M SAF GOME-2 operational atmospheric composition and UV radiation data products and data availability. Atmospheric Measurement Techniques 9, 383-407.

Hendrick, F., Mahieu, E., Bodeker, G.E., Boersma, K.F., Chipperfield, M.P., De Mazière, M., . . . Van Roozendael, M. (2016) Analysis of stratospheric NO_2 trends above Jungfraujoch using ground-based UV-visible, FTIR, and satellite nadir observations. Atmospheric Chemistry and Physics 12, 8851–8864.

Huang, H., Fu, D. & Qi, W. (2017) Effect of driving restrictions on air quality in Lanzhou, China: Analysis integrated with internet data source. Journal of Cleaner Production 142, 1013-1020.

Huijnen, V., Eskes, H., Amstrup, B., Bergstrom, R., Boersma, K., Elbern, H., . . . Gross, A. (2009) Comparison of OMI NO_2 tropospheric columns with an ensemble of global and European regional air quality models. Atmos. Chem. Phys. Discuss 9, 22271-22330.

Kramer, L.J., Leigh, R.J., Remedios, J.J. & Monks, P.S. (2008) Comparison of OMI and ground-based in situ and MAX-DOAS measurements of tropospheric nitrogen dioxide in an urban area. Journal of Geophysical Research: Atmospheres 113.

Krotkov, N.A., McLinden, C.A., Li, C., Lamsal, L.N., Celarier, E.A., Marchenko, S.V., . . . Duncan, B.N. (2016) Aura OMI observations of regional SO_2 and NO_2 pollution changes from 2005 to 2015. Atmospheric Chemistry and Physics 16, 4605-4629.

Lee, D., Köhler, I., Grobler, E., Rohrer, F., Sausen, R., Gallardo-Klenner, L., . . . Bouwman, A. (1997) Estimations of global NO emissions and their uncertainties. Atmospheric environment 31, 1735-1749.

Li, F., Wei, A., Mi, X. & Sun, G. (2016) An approach of GDP spatialization in Hebei province using NPP-VIIRS nighttime light data. Journal of Xinyang Normal University 29, 152-156.

Li, K. & Bai, K. (2019) Spatiotemporal Associations between $PM_{2.5}$ and SO_2 as well as NO_2 in China from 2015 to 2018. International journal of environmental research and public health 16, 2352.

Li, Y. & Wei, Y.D. (2010) The spatial-temporal hierarchy of regional inequality of China. Applied Geography 30, 303-316.

Liu, W., Chen, Z., Liu, J. & Xie, P. (2016) Stereoscopic monitoring technology and applications for the atmospheric environment in China. Chinese Science Bulletin 61, 3196-3207.

Ma, W., Li, Y. & Hou, X. (2016) Characteristics of Atmospheric NO2 Vertical Column Densities in Heating Period of Urumqi. Ecology and Environmental Sciences 25, 1351-1355.

Marinello, F. (2017) Last generation instrument for agriculture multispectral data collection. Agricultural Engineering

International: CIGR Journal 19, 87-93.

Memmesheimer, M., Jakobs, H.J., Wurzler, S., Hebbinghaus, H., Friese, E., Piekorz, G., . . . Ebel, A., (2010) Possible impact of increased fraction of NO_2-emissions due to road traffic on air pollutant concentration in Central Europe and North-Rhine Westphalia, EGU General Assembly Conference Abstracts, 9554.

Misra, P. & Takeuchi, W., (2016) Analysis of air quality and nighttime light for Indian urban regions, IOP Conference Series: Earth and Environmental Science. IOP Publishing, 012077.

Munro, R., Lang, R., Klaes, D., Poli, G., Retscher, C., Lindstrot, R., . . . Holdak, A. (2016) The GOME-2 instrument on the Metop series of satellites: instrument design, calibration, and level 1 data processing–an overview. Atmospheric Measurement Techniques 9, 1279-1301.

Peng, J., Chen, S., Lü, H., Liu, Y. & Wu, J. (2016) Spatiotemporal patterns of remotely sensed $PM_{2.5}$ concentration in China from 1999 to 2011. Remote Sensing of Environment 174, 109-121.

Premo, L.S. (2004) Local spatial autocorrelation statistics quantify multi-scale patterns in distributional data: an example from the Maya Lowlands. Journal of Archaeological Science 31, 855-866.

Qiu, P., Tang, X., Lu, M., Huang, Y. & Zhou, J. (2018) Forecast of changing air pollution trends in Wuhan city. Journal of Nanjing University of Information Science & Technology (Natural Science Edition) 10, 571-578.

Reed, G.F., Lynn, F. & Meade, B.D. (2002) Use of coefficient of variation in assessing variability of quantitative assays. Clinical and Vaccine Immunology 9, 1235-1239.

Richter, A., Burrows, J.P., Nüß, H., Granier, C. & Niemeier, U. (2005) Increase in tropospheric nitrogen dioxide over China observed from space. Nature 437, 129-132.

Schneider, P., Lahoz, W.A. & van der A, R. (2015) Recent satellite-based trends of tropospheric nitrogen dioxide over large urban agglomerations worldwide. Atmospheric Chemistry and Physics 15, 1205-1220.

Showstack, R. (2014) Sentinel satellites initiate new era in earth observation. EOS Transactions.

Steinfeld, J.I. (1998) Atmospheric chemistry and physics: from air pollution to climate change. Environment: Science and Policy for Sustainable Development 40, 26-26.

Stolarski, R.S., Bloomfield, P., McPeters, R.D. & Herman, J.R. (1991) Total ozone trends deduced from Nimbus 7 TOMS data. Geophysical Research Letters 18, 1015-1018.

Sun, C., Luo, Y. & Li, J. (2018) Urban traffic infrastructure investment and air pollution: Evidence from the 83 cities in China. Journal of Cleaner Production 172, 488-496.

Tian, H., Wang, Y., Zhao, D., Chai, F., Xing, Z. & Cheng, K. (2011) Formation and causes of NO_x pollution on the east side of the Taihang Mountains in China. Chinese Science Bulletin 56, 2044-2049.

Tobler, W. (2004) On the first law of geography: A reply. Annals of the Association of American Geographers 94, 304-310.

Tømmervik, H., Johansen, B. & Pedersen, J. (1995) Monitoring the effects of air pollution on terrestrial ecosystems in Varanger (Norway) and Nikel-Pechenga (Russia) using remote sensing. Science of the Total Environment 160, 753-767.

Van Der A, R., Eskes, H., Boersma, K., Van Noije, T., Van Roozendael, M., De Smedt, I., . . . Meijer, E. (2008) Trends, seasonal variability and dominant NO_x source derived from a ten year record of NO_2 measured from space. Journal of Geophysical Research: Atmospheres 113.

Van Der A, R., Peters, D., Eskes, H., Boersma, K., Van Roozendael, M., De Smedt, I. & Kelder, H. (2006) Detection of the trend and seasonal variation in tropospheric NO_2 over China. Journal of Geophysical Research: Atmospheres 111.

Veefkind, J., Aben, I., McMullan, K., Förster, H., De Vries, J., Otter, G., . . . Kleipool, Q. (2012) TROPOMI on the ESA Sentinel-5 Precursor: A GMES mission for global observations of the atmospheric composition for climate, air quality and ozone layer applications. Remote Sensing of Environment 120, 70-83.

Velders, G.J., Granier, C., Portmann, R.W., Pfeilsticker, K., Wenig, M., Wagner, T., . . . Burrows, J.P. (2001) Global

tropospheric NO_2 column distributions: Comparing three-dimensional model calculations with GOME measurements. Journal of Geophysical Research: Atmospheres 106, 12643-12660.

Wang, P., Wu, W., Zhu, B. & Wei, Y. (2013) Examining the impact factors of energy-related CO_2 emissions using the STIRPAT model in Guangdong Province, China. Applied Energy 106, 65-71.

Wheeler, D.C. & Calder, C.A. (2007) An assessment of coefficient accuracy in linear regression models with spatially varying coefficients. Journal of Geographical Systems 9, 145-166.

Xiao, Z., Jiang, H. & Cheng, M. (2011) Characteristics of atmospheric NO_2 over China using OMI remote sensing data. Acta Sci. Circumstantiae 31, 2080-2090.

Xie, X. & Liao, L. (2015) A study on the relationship between tourism development and economic growth in Yunnan Province based on spatial econometric model. Journal of Kunming University of Science and Technology (Natural Sciences) 15, 77-84.

Xue, T., Zheng, Y., Geng, G., Zheng, B., Jiang, X., Zhang, Q. & He, K. (2017) Fusing observational, satellite remote sensing and air quality model simulated data to estimate spatiotemporal variations of $PM_{2.5}$ exposure in China. Remote Sensing 9, 221.

Yang, W., Chen, B.Y., Cao, X., Li, T. & Li, P. (2017) The spatial characteristics and influencing factors of modal accessibility gaps: A case study for Guangzhou, China. Journal of Transport Geography 60, 21-32.

Yang, X., Yue, W., Xu, H., Wu, J. & He, Y. (2014) Environmental consequences of rapid urbanization in Zhejiang province, East China. International journal of environmental research and public health 11, 7045-7059.

Zhang, J. & Chen, J. (2007) Study on construction land distribution in Fujian and Taiwan Provinces based on spatial autocorrelation analysis. Progress in Geography 26, 11-17.

Zheng, X., Li, L. & Zhao, W. (2014) Spatial and temporal characteristics of atmospheric NO_2 in the Beijing-Tianjin-Hebei region. Ecology and Environmental Sciences 23, 1938-1945.

Zheng, Z., Chen, Y., Wu, Z., Ye, X., Guo, G. & Qian, Q. (2019) The desaturation method of DMSP/OLS nighttime light data based on vector data: Taking the rapidly urbanized China as an example. International Journal of Geographical Information Science 33, 431-453.

9. Global-scale detection of human activities and ecological status dynamics

9.1 Abstract

Over the past two decades, with the increasing capacity and scale of human modification of the Earth's surface, the ecological environment has been facing increasingly severe challenges. Although the dynamic analysis of regional human activities and ecological environment based on remote sensing images is advancing, long time series monitoring on a global scale still deserves to be optimized. As a positive response to SDGs, this study proposes a long-term monitoring scheme of human activities and regional ecological environment dynamics based on daytime optical remote sensing and nighttime light remote sensing products. The scheme was deployed on the GEE cloud platform, and an extensive amount of MODIS, Landsat and NTL satellite images stored on the server side were integrated to perform parallel analysis in the global anthropogenic zone through a tile-grid strategy. Compared with previous studies, our proposed scheme has higher stability and robustness, which overcomes 1) the stochasticity of RSEI for long-term and high-frequency dynamic analysis, and 2) the overestimation and pseudo-decreasing pixels of ENTL in urban areas. The dynamic monitoring results of 7894 grids worldwide show that there was a significant spatial heterogeneity between global human activity intensity and ecological environment status during the last two decades, and non-G7 developed countries and BRICS countries had significantly better coupling between human activity intensity and ecological environment than G7 countries and the least developed countries. In addition, our results further confirm that coastal regions have experienced higher human activity growth along with greater ecological and environmental challenges and sustainable development pressures compared to inland regions.
Keywords: Global scale; grids analysis; NTL; MRSEI

9.2 Introduction

Since the dawn of mankind, human activities have influenced and reshaped the earth's surface in various ways (Phillips, 1991; Crutzen, 2006; Tarolli and Sofia, 2016). According to the World Bank, the total global population has increased by 25% to 7.674 billion over the millennium, and urbanization has continued to advance, with the global average urbanization rate reaching 55.7%. Along with the growth of urbanization and the rise in total population, the demand and intensity of human activities for surface modification during that period was also far stronger than at any other time in history. There is growing evidence that the expansion of high-intensity human activities destabilizes surface habitats and causes a series of environmental problems such as climate warming (Du et al., 2004; Trenberth, 2018), sharp decline in biodiversity (Young et al., 2005; Katsanevakis et al., 2014), and atmospheric pollution (Li et al., 2016; Li et al., 2020a).

Currently, the interaction between human activities and environmental conditions (sustainable development) has become a topic of widespread concern. As an effort to actively address the challenges of human development and environmental change, the Sustainable Development Goals (SDGs) have been

proposed to give direction to the global sustainable development that follows (Menton et al., 2020). In order to achieve the goal of environmental sustainability in SDGs, it is crucial to understand the spatial and temporal patterns of human activities and environmental conditions, and to mitigate environmental damage in sensitive areas or ecologically valuable areas.

The development of remote sensing technology has led to unprecedented progress in signal capture (inversion) of surface ecological environment and human activity intensity. With the advantages of spatial and temporal coverage compared to traditional local sample surveys and approaches, remote sensing-based parameter inversion methods have been effectively used to assess local, regional and global environmental and human activity intensities (Deng and Wu, 2012; Yu et al., 2018; Li et al., 2019; Firozjaei et al., 2021). However, due to the complexity of environmental factors, it has been challenging to quantify the ecological conditions of the land surface due to the difficulty of integrating standard ecological levels (NDVI, LST, etc.) by single ecological indicators. The RSEI index is proposed to address this challenge by combining available indicators and data to reveal the regional ecological quality (Hu and Xu, 2018).

The RSEI-based ecological inversion has been applied in areas with different environmental backgrounds and development stages. It has been proved that RSEI is more comprehensive than other single ecological parameters to reflect the regional habitat conditions, and it is fully based on remote sensing parameters, which has good robustness (Xu et al., 2019; Yue et al., 2019; Ning et al., 2020). However, almost all existing RSEI-based analyses are limited to urban-scale case studies, and there is a lack of large-scale and long-span trend analysis, which cannot effectively help us understand the global habitat dynamics. Meanwhile, the development of nighttime light remote sensing has made it possible to capture the global anthropogenic footprint more effectively and accurately than ever before. For example, multiple human footprint (pressure) mapping between 1990-2010 have made full use of night-light remote sensing data (Venter et al., 2016; Mammides, 2020). These studies show that remote sensing data from Earth observation are an important cornerstone to support regional environmental and human activity intensity analysis, and can predict human activity perturbations to regional environments more efficiently and at lower cost. Therefore, capturing the dynamics of regional environmental and human activities at the global scale will be critical to achieving the goals in the SDGs and help us better understand the impact of human activities on the regional environment and the different patterns that they diverge. In addition, spatial heterogeneity analysis at the global scale can refine the differences and efforts at the local level in advancing the SDGs.

Here, the main motivation for our work is the desire to address the following questions: (1) How have the ecological conditions and the intensity of human activities in the global anthropogenic regions changed over the past 20 years? (2) What are the interactions between ecological changes and human activity intensity across regions? To answer the above questions, we conducted a quantitative tracking study of global anthropogenic zones (about 8000 grids) with a massive amount of MODIS, Landsat, and VIIRS remote sensing images during 2000-2020.

9.3 Methods

9.3.1 Overview

In order to achieve a long-span quantitative analysis of ecological and environmental conditions and human activity intensity at the global scale, a more mature and widely used satellite data was adopted. Since manipulation of massive satellite image data requires extremely high local computational resources, Google Earth Engine was selected as the data processing platform in this paper. The technology roadmap is illustrated in Figure 9.1.

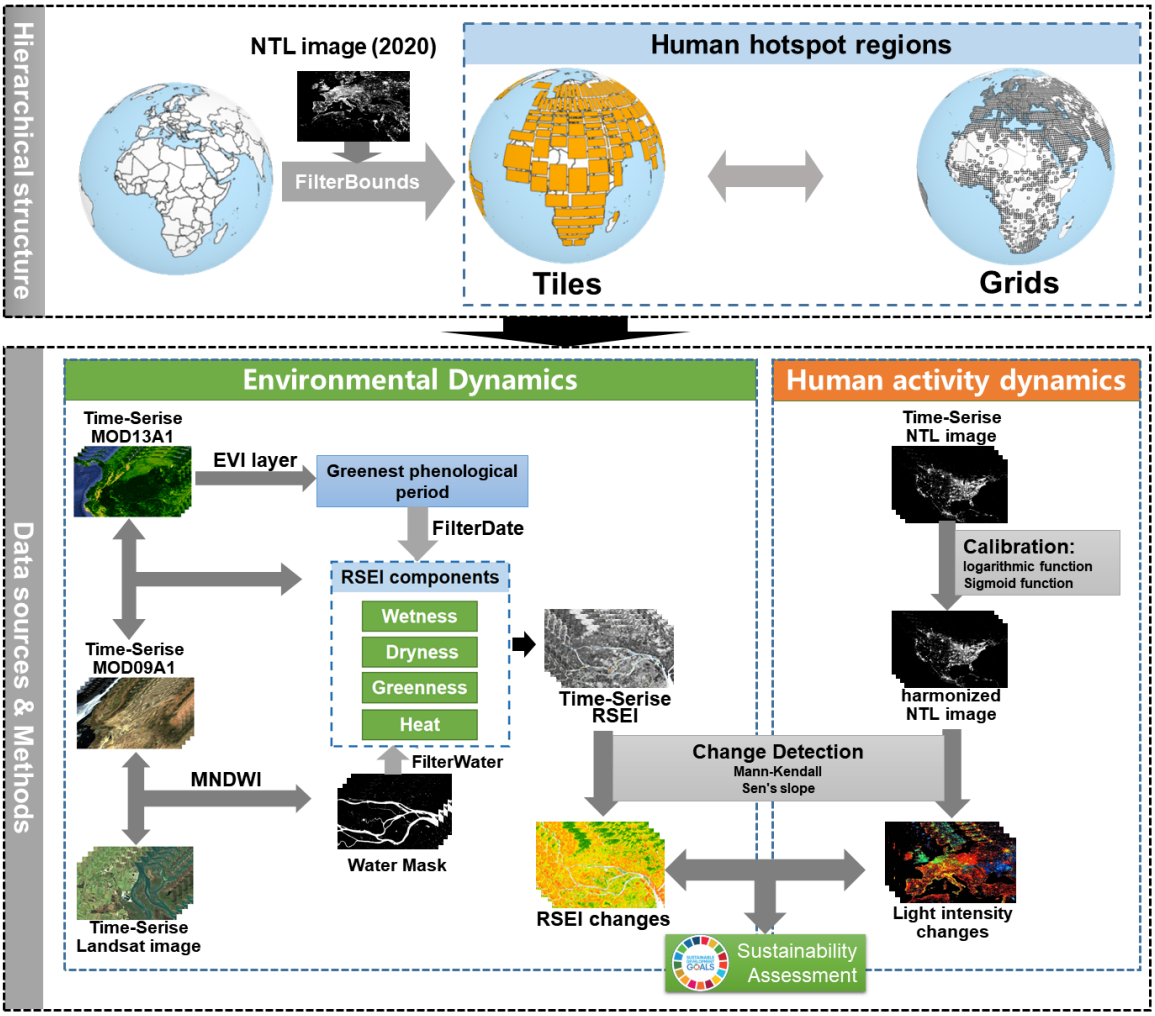

Figure 9.1. Flowchart of the global assessment of human activities and environmental conditions.

9.3.2 Defining the Human Activity Zone Grid

Although GEE is able to take full advantage of the huge computing power in the cloud, it still faces the fact that computing power resources are scarce when computing in parallel. In order to balance computational demands and parallel computing power for quantitative inversion of ecological conditions and human activities on a global scale for the period 2000-2020, we re-mapped the Earth's surface to facilitate data analysis and post-distribution. We used the 2020 version 1 suite of global average radiance composite images from the

VIIRS Day/Night Band (DNB) data to determine the extent of the latest human activity zone. The reason for choosing the anthropogenic area for the analysis is that our core purpose is to focus on the impact of human activities on the environment. Therefore, areas without lights could not be used for comparison experiments because of the lack of sufficient human activity. As the most advanced global-scale light data currently available, it has a finer spatial and temporal resolution than the DMSP/OLS light data products. It has a spatial resolution of 15 arc seconds and covers between 65-75 degrees north and south latitude. Since the VIIRS NTL product provided by the EOG group provides a monthly number of cloud-free observations, in this paper, cloud-free coverage is used as a weighting factor to reduce the interference of clouds when synthesizing the 2020 annual NTL imagery, and the weighting factor is calculated as follows:

$$W_{cf}^{m} = cf_m / \sum_{m=1}^{12} cf_m \tag{9.1}$$

$$VIIRS_a = \sum_{m=1}^{12} VIIRS_m \times W_{cf}^{m} \tag{9.2}$$

where W_{cf}^{m} is the weight determined according to the number of cloud-free observations in month m, and $VIIRS_a$ is the annual synthetic light radiation value, cf_m and $VIIRS_m$ are the number of cloud-free observations and monthly light radiation value in month m, respectively.

For the light radiation values in the year 2020, we used the K-value clustering method to divide the light radiation into lighted and non-lighted areas. During the construction of the grids, the world was divided into $1^{\circ} \times 1^{\circ}$ grids cells in this paper, and the grids were filtered using the lighted areas produced in the previous step, and a total of 7894 grids were selected. These grids are fed into GEE as spatial cells to perform subsequent parallel operations. Besides, we grouped the grid cells into 246 tiles according to their spatial locations to improve the parallel processing efficiency in GEE (Figure 9.2).

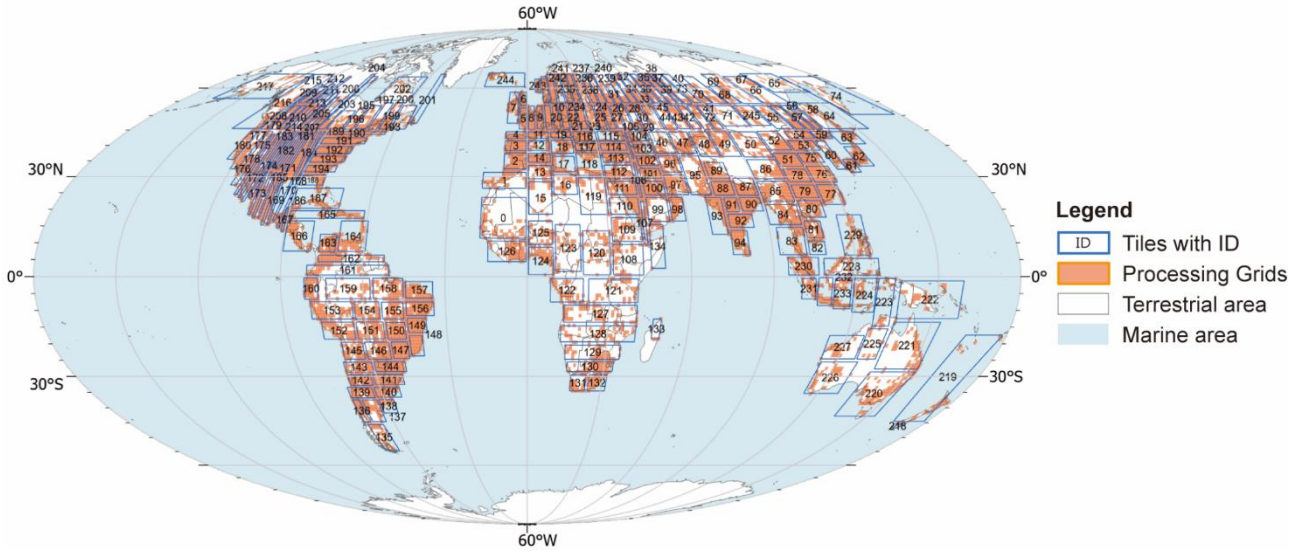

Figure 9.2. The distribution of grids and tiles in anthropogenic zone. To accelerate the subsequent GEE parallel processing process, the anthropogenic zone was divided into 246 tiles and 7894 grids.

9.3.3 Modified RSEI and its dynamics

Considering that the RSEI proposed by Xu (2013) has been considered in extensive practice to be effective, accurate, and objective in responding to the overall ecological environment of the region, we used the index to assess the long-term ecological condition of the global-scale cell grid. The index selects four indicators, such as greenness, humidity, heat and dryness, which people can directly feel, to reflect the regional ecological environment comprehensively, and integrates each indicator by principal component transformation. Thus, it overcomes the shortcomings of a single indicator while making the integration of the sub-indicators more reasonable. The formula is defined as:

$$RSEI = PCA1(Greeness, Heat, Wetness, Dryness) \tag{9.3}$$

For the Greenness component, the NDVI layer from the MOD13A1 V6 product was used, which provides a 500m spatial resolution, 16-day period synthetic vegetation index. The 8-day synthetic, 500m resolution multi-band surface reflectance product MOD09A1 was then used to extract the other three environmental components. In addition, for the heat component, considering the instability of the heat component LST in long span comparisons, the RSEI is improved in this paper (the modified RSEI is referred to as MRSEI in this section). Here, we choose the NDMI with better stability instead (Li et al., 2017), which is defined as:

$$NDMI = (\rho_{nir} - \rho_{swir})/(\rho_{nir} + \rho_{swir}) \tag{9.4}$$

Another improvement worth highlighting is the automatic detection of the inversion time window. Previous RSEI inversion studies have used an annual synthesis scheme, but this tends to obscure the true RSEI variability. In this paper, we used the scheme of similar phenological characteristics when setting the year-by-year time windows, that is, we calculated the vegetation index for each grid cell annually and selected the two months before and after the month with the highest vegetation index as the time windows. This solution can dynamically select the greenest phenological period as the time window for comparison according to the geographic context of the grids. In addition, since the above four components will have extreme values in the water body region, the water surface needs to be masked. In this paper, the Landsat image collections of the same period are called to extract the extent of the water bodies based on the MNDWI to improve the precision of the water body mask.

In addition, we found in our large-scale case study that the normalized RSEI for long time series suffered from a certain instability due to extreme values that could lead to abnormal data distribution shifts. Especially in regions with extreme environmental conditions, such as the Sahara Desert in Africa, the current RSEI dynamic detection results showed plenty of RSEI improved pixels, which was different from the actual situation where the natural conditions and ecology of the surface were largely unchanged. Here, quantile clustering approach was used to reduce potential anomalies in the data distribution caused by extreme values and to achieve a time-series dynamic analysis of the annual MRSEI. Specifically, all pixels within the grid cell were taken as samples, and the 10% gradient was set as a quantile interval to cluster according to the MRSEI value, and the pixels were re-assigned to 1-10 according to their quantile interval. The quantile clustering approach allows each interval to have the same number of pixels and eliminates the variance of distribution caused by extreme values.

Based on the annual clustered MRSEI layers for the period 2000-2020, Theil-Sen Median trend analysis and Mann-Kendall test were used to perform dynamic analysis. Theil-Sen Median trend analysis and Mann-Kendall test do not require the data to obey a certain distribution and have a strong resistance to data outliers (Tucker et al., 1991). For each grid cell, we calculate the significantly growing pixels ($Sen'slope > 0,\ p < 0.05$), significantly declining pixels ($Sen'slope < 0,\ p < 0.05$), constant pixels and insignificantly changing pixels ($p > 0.05$) within the grid, and count their percentages separately.

9.3.4 Long-term nighttime light dynamic identification

Since our study spans 2000-2020, multi-source NTL products (DMSP/OLS and NPP/VIIRS) were used for the study as a single NTL product could not serve the needs of the long time series study. Although several calibrated and extended NTL products have been developed and released, our previous study in "**Chapter 5**" showed that these products have some error pixels, especially in urban areas. Therefore, different from the previous approach which utilized ENTL to characterize long-term light radiation dynamics, the $PCI_{Standard}$ layer generated in "**Chapter 5**" was used in this Section. The $PCI_{Standard}$ layers for the period 2000-2020 were finally derived based on a double independent Theil-Sen Median trend analysis and Mann-Kendall test with post-logical rule judgment. Similarly, the PCIs layer also identified the significant dynamic characteristics of the light pixels over the last 20 years. The detailed generation method and logical judgment rules can be found in the method description in "**Chapter 5.4**".

9.4 Results

9.4.1 Global dynamics of nighttime light intensity

Based on the developed robust light radiation change identification method, we have identified the light radiation variation of the global grid, and the results are shown in Figure 9.3 and Figure 9.4, which depicts the percentage of pixels with significant increase and decrease.

According to the percentage distribution of significantly increased light radiation pixels, it shows an uneven rise of nighttime light radiation within the anthropogenic areas. For the continental average percentage of light radiation increase, Europe achieved the highest, reaching 8.88%, followed by Asia, 6.10%. The significant increased pixel of radiation in South America contributes 2.62%, while Africa and North America have a close share with 1.8% and 1.59%, respectively. Oceania recorded the lowest rate of increase in light radiation, at 0.76%. In more detail, the grid with more than 40% of significantly increased pixels were mainly concentrated in west-central Europe, China in East Asia, and India in South Asia (Figure 9.3(b)). These regions, especially China and India, are the most dramatically urbanized regions in the past two decades, with large numbers of people gathering from rural to urban areas, resulting in rapid expansion of built-up areas, which triggered the rapid equipping of nighttime lighting facilities and caused a significant increase in nighttime lighting radiation. In addition, there are some phenomena worth mentioned. For example, the eastern part of

Brazil also experienced a considerable rise in light radiation, with more than a 12% rise in most of the grids. As one of the BRICS countries, Brazil has experienced rapid economic development over the past 20 years, and with its rich natural resources and complete industrial base, Brazil ranks first in South America in terms of GDP and is the seventh largest economy in the world. Alternatively, the United States, as the world's largest economy and recognized as the largest developed country, its proportion of increased light radiation pixels within the grid are mostly below 6%. Although it has the largest economic volume, its incremental light radiation is slightly insufficient compared to the emerging development countries since the 21st century.

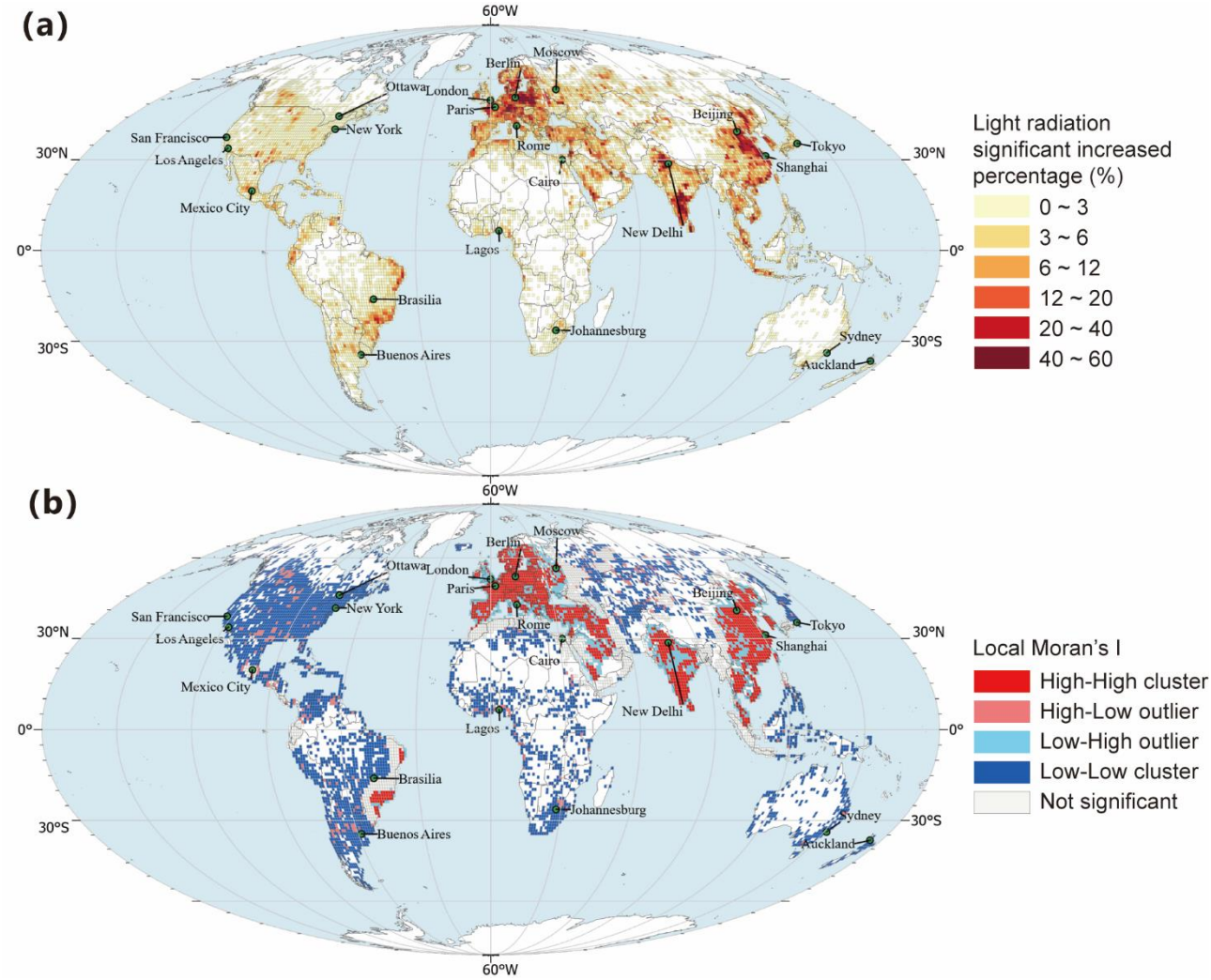

Figure 9.3. Percentage of pixels with (a) increased light radiation of each grid and its (b) local Moran's distribution.

Similarly, we also counted the percentage of pixels with decreased light radiation for the global grid, as shown in the Figure 9.4(a). The results show that North America is the continent with the highest percentage of average light radiation decline (7.59%), Europe and Asia followed by 5.10% and 2.78% respectively, Africa and Oceania are closer, 1.5% and 1.34% respectively, and South America has the lowest percentage of light radiation decline pixels, only 0.98%. At the grid scale, it can be observed that the grid cells with more than 20% of the decreased pixels of light radiation are mainly located in the east-central part of the United States, eastern Europe, western India and Japan (Figure 9.4(b)). These areas have shown a clear trend of declining

light radiation over the past 20 years. Possible reasons for the decline in nighttime urban lighting intensity can be attributed to the slowdown in economic growth, the anti-urbanization process, and the renewal of illumination facilities.

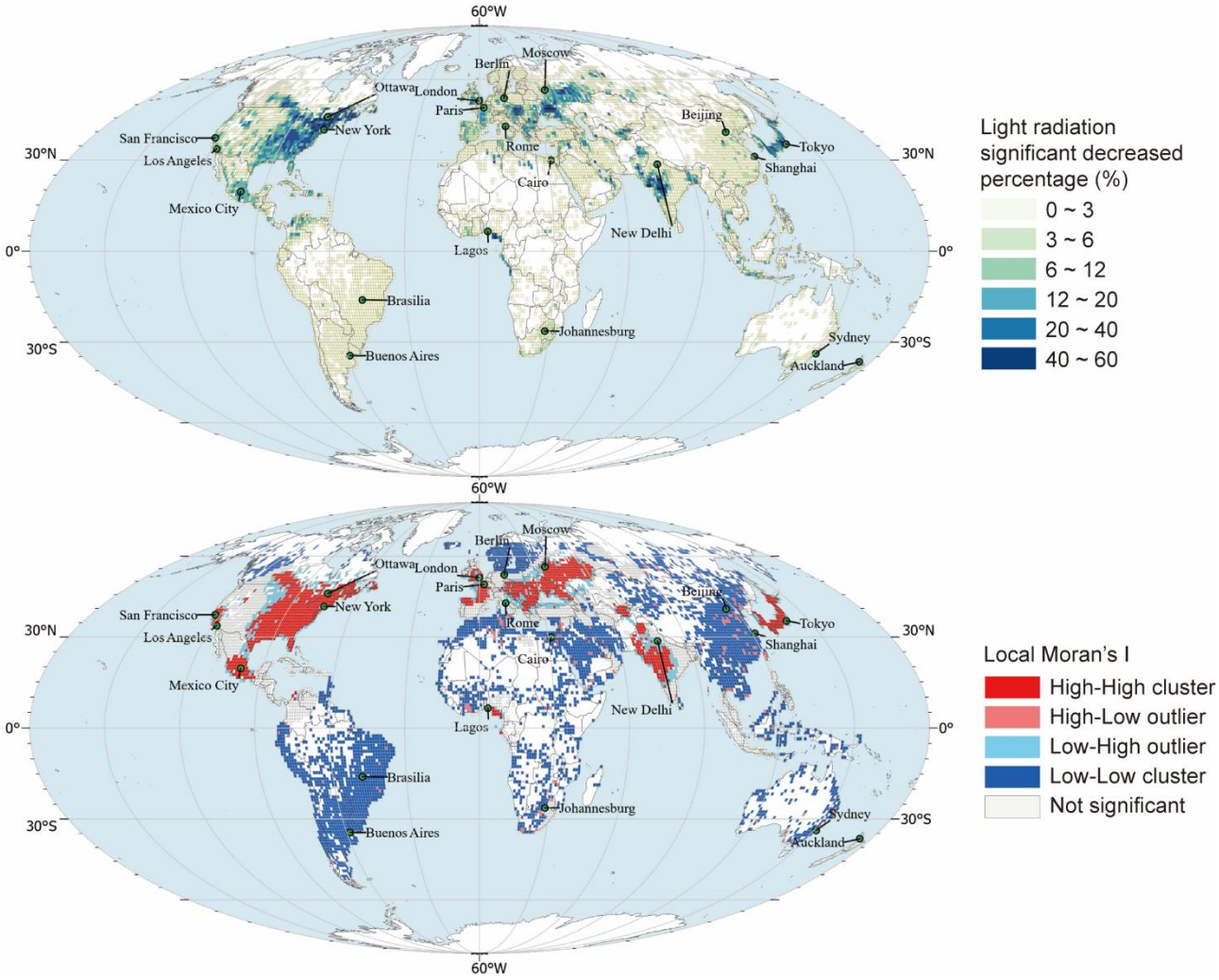

Figure 9.4. Percentage of pixels with (a) decreased light radiation of each grid and its (b) local Moran's distribution.

9.4.2 Global environmental conditions dynamics

Based on the MRSEI over the past 20 years, we performed dynamic identification of each grid cell and counted the percentage of significantly increased and significantly decreased pixels. Figure 9.5 illustrates the percentage of pixels with significantly increased MRSEI in the global grid cells. The results of the local autocorrelation analysis indicate that the high percentage grid with significantly increased MRSEI were mainly clustered in east-central China, north-central India, eastern Europe, east-central US and southeastern Brazil. Among them, the grids with more than 30% of MRSEI increased pixels were mainly located in the Sichuan Basin in southwestern China, northern Baikal Lake and the Great Lakes region in the United States. Meanwhile, the cold spot regions (Low-Low cluster) were mainly distributed in the regions of Southern Europe, North Africa, Midwest USA, Central Asia and Japan.

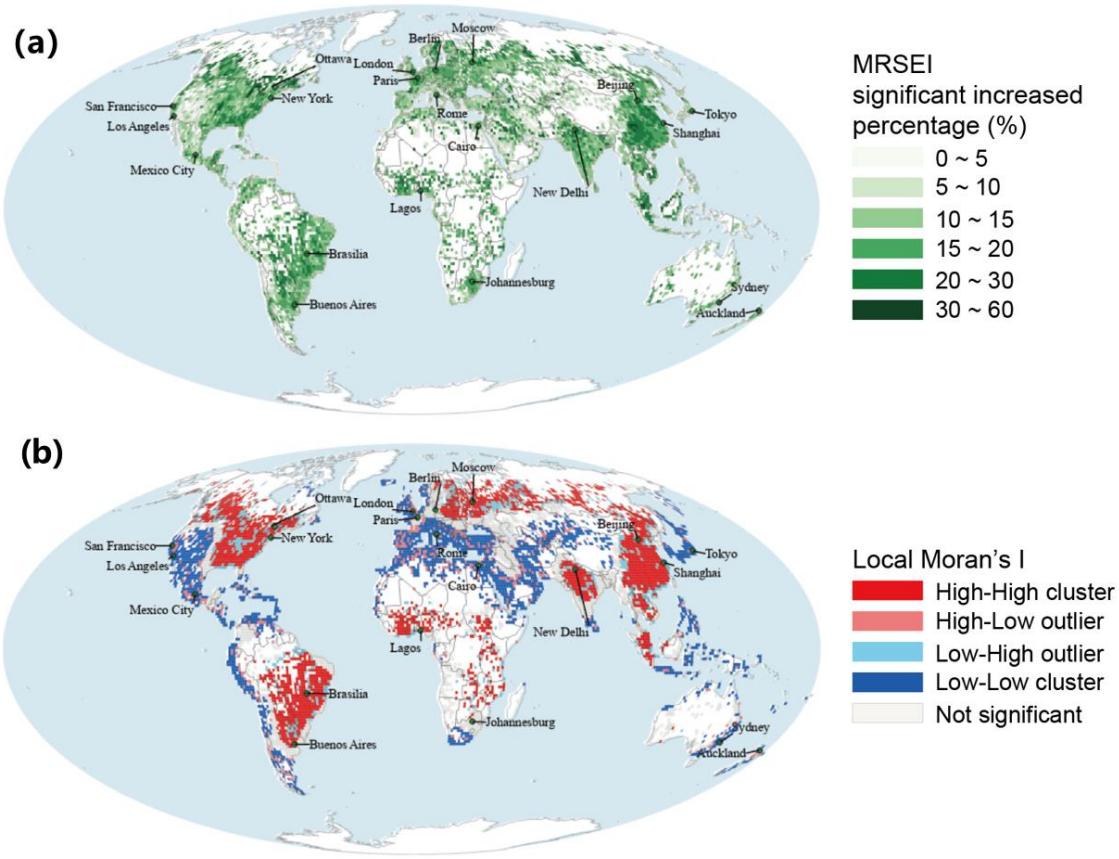

Figure 9.5. The percentage of pixels with (a) significantly increased MRSEI of each grid and (b) its local Moran's I.

Correspondingly, Figure 9.6 counts the percentage of pixels with significantly decreased MRSEI in the global grid cells. According to the local autocorrelation aggregation, it can be found that the distribution of the MRSEI significantly decreased pixel grid has very similar distribution characteristics to the MRSEI significantly increased grid in Figure 9.7. Specifically, the high percentage of significantly decreased MRSEI units were concentrated in east-central China, southeastern Brazil, southeastern U.S., central Canada, eastern Europe and central India. In addition, a slight difference can be observed in the Middle East (Iraq), South Africa and the Sub-Saharan region where there were also significant clusters of high percentage of decreased MRSEI units, indicating that the above region experienced significant ecological degradation during the last 20 years.

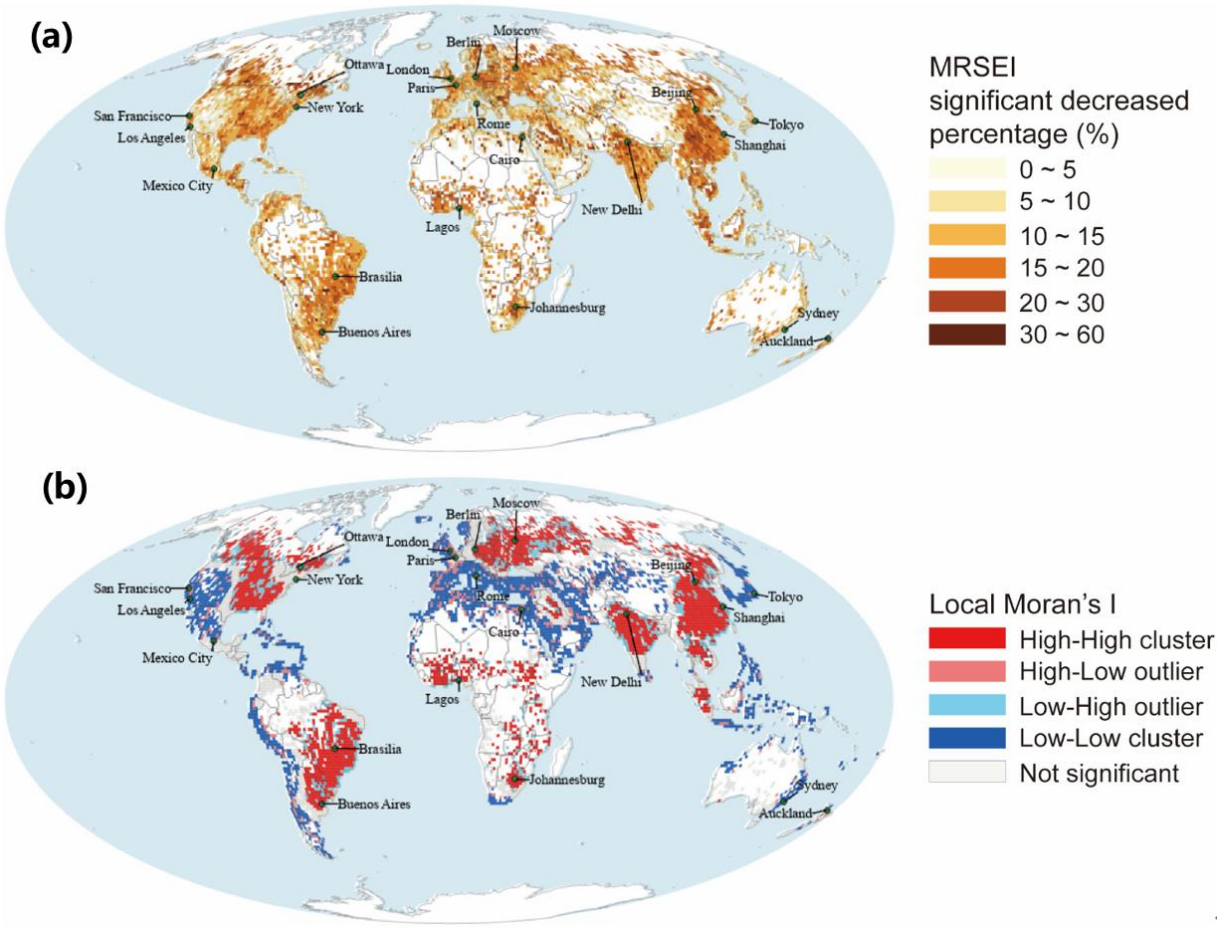

Figure 9.6. The percentage of pixels with (a) significantly decreased MRSEI of each grid and (b) its local Moran's I.

Further, we performed a regression analysis of the percentage of significantly increased and decreased MRSEI for all grids, and the scatter plots are as follows (Figure 9.7). The results of the linear correlation analysis of the global grid showed that the percentage of significantly increased pixels of MRSEI was strongly consistent with the percentage of decreased ones, with Adj.R^2 reaching up to 0.76. Meanwhile, we conducted grouped linear analysis for each continent separately, and the results showed that 1) the linear correlations of the grids in Africa and Oceania were higher than the global average, with Adj.R^2 reaching over 0.87; 2) the linear correlation of the grids in Europe, Asia and South America was close to the global average; the Adj.R^2 of the grids in South America was only 0.62, and the linear correlation was lower than the global average. These results suggest that there is usually a concomitant phenomenon of ecological deterioration and improvement. We speculate that the reason for this phenomenon is related to the way RSEI is calculated. Since RSEI is a relative value, once the RSEI of a large number of pixels increases, it will inevitably lead to a "relative decrease" in the RSEI of the rest of the pixels.

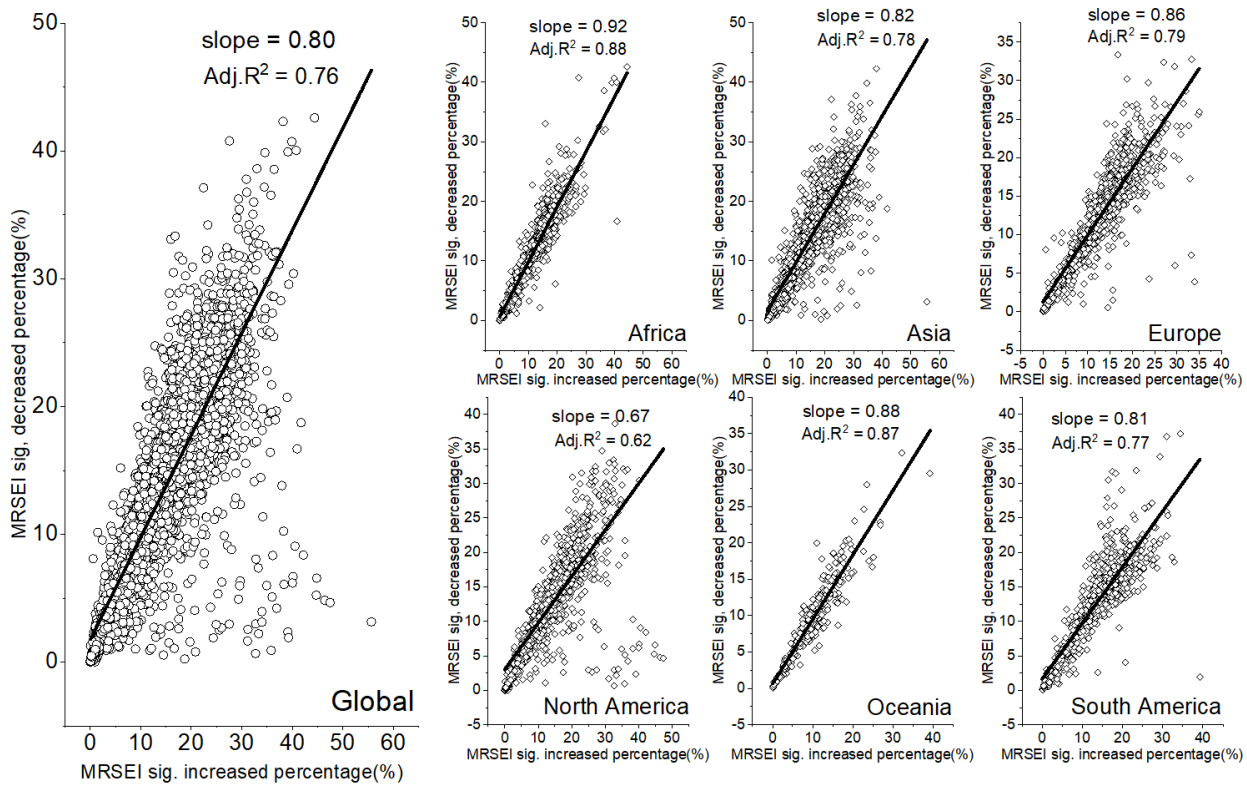

Figure 9.7. Linear correlation between the percentage of significantly increased and decreased MRSEI for the global and different continental grids.

9.4.3 Coordination coupling between human activities and eco-environment

Originally used as a physical concept, coupling refers to the phenomenon of two (or more) systems or forms of motion affecting each other through various interactions. The coupling degree is to describe the level of interaction of the system or elements. As a quantitative indicator, the coupling degree plays an important role in identifying the strength of the coupling between urbanization and ecology and the time interval of the coupling, as well as in predicting the development status among them. In addition, due to the dynamic and unbalanced nature of the respective development levels of the urban level and the ecosystem, the coupling degree between the two subsystems may appear as a "false coordination" phenomenon. Therefore, to avoid this defect we used a supplementary coordination model based on the coupling degree to objectively reflect the level of coordinated development of the urbanization level system and the ecological environment system. It is worth to highlight that, unlike other coupling coordination degrees that characterize the level of instantaneous system coupling coordination, the 2-indicators measured by CCD in this paper were dynamic characteristics over the past 20 years, which can reflect the interaction between the increased level of regional human activities and the improvement of regional ecological environment over the past 20 years. The specific formulation about the coordination coupling degree (CCD) model can be found in **Chapter 7**.

Table 9.1 showed the global and individual continent-based average pixel percentage of NTL radiation and MRSERI significantly increased and their coordination coupling degree. It can be found that the NTL

radiation increase pixel ratios in Europe and Asia were much higher than the global average, while the MRSEI increase pixel ratios in South America, North America and Asia were slightly higher than the global average. Accordingly, the statistical results by continent showed that the CCD levels in Europe and Asia were higher than the global average, while the CCD in South America was 1.85, slightly lower than the global average, and the CCDs in Africa and North America were closer, at 1.54 and 1.52, respectively, while the CCD in Oceania was the lowest, at 1.2.

Table 9.1 The average pixel percentage of NTL radiation and MRSERI significantly increased and their coordination coupling degree.

Regions	NTL radiation Sig. increased pixel (%)	MRSEI Sig. increased pixel (%)	CCD
Africa	1.80	12.27	1.54
Asia	6.10	13.30	2.35
Europe	8.88	12.69	2.75
North America	1.59	13.75	1.52
Oceania	0.76	10.18	1.20
South America	2.61	13.63	1.85
Global	**4.50**	**13.11**	**2.05**

Further, Figure 9.8 plotted the CCD of the global grid cell and its spatial aggregation distribution. It can be seen that the hotspot regions (aggregation areas with high coordinated coupling grids) of the grid CCD mainly include southeastern China, north-central Europe, and northwestern and southern India. Besides, the eastern and southeastern coasts of Brazil, and Central Asia also have some aggregations of high CCD units. These hotspot units had an average share of 15.38% for lighting radiation increasing pixels while the share of MRSEI increasing pixels was 15.49%. The average pixel percentages of these two indicators are very close and well above the global average, which means that they are an environmentally friendly development model that has experienced a significant increase in human activity over the last 20 years while well maintaining the environmental quality of the region.

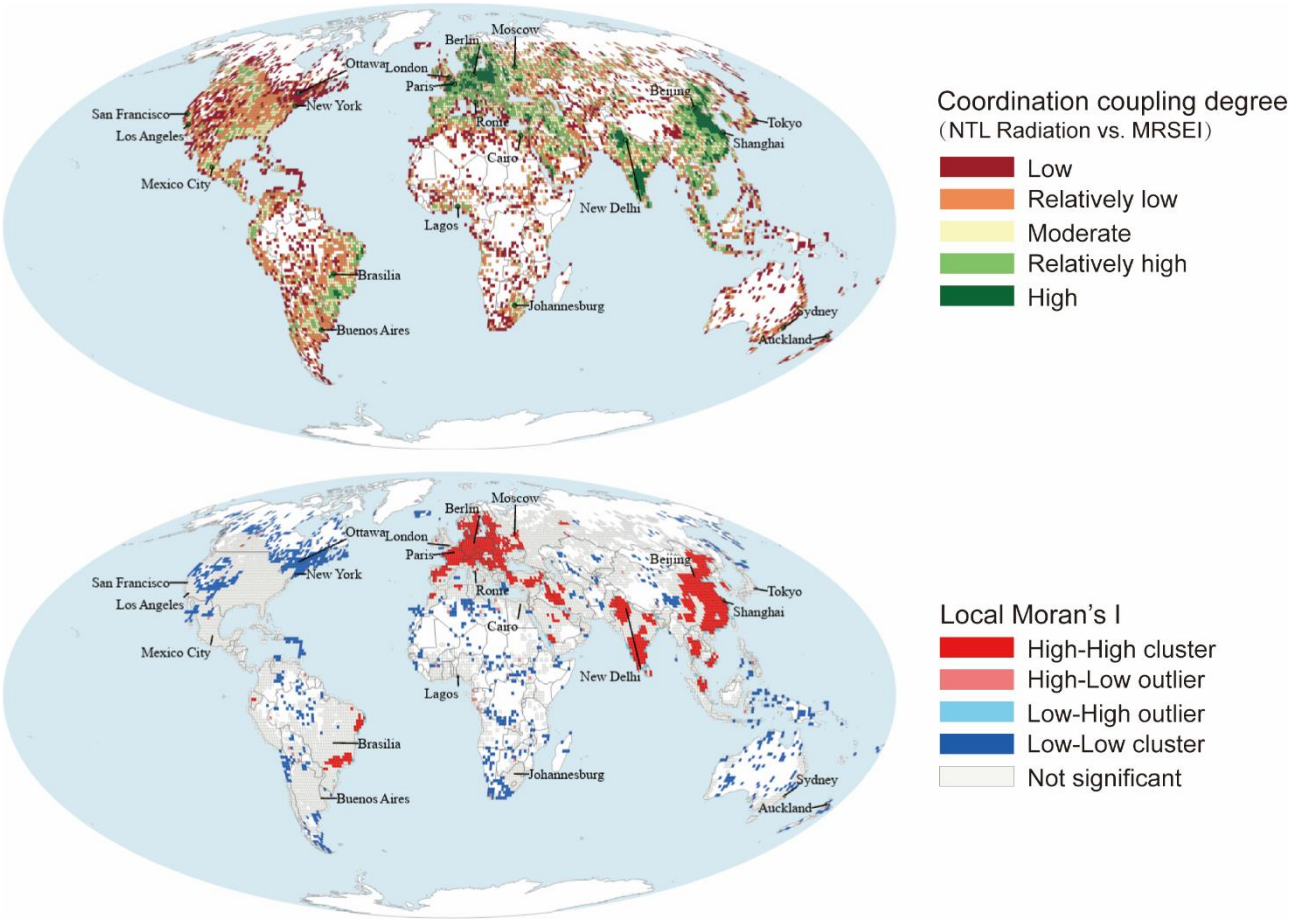

Figure 9.8. The (a) coordination coupling degree of each grid and (b) its spatial aggregation distribution.

Meanwhile, the cold spot regions (aggregation areas with low coordinated coupling grids) were dispersed and mainly distributed in the northeastern and west-central United States, southern Africa and northern Shahra Desert, central Chile, northern Brazil, southwestern China, and southern Argentina. The average share of light radiation added pixels for these cold spot units was only 0.45%, and the share of MRSEI added pixels was 11.1%, which were lower than the global average.

9.5 Discussion

9.5.1 Performance validation of MRSEI and PCI layers

As described in the methodology, we modified the traditional time-series evaluation models for lighting and RSEI to be applicable to global-scale analysis. To check the performance of the model, we compared the results before and after the improvement of NTL dynamics and MRSEI dynamics.

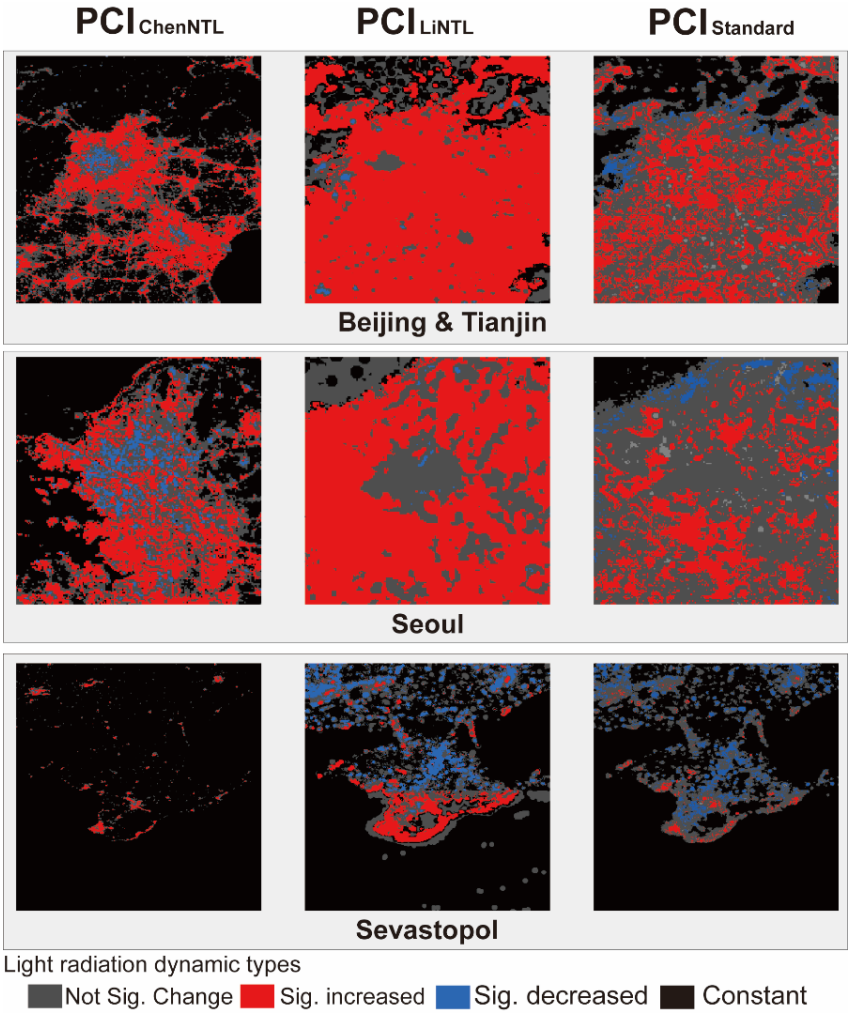

Figure 9.9. Comparison of dynamic identification results of light radiation based on ChenNTL, LiNTL and logic diagnostics result based on DMSP/OLS and NPP/VIIRS combination.

Figure 9.9 shows the dynamic identification of light radiation by three different methods (ENTL data sources) at three different regions. Among them, PCI_{LiNTL} and $PCI_{ChenNTL}$ were identified from the ENTL products developed by Li et al. (2020b) and Chen et al. (2021) respectively, and the specific production details can be found in **Chapter 5**. It can be found that there are significant differences between the above three radiation dynamic identification results. For regions with more rapid urbanization, such as Beijing, Tianjin and Seoul, the significantly increased pixels show a large patchy distribution in PCI_{LiNTL}, while they are more fragmented in $PCI_{ChenNTL}$ and $PCI_{Standard}$. In addition, a significant difference between $PCI_{ChenNTL}$ and $PCI_{Standard}$ is that a large number of significantly decreased blue pixels can be observed in the urban center of $PCI_{ChenNTL}$, which we call the "blue center" phenomenon. The "blue center " typically located in the downtown area, where the most intense human activity and extensive artificial illumination equipment aggregated. Theoretically, it is not reasonable to observe numerous significantly decreased pixels in rapidly growing urban centers. In addition, PCI_{LiNTL} suffered from pixel segmentation at the 45° N which greatly restricted the application of this dataset to data at the global scale. Instead, the $PCI_{Standard}$ used in this section based on a double independent Theil-Sen median trend analysis and Mann-Kendall tests with post-logical rule judgments were able to robustly identify

the dynamics of light pixels over the last 20 years.

Similarly, we selected special grid cells with different environmental conditions in different geographical regions of the world to compare the performance of the ecological environmental index proposed in this Chapter. As shown in Figure 9.10, T16G7, T118G7 and T48G5 were located in the central Sahara Desert, southwest Cairo and northwest Saudi Arabia, respectively. These regions showed similar ecology and land cover, with deserts and oases (desert agriculture) being dominated, and relatively minor changes in land cover and ecological conditions during the study period. T53G11-12 covers the urban areas of Beijing and Tianjin and the surrounding hinterland, and the condition of the ecological environment varied during the study period.

For grid cells with slight ecological changes, especially in desert areas where the ecology can be roughly defined as constant, we observed significant differences in the dynamic detection signs of RSEI and MRSEI. According to the sample grid comparisons, RSEI generally tends to overestimate environmental conditions in desert areas and lead to numerous pixels with significantly increased environmental conditions, while MRSEI is more conservative. In addition, MRSEI is more sensitive to the detection of agricultural facilities in desert areas, and its dynamic identification results are consistent with the land cover changes. For areas with more complex ecological changes, we found that the dynamic identification results of RSEI usually underestimate the ecological condition of the area and show unnatural aggregation. In contrast, the dynamic identification results of MRSEI appear more natural and realistic, that is, the ecological environment in rapidly urbanizing areas shows a decreasing trend, while the hinterland far from urban areas shows no significant change or ecological improvement.

Overall, we consider that the stability and robustness of the optimized light radiation and MRSEI dynamic identification results have been significantly improved which could be more suitable for long-term and global scale research.

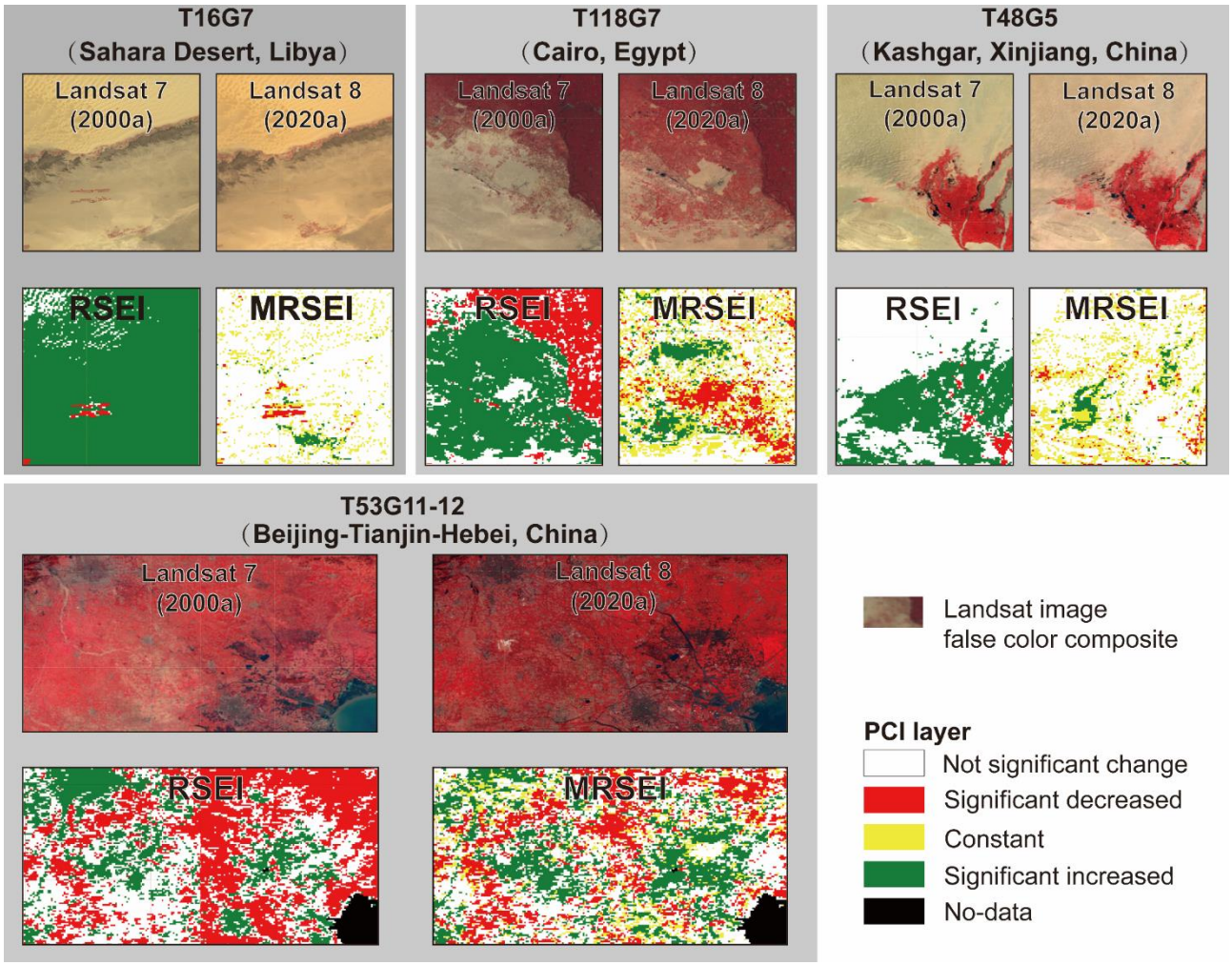

Figure 9.10. RSEI and MRSEI of special grids for different environmental conditions, including Sahara Desert, Cairo, Kashgar and Beijing-Tianjin-Hebei Region.

9.5.2 Spatial heterogeneity of human activities on the environment

With the increasing climate change and human activities, ecological and environmental problems seriously threaten regional ecological security and sustainable economic and social development. Accurate evaluation of the history and current situation of regional ecological environment is helpful for decision makers to understand the regional ecological environment and then take positive measures to achieve sustainable and coordinated development of human and nature. According to a panel of data from the World Bank, global human activities and ecology have been changing rapidly over the past 20 years, and environmental pressures are becoming more severe. As shown in Figure 9.11 (a), the global population has increased by 1.5 billion and the built-up area has expanded by 53,776 km² while the forest area has decreased by about 600,000 km² over the last 20 years. The continuous high-intensity urbanization and economic and social development have led to an unprecedented increase in the ability and intensity of human activities to modify the natural environment. It should be noted that the effects (patterns) of the impact of human activities on the ecological environment are unbalanced on a global scale due to historical reasons and inconsistencies in development patterns and stages. As shown in Figure 9.11(b), it can be clearly found that the transition from and to natural and semi-

natural vegetation cover ground surface over the past 20 years is diverse across different countries or groups. Although the area transferred to natural or semi-natural vegetated land is more than the area transferred from natural land globally, however, the reverse situation can be found in countries (groups) such as the US, China, Australia, G7, G20, BRIICS, etc.

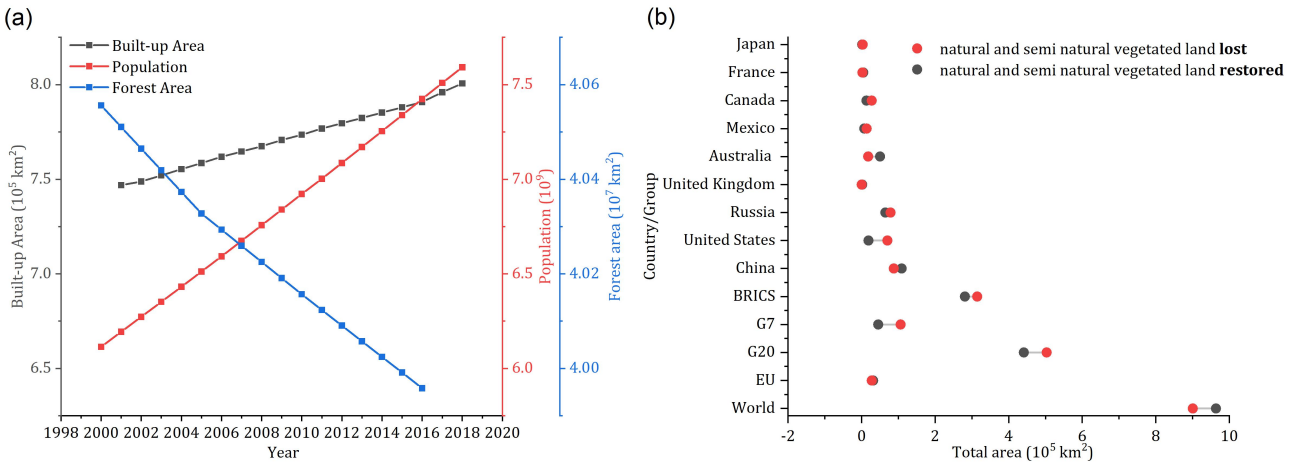

Figure 9.11. Global population, forests, built-up area change and area of natural land conversion over the last 20 years. (Note: the data used can be found via https://databank.worldbank.org/home.aspx)

In fact, before the mature application of remote sensing technology, the monitoring of ecological environment and human activities at large scale is a great challenge due to the complex geography and dynamic changes. With the development of remote sensing technology, including daytime optical remote sensing and nighttime light remote sensing, it has become possible to continuously observe the surface environment and human activity dynamics from the space. The continuous accumulation of images acquired by the satellite project provides a favorable data foundation for global-scale anthropogenic and environmental monitoring, but available long time series RSEI and NTL dynamic studies were mostly limited to local scales, as it was a heavy computational power-demanding study. Recently, the rapid development of the GEE cloud platform, which integrates massive image data and distributed computing power, provides solutions for performing planetary-scale analysis of surface human activities and ecological environment dynamics.

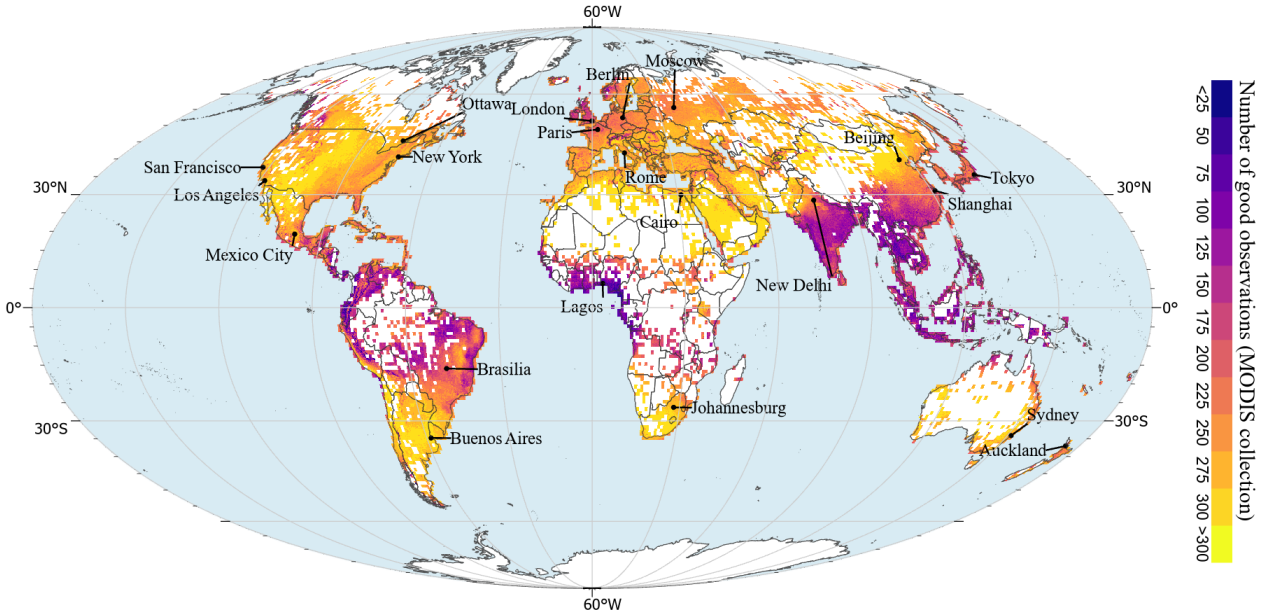

Figure 9.12. Volume of MODIS collections used within the global grids.

With the GEE platform, we used an average of over 200 MODIS images (Figure 9.12) in each grid cell and to calculate MRSEI dynamics, and iterated through all DMSP/OLS and NPP/VIIRS nighttime light images after 2000 to generate the dynamics of light radiation. Our computations produced a dynamic analysis of human activity intensity and environmental conditions in the global anthropogenic zone over the past 20 years.

The results of the inversion revealed that there was a spatial heterogeneity in the human activities and ecological conditions. Here, we counted the mean significantly increased pixel percentage of light radiation, MRSEI and the CCD between them for regions and organizations at different levels of development (Figure 9.13). The results show that 1) the non-G7 developed regions and the emerging regions represented by BRICS possessed a higher growth rate of light radiation, while the least developed regions showed the lowest growth rate of light radiation, less than 2%. 2) BRICS, G7 and least developed regions had higher growth rates of MRSEI than 13%, while emerging regions MIKT showed the lowest MRSEI. 3) The CCD between the increase of light radiation and MRSEI in non-G7 developed regions and BRICS countries were obviously higher than those in G7 developed regions and least developed regions. The G7 was established in 1976, and its members were the countries with the highest GDP, occupying the majority of the total global GDP. With the explosive development of emerging markets and the weak economic development of G7 countries, it has led to the growth rate of light radiation in emerging regions represented by BRICS and non-G7 developed countries to significantly exceed that of G7 countries in the last 20 years. Different economic bases and development patterns are one of the reasons for the differences in the growth rates of human activities and ecological environment. For the ecological environment, developed and BRICS countries, with their good economic foundation and constant emphasis on green development and sustainable development, have been able to maintain a high rate of ecological recovery in the last 20 years. Different from developed countries, for the least developed countries, limited or even almost stagnant human activities and climate warming have contributed to maintain a high rate of increase in MRSEI production in the region. However, for most

developing countries, although they have achieved positive economic growth in recent years, they are unable to maintain the same balance between economic development and environmental protection as large economies due to their limited economic volume, which makes sustainable development a challenge.

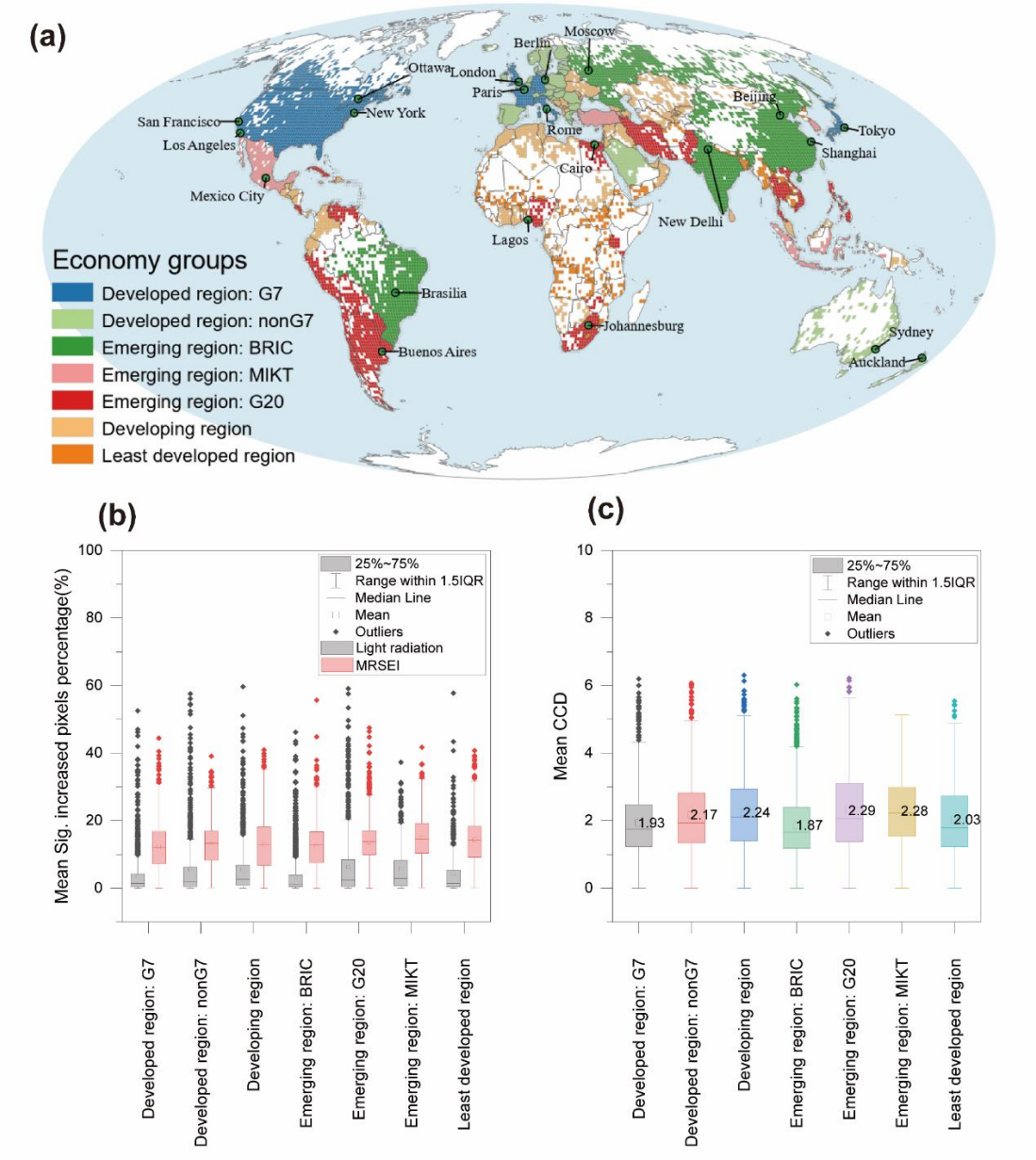

Figure 9.13. Average percentage of significantly increased pixels of light radiation and MRSEI for different regions and organizational groups and the CCD between them. Among them, (a) is the distribution of the grid in different economic groups, (b) is the mean light and MRSEI significant increased percentage of the grid in different economic groups, and (c) is the mean CCD (human activity intensity and ecological condition) of the grid in different economic groups.

Moreover, as pointed out in **Chapter 7**, the coastal zone is both the zone of strongest land-sea interactions and the spatial unit under the dual influence of high intensity human activities and global climate change. On the land side of nearly 50 x 10^5 km of coastline worldwide, more than half of the world's population lives

within about 60 km of the coast, and two-thirds of cities with a population of 2.5 million or more are located near tidal estuaries (Luo, 2016). Therefore, we used the global coastlines to extract a grid within 1° of the coastlines as the coastal zone area, and the rest as the inland area. The results of the zonal statistics (Figure 9.14) confirm that the growth rate of light radiation in the coastal area grid was 4.99%, which was higher than that of the inland area by 2.24%. Meanwhile, the growth rate of MRSEI in the coastal area was only 9.57%, while inland area increased by 14.76%. The above statistics further support the fact that the coastal region has experienced increasing human activity over the past 20 years while still facing ecological pressures that cannot be underestimated. With the advancement and implementation of the United Nations' Sustainable Development Goals, the coastal region is recommended to promote environmental protection more actively under high intensity human activities by virtue of good economic and technological accumulation.

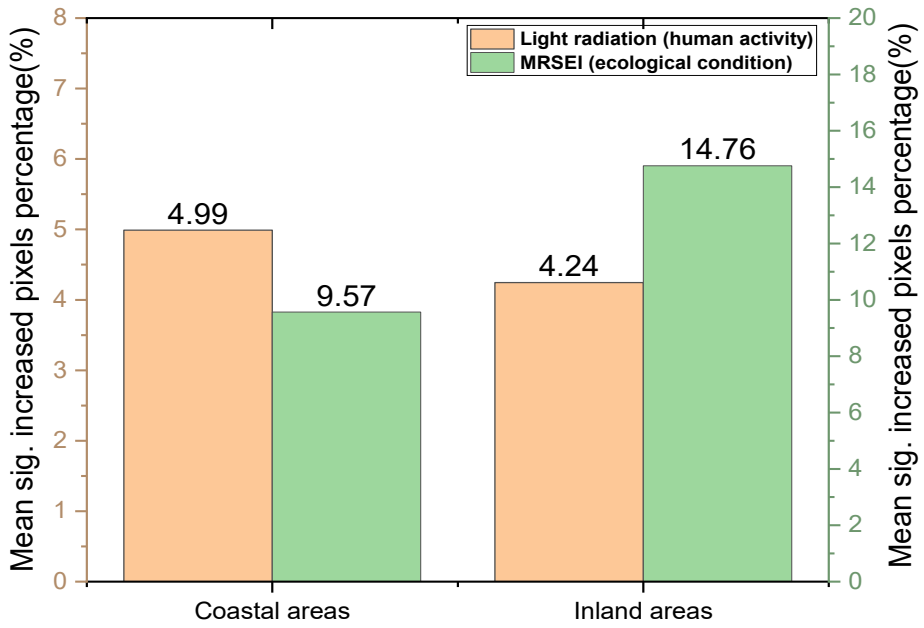

Figure 9.14. Average percentage of light radiation and MRSEI significantly increased pixels in coastal zone areas and inland areas.

9.6 Conclusions

This study refined a monitoring scheme for long-term human activities and regional ecological environment dynamics based on daytime optical remote sensing and nighttime light remote sensing products. The scheme was deployed to the GEE cloud platform, and we integrated the massive MODIS, Landsat and NTL satellite images stored on the server side and perform parallel analysis in the global anthropogenic zone by the tile grid approach. Compared with previous studies, our proposed scheme provides higher stability and robustness, and it overcomes **1)** the deficiency that RSEI was not suitable for conducting long-term and high frequency dynamic analysis, and **2)** the overestimation and pseudo-descent pixels of ENTL in urban areas. In addition, our dynamic monitoring results of the global 7894 grids showed that there was significant spatial heterogeneity between global human activity intensity and ecological environment status over the past two decades, with non-G7 developed countries and BRICS countries performing significantly better coupling

degrees between human activity intensity and ecological environment than G7 countries and least developed countries. Moreover, compared to inland areas, coastal areas have faced greater ecological challenges and sustainable development pressures while experiencing higher increases in human activity.

We will open source the dataset and code for this study to better serve the SDGs research. The dataset includes 1) dynamic identification raster layers of MRSEI and light radiation of the global grid, and 2) statistical tables of the variation area of grid cells. These data sets were compressed into a single 7-zip file archive, where “dataset 1” is in GEOTIFF format and “dataset 2” is in csv format, and the amount of change in MRSEI and light radiation for each cell can be queried in the tables. The JavaScript code handled by the GEE platform can be accessed via links (note that visitors need to register and log in to their earth engine account to view all code).

Author Contributions: Conceptualization, Z.Z and F.M.; Funding acquisition, Z.W. and F.M.; Methodology, Z.Z.; Project administration, Z.W.; Software, Z.Z. and Z.Y.; Supervision, Z.W. and F.M.; Validation, Z.Z. and Z.Y.; Writing-original draft, Z.Z.; Writing-review & editing, F.M..

Acknowledgments: We acknowledge the Google GEE platform for providing the computing power and cloud-based data.

Conflicts of Interest: The authors declare no conflict of interest.

References

Chen, Z., Yu, B., Yang, C., Zhou, Y., Yao, S., Qian, X., . . . Wu, J. (2021) An extended time series (2000–2018) of global NPP-VIIRS-like nighttime light data from a cross-sensor calibration. Earth System Science Data 13, 889-906.

Crutzen, P.J., (2006) The “anthropocene”, Earth System Science in the Anthropocene. Springer, 13-18.

Deng, C. & Wu, C. (2012) BCI: A biophysical composition index for remote sensing of urban environments. Remote Sensing of Environment 127, 247-259.

Du, M., Kawashima, S., Yonemura, S., Zhang, X. & Chen, S. (2004) Mutual influence between human activities and climate change in the Tibetan Plateau during recent years. Global and Planetary Change 41, 241-249.

Firozjaei, M.K., Fathololoumi, S., Kiavarz, M., Biswas, A., Homaee, M. & Alavipanah, S.K. (2021) Land Surface Ecological Status Composition Index (LSESCI): A novel remote sensing-based technique for modeling land surface ecological status. Ecological Indicators 123, 107375.

Hu, X. & Xu, H. (2018) A new remote sensing index for assessing the spatial heterogeneity in urban ecological quality: A case from Fuzhou City, China. Ecological Indicators 89, 11-21.

Katsanevakis, S., Coll, M., Piroddi, C., Steenbeek, J., Ben Rais Lasram, F., Zenetos, A. & Cardoso, A.C. (2014) Invading the Mediterranean Sea: biodiversity patterns shaped by human activities. Frontiers in Marine Science 1, 32.

Li, B., Wang, H., Qin, M. & Zhang, P. (2017) Comparative study on the correlations between NDVI, NDMI and LST. Progress in Geography 36, 585-596.

Li, C., Li, G., Tao, G., Zhu, Y., Wu, Y., Li, X. & Liu, J. (2019) DMSP/OLS night-time light intensity as an innovative indicator of regional sustainable development. International journal of remote sensing 40, 1594-1613.

Li, L., Li, Q., Huang, L., Wang, Q., Zhu, A., Xu, J., . . . Li, R. (2020a) Air quality changes during the COVID-19 lockdown over the Yangtze River Delta Region: An insight into the impact of human activity pattern changes on air pollution variation. Science of the Total Environment 732, 139282.

Li, X., Yang, Y., Xu, X., Xu, C. & Hong, J. (2016) Air pollution from polycyclic aromatic hydrocarbons generated by human activities and their health effects in China. Journal of Cleaner Production 112, 1360-1367.

Li, X., Zhou, Y., Zhao, M. & Zhao, X. (2020b) A harmonized global nighttime light dataset 1992–2018. Scientific data 7, 1-9.

Luo, Y. (2016) Sustainability associated coastal eco-environmental problems and coastal science development in China. Bull. Chin. Acad. Sci 31, 1133-1142.

Mammides, C. (2020) A global assessment of the human pressure on the world's lakes. Global Environmental Change 63, 102084.

Menton, M., Larrea, C., Latorre, S., Martinez-Alier, J., Peck, M., Temper, L. & Walter, M. (2020) Environmental justice and the SDGs: from synergies to gaps and contradictions. Sustainability Science 15, 1621-1636.

Ning, L., Jiayao, W. & Fen, Q. (2020) The improvement of ecological environment index model RSEI. Arabian Journal of Geosciences 13, 1-14.

Phillips, J.D. (1991) The human role in earth surface systems: some theoretical considerations. Geographical analysis 23, 316-331.

Tarolli, P. & Sofia, G. (2016) Human topographic signatures and derived geomorphic processes across landscapes. Geomorphology 255, 140-161.

Trenberth, K.E. (2018) Climate change caused by human activities is happening and it already has major consequences. Journal of Energy & Natural Resources Law 36, 463-481.

Tucker, C., Newcomb, W., Los, S. & Prince, S. (1991) Mean and inter-year variation of growing-season normalized difference vegetation index for the Sahel 1981-1989. International journal of remote sensing 12, 1133-1135.

Venter, O., Sanderson, E.W., Magrach, A., Allan, J.R., Beher, J., Jones, K.R., . . . Fekete, B.M. (2016) Sixteen years of

change in the global terrestrial human footprint and implications for biodiversity conservation. Nature communications 7, 1-11.

Xu, H. (2013) A remote sensing urban ecological index and its application. Acta Ecologica Sinica 33, 7853-7862.

Xu, H., Wang, Y., Guan, H., Shi, T. & Hu, X. (2019) Detecting ecological changes with a remote sensing based ecological index (RSEI) produced time series and change vector analysis. Remote Sensing 11, 2345.

Young, J., Watt, A., Nowicki, P., Alard, D., Clitherow, J., Henle, K., . . . Matouch, S. (2005) Towards sustainable land use: identifying and managing the conflicts between human activities and biodiversity conservation in Europe. Biodiversity & Conservation 14, 1641-1661.

Yu, B., Deng, S., Liu, G., Yang, C., Chen, Z., Hill, C.J. & Wu, J. (2018) Nighttime light images reveal spatial-temporal dynamics of global anthropogenic resources accumulation above ground. Environmental Science & Technology 52, 11520-11527.

Yue, H., Liu, Y., Li, Y. & Lu, Y. (2019) Eco-environmental quality assessment in China's 35 major cities based on remote sensing ecological index. Ieee Access 7, 51295-51311.

10. Discussion

This thesis aims to explore the feasibility of multi-perspective and multi-scale human footprint tracking and dynamic analysis of environmental conditions based on integrated daytime optical remote sensing and nighttime light remote sensing, which can help us understand the Earth in the context of climate change more comprehensively and respond to the UN Sustainable Development Goals in a more positive manner. We identified six specific goals in order to get closer to this goal. Based on these goals, we advanced our work at the data and application layers (the organization between these efforts is shown in Figure 1.4).

For the **first** objective, we want to develop the data calibration models for NTL and fix the deficiencies that current NTL data faced in the application. This goal is the foundation and prerequisite to achieve subsequent applications. **Chapters 2**, **3**, and **4** were efforts that respond to this objective. In **Chapter 2**, we highlighted the significant saturation of the current DMSP/OLS NTL in characterizing the intensity of urban light radiation, which seriously affects the accuracy of NTL data in quantitative analysis at small scales (Zhang et al., 2013). The reason for the saturation phenomenon was that due to rapid urban development, the actual nighttime light intensity in urban centers had far exceeded the upper limit of what can be recorded by the DMSP/OLS sensors, and the radiation intensity in the NTL images was locked at a specific value. Although several correction models had been proposed, most of them were desaturated with natural element layer. However, nighttime lighting data were directly determined by the density of artificial lighting devices in the area, which was more closely linked to the socio-economic elements. Therefore, the desaturation results based on the reference of natural indicators will inevitably be biased. To this end, a desaturation model based on vector and social data was proposed in **Chapter 2**. Given the lossless scaling and high social relevance of vector data, the results of the study yielded NTL index layers with higher spatial and radiometric resolution. The results were valuable for conducting local urban structure analysis and quantitative assessment. In addition to the saturation phenomenon of DMSP/OLS NTL data, the discontinuity of annual light radiation was another challenge that cannot be ignored, especially in time-series analysis (Pandey et al., 2017). The discontinuity of DMSP/OLS was mainly manifested in two aspects, 1) disorder of interannual continuity of the same sensor and 2) bias between different sensors in the same year. Therefore, in **Chapter 3**, a cross-sensor calibration scheme based on automatic PIF identification was developed, validated and applied globally. The proposed calibration model was not only efficient in improving the continuity of the time series NTL and reducing the inter-sensor variation, but also its derived pixel-level fluctuation coefficients could reveal more robustly the spatial heterogeneity in the intensity of human activities.

While the two efforts described above were for DMSP/OLS data products, **Chapter 4** developed a method for acquiring near real-time monthly low-interference light images based on NPP/VIIRS products. Although the VIIRS NTL product as we knew it was released on a monthly schedule, the imaging interval was actually up to daily. Due to complex algorithms and processing streams, even monthly synthetic products were not released in near real-time, which made it difficult to track special surface events and human activities. To fully

utilize the value of the VIIRS DNB products, NASA has developed a new standard product suite, the Black Marble product suit, which represented the latest technology available in NTL applications (Román et al., 2018). The near real-time release of the VNP46A1 product in this suite was subject to interference from factors such as cloud cover and moonlight, which limited its ability to track light emissions in short periods. The processing chain proposed in **Chapter 4** was able to synthesize cloud-free, low-moonlight-interference monthly images based on the near-real-time daily VNP46A1 product, which was essential for conducting short-period monitoring applications. Until now, this scheme has been referenced to produce near real-time NTL images for COVID-19 human activity change monitoring by scholars (Xu et al., 2021a; Yin et al., 2021).

The **second** specific objective was to develop NTL data quality monitoring tools to improve our understanding of time-series NTL. As light-based data applications continue to be expanded, the combination of DMSP/OLS and VIIRS NTL products to achieve long time series of human footprint tracking becomes a solution full of potential. Given that the two light capture sensors had completely different performance parameters, a series of cross-sensor calibration models were proposed, and the produced ENTL was applied to the inversion of light radiation trajectories in different regions and scales. Of concern is that, despite the widespread use of these ENTLs, quality reports for these data products were rarely heard. As ENTL was more unscrupulously and directly introduced into a wide variety of applications, it was urgent to provide fine-grained data quality monitoring flags for these products. **Chapter 5** was to propose an efficient and robust quality assessment methodology for this requirement, and the global quality identification layers for the two most widely used ENTL products today were provided. These layers were able to label continuity errors in ENTL products at the pixel scale. In addition, the identification layers were released open source to facilitate reference by other study.

The **third** objective was to evaluate the applicability of NTL data in the measurement of light pollution. While improving the quality of life of human beings, the extensive use of artificial illumination devices at night has also disturbed the natural light and dark cycle, putting additional light pressure on nature and biology, which was called light pollution. On the one hand, nighttime lights alter the abundance, distribution and ecosystem function of photosensitive species, threatening biodiversity and accelerating species extinction, and on the other hand, the presence of nighttime lights was frequently accompanied by strong human activities, which will directly compress the living space of organisms. As a special geospatial unit, the protected area protects representative natural ecosystems, rare and endangered wildlife species by setting aside a certain area in accordance with the law. Thus, exploring the light pollution dynamics in protected areas is typical and urgent for maintaining biodiversity and ecological balance. **Chapter 6** demonstrated the tracking and quantification of light pollution based on multi-source NTL data for various types and control levels of protected areas in Africa. This work fully explored the high potential of NTL in light pollution monitoring, which was a valuable reference for maintaining biodiversity and setting the boundaries of protected areas more strategically.

The **fourth** objective was to validate the performance of the new satellite data in tracking the human footprint. Recently, with the rapid development of sensor technology and satellite technology, a series of Earth

observation programs have been proposed and the development of thematic satellites has ushered in new opportunities. Among them, the satellite-based atmospheric pollutant observation program has also been pushing forward, with sensors such as TOMS, GOME, SCIAMACHY and OMI successively launched and supplied massive atmospheric pollution images. To bridge the data gap between SCIAMACHY and Sentinel-5, Sentinel-5P with the latest trace gas monitor TROPOMI was successfully launched in 2017 (Berger et al., 2012). Considering that the application and analysis of data products for Sentinel-5P are still lacking, **Chapter 8** has analyzed and modeled the distribution characteristics of NO_2 in the troposphere of China based on TROPOMI data, showing the great application value of Sentinel-5P atmospheric pollutant concentration data. Moreover, the near-real-time data delivery capability has made it and the near-real-time NTL data in **Chapter 4** become the "highly-accessed" data during COVID-19, which has been widely used in the assessment of epidemic effects (Ali et al., 2021; El Kenawy et al., 2021; Parida et al., 2021). In addition, another application experiment was reported in **Annex 1**. In that case, the satellite observations were used to track the development characteristics of integrated cities in the urbanization process and to reveal the differences of integrated cities at different levels of development.

The **fifth** objective was to assess the feasibility of RSEI in medium- and large-scale applications. Here, **Chapters 7** and **9** showed the application potential and challenges of RSEI at regional and global scales, respectively. As an integrated eco-environmental indicator, RSEI has been widely applied to assess and track environmental conditions at local scales in different geographical contexts. It should be acknowledged that the proposal of RSEI is of great value because it characterizes multiple ecological elements, low subjective involvement of the inversion process and good spatial visualization of the results. Previous RSEI-based studies have fully validated the applicability of Landsat satellite imagery, but it is still worthwhile to confirm the applicability of MODIS satellite data at medium resolution. The Chinese coastal zone with the strongest population concentration and human activities was selected as the area of interest in **Chapter 7**, and its eco-environmental status in the last 20 years was analyzed based on MODIS images. The results of the study show that RSEI exhibits encouraging results in medium-scale applications. In addition, the stability and performance of the RSEI in global scale scenarios were explored in **Chapter 9.** The cases in **Chapter 9** revealed some new findings that RSEI would produce overestimation in extreme environments and was unstable in the time series analysis. These new insights were critical to improving our understanding of RSEI and even improving it. Besides, a two-dimensional planarized model for coordination assessment in urban agglomeration development was also reported in **Annex 2**.

The **sixth** objective was to state a few preliminary recommendations to promote the harmonization of human activities with the environment. The previous research cases, especially the examples at the application level, measure the ecological impacts of human activities at local, regional and global scales. In these works, we purposefully gave preliminary suggestions and discussions according to different themes, which we expected to alleviate the conflict between human activities and eco-environment. For example, the impact threshold of human activities on light pollution within protected areas was identified in **Chapter 6** based on

multiple buffer analysis. The detection of thresholds could be used to guide protected area planning, as well as to eliminate light pollution from protected areas more precisely. In **Chapter 8**, it was stated that the topography, population density and industrial concentration in North and East China have formed the "North China-East China NO_2 pollution system". For the region, the thesis suggested that the industrial structure should be optimized and the investment in R&D of exhaust gas treatment technology should be increased to reduce the direct NO_2 emissions. In addition, considering that NO_2 pollution follows the seasonal pattern, it was necessary and effective to adjusted NO_2 emission strategy seasonally. In **Chapter 7**, the variation inequality of RSEI with human activity intensity gradient in China's coastal zone was reported, that is, the main contribution of the increased RSEI originated from the low human activity intensity areas, while the urban areas with higher human activity intensity contributed less. This is a new finding since traditional panel data cannot be spatially detected, which conceals the variability behind environmental changes. The study emphasized that while restoring forest and vegetation cover in peri-urban areas, more efforts should be made to restore the eco-environment within the urban areas. Rational allocation and optimization of green spaces (parks, water bodies, greenways, etc.) within the city were recommended strategies to achieve the harmonious development of eco-environment and human activities.

This thesis has achieved some encouraging results in terms of both data and applications, but there is also some work that deserves to be further refined and expanded. For the data, cross-sensor calibration is still a task that needs to be advanced. As reported in **Chapter 5**, the most widely used ENTL today still has some shortcomings, such as about 10% of the error pixels detected in LiNTL and ChenNTL, which is not a negligible noise for quantitative tracking of human footprints. Given that the identification of global ENTL error pixels has been done in **Chapter 5**, it can provide guidance for carrying out the repair of error pixels. In addition, to realize the long-term tracking of RSEI, a quantile grading scheme was proposed in **Chapter 9**. Despite the improved stability of the graded RSEI, it still faces some uncertainties that need to be fully evaluated in the next work. For applications, the NTL and RSEI were applied in **Chapters 7** and **9** to invert the human activity intensity and environmental conditions, respectively, and the coupling coordination between them was assessed based on the CCD model. The results of the assessment provide an evaluation indicator for the sustainable development of the region, which is worth being recognized. However, the knowledge of the rationale and mechanism behind it is still insufficient. With the development and availability of UAV-based platforms, we will expand the environmental factors and perspectives being monitored in the upcoming work. The data acquired will contribute to our comprehensive understanding of environmental change and the role humans play in it.

11. Conclusions

Accelerated human activity and the climate change it drives are profoundly affecting local, regional and global processes on Earth and presenting challenges to scientists and policy makers in understanding and responding to sustainable development under global change. Meanwhile, new geographic concepts, datasets, and technologies are emerging that provide a new approach to advancing our understanding of concepts related to urbanization, environmental change, sustainability, and global change. Among the various opportunities, images of the Earth's surface observed from space show great potential for monitoring, analyzing, assessing, and predicting the Earth's surface dynamics, making it possible to quantify and track the dynamics of human activities and their environmental impacts. Although satellite remote sensing-based surface process monitoring programs continue to be proposed, this work still deserves to be refined and advanced, due to the increasing urgency for SGDs advancement. Therefore, the integration of day-night remote sensing models for human footprint tracking and dynamic assessment of environmental conditions may be a fundamental study to support the implementation of SGDs.

To implement the potential exploration, this thesis makes a series of efforts at the data and application levels in an attempt to 1) address the gaps in existing NTL data and models for tracking human footprints, and 2) assess the feasibility of NTL and RSEI at different scales and give preliminary suggestions on the corresponding topics. Although these efforts deserve to be advanced and refined, the work of the current thesis has led to some new knowledge findings. The models and data products developed in the work have been successfully noticed and applied by other scholars to regional studies in different contexts, which is inspiring. In summary, the work of the thesis expands the perspective of Earth observation and contributes positively to help us understand human-environment interactions more deeply. In the future, I hope to further reduce uncertainty at the methodological level based on the above research, while achieving knowledge discovery at a larger scale based on more sources of data and GEE.

References

Abrahams, A., Oram, C. & Lozano-Gracia, N. (2018) Deblurring DMSP nighttime lights: A new method using Gaussian filters and frequencies of illumination. Remote Sensing of Environment 210, 242-258.

Ali, G., Abbas, S., Qamer, F.M., Wong, M.S., Rasul, G., Irteza, S.M. & Shahzad, N. (2021) Environmental impacts of shifts in energy, emissions, and urban heat island during the COVID-19 lockdown across Pakistan. Journal of Cleaner Production 291, 125806.

Allen, R.G., Tasumi, M. & Trezza, R. (2007) Satellite-based energy balance for mapping evapotranspiration with internalized calibration (METRIC)—Model. Journal of irrigation and drainage engineering 133, 380-394.

Bastiaanssen, W.G., Menenti, M., Feddes, R. & Holtslag, A. (1998) A remote sensing surface energy balance algorithm for land (SEBAL). 1. Formulation. Journal of hydrology 212, 198-212.

Basu, T. & Das, A. (2021) Systematic review of how eco-environmental transformation due to urbanization can be investigated in the sustainable development of Indian Cities. Environmental Challenges, 100099.

Berger, M., Moreno, J., Johannessen, J.A., Levelt, P.F. & Hanssen, R.F. (2012) ESA's sentinel missions in support of Earth system science. Remote Sensing of Environment 120, 84-90.

Cao, C., Shao, X. & Uprety, S. (2013) Detecting light outages after severe storms using the S-NPP/VIIRS day/night band radiances. IEEE Geoscience and Remote Sensing Letters 10, 1582-1586.

Ceola, S., Laio, F. & Montanari, A. (2014) Satellite nighttime lights reveal increasing human exposure to floods worldwide. Geophysical Research Letters 41, 7184-7190.

Ceola, S., Laio, F. & Montanari, A. (2019) Global-scale human pressure evolution imprints on sustainability of river systems. Hydrology and Earth System Sciences 23, 3933-3944.

Chen, Z., Elvidge, C.D. & Jansen, W.T., (1993) Description of derivative-based high-spectral-resolution (AVIRIS) green vegetation index, Imaging Spectrometry of the Terrestrial Environment. International Society for Optics and Photonics, pp. 43-54.

Chen, Z., Yu, B., Song, W., Liu, H., Wu, Q., Shi, K. & Wu, J. (2017) A new approach for detecting urban centers and their spatial structure with nighttime light remote sensing. IEEE Transactions on Geoscience and Remote Sensing 55, 6305-6319.

Chen, Z., Yu, B., Yang, C., Zhou, Y., Yao, S., Qian, X., . . . Wu, J. (2021) An extended time series (2000–2018) of global NPP-VIIRS-like nighttime light data from a cross-sensor calibration. Earth System Science Data 13, 889-906.

Chettry, V. & Surawar, M. (2021) Assessment of urban sprawl characteristics in Indian cities using remote sensing: case studies of Patna, Ranchi, and Srinagar. Environment, Development and Sustainability, 1-23.

Chwałczyk, F. (2020) Around the Anthropocene in Eighty Names—Considering the Urbanocene Proposition. Sustainability 12, 4458.

Du, M., Wang, L., Zou, S. & Shi, C. (2018) Modeling the census tract level housing vacancy rate with the Jilin1-03 satellite and other geospatial data. Remote Sensing 10, 1920.

El Kenawy, A.M., Lopez-Moreno, J.I., McCabe, M.F., Domínguez-Castro, F., Peña-Angulo, D., Gaber, I.M., . . . Hereher, M.E. (2021) The impact of COVID-19 lockdowns on surface urban heat island changes and air-quality improvements across 21 major cities in the Middle East. Environmental Pollution 288, 117802.

Elshorbagy, A., Bharath, R., Lakhanpal, A., Ceola, S., Montanari, A. & Lindenschmidt, K.-E. (2017) Topography-and nightlight-based national flood risk assessment in Canada. Hydrology and Earth System Sciences 21, 2219-2232.

Gatti, L.V., Basso, L.S., Miller, J.B., Gloor, M., Gatti Domingues, L., Cassol, H.L., . . . Peters, W. (2021) Amazonia as a carbon source linked to deforestation and climate change. Nature 595, 388-393.

Goward, S.N., Markham, B., Dye, D.G., Dulaney, W. & Yang, J. (1991) Normalized difference vegetation index measurements from the Advanced Very High Resolution Radiometer. Remote Sensing of Environment 35, 257-277.

Guk, E. & Levin, N. (2020) Analyzing spatial variability in night-time lights using a high spatial resolution color Jilin-1

image–Jerusalem as a case study. ISPRS Journal of Photogrammetry and Remote Sensing 163, 121-136.
Hillger, D., Kopp, T., Lee, T., Lindsey, D., Seaman, C., Miller, S., . . . Jasmin, T. (2013) First-light imagery from Suomi NPP VIIRS. Bulletin of the American Meteorological Society 94, 1019-1029.
Huete, A.R. (1988) A soil-adjusted vegetation index (SAVI). Remote Sensing of Environment 25, 295-309.
IPCC, (2021) Climate change widespread, rapid, and intensifying, Sixth Assessment Report.
Jasiński, T. (2019) Modeling electricity consumption using nighttime light images and artificial neural networks. Energy 179, 831-842.
Jiménez-Muñoz, J.C., Cristóbal, J., Sobrino, J.A., Sòria, G., Ninyerola, M. & Pons, X. (2008) Revision of the single-channel algorithm for land surface temperature retrieval from Landsat thermal-infrared data. IEEE Transactions on Geoscience and Remote Sensing 47, 339-349.
Kavvada, A., Metternicht, G., Kerblat, F., Mudau, N., Haldorson, M., Laldaparsad, S., . . . Chuvieco, E., (2020) Towards delivering on the sustainable development goals using earth observations. Elsevier.
Kim, S.W. & Brown, R.D. (2021) Urban heat island (UHI) intensity and magnitude estimations: A systematic literature review. Science of the Total Environment, 146389.
Lan, T., Shao, G., Tang, L., Xu, Z., Zhu, W. & Liu, L. (2021) Quantifying spatiotemporal changes in human activities induced by COVID-19 pandemic using daily nighttime light data. IEEE Journal of Selected Topics in Applied Earth Observations and Remote Sensing 14, 2740-2753.
Levin, N. (2017) The impact of seasonal changes on observed nighttime brightness from 2014 to 2015 monthly VIIRS DNB composites. Remote Sensing of Environment 193, 150-164.
Levin, N., Johansen, K., Hacker, J.M. & Phinn, S. (2014) A new source for high spatial resolution night time images—The EROS-B commercial satellite. Remote Sensing of Environment 149, 1-12.
Li, J., Dong, H., Wang, X. & You, L. (2018) Reconstructing missing data in soil moisture content derived from remote sensing based on optimum interpolation. Remote Sensing for Land & Resources, 45-52.
Li, J., Pei, Y., Zhao, S., Xiao, R., Sang, X. & Zhang, C. (2020) A review of remote sensing for environmental monitoring in China. Remote Sensing 12, 1130.
Li, X., Chen, F. & Chen, X. (2013) Satellite-observed nighttime light variation as evidence for global armed conflicts. IEEE Journal of Selected Topics in Applied Earth Observations and Remote Sensing 6, 2302-2315.
Li, X., Li, D., Xu, H. & Wu, C. (2017) Intercalibration between DMSP/OLS and VIIRS night-time light images to evaluate city light dynamics of Syria's major human settlement during Syrian Civil War. International journal of remote sensing 38, 5934-5951.
Li, Y., Li, Y., Zhou, Y., Shi, Y. & Zhu, X. (2012) Investigation of a coupling model of coordination between urbanization and the environment. Journal of environmental management 98, 127-133.
Ma, J., Guo, J., Ahmad, S., Li, Z. & Hong, J. (2020) Constructing a new inter-calibration method for DMSP-OLS and NPP-VIIRS nighttime light. Remote Sensing 12, 937.
Ma, T., Zhou, C., Pei, T., Haynie, S. & Fan, J. (2012) Quantitative estimation of urbanization dynamics using time series of DMSP/OLS nighttime light data: A comparative case study from China's cities. Remote Sensing of Environment 124, 99-107.
Ma, X. & Peng, S. (2021) Assessing the quantitative relationships between the impervious surface area and surface heat island effect during urban expansion. PeerJ 9, e11854.
Major, D., Baret, F. & Guyot, G. (1990) A ratio vegetation index adjusted for soil brightness. International journal of remote sensing 11, 727-740.
Mao, K., Zuo, Z., Shen, X., Xu, T., Gao, C. & Liu, G. (2018) Retrieval of land-surface temperature from AMSR2 data using a deep dynamic learning neural network. Chinese Geographical Science 28, 1-11.
Nagler, P.L., Scott, R.L., Westenburg, C., Cleverly, J.R., Glenn, E.P. & Huete, A.R. (2005) Evapotranspiration on western US rivers estimated using the Enhanced Vegetation Index from MODIS and data from eddy covariance and Bowen

ratio flux towers. Remote Sensing of Environment 97, 337-351.
Nathaniel, S.P. & Adeleye, N. (2021) Environmental preservation amidst carbon emissions, energy consumption, and urbanization in selected African countries: implication for sustainability. Journal of Cleaner Production 285, 125409.
Nijhuis, S. & Jauslin, D. (2015) Urban landscape infrastructures: Designing operative landscape structures for the built environment. Research in Urbanism Series 3, 13-34.
Ou, J., Liu, X., Liu, P. & Liu, X. (2019) Evaluation of Luojia 1-01 nighttime light imagery for impervious surface detection: A comparison with NPP-VIIRS nighttime light data. International Journal of Applied Earth Observation and Geoinformation 81, 1-12.
Pandey, B., Zhang, Q. & Seto, K.C. (2017) Comparative evaluation of relative calibration methods for DMSP/OLS nighttime lights. Remote Sensing of Environment 195, 67-78.
Paranunzio, R., Ceola, S., Laio, F. & Montanari, A. (2019) Evaluating the effects of urbanization evolution on air temperature trends using nightlight satellite data. Atmosphere 10, 117.
Parida, B.R., Bar, S., Roberts, G., Mandal, S.P., Pandey, A.C., Kumar, M. & Dash, J. (2021) Improvement in air quality and its impact on land surface temperature in major urban areas across India during the first lockdown of the pandemic. Environmental research 199, 111280.
Petrakopoulou, F., Robinson, A. & Olmeda-Delgado, M. (2020) Impact of climate change on fossil fuel power-plant efficiency and water use. Journal of Cleaner Production 273, 122816.
Richardson, A.J. & Wiegand, C. (1977) Distinguishing vegetation from soil background information. Photogrammetric engineering and remote sensing 43, 1541-1552.
Ritchie, H. & Roser, M., (2018) Urbanization, Our world in data.
Román, M.O., Wang, Z., Sun, Q., Kalb, V., Miller, S.D., Molthan, A., . . . Pandey, B. (2018) NASA's Black Marble nighttime lights product suite. Remote Sensing of Environment 210, 113-143.
Sagan, V., Peterson, K.T., Maimaitijiang, M., Sidike, P., Sloan, J., Greeling, B.A., . . . Adams, C. (2020) Monitoring inland water quality using remote sensing: potential and limitations of spectral indices, bio-optical simulations, machine learning, and cloud computing. Earth-Science Reviews 205, 103187.
Shao, Z., Ding, L., Li, D., Altan, O., Huq, M. & Li, C. (2020) Exploring the relationship between urbanization and ecological environment using remote sensing images and statistical data: A case study in the Yangtze River Delta, China. Sustainability 12, 5620.
Shi, K., Yu, B., Hu, Y., Huang, C., Chen, Y., Huang, Y., . . . Wu, J. (2015) Modeling and mapping total freight traffic in China using NPP-VIIRS nighttime light composite data. GIScience & Remote Sensing 52, 274-289.
Shin, J.C., Parab, K.V., An, R. & Grigsby-Toussaint, D.S. (2020) Greenspace exposure and sleep: A systematic review. Environmental research 182, 109081.
Small, C., Pozzi, F. & Elvidge, C.D. (2005) Spatial analysis of global urban extent from DMSP-OLS night lights. Remote Sensing of Environment 96, 277-291.
Srinivasan, V., Seto, K.C., Emerson, R. & Gorelick, S.M. (2013) The impact of urbanization on water vulnerability: A coupled human–environment system approach for Chennai, India. Global Environmental Change 23, 229-239.
Sutton, P.C. (2003) A scale-adjusted measure of “urban sprawl” using nighttime satellite imagery. Remote Sensing of Environment 86, 353-369.
Tan, M., Li, X., Li, S., Xin, L., Wang, X., Li, Q., . . . Xiang, W. (2018) Modeling population density based on nighttime light images and land use data in China. Applied Geography 90, 239-247.
Tselios, V. & Stathakis, D. (2020) Exploring regional and urban clusters and patterns in Europe using satellite observed lighting. Environment and Planning B: Urban Analytics and City Science 47, 553-568.
Uttara, S., Bhuvandas, N. & Aggarwal, V. (2012) Impacts of urbanization on environment. International Journal of Research in Engineering and Applied Sciences 2, 1637-1645.
Wan, Z. & Dozier, J. (1996) A generalized split-window algorithm for retrieving land-surface temperature from space.

IEEE Transactions on Geoscience and Remote Sensing 34, 892-905.
Wang, J., Aegerter, C., Xu, X. & Szykman, J.J. (2016) Potential application of VIIRS Day/Night Band for monitoring nighttime surface PM2. 5 air quality from space. Atmospheric environment 124, 55-63.
Wang, X., Mu, X. & Yan, G. (2020) Quantitative Analysis of Aerosol Influence on Suomi-NPP VIIRS Nighttime Light in China. IEEE Journal of Selected Topics in Applied Earth Observations and Remote Sensing 13, 3557-3568.
Xu, G., Xiu, T., Li, X., Liang, X. & Jiao, L. (2021a) Lockdown induced night-time light dynamics during the COVID-19 epidemic in global megacities. International Journal of Applied Earth Observation and Geoinformation 102, 102421.
Xu, H. (2013) A remote sensing urban ecological index and its application. Acta Ecologica Sinica 33, 7853-7862.
Xu, H., Wang, M., Shi, T., Guan, H., Fang, C. & Lin, Z. (2018) Prediction of ecological effects of potential population and impervious surface increases using a remote sensing based ecological index (RSEI). Ecological Indicators 93, 730-740.
Xu, L., Wang, J., Xiao, F., Sherif, E.-B. & Awed, A. (2021b) Potential strategies to mitigate the heat island impacts of highway pavement on megacities with considerations of energy uses. Applied Energy 281, 116077.
Yang, D., Luan, W., Qiao, L. & Pratama, M. (2020) Modeling and spatio-temporal analysis of city-level carbon emissions based on nighttime light satellite imagery. Applied Energy 268, 114696.
Yao, Y., Qin, Q., Fadhil, A.M., Li, Y., Zhao, S., Liu, S., . . . Dong, H. (2011) Evaluation of EDI derived from the exponential evapotranspiration model for monitoring China’s surface drought. Environmental earth sciences 63, 425-436.
Yin, R., He, G., Jiang, W., Peng, Y., Zhang, Z., Li, M. & Gong, C. (2021) Night-Time Light Imagery Reveals China's City Activity During the COVID-19 Pandemic Period in Early 2020. IEEE Journal of Selected Topics in Applied Earth Observations and Remote Sensing 14, 5111-5122.
Yu, B., Shu, S., Liu, H., Song, W., Wu, J., Wang, L. & Chen, Z. (2014) Object-based spatial cluster analysis of urban landscape pattern using nighttime light satellite images: A case study of China. International Journal of Geographical Information Science 28, 2328-2355.
Zhang, C., Pei, Y., Li, J., Qin, Q. & Yue, J. (2020) Application of luojia 1-01 nighttime images for detecting the light changes for the 2019 spring festival in western cities, China. Remote Sensing 12, 1416.
Zhang, Q., Schaaf, C. & Seto, K.C. (2013) The vegetation adjusted NTL urban index: A new approach to reduce saturation and increase variation in nighttime luminosity. Remote Sensing of Environment 129, 32-41.
Zhao, M., Zhou, Y., Li, X., Zhou, C., Cheng, W., Li, M. & Huang, K. (2019) Building a series of consistent night-time light data (1992–2018) in Southeast Asia by integrating DMSP-OLS and NPP-VIIRS. IEEE Transactions on Geoscience and Remote Sensing 58, 1843-1856.
Zhao, S., Yang, Y., Qiu, G., Qin, Q., Yao, Y., Xiong, Y. & Li, C. (2010) Remote detection of bare soil moisture using a surface-temperature-based soil evaporation transfer coefficient. International Journal of Applied Earth Observation and Geoinformation 12, 351-358.
Zhao, X., Yu, B., Liu, Y., Yao, S., Lian, T., Chen, L., . . . Wu, J. (2018) NPP-VIIRS DNB daily data in natural disaster assessment: Evidence from selected case studies. Remote Sensing 10, 1526.
Zheng, Q., Weng, Q. & Wang, K. (2019) Developing a new cross-sensor calibration model for DMSP-OLS and Suomi-NPP VIIRS night-light imageries. ISPRS Journal of Photogrammetry and Remote Sensing 153, 36-47.
Zheng, X., Sun, Y., Qin, Q., Ren, H., Gao, Z., Wu, L., . . . Wang, J. (2015) Bare soil moisture inversion model based on visible-shortwave infrared reflectance. Spectroscopy and Spectral Analysis 35, 2113-2118.
Zheng, Z., Wu, Z., Chen, Y., Guo, G., Yang, Z. & Marinello, F. (2021) A simple method for near-real-time monthly nighttime light image production. IEEE Geoscience and Remote Sensing Letters.
Zhou, Y., Chen, M., Tang, Z. & Mei, Z. (2021) Urbanization, land use change, and carbon emissions: Quantitative assessments for city-level carbon emissions in Beijing-Tianjin-Hebei region. Sustainable cities and society 66, 102701.

Zhu, C., Zhang, X., Zhou, M., He, S., Gan, M., Yang, L. & Wang, K. (2020) Impacts of urbanization and landscape pattern on habitat quality using OLS and GWR models in Hangzhou, China. Ecological Indicators 117, 106654.

Annexes

Annex 1: Detection of city integration processes in rapidly urbanizing areas based on remote sensing imagery [8]

Background

Since China's reform and opening up policies commenced in 1978, the country has experienced a rapid process of urbanization, with the urbanization rate rising from 17.9% in 1978 to 60.34% in 2020 (Zhu et al., 2011; Gu et al., 2012; Ye and Wu, 2014). On the one hand, continuous and high-intensity urbanization has become the engine that drives China's rapid economic growth, but on the other hand, problems such as over-concentration of population, tight urban land resources, and ecological environmental impacts that appear in the process of urbanization also constantly restrict and affect the sustainable development of cities (Grimmond, 2007; Cui and Shi, 2012; Ariken et al., 2020). The expansion of urban built-up areas makes cities with adjacent geographic locations gradually form a regional synergistic development pattern, which is often referred to as city clusters, sister cities, and integrated cities in the urban structure (Rotmans et al., 2000; De et al., 2009; Shieh, 2011).

Compared with traditional developed countries, China's continuous and rapid urbanization in the last two decades makes it an ideal experimental field for current research on urban integration. Considering the timeliness, periodicity, and efficiency of remote sensing technology, this paper is based on a daytime-nighttime remote sensing data source and uses typical integrated cities in China as an example to carry out land surface change monitoring and vitality assessment in the border areas of cities.

Study areas

This study takes four of the most representative and well-known integrated cities in China as examples, including Guangfo (composed of Guangzhou and Foshan), Guanshen (composed of Dongguan and Shenzhen), Xixian (composed of Xi'an and Xianyang), and Husu (composed of Shanghai and Suzhou). Among them, Guangfo and Guanshen are located in the Pearl River Delta in southern China; Husu is located in the Yangtze River Delta in eastern China; finally, Xixian is located in the Guanzhong Plain, the hinterland of Northwest China (Figure A1.1).

[8] This Chapter relies on the paper "Zheng, Z., Wu, Z., Chen, Y., Yang, Z., & Marinello, F. (2020). Detection of city integration processes in rapidly urbanizing areas based on remote sensing imagery. Land, 9,378.". https://doi.org/10.3390/land9100378".

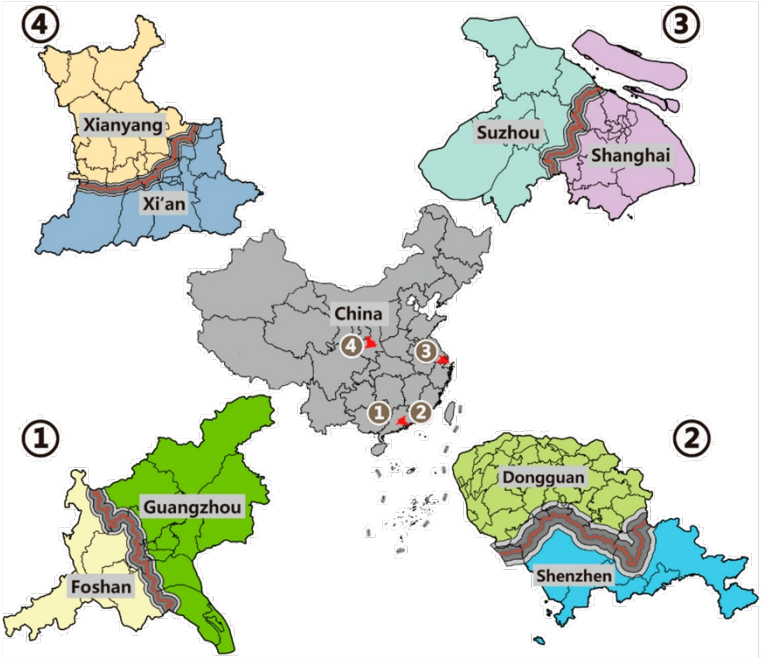

Figure A1.1. Location distribution of four integrated cities in China: Guangfo City (1), Guanshen City (2), Husu City (3), and Xixian City (4).

With China's increasing urbanization, these four groups of cities are experiencing rapid urban expansion (Table A1.1), and the economic, social, natural, and ecological ties between them are becoming close and developing towards city integration. As shown in Figure A1.1, we especially focus on the border area among the integrated cities, and construct 1 km, 3 km, and 5 km buffer zones at the borders of neighboring cities as the target areas for remote sensing monitoring analysis.

Table A1.1. Basic statistic information of sample integrated cities.

Integrated city	City composition	Population/million	Area/km^2	GDP/billion
Guangfo	Guangzhou	15.3	7434.4	2362.9
	Foshan	8.2	3797.7	1075.1
Guanshen	Dongguan	8.4	2460.1	948.3
	Shenzhen	13.4	1997.5	2692.7
Xixian	Xi'an	10.2	10752	932.1
	Xianyang	4.4	9543.6	219.5
Husu	Shanghai	24.3	6340.5	3815.5
	Suzhou	10.75	8657.3	1923.6

Satellite images

In this case, the dataset used in the integrated analysis mainly includes four types: nighttime light data, multi-spectral image data and high-resolution satellite street view data. Specifically, the SNPP/VIIRS nighttime light data used was the monthly VIIRS Cloud Mask product (VCM) from April 2012 to May 2018, with a total of 74 images. In addition, Landsat-8 multi-spectral images in 2013, 2015, and 2017 were used to monitor land cover change in the integrated city boundary zone. Since the spatial resolution of the Landsat-8 multi-spectral band is limited to 30 m, it cannot further support the requirements for the identification of typical features. Therefore, we used time-series high-resolution satellite image on the Google Earth platform

to identify the typical plots within the boundary zone.

Results

A. Land-Use Change

During the integration process, the downtown area of neighboring cities continues to expand and the boundaries of the built-up areas approach the administrative boundaries, leading to significant adjustments in the land-use structure characterizing the urban boundary zones. We extracted the land use within the multi-level buffer zones constructed along the boundary lines of four groups of integrated cities, the results of this extraction are shown in Figure A1.2.

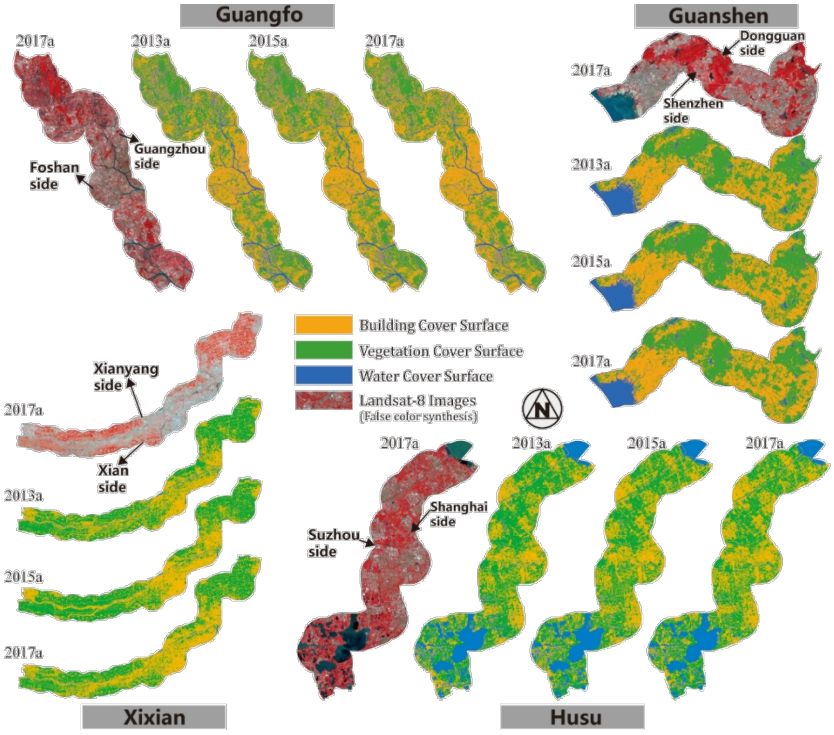

Figure A1.2. The land-use classification results of boundary zones among the integrated cities in 2013, 2015, and 2017.

During 2013-2017, the surface cover of the above boundary zones of four integrated cities changed significantly. Among them, 1) the building area expanded markedly, with Xixian growing the most and Guanshen growing the least; 2) both vegetation cover and water body were occupied, with the average cover decreasing by 49.59% and 10.61%, respectively. In other words, roughly one-sixth of the new construction land was converted from water cover and one-fifth was converted from vegetation cover. Besides, for the expansion rate of the building area within the boundary zone of different widths, the growth rate of Guangfo and Guanshen was more stable, while the growth rate of Husu and Xixian decreased with the buffer distance increases.

B. Nighttime Light Intensity Changes

The results (Table A1.2) show that from 2012 to 2018, the average light intensity within the boundary zone maintained an upward trend, with an increase of 35%, 44%, 36%, and 73% for Guangfo, Guanshen, Husu, and Xixian, respectively. Although Xixian achieved the highest light growth rate (over 70%), the absolute value of light intensity is still apparently lower than that of other integrated cities.

Table A1.2. The light intensity fluctuation and its linear regression of boundary zones.

City	Light intensity (nW/cm^2/sr)							Increase rate (%)	Fitting equation	R^2
	2012	2013	2014	2015	2016	2017	2018			
Guangfo	7.95	9.12	9.52	9.98	9.51	9.88	10.79	35	y = 0.34x + 8.10	0.79
Guanshen	8.75	9.37	10.43	10.3	10.56	11.27	12.62	44	y = 0.55x + 8.25	0.91
Husu	6.34	6.76	7.66	7.64	7.17	8.29	8.53	36	y = 0.33x + 6.17	0.80
Xixian	3.42	3.75	2.72	4.02	3.88	5.74	5.93	73	y = 0.45x + 2.40	0.67

To investigate the triggers of light fluctuations in the boundary area, we selected plots with remarkable changes in light intensity in the study area and combined Google Earth high-resolution satellite images for comparative analysis (Figure A1.3). The comparison shows that the land use types in the light attenuation area are mainly vegetation and water bodies, while the light increase area is mainly industrial land (industrial parks and logistics parks), transportation land, and some commercial land.

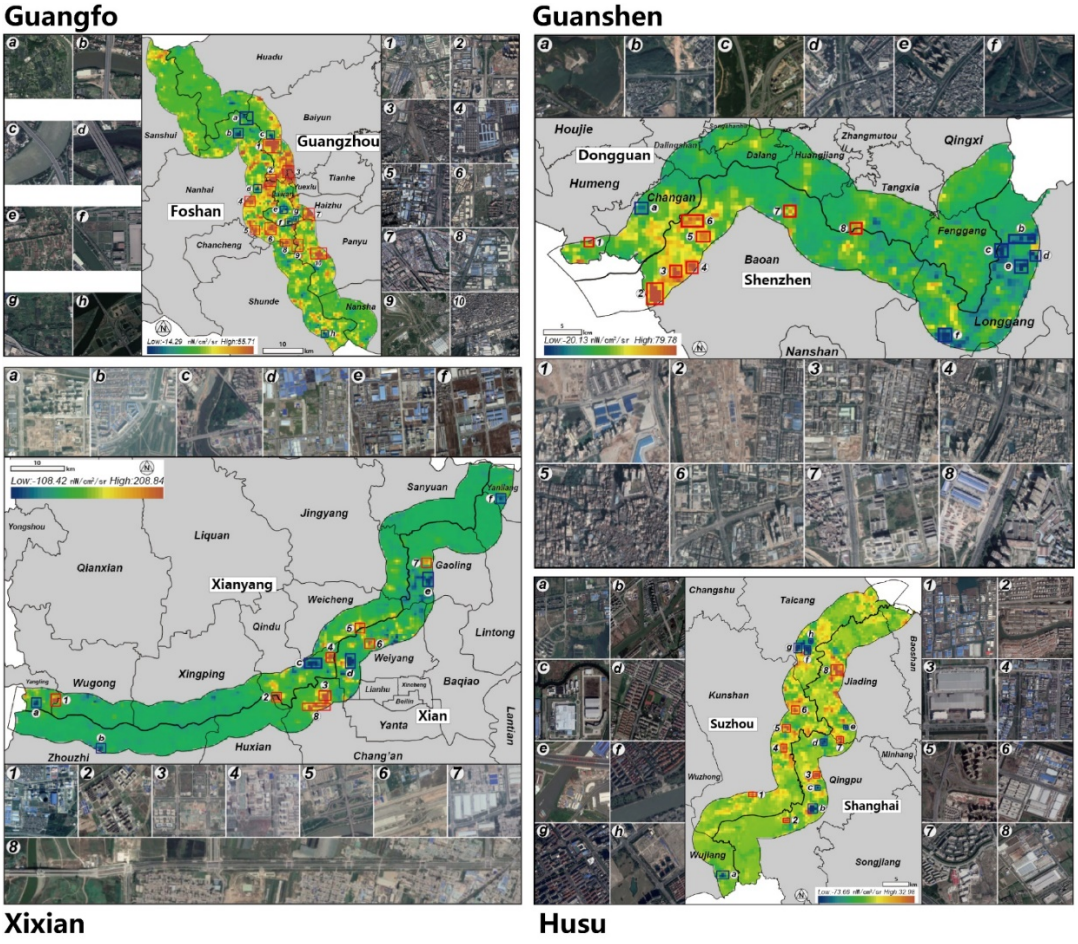

Figure A1.3. Plots with dramatic lighting changes in the boundary zone and their feature structures. Note: light intensity decreases in plots marked by letters and increases in plots marked by numbers.

C. The Shifting of the NTLGC

In this case, the NTLGC model was introduced to reveal the differences in the direction of expansion between cities during the integration process (Figure A1.4).

1) Guangfo: the NTLGC's shift in direction was "southeast–northwest", and the offset distance increased from 545 m (2013a-2015a) to 695 m (2015a-2017a), reflecting the fact that the NTLGC kept moving towards the Foshan side and the integration process advanced gradually.

2) Guanshen: the offset distance of the NTLGC increased from 1699 m (2013a-2015a) to 2086.33 m (2015a-2017a), showing a long-span and incremental characteristic.

3) Husu: the shift trajectory of NTLGC in Husu presented a "V" structure.

4) Xixian: the shift direction was maintained as being "northeast–southwest".

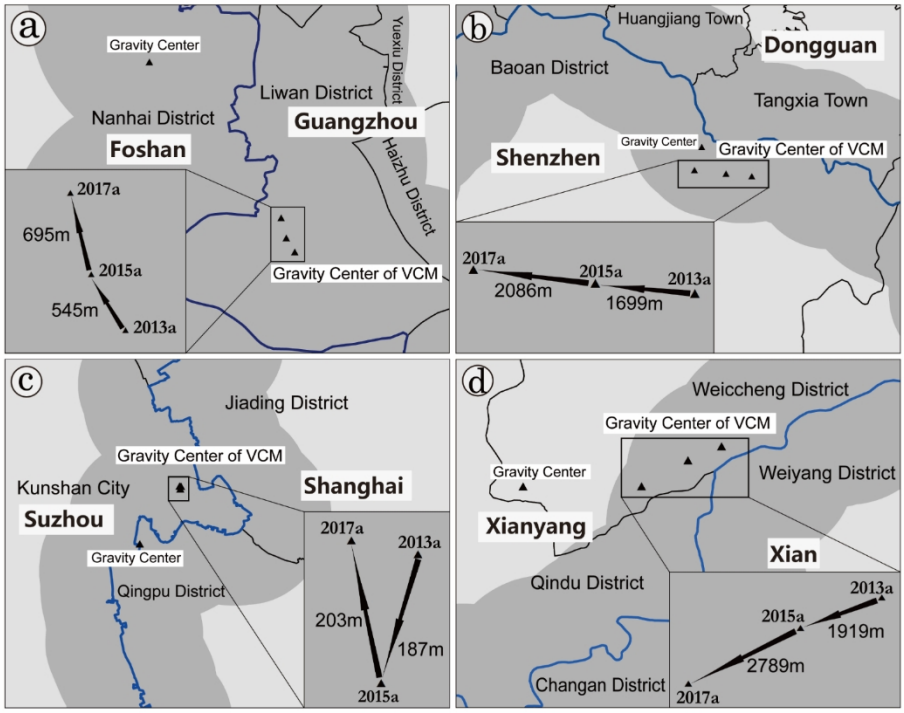

Figure A1.4. The nighttime light gravity center shift trajectories of integrated cities in 2013, 2015, and 2017. Note: the light gravity center shift trajectory is listed as: a) Guangfo; b) Guanshen; c) Husu and d) Xixian.

References

Ariken, M., Zhang, F., Liu, K., Fang, C. & Kung, H.-T. (2020) Coupling coordination analysis of urbanization and eco-environment in Yanqi Basin based on multi-source remote sensing data. Ecological Indicators 114, 106331.

Cui, L. & Shi, J. (2012) Urbanization and its environmental effects in Shanghai, China. Urban Climate 2, 1-15.

De, W., Yu, S., Chi, S. & Chasong, Z., (2009) A review on the implementation of city integration strategy, Urban Planning Forum, pp. 74-78.

Grimmond, S.U. (2007) Urbanization and global environmental change: local effects of urban warming. Geographical Journal 173, 83-88.

Gu, C., Wu, L. & Cook, I. (2012) Progress in research on Chinese urbanization. Frontiers of Architectural Research 1, 101-149.

Rotmans, J., van Asselt, M. & Vellinga, P. (2000) An integrated planning tool for sustainable cities. Environmental impact assessment review 20, 265-276.

Shieh, L. (2011) Becoming urban: rural-urban integration in Nanjing, Jiangsu province. Pacific Affairs 84, 475-494.

Ye, L. & Wu, A.M. (2014) Urbanization, land development, and land financing: Evidence from Chinese cities. Journal of Urban Affairs 36, 354-368.

Zhu, Y., Ioannidis, J.P., Li, H., Jones, K.C. & Martin, F.L. (2011) Understanding and harnessing the health effects of rapid urbanization in China. Environmental Science & Technology.

Annex 2: The balance of eco-environment and urbanization development in the Yangtze River Delta Urban Agglomeration based on GEE [9]

Background

With the continuous promotion of global urbanization, the current development and competition among cities is no longer limited to individual cities, but more and more presents the development mode of city cluster competition. Currently, urban agglomerations have become the core engine of China's rapid economic development, with the three major urban agglomerations consisting of the Yangtze River Delta, the Pearl River Delta, and Beijing-Tianjin-Hebei accounting for more than 40% of GDP (Zhang et al., 2020).

However, with the rapid economic development and continuous urbanization of urban agglomerations, the intensity of human activities in the region is rising (construction land expansion (Liu et al., 2015; Qian et al., 2016; Chen et al., 2018; Guan et al., 2018), heat island effect (Jin et al., 2011; Feng et al., 2014; Li et al., 2018; Zhou and Chen, 2018), atmospheric pollution (Liu et al., 2018; Wang and Zhao, 2018; Wang et al., 2020), which puts the natural and eco-environment under great pressure. In the process of interaction between urbanization and eco-environment, the continuous push of urbanization on the one hand will inevitably disturb or even destroy the regional eco-environment, while the deterioration of eco-environment on the other hand will in turn constrain urbanization and sustainable development. Since the existing analyses of coupled urbanization and ecological coordination are mostly based on panel statistics and lack of detailed spatial information. Therefore, we hope to carry out a case study of urban cluster areas in China with the help of remote sensing solutions.

Study areas

The Yangtze River Delta Urban Agglomeration (YRDUA) is located in the downstream area of the Yangtze River, bordered by the Yellow Sea and the East China Sea, and situated at the confluence of rivers and seas, with numerous coastal ports along the river (Figure A2.1). According to the 2019 YRUDA Integrated Development Plan, YRUDA currently includes Shanghai, 16 prefecture-level cities in Anhui Province, 13 prefecture-level cities in Jiangsu Province and 11 prefecture-level cities in Zhejiang Province, a total of 41 cities with an area of 359,000 km^2 and a resident population of about 230 million people, accounting for 16.22% of the total population of China.

As the most economically active and open region in China, the Yangtze River Delta city cluster occupies a strategic position in the modernization and all-round reform and opening up of the country. Since the 18th Party Congress, the integrated development of the Yangtze River Delta urban agglomeration has been

[9] This Chapter relies on the paper "Zheng, Z., Wu, Z., Chen, Y., Yang, Z., & Marinello, F. (2021). Analyzing the ecological environment and urbanization characteristics of the Yangtze River Delta Urban Agglomeration based on Google Earth Engine. Acta Ecologica Sinica, 41(2),717-729.".

remarkable and has become the most typical region of urbanization in China. Behind the rapid urbanization development, the pressure on the ecological environment of the region is becoming more and more severe.

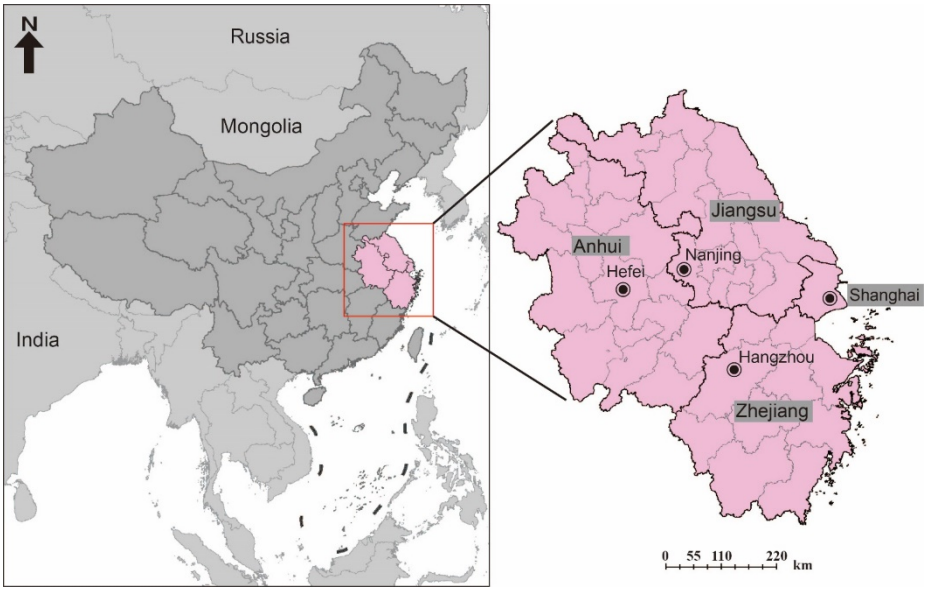

Figure A2.1. Location map of the Yangtze River Delta Urban Agglomeration.

Methods

Coupled coordination distance model

In order to quantitatively assess the coupling coordination between urbanization level and ecological environment within the YRDUA, this case proposes a two-dimensional plane coupling model based on the existing coupling degree models (Liu et al., 2015; Liu et al., 2018). Figure A2.2 depicts an existing two-system coupling model function in which the Z-value is used to quantitatively characterize the coupling degree between variables. In this case, to reduce the dimensionality of the model function, a coupled coordination distance model is constructed by mapping in the "X-Y" plane. The model plots the "urbanization-environment" coordinate points using the CNLI of the city as the horizontal coordinate and the RSEI as the vertical coordinate.

Specifically, the higher the level of urbanization and ecological environment coordination, the closer the "urbanization-environment" coordinate point will be to the "1:1" diagonal. Therefore, the smaller the distance between the "urbanization-environment" coordinate points and the diagonal of the coordinate system, the higher the degree of coupling. In addition, when city A and city B are at the same distance from the diagonal, the distance between the city coordinate point and the limit point (1,1) is introduced to further differentiate them. Therefore, the coupled coordinative distance d is defined as the sum of the distances between the "urbanization-environment" coordinate points and the diagonal and the limit points, as follows:

$$d_i = \frac{|x_i - y_i|}{\sqrt{2}} + \sqrt{(x_i - 1)^2 + (y_i - 1)^2} \quad \text{(A2.1)}$$

where x_i and $y_i$are the horizontal and vertical coordinates of "urbanization-environment" coordinates, i.e.,

the normalized CNLI index and RSEI index, respectively; d_i is the coupling coordination distance of city i. The smaller d_i is, the higher the coupling coordination of city between the urbanization level of and the ecological environment condition.

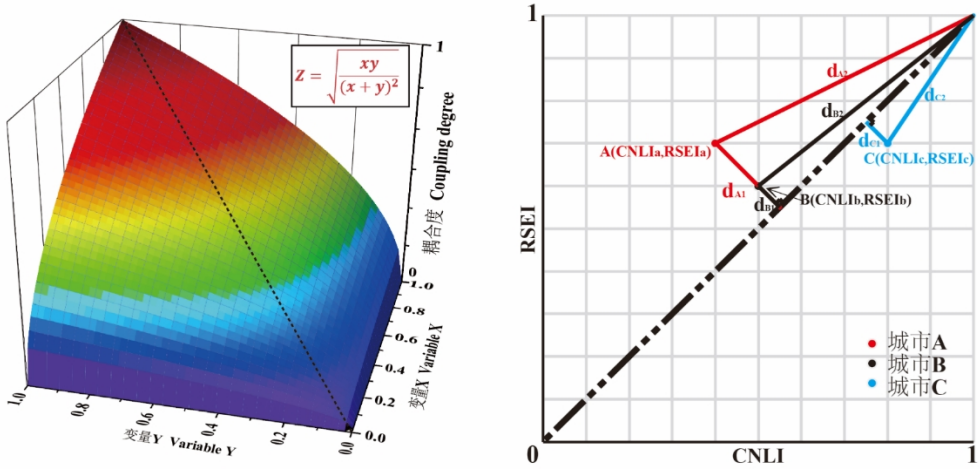

Figure A2.2. Schematic diagram of Coupled Coordination Distance Model. Note: RSEI means Remote Sensing-based ecological index, CNLI means Comprehensive nighttime light index.

Results

Table A2.1 presents the mean values of RSEI for the study area as a whole and by province (municipality directly under the central government). It can be seen that: 1) the RSEI of YRDUA has shown a relatively stable growth trend over the past 20 years, with the RSEI increasing from 0.54 in 2000 to 0.64 in 2019, an increase of about 18.5%; 2) there is a certain variability in the changes of the mean value of RSEI under the provincial unit, with Jiangsu Province showing a relatively stable upward trend in RSEI over the study period (up 23%), Anhui Province showing a more pronounced increase before 2010 and maintaining a relatively stable level after 2010 (20.8%), and Zhejiang Province and Shanghai showing a lower increase in the mean RSEI values than the overall study area average of 12.7% and 5.2%, respectively.

Table A2.1 The RSEI and its changes of urban agglomerations and provincial (municipality) units in the Yangtze River Delta

Year		2000	2005	2010	2015	2019	Trends
RSEI		0.54	0.56	0.59	0.60	0.64	
Provincial unit	Anhui	0.48	0.52	0.59	0.60	0.58	
	Jiangsu	0.52	0.59	0.61	0.62	0.64	
	Zhejiang	0.63	0.57	0.60	0.57	0.71	
	Shanghai	0.58	0.48	0.50	0.51	0.61	

In addition, Figure A2.3 shows the changes of RSEI between 2000 and 2019. It can be seen that most of the declining RSEI stators in the past nearly 20 years were located in the northern Anhui and southern Jiangsu regions, while most of the stators with an RSEI increase of more than 0.2 were concentrated in the central Anhui and northern Jiangsu regions.

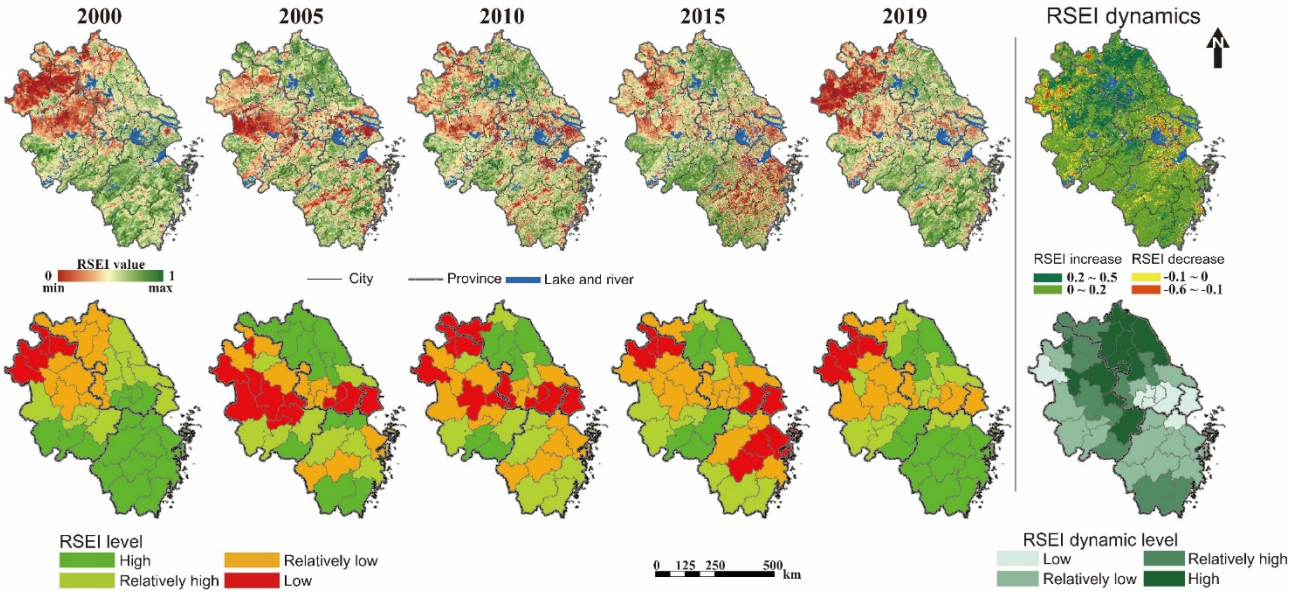

Figure A2.3. The change and distribution of RSEI in the YRDUA from 2000 to 2019.

According to the light index model, the MLI, LAP and CNLI indices of YRDUA and provincial units (municipalities directly under the central government) in the past nearly 20 years were counted in this case, as shown in Figure A2.4. The change of MLI index reflects that 1) the overall light intensity of YRDUA showed a stable upward trend; 2) the average light intensity of Shanghai increased more significantly than the other three provinces, the light intensity and change trend of Zhejiang Province and Jiangsu Province were close, although Anhui Province showed an upward trend, but the increase was lower than the average level of the study area.

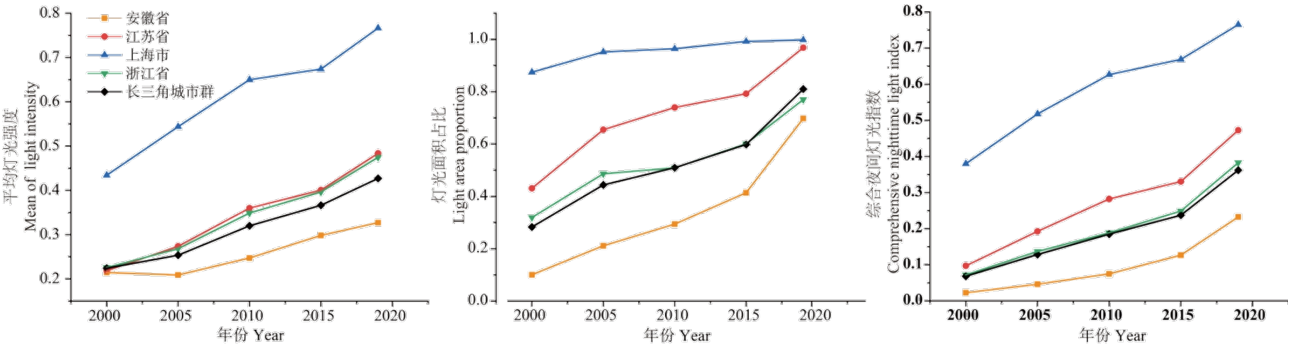

Figure A2.4 Changes of MLI, LAP and CNLI under the urban agglomeration and provincial units (municipalities)

The results based on the constructed coupled coordination distance model for YRDUA during the study period are shown in Figure A2.5. Since the values of RSEI and CNLI of the normalized urban units are in the range of 0-1, this paper uses (0.5,0.5) as the origin to divide the "urbanization-environment" coordinate points into four different quadrants.

Among them:

1) cities in the first quadrant (CNLI>0.5, RSEI>0.5) have a high level of both eco-environment and urbanization and belong to the type of good coupling and coordination.

2) cities in the second quadrant (CNLI<0.5, RSEI>0.5) have a relatively higher level of eco-environment than urbanization and belong to the type of urbanization lagging behind ecological environment.

3) cities in the third quadrant (CNLI <0.5, RSEI<0.5) are close to but low in urbanization and eco-environment and belong to the type of primary coordination.

4) cities in the fourth quadrant (CNLI>0.5, RSEI<0.5) are ahead of ecological environment in urbanization and belong to the type of eco-environment lagging behind urbanization.

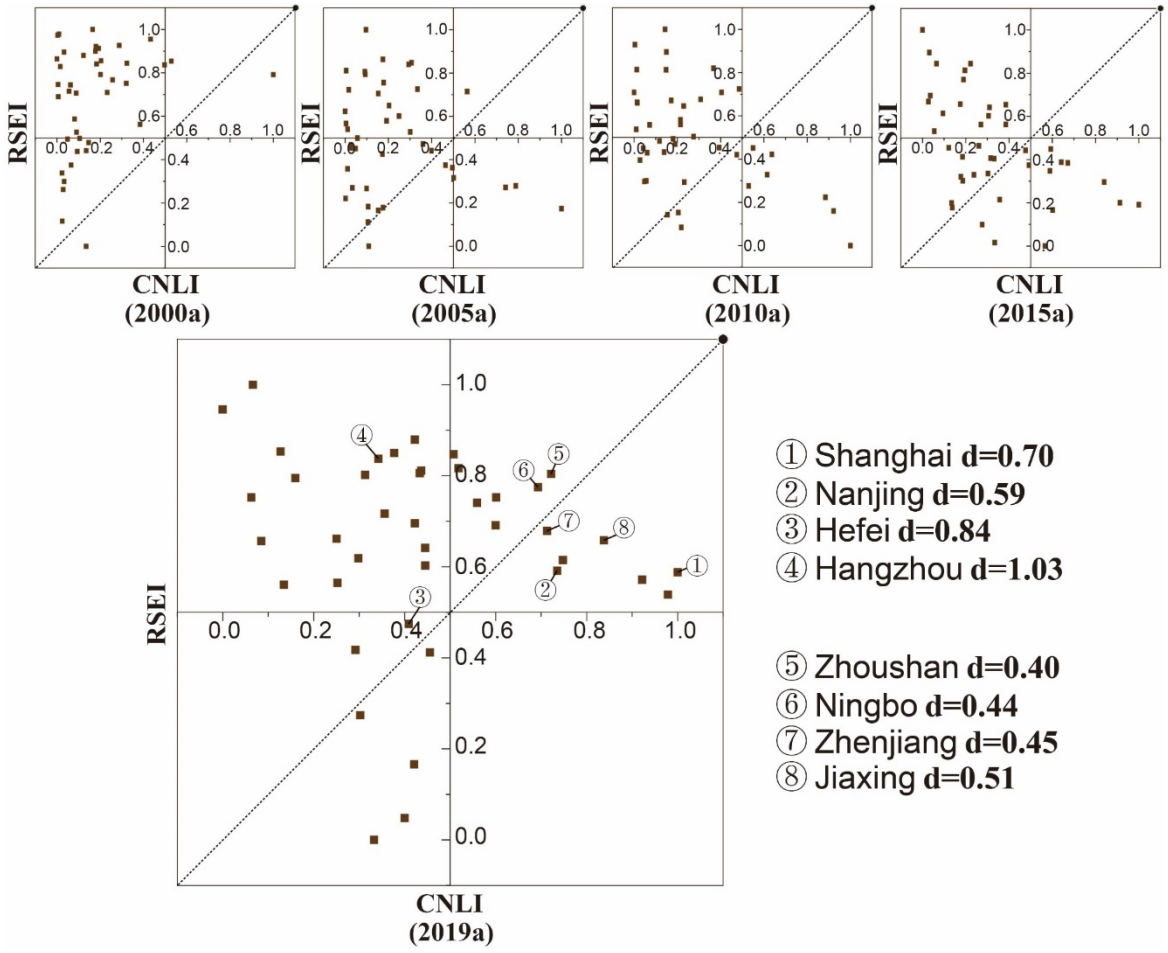

Figure A2.5. Scatter map of "CNLI-RSEI" in YRDUA in 2000-2019.

According to the change of quadrant distribution of coordinate points in the figure, it can be seen that most of the "urbanization-environment" coordinate points in 2000 were concentrated in the second quadrant, which indicates that the CNLI of cities within urban agglomerations was mostly below 0.5 while the RSEI was above 0.5, and they were in the stage of urbanization lagging behind ecological and environmental development. The number of cities in the fourth quadrant increased significantly in 2005, 2010 and 2015, reflecting that the above cities had accelerated their urbanization level (CNLI>0.5) while neglecting the protection of eco-environment (RSEI<0.5), causing the eco-environmental status to lag behind the urbanization development. Since 2016, with the promulgation of the YRDUA Development Plan, YRDUA has increased ecological protection and ecological construction in the region. After several years of benign development, the

fourth quadrant cities shift to the first quadrant in 2019 as the RSEI index rises, and urbanization development and eco-environmental conditions were at a well-coupled and coordinated stage.

References

Chen, M., Liu, W., Lu, D., Chen, H. & Ye, C. (2018) Progress of China's new-type urbanization construction since 2014: A preliminary assessment. Cities 78, 180-193.

Feng, H., Zhao, X., Chen, F. & Wu, L. (2014) Using land use change trajectories to quantify the effects of urbanization on urban heat island. Advances in Space Research 53, 463-473.

Guan, X., Wei, H., Lu, S., Dai, Q. & Su, H. (2018) Assessment on the urbanization strategy in China: Achievements, challenges and reflections. Habitat International 71, 97-109.

Jin, M.S., Kessomkiat, W. & Pereira, G. (2011) Satellite-observed urbanization characters in Shanghai, China: Aerosols, urban heat island effect, and land–atmosphere interactions. Remote Sensing 3, 83-99.

Li, G., Zhang, X., Mirzaei, P.A., Zhang, J. & Zhao, Z. (2018) Urban heat island effect of a typical valley city in China: responds to the global warming and rapid urbanization. Sustainable cities and society 38, 736-745.

Liu, T., Liu, H. & Qi, Y. (2015) Construction land expansion and cultivated land protection in urbanizing China: Insights from national land surveys, 1996–2006. Habitat International 46, 13-22.

Liu, W., Jiao, F., Ren, L., Xu, X., Wang, J. & Wang, X. (2018) Coupling coordination relationship between urbanization and atmospheric environment security in Jinan City. Journal of Cleaner Production 204, 1-11.

Qian, J., Peng, Y., Luo, C., Wu, C. & Du, Q. (2016) Urban land expansion and sustainable land use policy in Shenzhen: A case study of China’s rapid urbanization. Sustainability 8, 16.

Wang, S., Gao, S., Li, S. & Feng, K. (2020) Strategizing the relation between urbanization and air pollution: empirical evidence from global countries. Journal of Cleaner Production 243, 118615.

Wang, Y. & Zhao, T. (2018) Impacts of urbanization-related factors on CO_2 emissions: evidence from China's three regions with varied urbanization levels. Atmospheric Pollution Research 9, 15-26.

Zhang, G., Wang, J., Wu, K. & Xu, Z. (2020) Spatial-temporal characteristics and influencing factors of coordination between economic and environmental development of three major urban agglomerations in China. Geographical Research 39, 272-288.

Zhou, X. & Chen, H. (2018) Impact of urbanization-related land use land cover changes and urban morphology changes on the urban heat island phenomenon. Science of the Total Environment 635, 1467-1476.